15:28:35 OCA PAD INITIATION - PROJECT HEADER INFORMATION 02/07/89

FILE UNDER E-21-668

Active

Project #: A-8290 Cost share #: Rev #: 0
Center # : R6440-000 Center shr #: OCA file #:
Work type : RES
Contract#: 57-6152 Mod #: Document : CONT
Prime #: Contract entity: GTRC

Subprojects ? : N
Main project #: E-21-668

Project unit: EML-PSD Unit code: 01.021.322
Project director(s):
MEEKS E L EML-PSD (404)894-3420

Sponsor/division names: SANDIA NAT'L LABS / WESTERN ELECTRIC CO INC
Sponsor/division codes: 240 / 003

Award period: 871217 to 890316 (performance) 890316 (reports)

Sponsor amount	New this change	Total to date
Contract value	4,000.00	4,000.00
Funded	4,000.00	4,000.00
Cost sharing amount		0.00

Does subcontracting plan apply ?: N

Title: DESIGN AND FABRICATION OF HIGH EFFICIENCY SILICON SOLAR CELLS

PROJECT ADMINISTRATION DATA

OCA contact: David B. Bridges 894-4820

Sponsor technical contact

JAMES GEE
(505)844-7812
SANDIA NATIONAL LABORATORIES
P.O. BOX 5800
ALBUQUERQUE, NM 87185-5800

Sponsor issuing office

E.B. UNDERHILL
(505)844-5174

SAME

Security class (U,C,S,TS) : U
Defense priority rating : DMS/R1
Equipment title vests with: Sponsor X GIT

ONR resident rep. is ACO (Y/N): N
GOVT supplemental sheet

Administrative comments -
SUBPROJECT INITIATION DTD 1/23/89; MAIN PROJ: E-21-668; PERIOD OF PERFORMANCE 1/1/89 THRU 3/16/89; TRANSFER $4000 FROM MAIN PROJECT;

GEORGIA INSTITUTE OF TECHNOLOGY
OFFICE OF CONTRACT ADMINISTRATION

NOTICE OF PROJECT CLOSEOUT

Date 10/24/89

Project No. E-21-668 Center No. R6440-0A0

Project Director A. Rohatgi School/Lab EE

Sponsor Sandia National Laboratories

Contract/Grant No. 57-6152 GTRC XX GIT ___

Prime Contract No. N/A

Title Design and Fabrication of High Efficiency Silicon Solar Cells

Effective Completion Date 3/16/89 (Performance) 3/16/89 (Reports)

Closeout Actions Required:

___ None
X Final Invoice or Copy of Last Invoice
X Final Report of Inventions and/or Subcontracts - Patent questionnaire sent to P.
___ Government Property Inventory & Related Certificate - Already submitted.
___ Classified Material Certificate
___ Release and Assignment
___ Other

Includes Subproject No(s). A-8290/Meeks/EML // E-25-M37/Dewald/ME

Subproject Under Main Project No. ___

Continues Project No. ___ Continued by Project No. ___

Distribution:

X Project Director
X Administrative Network
X Accounting
2 Procurement/GTRI Supply Services
X Research Property Management
___ Research Security Services
X Reports Coordinator (OCA)
X GTRC
___ Project File
2 Contract Support Division (OCA)
___ Other

GEORGIA INSTITUTE OF TECHNOLOGY
SCHOOL OF ELECTRICAL ENGINEERING
ATLANTA, GEORGIA 30332

TELEPHONE: (404) 894-7337

March 30, 1988

Mr. J. Gee
Sandia National Laboratories
P. O. Box 5800
Albuquerque, NM 87185-5800

Re: Contract No. 57-6152
Project Director: A. Rohatgi

Dear Mr. Gee:

Enclosed please find copies of the Monthly Technical Progress Reports for the periods 12/17/87-1/16/88 and 1/17/88-2/16/88 on the above referenced contract.

If you have any questions, please feel free to contact me.

Sincerely,

Pam Majors
Research Administrator

pm
Enclosures

SLOW POSITRON ANNIHILATION SPECTROSCOPY OF HETERO AND HOMO JUNCTIONS OF GaAs BASED SEMICONDUCTOR THIN FILMS

R.L. Frost, A.B. DeWald, J.P. Schaffer, and A. Rohatgi

Georgia Institute of Technology, Atlanta, 30332

B. Nielsen and K.G. Lynn

Brookhaven National Laboratory, Upton, NY 11973

Slow positron annihilation spectroscopy of an AlGaAs/GaAs thin film heterostructure has been performed as a function of applied external bias. The defect density profile with zero bias indicates the presence of surface trap states and a high concentration of defects at the AlGaAs/GaAs interfaces. The defects are thought to be dislocations created by the lattice mismatch at the interface. Application of an external bias changes the observed Doppler parameter due to an apparent electrical activity of a variety of trapping mechanisms within the film.

Corresponding Author: Robert L. Frost
Nuclear Program/ESM Building
Georgia Institute of Technology
Atlanta, GA 30332
(404)-894-3720
FAX: (404)-894-3120
Verify: (404)-894-6951

I. INTRODUCTION

Positron Annihilation Spectroscopy (PAS), has been applied to the characterization of semiconductor materials over the past two decades. Until recently, the continuous energy distribution of positrons emitted from conventional sources limited the capabilities of the PAS probe to the determination of a spatial average of defect and charge states. However, within the last few years, the development of slow PAS (SPAS), a technique for controlling the positron implantation depth, has provided the means for profiling the local defect and charge distributions in semiconductors from 10Å to several microns below the surface.[1-3] Since SPAS is a noncontact NDE technique with the ability to selectively profile defect distributions and material interfaces, it is potentially powerful analytical tool.

Previous PAS studies using continuous energy positron sources have investigated such diverse phenomena as laser damage and annealing,[4] radiation damage[5-7] and plastic deformation[8] of Si, GaAs, HgCdTe, and other semiconductors. The majority of these studies have been limited to single crystals, although some results have been reported on polycrystalline[9] as well as thin-film semiconductors.[10-14] Very recent SPAS studies have investigated solar-cell heterojunctions[1] and prior substrate conditioning upon the growth of Si on a (100) silicon wafer.[3]

The purpose of this paper is to continue the development of SPAS for profiling multi-layered heterojunctions by investigating

an AlGaAs/GaAs solar cell for which a number of preliminary results have been presented previously.[1] The variable-energy PAS spectra obtained, in the previous work, were quite complex and could not be resolved using a simple gaussian fitting function. Specifically, local minima in the PAS spectra were observed at the AlGaAs/GaAs (window/emitter) and the p-n junction (emitter/base) interfaces. These minima were attributed to space-charge depletion effects, interfacial defects, and local quality of the semiconductor material. A series of experiments have been performed on one of the previous semiconductor structures, as a function of applied bias, in order to delineate the positron/space-charge interactions.

II. EXPERIMENT

The $Al_xGa_{1-x}As$/GaAs (x=0.9, for brevity, we will refer to the structure as AlGaAs) solar cell's structure is summarized in Table I. This device was grown via MOCVD in a Spire MO-450 reactor using trimethyl gallium, trimethyl aluminum, and arsine reactants. Acceptor dopants are Zn, while donors are Si. A rectangular Au contact was deposited around the perimeter of the 872B sample. A grid contact was rejected because of potential interference with the positron measurements. The back contact covered the entire surface. Copper wires were attached to the contacts using silver epoxy. A Hewlet Packard 6281A DC power source was used to apply a variable bias to the solar cell.

Slow PAS responses were investigated for -2.0, zero, and +0.25 volts. The applied voltage was observed to have approximately a ±.05 V drift through the duration of each experiment, possibly due to charge buildup.

The variable-energy positron beam has been described elsewhere.[15] In brief, the system consists of a Na-22 positron source moderated by a single crystal tungsten foil of efficiency ~5 x 10^{-4} and magnetically focused onto the sample. The source end of the chamber is floated at various potentials, providing a beam energy from essentially 0 to 75 keV. Since the primary focus of the experiments was directed towards subsurface features within the solar cell, less stringent vacuum conditions of ≈2 x 10^{-7} Torr were used for all PAS measurements. At each positron implantation energy, 2 x 10^{6} counts (annihilation events) were recorded, with a count rate of 1.7 kHz. The change in the annihilation energy distribution (which is related to the electron momentum distribution) has been calculated using the Doppler S-parameter, which is defined as the number of detected events in a narrow window around 511 keV divided by the total number of detected annihilation events.[16]

III. SPAS MODELING

The data have been modeled using a variation of an analysis used successfully in the investigation of an SiO_2/Si interface.[2]

The implantation profile of positrons, P(z,E) may be described by a Makhovian profile[17]

$$P(z,E) = \frac{d}{dz}[\exp(-z/z_o)^m] \qquad (1)$$

$$z_o = \Gamma(1 + 1/m)\bar{z}$$

$$\bar{z} = (\alpha/\rho)E^n$$

where ρ is the material density, and the constants $\alpha = 4 \pm 0.4$ $\mu g/cm^2$, $n \approx 1.6$, and $m = 2$.[12] The Doppler response, S(E), is found by the summation of the integral of P(z,E) over each layer and weighted by the characteristic S value for that layer. Such an approach assumes the homogeneity of each layer and a negligible positron diffusion coefficient, in addition to the absence of extended interfacial traps and/or electric field effects. However, if positron diffusion across an interface is important, then a model for S(E) incorporating the effects of layer inter-diffusion and interfacial effects is required.[2]

In the AlGaAs/GaAs sample of this study, the resolved S characteristic of the AlGaAs is significantly greater than in the GaAs layers, and is suggestive of a higher defect concentration relative to the GaAs layers.[1] Thus, the positron diffusion length in the AlGaAs layer is assumed to be negligible relative to the GaAs layers. Therefore, both AlGaAs boundaries have the appearance of an extended trap to positrons diffusing towards them from the adjacent GaAs layers (cap and emitter). The

probability that a positron will diffuse out of a p-GaAs layer into the AlGaAs layer is given by

$$P_{d_i}(z) = \exp[-|z-d_i|/L^+] \tag{2}$$

where d_i is the depth of layer i below the surface, and L^+ is the positron diffusion length in p-GaAs (cap and emitter) layers. The fractions of positrons annihilating in the cap, window, and emitter layers (i = 1,2,3) are defined as follows:

$$\varepsilon_1 = \int_0^{d_1} P(z,E)[1 - P_{d_1}(z)]dz \tag{3}$$

$$\varepsilon_2 = \int_{d_1}^{d_2} P(z,E)dz + \int_0^{d_1} P(z,E)Pd_1(z)dz + \int_{d_2}^{d_3} P(z,E)P_{d_2}(z)dz \tag{4}$$

$$\varepsilon_3 = \int_{d_2}^{d_3} P(z,E)[(1 - P_{d_2}(z)]dz \tag{5}$$

For a multilayer system the implantation profile must be modified to account for differences in material densities:

$$P(z,E) = \exp(-(z - \delta_1)^2/(z_o)^2 \tag{6}$$

where δ_i is defined by the requirement of continuous positron transmission:[17]

$$\delta_i = d_i - (z_{oi}/z_{oi-1})(d_i - \delta_{i-1}) \quad (7)$$

The energy dependent Doppler response, S(E), is then defined as:

$$S(E) = \Sigma S_i \varepsilon_i \quad (8)$$

The general trends of S(E) are better described by the above model than in the earlier analysis;[1] however, a much more sophisticated treatment will be necessary to account properly for localized defect, matrix, and compositional discontinuities within the layers and at layer interfaces.

IV. RESULTS

The measured S(E) responses as a function of applied bias have been plotted for 0 and -2 volts (Figure 1), and 0 and +.25 volts (Figure 2). The error bars result from a statistical analysis alone. Doppler S-parameter data may be statistically described by a binomial distribution[18] representing photons that either fall inside or outside of the fixed energy window about 511 keV. Therefore, the mathematical uncertainty is defined as $[S(1-S)/N]^{1/2}$, where N is the total number of observations

$\approx 2 \times 10^6$ (counts). The uncertainty is approximately ±.00035 for all observed S(E) values.

The forward and reverse biases produced radically different results in the near surface region. Away from the surface region the reverse bias curve differs from the zero bias by an amount that is a function of distance, while the forward bias curves differ only in the near surface and AlGaAs regions.

The fine structure of the zero-bias S(E) profile of this study is in good agreement with zero-bias measurements from the previous study,[1] even though it is highly unlikely the same spot on the solar cell surface has been sampled. Thus, it appears that the sharper spectral details are reproducible, and are not random statistical artifacts.

The continuous curve in Figure 1 for zero-bias is the best fit obtained (through the emitter layer) according to the theoretical model described in the text. The SPAS model values used for the zero-bias fit are $S_1 = .484$, $S_2 = .498$, $S_3 = .4845$, $L^+ = .05$ μm, $\alpha = 4.0$, and $n = 1.65$. The -2.0V bias curve has been generated by adding a constant $\delta S = 0.0019$ to each of the S(E) values from the zero-bias fit.

V. DISCUSSION

Comparison of the S(E) response as a function of the applied bias indicates that the changes are nonuniform with respect to zero-bias. The nonuniformity shown in Figure 1 has

been made more apparent since the curve generated by adding a constant to the zero-bias fitted S(E) curve is insufficient to explain the observed differences, especially at the homo- and heterojunctions. This indicates that a number of different effects may be responsible for the applied bias S_i characteristic values. The difference between the reverse and zero bias is smallest near the p-n junction and largest in the AlGaAs layer. In contrast, the only differences observed between forward and zero bias occur about the AlGaAs layer.

A systematic rise in the characteristic S_i values could result from an increase in free carrier electron concentration. Excess free carriers are generated by the application of an external bias and by raising the temperature of the sample. In a p-type region, electrons are the minority carrier; their concentration varies as the exponential of the applied bias V_A, increasing by 5 orders of magnitude with a forward bias of +.25 volts. However, due to the high doping levels in the 872B sample, the minority carrier electron concentration at equilibrium is only $10^{-4}/cm^{-3}$. Thus an increase of 5 orders of magnitude results in a concentration of only $10/cm^{-3}$, which is negligible compared to a total electron concentration of $10^{23}/cm^3$. Additionally, application of a reverse bias would actually decrease this concentration, decreasing the S_i values, which is in contradiction to the observed trends. Free carrier differences caused by varying doping levels and dopant types

have been previously observed to have a negligible effect on the positron lifetime in GaAs.[19]

The intrinsic carrier concentration n_i is a strong function of temperature. The voltage-current relationship for the sample was measured, and indicates a maximum heat dissipation rate of ≈.17 watts. Assuming only radiative heat transfer, a steady state temperature of ≈77 C is found. This is actually a very conservative value, since the method by which the sample was mounted permitted significant conductive transfer as well. At 77 C, Sze[20] lists an intrinsic carrier concentration of $n_i \approx 5 \times 10^8$ /cm^3, resulting in a minority carrier electron concentration of the order of 1/cm^3, which is negligible compared to the total electron concentration. Thus, an increase in minority carrier electron concentration by heating or bias effects is expected to be insignificant for the experimental conditions employed.

The complex spectra near the AlGaAs/GaAs heterojunction and the p-n homojunction indicates the junction regions play a key role in the S_i response. The electric field generated in the depletion region associated with the p-n junction may be the reason for the S_i behaviour in the emitter layer for reverse bias. Assuming the depletion approximation is valid, the width of the depletion region and the p-side electric field for a step junction are given by:[20]

$$W = \frac{2\varepsilon(V_{bi} - V_A)(N_A + N_D)}{qN_AN_D} \qquad (8)$$

$$E(x) = \frac{-qN_A(x_p + x)}{\varepsilon} \qquad (9)$$

where V_A and V_{bi} are respectively the applied potential and built in potential, N_A and N_D are the acceptor and donor doping levels, ε is the dielectric constant for GaAs, and q is the charge of an electron. E(x) on the n-side is given by a similar expression. Applying a reverse bias ($V_A < 0$) increases the width of the depletion region, and increases the strength of the electric field, while a forward bias will have the opposite effect. With a reverse bias of 2 volts the depletion width is $\approx$.16 μm, and the electric field strength is on the order of 10^5 V/cm. Since $E(x) < 0$ for the entire region, eV positrons implanted in or near the depletion region will be swept back toward the AlGaAs layer. This anisotropic drift coupled with a positron sink in the AlGaAs layer could generate an unbalanced positron current directed toward the presumably more defective window, resulting in an artificially enhanced S_1 value in the emitter. Figure 1 shows an increased S(E) value in the emitter layer for the reverse bias case, including a smoothing effect in the depletion region itself. Figure 2 shows no significant rise in S(E) in the emitter region for forward bias, consistent with a decreasing depletion region and electric field.

The value of S(E) at the surface for zero bias is raised above the rest of the cap layer, most likely due to the presence of extended defect trap states, which are known to exist at a

semiconductor surface. Figure 1 shows an increased S(E) at the surface for the reverse bias case, while Figure 2 shows a decreased surface S(E). This effect is most likely caused by band bending at the semiconductor-metal contact interface. A change in the charge state of defects has been previously observed by Dannefaer et al[21] when the Fermi level is moved by heating the sample. Application of a reverse bias causes a local change as the valence band bends up toward the Fermi level, converting some trapping levels to neutral states. The free electrons created in this process have a lower energy than the trapped electrons, and thus result in a higher S value when they annihilate. In contrast, a forward bias bends the conduction band away from the Fermi level, creating new negative trap states, and, by analogy, decreasing S. The minima in S(E) in the cap layer in both curves in Figure 1 most likely corresponds to the characteristic value S_1 for this layer. It appears as a minima simply because it is sandwiched between defective surface and interfacial regions.

The positron behaviour at the surface may be modeled by the addition of a separate surface state in analogous treatment as prescribed in Section III. Both the characteristic S_1 value and the "depth," d_1, that surface traps extend into the cap layer will depend the valence band bending induced by the applied bias.

For all values of applied bias, the maximum S_1 is in the AlGaAs layer. The lattice constant of $Al_xGa_{1-x}As$ is a function of the fraction x of aluminum present in the matrix. The lattice

parameter mismatch at the AlGaAs/GaAs interface may result in the production of a significant interfacial dislocation density. Thus, the characteristic S_1 value of the AlGaAs layer may result from a high interfacial defect trapping rate. Dlubek et al[22] have estimated that positron trapping at dislocations in GaAs becomes significant at a density of $\approx 10^6/cm^2$. The enhancement with applied bias of S_1 in the AlGaAs layer is not understood at this time, and will be the subject of future study.

Summary

The Doppler response function S(E) in the AlGaAs/GaAs structure studied has been modeled by modifying the implantation profile to account for diffusion of positrons to the presumably more defective AlGaAs layer. This model reproduces the general trends in S(E), but fails to account for the fine structure or surface behaviour. A systematic rise in S(E) with applied external bias cannot be attributed to a change in minority carrier electron concentration, due to the small magnitudes of the concentrations involved. The enhancement of S_1 in the emitter region for reverse bias may be caused by an anisotropic drift of positrons towards the AlGaAs layer as a result of the depletion region electric field. An abundance of defect levels at the surface of the cap layer causes an enhanced S_1 value at equilibrium. Band bending with application of an external bias

results in an increase in the surface S_1 for reverse bias, and a decrease for forward bias.

A full realization of the SPAS's potential for characterizing multi-layered semiconductors will require delineation of the effects at the heterojunction interface and at the p-n junction, a more accurate estimate of the positron diffusion length in AlGaAs and GaAs, and improved statistics of the finer details of the S(E) response function. Since SPAS is a relatively new technique, correlation with established techniques should be made wherever possible. TEM and X-ray studies of the AlGaAs/GaAs interface would provide insight into the dislocation density and the extent of the defective regions, while DLTS could identify trapping levels. Finally, a model which can properly treat interfaces, bulk positron diffusion, and positron drift in an electric field will be required to properly deconvolute the data. Ongoing studies of AlGaAs/GaAs and other semiconductor structures are expected to address these issues in the near future.

Acknowledgements

The authors would like to thank Mike Harris of the Georgia Tech Research Institute for depositing the gold contacts on the sample, and Dr. R.J. Higgins of the Electrical Engineering Department at Georgia Tech for his enlightening discussions. This research was supported in part by the U.S. Department of Energy, Division of Material Sciences, Office of Basic Energy Sciences under contract no. DE/AC02-76CH00016.

References

[1] A.B. DeWald, R.L. Frost, S.A. Ringel, J.P. Schaffer, A. Rohatgi, B. Nielsen, and K.G. Lynn, to be published in J. Vac. Sci. Technol. A.

[2] B. Nielsen, K.G. Lynn, Yen-C Chen, and D.O. Welch, Appl. Phys. Lett., **51**, 1022 (1987).

[3] P.J. Schultz, K.G. Lynn, E. Tandberg, N. Nielsen, T.E. Jackman, L.C. Feldman, J. Bean, and M.W. Denhoff, submitted to Phys. Rev. Lett.

[4] A.P. Druzhkov, I.B. Khaibullin, and R.M. Bayazitov, E.I. Shtyrkov, and L.A. Suslov, Sov. Phys. Semicond., **13**, 574 (1979).

[5] J. C. Bourgoin, H.J. von Bardeleben, and D. Stievenard, Phys. Stat. Sol. (a), **102**, 499 (1987).

[6] K.P. Aref'ev, V.N. Brudnyi, D.L. Budnitskii, S.A. Vorob'ev, and A.A. Tsoi, Sov. Phys. Semicond. **13**, 669 (1979).

[7] S.E. Bochkarev, L.A. Ivanyutin, V.P. Komlev, E.P. Prokop'ev, V.M. Samollov, V.G. Firsov, and Yu. V. Funtikov, Sov. Phys. Solid State, **23**, 118 (1981).

[8] S. Dannafaer, N. Fruensgaard, S. Kupca, B. Hogg, and D. Kerr, Can. J. Phys., **61**, 451 (1983).

[9] P. Hautojarvi, P. Moser, M. Stucky, C. Corbel, and F. Plazaloa, Appl. Phys. Lett., **48**, 809 (1986).

[10] K.P. Aref'ev, S.A. Vorob'ev, and V.G. Stardubov, Sov. Phys. Semicond., **8**, 794 (1974).

[11]A.P. Druzhkov, E.P. Prokop'ev, Y.N. Kuznetsov, A.I. Sidorov, and V.A. Fedorov, Sov. Phys. Semicond., **14**, 119 (1980).

[12]Y.J. He, M. Hasegawa, R. Lee, S. Berko, D. Adler, A. Lung, Phys. Rev. B, **33**, 5924 (1985).

[13]H.E. Schaefer, R. Wurschum, R. Schwarz, D. Slobodin, and S. Wagner, Appl. Phys. A, **40**, 145 (1986).

[14]V.G. Bhide, R.O. Dusane, S.V. Rajarshi, A.D. Shaligram, and S.K. David, J. Appl. Phys., **62**, 108 (1987).

[15]K.G. Lynn, B. Nielsen, and T.H. Quateman, Appl. Phys. Lett., **47**, 239 (1985).

[16]I.K. MacKenzie, J.A. Eady, and R.R. Gingerich, Phys. Lett., **33A**, 279 (1970).

[17]A. Vehanen, K. Saarinen, P. Hautojarvi, and H. Huomo, Phys. Rev. B, **35**, 4606 (1987).

[18]J.L. Campbell, Appl. Phys., **13**, 365 (1977).

[19]O. Takai, Y. Hisamatsu, N. Owada, H. Ishimura, K. Hinode, S. Tanigawa, and M. Doyama, Phys. Lett. **76A**, 157 (1980).

[20]S.E.Sze, Physics of Semiconductors, (Wiley-Interscience, New York, 1981).

[21]S. Dannefaer, B.G. Hogg, and D.P. Kerr, Phys. Rev. B, **30**, 3355 (1984).

[22]G. Dlubek, O. Brummer, F. Plazaola, and P. Hautojarvi, J. Phys. C, **19**, 331 (1986).

TABLE 1

SOLAR CELL HETEROJUNCTION STRUCTURE *

LAYER	MATERIAL	THICKNESS (μm)	TYPE	DOPING
Cap	GaAs	0.143	p^+	8.0×10^{19}
Window	AlGaAs	0.05	p^+	1.0×10^{18}
Emitter	GaAs	0.5	p	1.5×10^{18}
Base	GaAs	2.0	n	2.0×10^{17}
Buffer	GaAs	2.0	n	2.0×10^{18}
Substrate	GaAs			

* (the above structure was previously identified as $872B^1$)

Figure Captions

Figure 1. Results of SPAS profiling of the AlGaAs/GaAs structure with no bias and 2 volts reverse bias applied. The lower dashed curve represents the best fit to the zero bias response. The upper dashed curve was generated by adding 0.0019 to the characteristic S_i values used to generate the lower curve.

Figure 2. Forward bias (+0.25 volt) SPAS response profile compared to the zero bias case.

FIGURE 1

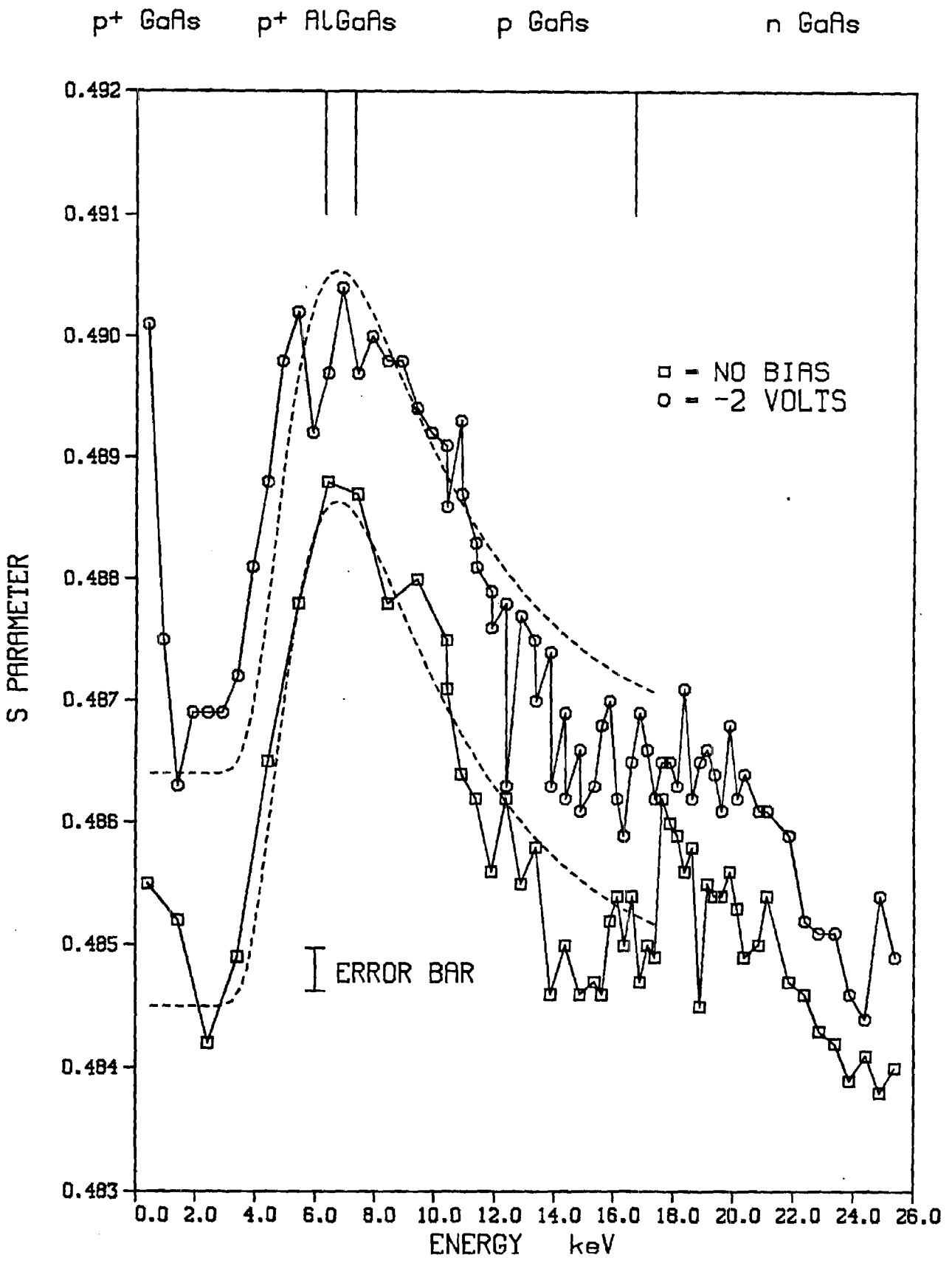
p+ GaAs
p+ AlGaAs
p GaAs
n GaAs
0.492
0.491
0.490
0.489
0.488
0.487
0.486
0.485
0.484
0.483
S PARAMETER
□ = NO BIAS
o = -2 VOLTS
ERROR BAR
0.0 2.0 4.0 6.0 8.0 10.0 12.0 14.0 16.0 18.0 20.0 22.0 24.0 26.0
ENERGY keV

FIGURE 2

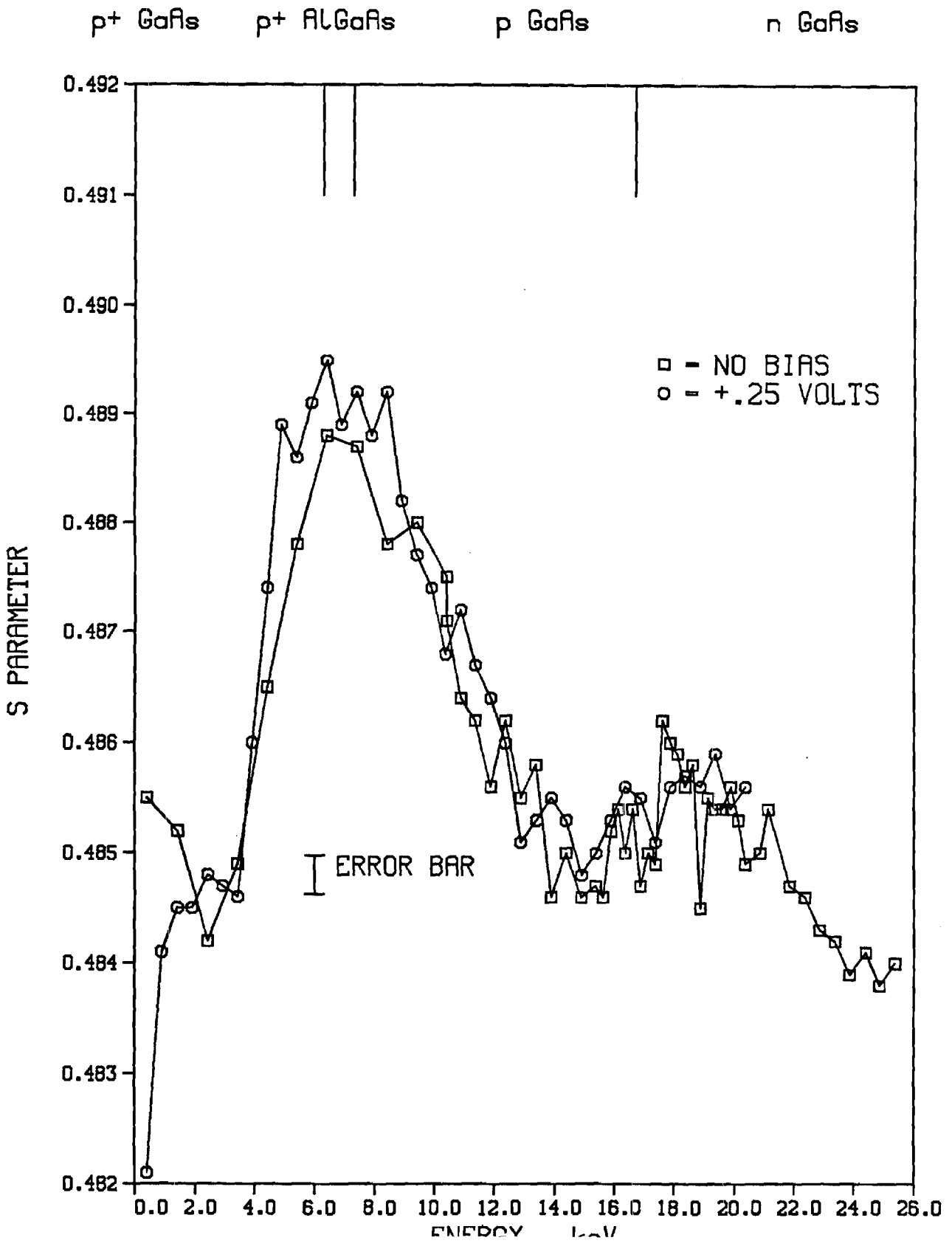
p+ GaAs
p+ AlGaAs
p GaAs
n GaAs
0.492
0.491
0.490
0.489
0.488
0.487
0.486
0.485
0.484
0.483
0.482
S PARAMETER
□ = NO BIAS
o = +.25 VOLTS
ERROR BAR
0.0 2.0 4.0 6.0 8.0 10.0 12.0 14.0 16.0 18.0 20.0 22.0 24.0 26.0
ENERGY keV

GEORGIA INSTITUTE OF TECHNOLOGY
SCHOOL OF ELECTRICAL ENGINEERING
ATLANTA, GEORGIA 30332

TELEPHONE: (404) 894-7337

March 30, 1988

Mr. J. Gee
Sandia National Laboratories
P. O. Box 5800
Albuquerque, NM 87185-5800

Re: Contract No. 57-6152
Project Director: A. Rohatgi

Dear Mr. Gee:

Enclosed please find copies of the Monthly Technical Progress Reports for the periods 12/17/87-1/16/88 and 1/17/88-2/16/88 on the above referenced contract.

If you have any questions, please feel free to contact me.

Sincerely,

Pam Majors
Research Administrator

pm
Enclosures

Parameter Modeling of Textured High Efficiency Silicon Solar Cells

Arlynn W. Smith, Stanley C. Neel, Ajeet Rohatgi
Georgia Institute of Technology

Extended Abstract

Methods of trapping weakly absorbed light into a cell with a high lifetime (1-10 msec) base can lead to practically achievable one sun efficiencies approaching 25%. Recently attempts have been made to determine the effectiveness of different trapping schemes. At the same time the material quality has improved to the point where lifetimes greater than 10 msec are possible. The purpose of this paper is to model the light trapping induced improvements for various promising surface geometries in combination with the very high lifetime materials to design ≥ 25% efficiency one sun cells. A ray tracing program created generation profiles for regular pyramid, lambertian, and perpendicular slat texturing geometries, these profiles were used as input into PC-1D model to design high efficiency silicon solar cells.

One step in attempting to increase the cell efficiency due to textured surfaces would be to increase the short-circuit current without making a sacrifice in either the fill factor or open-circuit voltage. To increase the short-circuit current the cell must appear optically thick to the incoming radiation. This may be accomplished by making the cell physically thick or by incorporating some form of light trapping, in which photons remain within the cell by internal reflection until absorbed. Physically thickening the cell would increase the amount of recombination losses thereby reducing the voltage and fill factor. The cell designer's only choice is to implement light trapping to improve the short-circuit current.

Given that the cell designer must employ light trapping, the next question arises as to which geometry will produce the best results. The maximum short-circuit current as a function of cell thickness for various texturing geometries is shown in reference 1. It shows that lambertian and perpendicular slats geometry give the best results. To model this increase in the short-circuit current the generation profile must be altered to account for the photons which have been trapped. This modification has already been introduced for lambertian surfaces using PC-1D[2], this method has been extended for two additional geometries, pyramids and perpendicular slats, using information from reference 1. This will be accomplished by using Monte Carlo methods in a ray tracing program. The increased fluxes which are required to simulate the lambertian and perpendicular slats geometries are given in Table 1.

Figure 1 shows that as the cell thickness is increased the short-circuit current increases. Yet, figure 2 shows that the efficiency reaches its maximum at a base thickness of

approximately 200 microns, for the Lambertian surface texturing. As the cell thickness is increased the recombination in the base region decreases the open-circuit voltage, figure 3. Therefore, it is not enough just to increase the short-circuit current by light trapping, it is also critical to increase the material quality to achieve greater efficiencies. Figure 2 shows the gain in efficiencies that were calculated for a lambertian textured cell when the minority carrier lifetime was raised from 5 msec to 10 msec. Figure 4 shows the efficiencies which were calculated for the best cell design using both lambertian and perpendicular slats trapping geometries, the values of the current for the perpendicular slats geometry are taken from reference 1.

Modeling cells using PC-1D and incorporating the light trapping and high lifetimes into the calculations should give a clear picture of what efficiencies are obtainable with current technology. By varying certain cell design parameters, some idea of the effects that parameter has on cell efficiency may be gained. In most cases the base lifetime effect was calculated at several values in case the cell processing degraded it from it initial value. This paper shows that a) ray tracing can be incorporated into PC-1D model, b) different surface geometries introduce different light trapping schemes, c) the efficiency does not depend upon the short-circuit current alone but on the short-circuit current and the proper thickness, d) efficiencies of approximately 25% can be obtained with perpendicular slats and 10 msec lifetime material.

This work was supported in part by DOE/SERI on contract number XB7-06070-1

1. Green, M., High Efficiency Silicon Solar Cells, Trans Tech Publications, 1987, pp74-77

2. Basore, P.A., Production Efficiency Goals for Silicon Solar Cells, 19th IEEE Photovoltaic Specialists Conference, May 1987

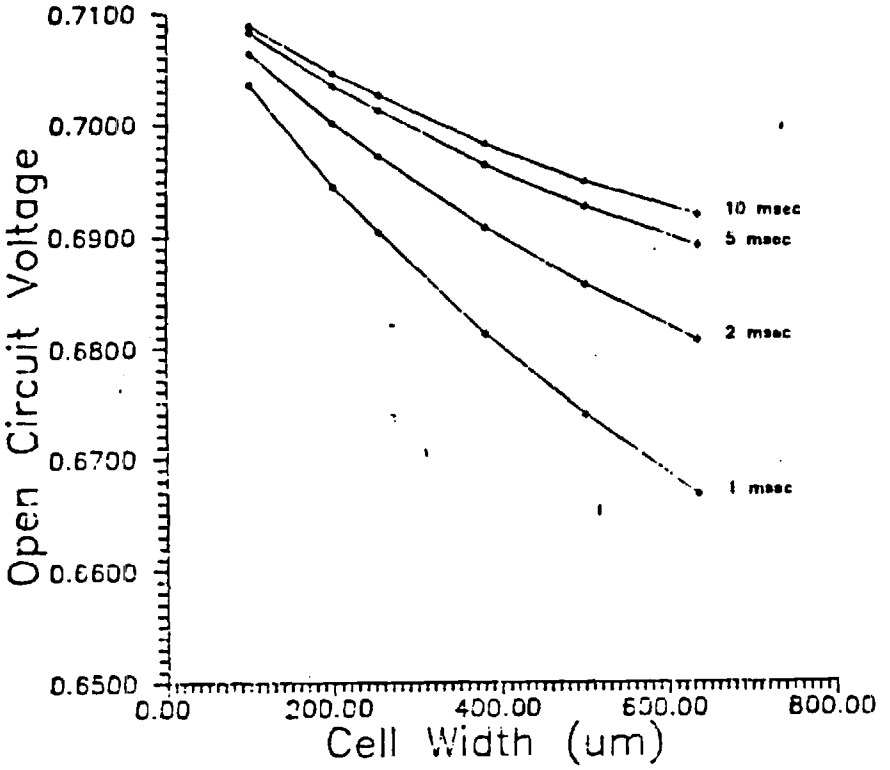

Figure 3 . Open Circuit Voltage as a function of cell width for 200 ohm-cm material with FSRV and BSRV of 100 cm/sec and series resistance of 0.04 ohms

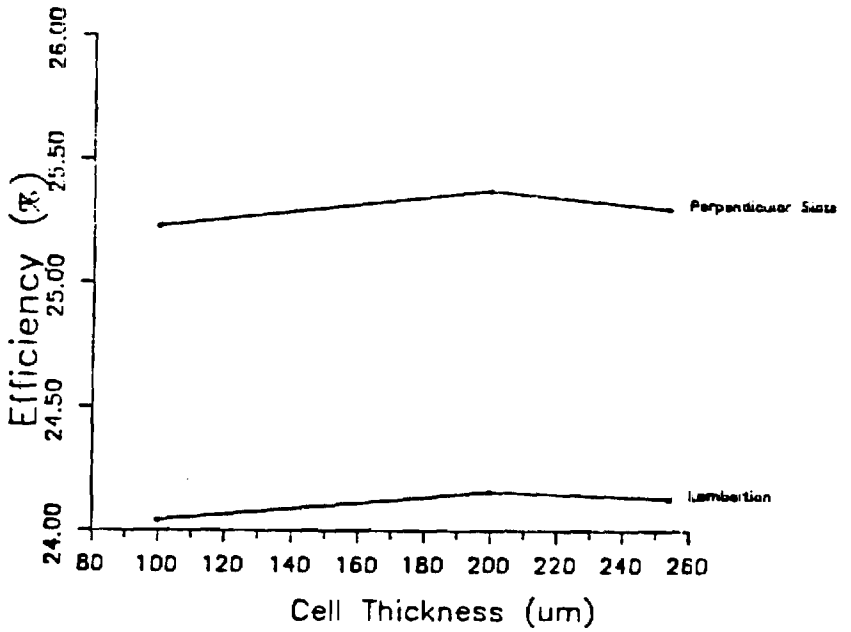

Figure 4. Comparison of perpendicular slots and Lambertian gemometry trapping schemes, the values for the perpendicular slots is from reference 1 while the lambertian is from reference 2.

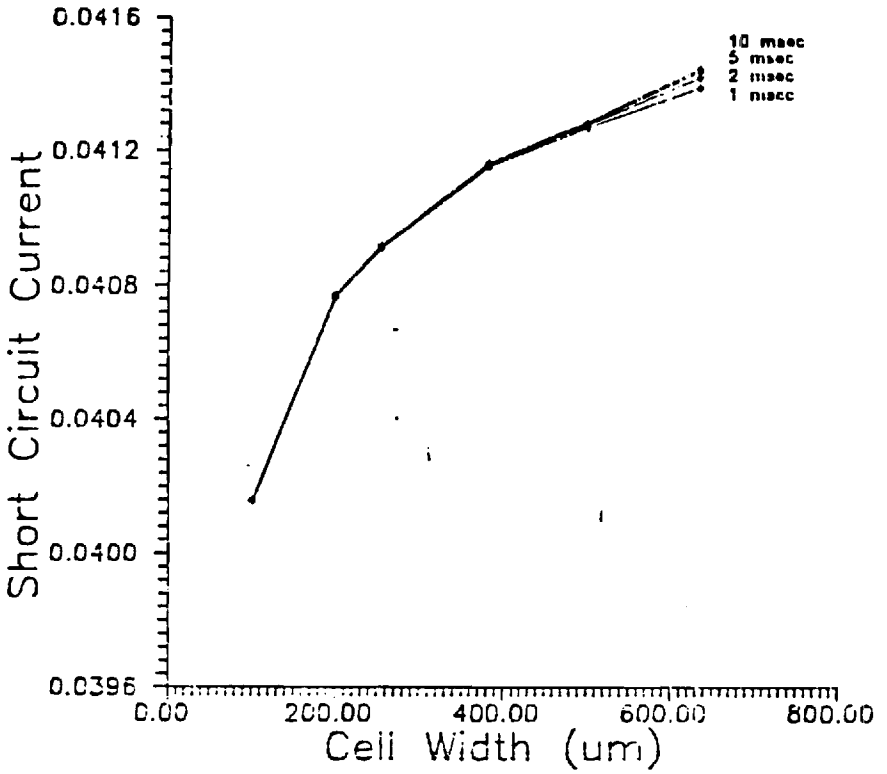

Figure 1 . Short circuit current as a function of cell width for 200 ohm-cm material with FSRV of 100 cm/sec, BSRV of 500 cm/sec, and series resistance of 0.04 ohms.

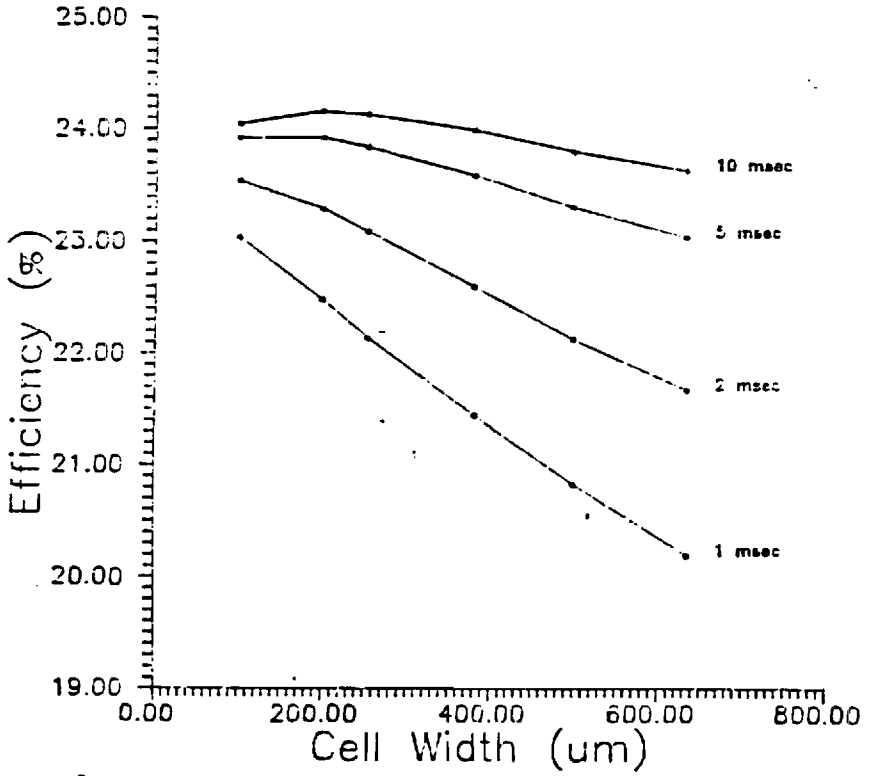

Figure 2 . Efficiency as a function of cell width for 200 ohm-cm material with series resistance of 0.04 ohms and FSRV and BSRV of 100 cm/sec.

GEORGIA INSTITUTE OF TECHNOLOGY
SCHOOL OF ELECTRICAL ENGINEERING
ATLANTA, GEORGIA 30332

TELEPHONE: (404) 894-7337

June 15, 1988

Mr. J. Gee
Sandia National Laboratories
P. O. Box 5800
Albuquerque, NM 87185-5800

Re: Contract No. 57-6152
Project Director: A. Rohatgi

Dear Mr. Gee:

Enclosed please find copies of the Monthly Cost Status Report for the period 5/1/88-5/31/88 on the above referenced contract.

If you have any questions, please feel free to contact me.

Sincerely yours,

Pam Majors
Research Administrator

pm
Enclosures

CONTRACTOR: Complete all spaces and the bottom block.

Sandia National Laboratories

PURCHASING ORGANIZATION Georgia Tech

ALBUQUERQUE, NEW MEXICO 87185
LIVERMORE, CALIFORNIA 94550

J. Gee
Sandia Contracting Representative

MONTHLY COST STATUS REPORT

CONTRACT NO. 57-6152

PERIOD ENDING (1) May 31, 1988

Contractor must forecast as a minimum the first three months, Balance of Fiscal Year, and Subsequent Fiscal Years when costs will be incurred in these months and years.

Contractor must forward this report to reach the Sandia Contracting Representative by the 15th of the month following the Report Period or at such other time as requested by the Sandia Contracting Representative.

TOTAL FUNDS AUTHORIZED		$ 72,448.00
ACTUAL COST INCURRED TO DATE(2)		6,342.39
ESTIMATED COST TO COMPLETE:(3)		
1st MONTH FOLLOWING "PERIOD ENDING" as specified above	6,610.56	
2nd MONTH	6,610.56	
3rd MONTH	6,610.56	
4th MONTH	6,610.56	
5th MONTH		
6th MONTH		
BALANCE OF FISCAL YEAR(4)		
SUBSEQUENT FISCAL YEARS	39,663.33	
TOTAL ESTIMATE TO COMPLETE		66,105.57
TOTAL ESTIMATED COST AT COMPLETION		$ 72,448.00

NOTES:
(1) Last full month for which actual costs are available.
(2) Cost includes applicable fee.
(3) Estimates for costs to be incurred (Do not include commitments), including applicable fee.
(4) Fiscal year is 10/1 through 9/30. Balance of fiscal year means all months remaining in the fiscal year following the 6th month shown on the line above. If the 6th month is September, then balance of fiscal year is 10/1 through 9/30 of the next fiscal year.

Contractor (name and address)	Signature of Contractor's Representative, Date and Phone
Georgia Tech Research Corporation School of Electrical Engineering Georgia Institute of Technology Atlanta, GA 30332	Pam Majors Pam Majors, Research Adm. 404-894-7337 6/15/88

F6432-CS(1-85)

CHARACTERIZATION AND MODELING OF HIGH EFFICIENCY GaAs HETEROFACE SOLAR CELLS

A. Rohatgi and S. A. Ringel
School of Electrical Engineering
Georgia Institute of Technology
Atlanta, Georgia 30332-0250

ABSTRACT

The objective of this research is to improve the basic understanding of internal loss mechanisms in GaAs solar cells, particularly their origin and ultimate influence on design criteria. The development of characterization techniques coupled with computer modeling was found essential to achieve the goal. A methodology consisting of electrical characterization and computer modeling which allows the determination of internal loss mechanisms in an MOCVD grown GaAs p-n heteroface solar cell is presented in this paper. Parameters of particular interest are minority carrier lifetimes, bulk and interfacial recombination velocities, and deep levels. The cell performance is evaluated on the basis of these internal recombination parameters through extensive computer modeling. Device modeling is also used to show how a complete understanding of lifetime limiting mechanisms in GaAs coupled with clever cell design can result in cell efficiencies in excess of 25%.

MOCVD grown p-n heteroface solar cells were subjected to depth-resolved surface photovoltage, DLTS, I-V-T, spectral response, light and dark I-V measurements, followed by PC-1D and recombination velocity modeling to provide guidelines for higher efficiency cells. The cell structure consisted of 0.5 μm p-type emitter (2×10^{17} cm^{-3}) on a 2 μm n-type base (2×10^{17} cm^{-3}) with an n+ buffer layer and a p+ $Al_xGa_{1-x}As$ ($x = 0.90$) passivating window layer. This particular cell had $V_{oc} = 1.01$ V, $J_{sc} = 24.5$ mA/cm^2, and an efficiency of 21.2%.

Depth-resolved DLTS measurements revealed a hole trap in the n-base at $E_v + 0.91$ eV with trap density increasing as we approach the p-n interface. This was further supported by SPV measurements taken at different depths in the device using an electrochemical profiler. I-V-T measurements confirmed that this trap controls the space charge (J_{02}) component of the cell leakage current. Transformed I-V data indicates that $J_{01} \sim J_{02}$ at the cell operating point, hence removal of this trap should appreciably reduce the cell leakage current and improve performance.

To determine the surface recombination velocity and minority carrier lifetime in this cell, the PC-1D model was used first to match the measured spectral response. A net base lifetime of 8 ns with a front surface recombination velocity (FSRV) of 1.25×10^5 cm/s was necessary for the good match. The validity of these choices was checked using an effective recombination velocity (S_e) model which calculates S_e everywhere in the cell based on FSRV, BSRV, and lifetime. From this, J_{0B} and J_{0E} were found to be 0.89×10^{-19} and 0.51×10^{-19} A/cm^2, respectively, resulting in $J_{01} = J_{0B} + J_{0E} = 1.40\times10^{-19}$ A/cm^2, in close agreement with the measured J_{01} of $\sim1.30\times10^{-19}$ A/cm^2, supporting the selection of FSRV and lifetime. The large emitter component (33% of J_{01}) suggests that this cell performance can also be improved by better emitter design or lower FSRV. The above values of S and T were fed into the PC-1D model again to calculate J_{sc}, V_{oc}, and efficiency for this cell. An excellent match between the experimental data and calculated values was obtained, reinforcing our analysis.

Further modeling showed that the efficiency of this cell can be increased to 24.1% by moderate front surface passivation (FSRV = $1x10^4$ cm/s) and improving T_b to 15 ns. BSRV was found to have negligible effect on this device structure. Design optimization showed that ~25% efficient cells can be achieved by thinning the base and buffer regions, passivating the back surface, and optimizing the doping concentration throughout the device structure.

The MOCVD grown GaAs p-n heteroface solar cell used here is shown in Figure 1. Depth-resolved SPV measurements, Figure 2, were performed to study material uniformity. Positron annihilation spectroscopy (PAS) was used to reveal defect profile in the device with the lineshape parameter, S, as a function of implant energy (depth) shown in Figure 3. DLTS measurements indicates the presence of a deep level in the n-base shown in Figure 4. This same trap was detected by I-V-T technique, Figure 5, indicating it controls the J_{02} leakage current component. Figure 6 shows the transformed I-V plot separating diffusion and space charge components. The measured and modeled (PD-1D) spectral response are compared in Figure 7. Based on the lifetime necessary for the spectral response match, the effective recombination velocity, S_e, was plotted in Figure 8 for different values of FSRV and BSRV. Figure 9 shows the effect of material quality, i.e., lifetime, on S_e for the device structure in Figure 8. The S_e plots for an optimized heteroface design is shown in Figure 10 for high quality material (T_b = 20 ns) and different values of FSRV and BSRV. The J_{0E} and J_{0B} leakage components indicated are for a 25% efficient cell. Table 1 shows the progression from the actual cell with 21.2% efficiency to an optimized 25% cell using PC-1D modeling.

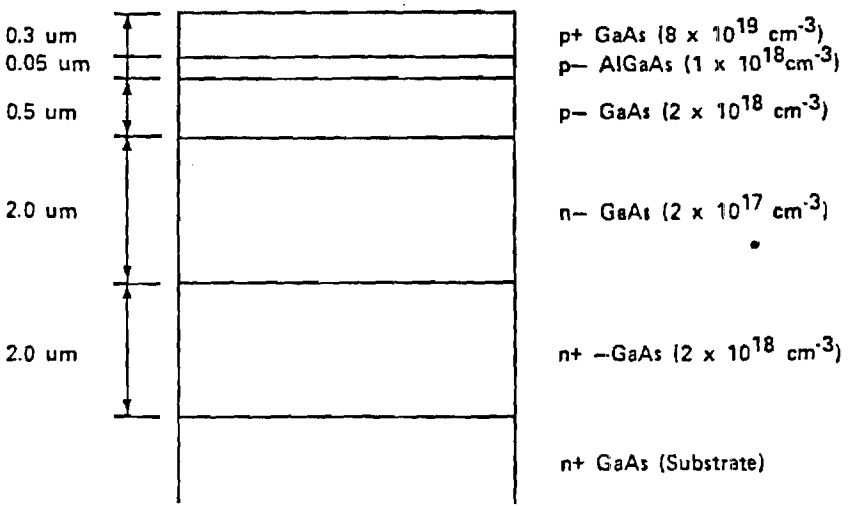

GaAs solar cell structure used in these experiments

V_{oc} = 1.013V J_{sc} = 24.5 mA/cm^2

F.F. = 0.867 Eff = 21.2%

Figure 1. GaAs p-n heteroface solar cell structure used in this study.

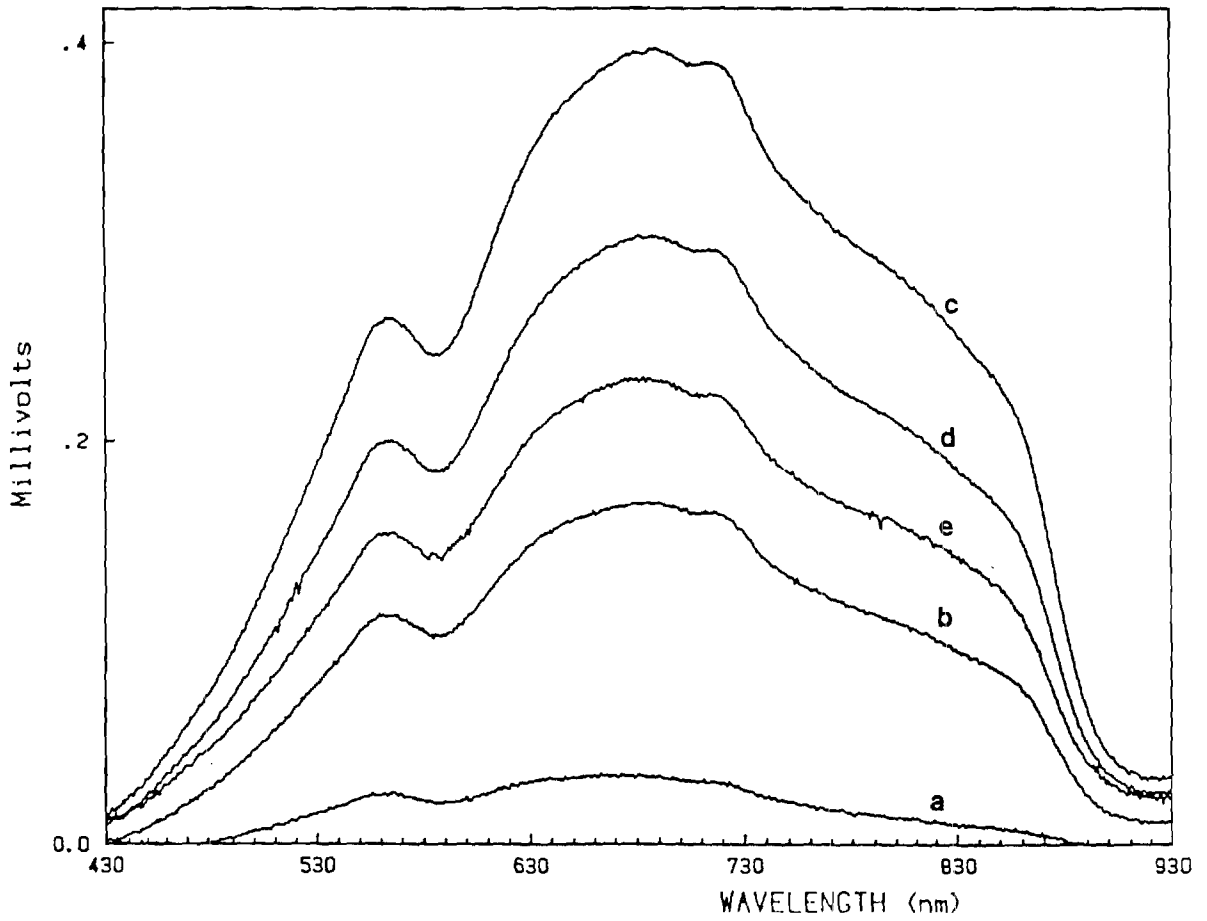

Figure 2. SPV spectra taken at different etch depths in the device. Etch depths are: a = 0.12 μm; b = 0.14 μm; c = 0.21 μm; d = 0.30 μm; e = 0.42 μm.

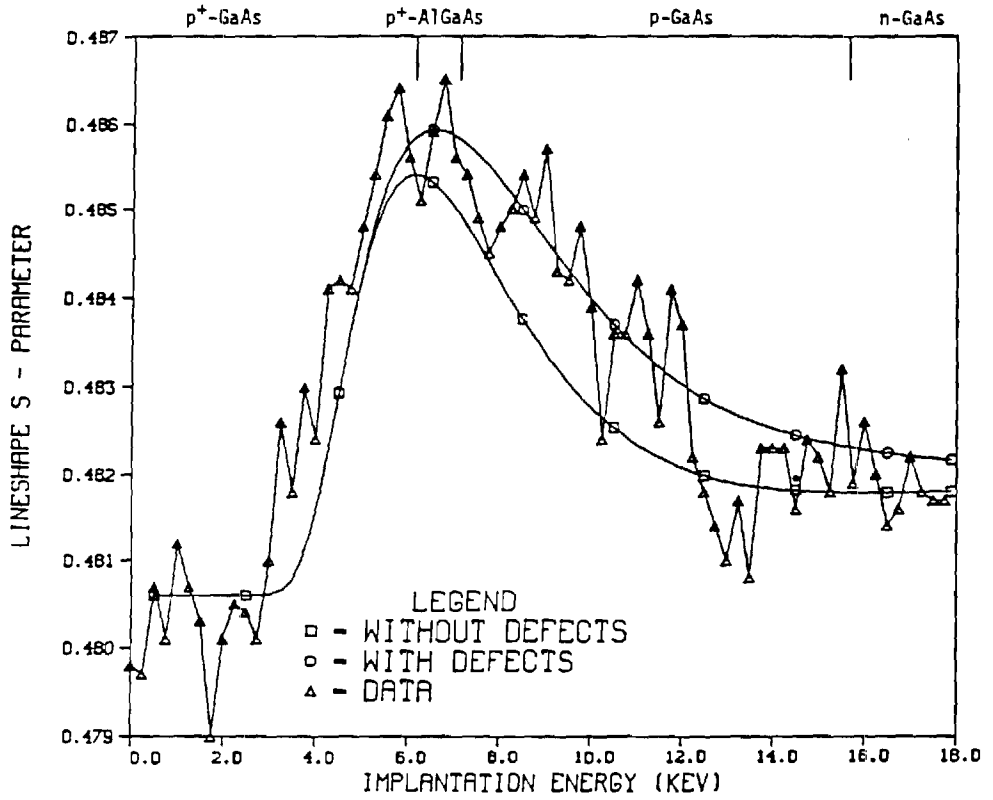

Figure 3.

Variation of positron line-shape parameter, S, with position implant energy, i.e., depth into device structure.

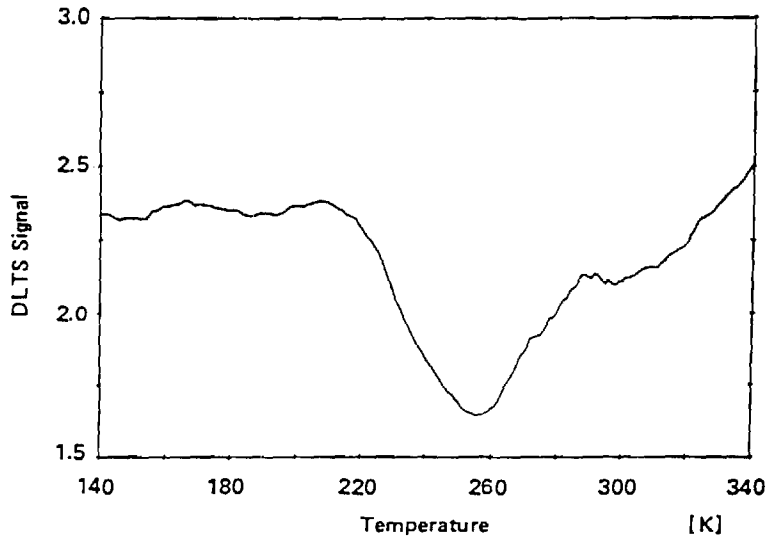

(a)

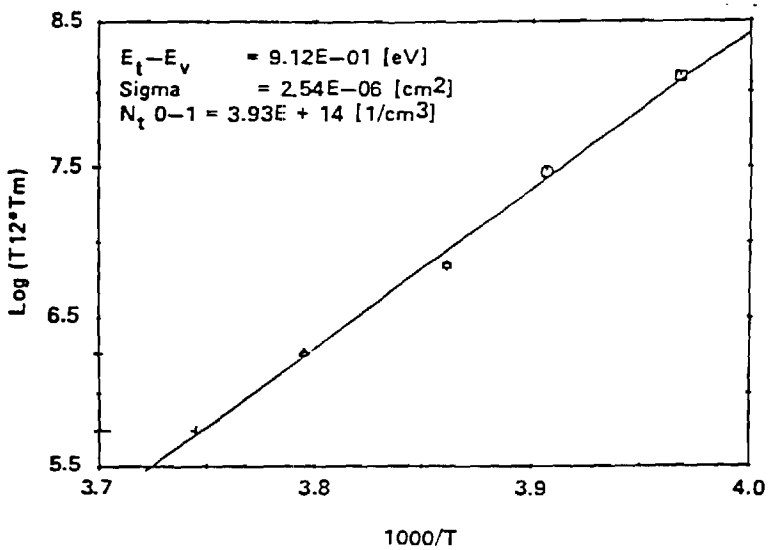

(b)

Figure 4.

DLTS spectrum (a) and Arrhenius plot (b) of a trap located in the n-base near the p-n junction.

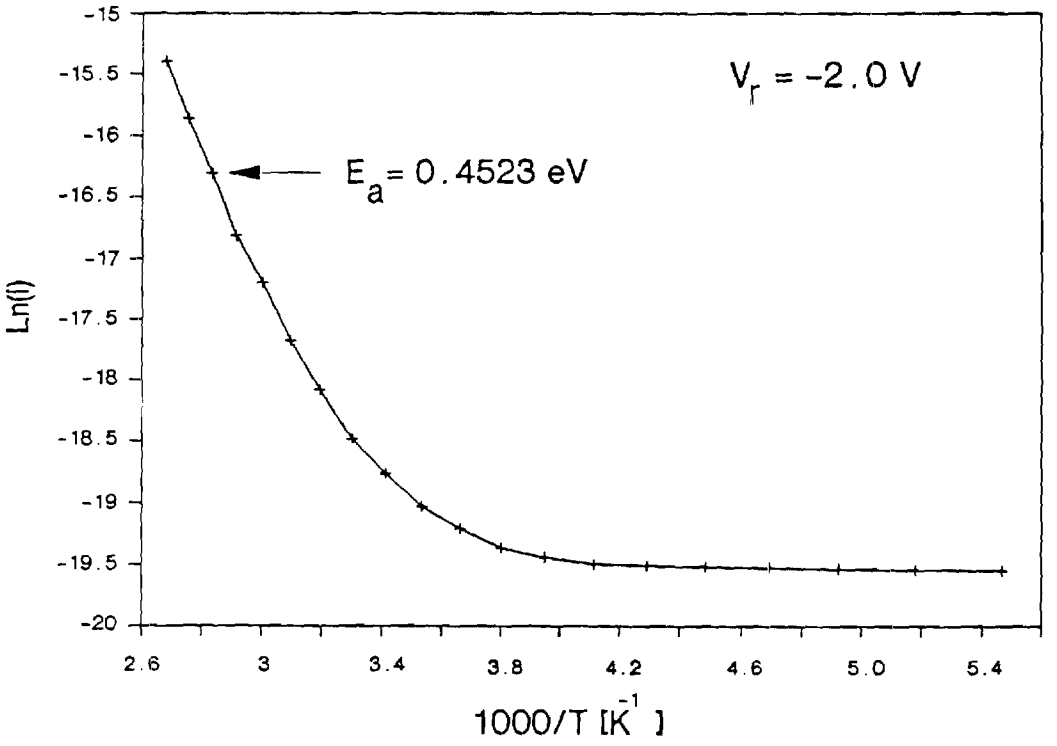

Figure 5. I-V-T plot indicating activation energy of deep level controlling the leakage current.

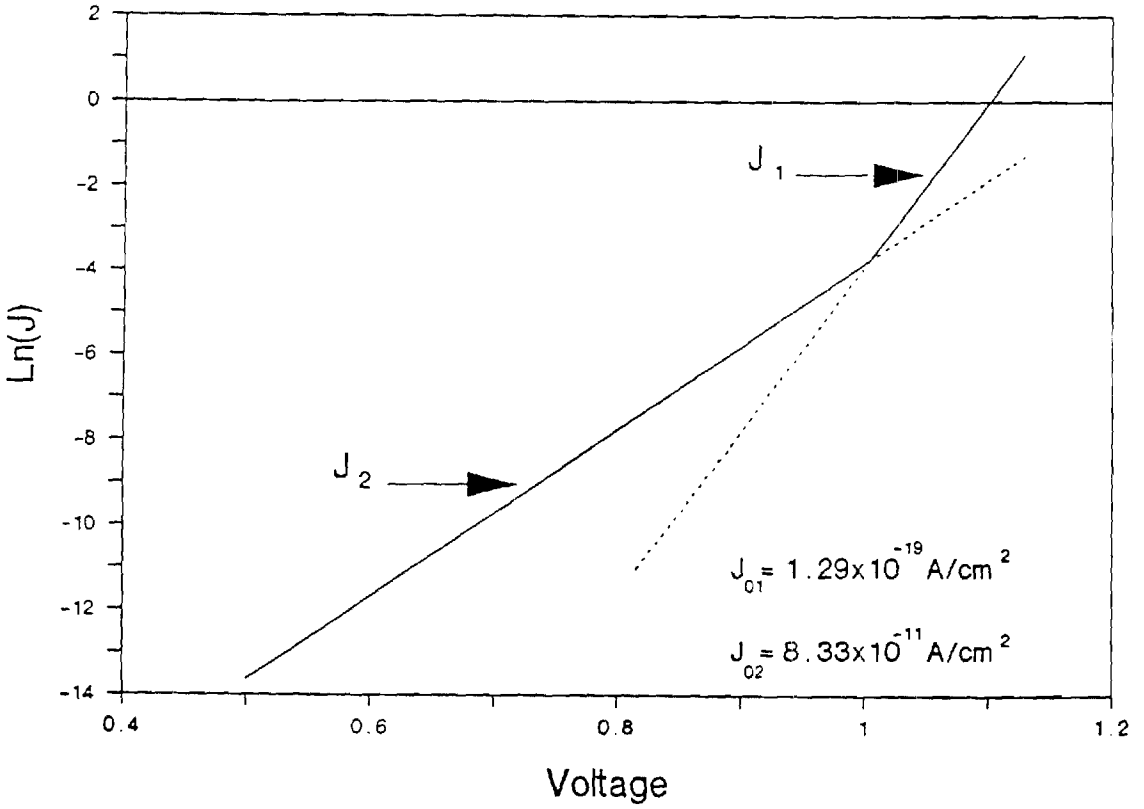

Figure 6. Transformed I-V plot showing values for the diffusion (J_{01}) and space charge (J_{02}) components of leakage current.

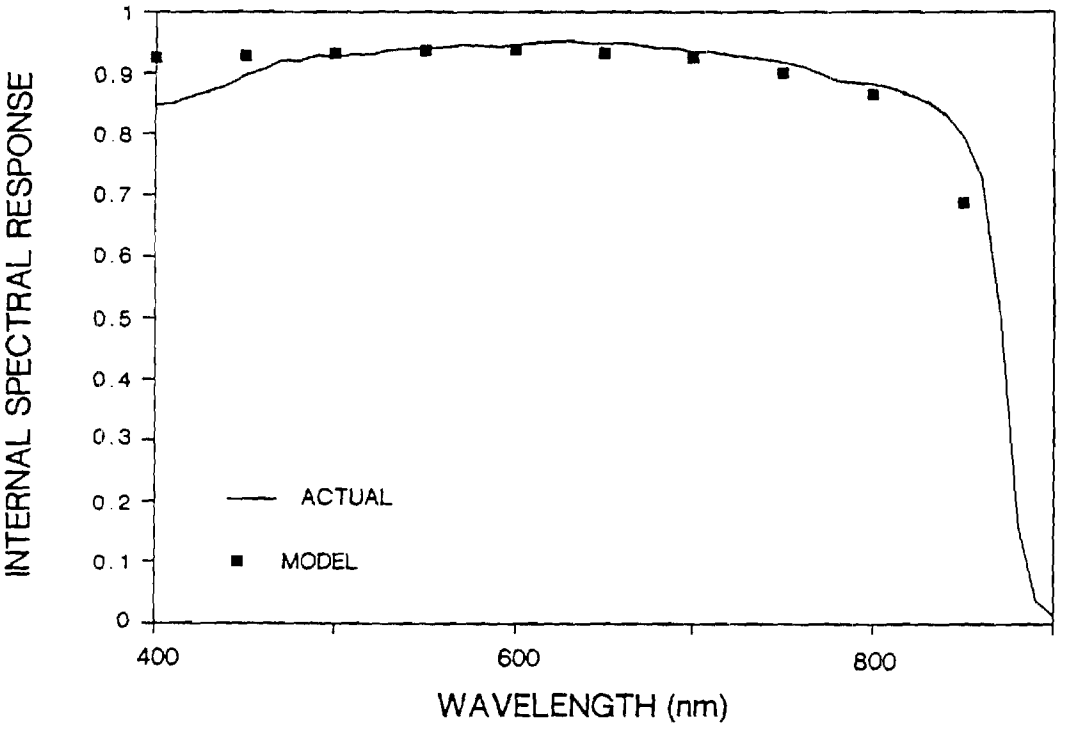

Figure 7. Comparison of measured spectral response and simulated (PC-1D) spectral response for this cell structure.

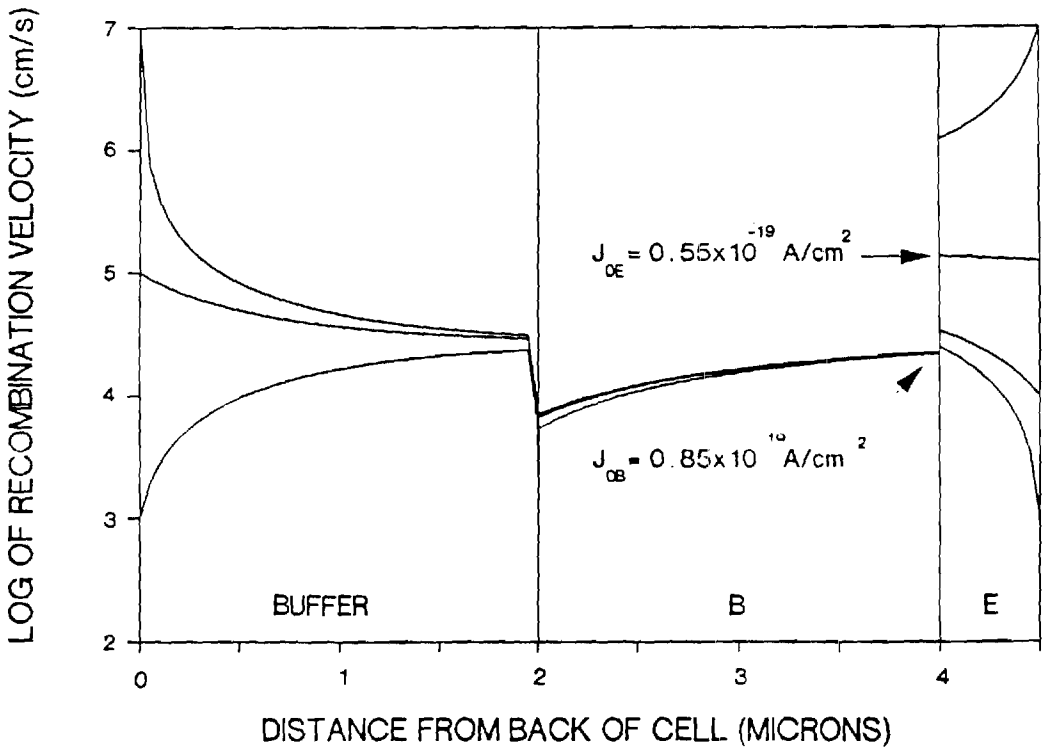

Figure 8. Plot of effective recombination velocity throughout device structure for various values of FSRV and BSRV. T_b = 8 ns, T_e = 20 ns, and T_{boff} = 4.9 ns, with N_A(emitter) = 2x10^{18} cm^{-3}, N_D(base) = 2x10^{17} cm^{-3}, and N_D(buffer) = 2x10^{18} cm^{-3} in this plot. Values of J_{0E} and J_{0B} for cell match are indicated.

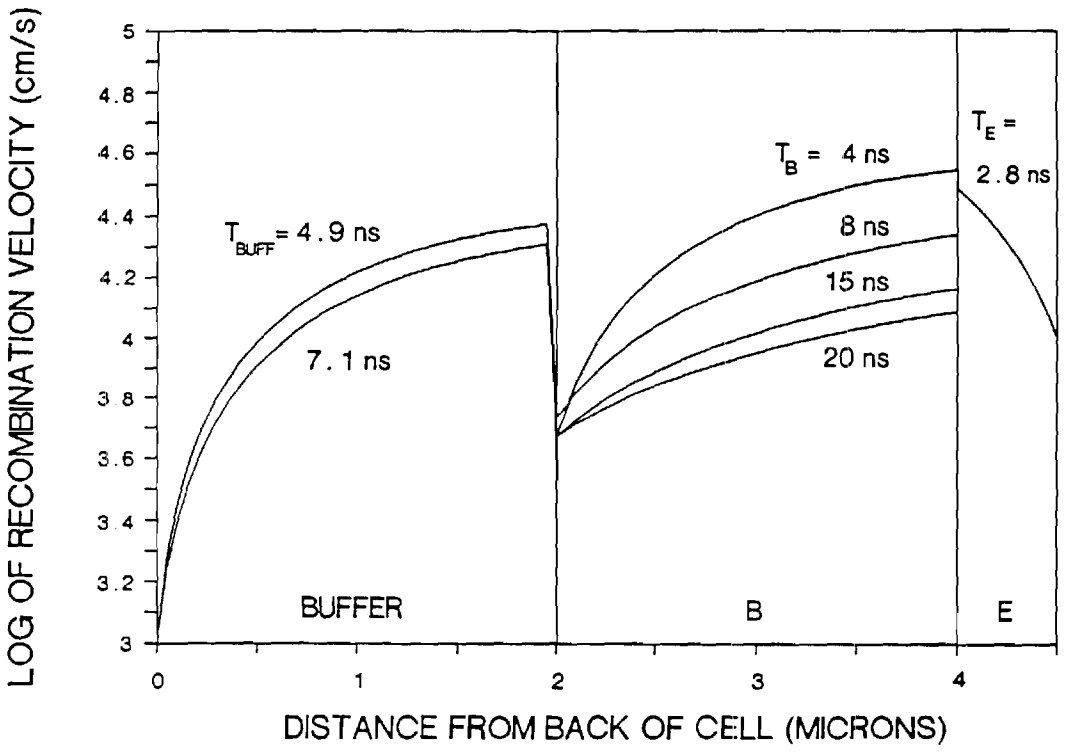

Figure 9. Plot of effective recombination velocity for different lifetimes in the base and buffer indicating importance of material quality. Doping in each region is the same as in Figure 8.

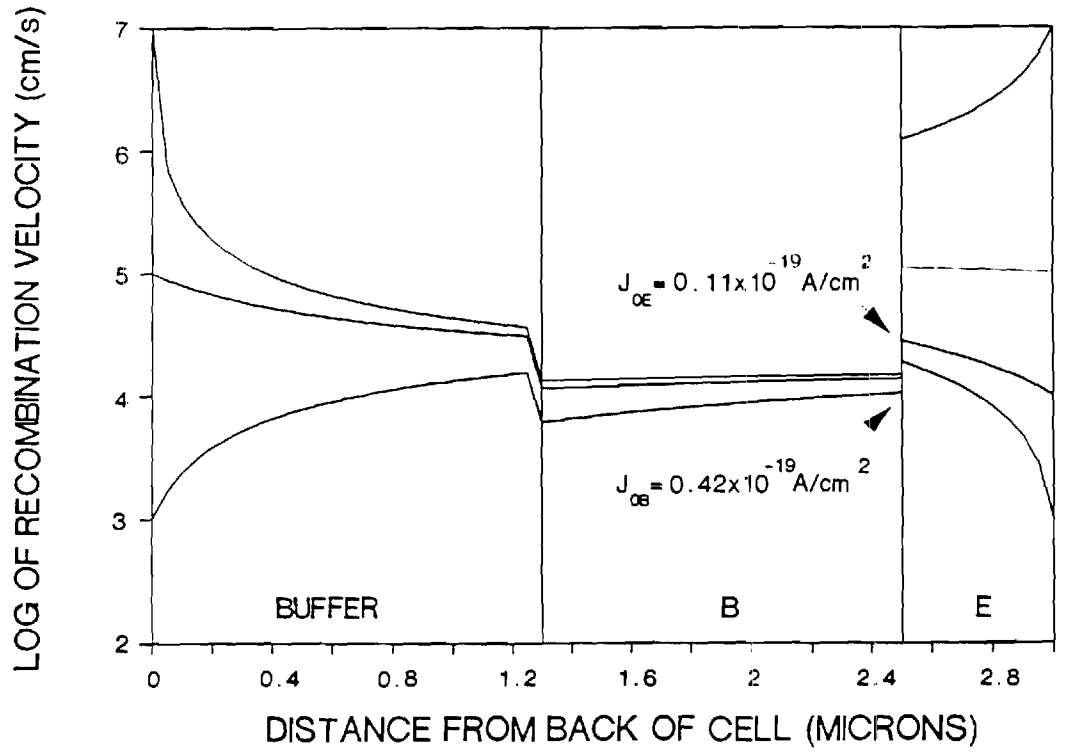

Figure 10. Plot of effective recombination velocity of optimized heteroface design. T_b = 20 ns, T_e = 2.8 ns, T_{buff} = 7.1 ns, N_A(emitter) = 2x10^{18} cm^{-3}, N_D(base) = 6x10^{17} cm^{-3}, and N_D(buffer) = 2.5x10^{18} cm^{-3} for this structure. A 25% efficient cell was modeled for the indicated values of J_{0E} and J_{0B} corresponding to FSRV = 1x10^4 cm/s and BSRV = 1x10^3 cm/s

Table 1. Guideline for cell optimization using PC-1D and effective recombination velocity modeling. Actual cell data and best match are shown. Cells 6 and 7 (starred entries) are thinned base and buffer structures.

Cell ID	N_d (cm^{-3})	N_a (cm^{-3})	N_{buff} (cm^{-3})	FSRV (cm/s)	BSRV (cm/s)	T_b (ns)	V_{oc} (Volts)	J_{sc} (A/cm^2)	Eff.
Actual	$2x10^{17}$	$2x10^{18}$	$2x10^{18}$	--	--	--	1.0131	24.5	21.2
Match	$2x10^{17}$	$2x10^{18}$	$2x10^{18}$	$1.25x10^{5}$	$1.0x10^{6}$	8	1.01	24.56	21.3
1	$2x10^{17}$	$2x10^{18}$	$2x10^{18}$	$1.0x10^{4}$	$1.0x10^{6}$	8	1.016	26.59	23.02
2	$2x10^{17}$	$2x10^{18}$	$2x10^{18}$	$1.0x10^{4}$	$1.0x10^{4}$	8	1.017	26.71	23.13
3	$2x10^{17}$	$2x10^{18}$	$2x10^{18}$	$1.0x10^{4}$	$1.0x10^{4}$	15	1.032	27.11	24.17
4	$5x10^{17}$	$2x10^{18}$	$2.5x10^{18}$	$1.0x10^{4}$	$1.0x10^{4}$	15	1.048	26.83	24.40
5	$5x10^{17}$	$2x10^{18}$	$2.5x10^{18}$	$1.0x10^{4}$	$1.0x10^{4}$	20	1.054	26.95	24.76
6	$6x10^{17}$	$2x10^{18}$	$2.5x10^{18}$	$1.0x10^{4}$	$1.0x10^{3}$	15	1.055	27.04	24.74
7	$6x10^{17}$	$2x10^{18}$	$2.5x10^{18}$	$1.0x10^{4}$	$1.0x10^{3}$	20	1.0596	27.10	25.04

MODELING AND ANALYSIS OF HIGH EFFICIENCY SILICON CELLS

A. Rohatgi and A. W. Smith
School of Electrical Engineering
Georgia Institute of Technology
Atlanta, Georgia 30332-0250

ABSTRACT

The objective of this research is to investigate the effects of light trapping and defect levels in high efficiency silicon solar cells. The development of computer models for various physical phenomena are incorporated into existing models which either did not have the capability or had simplifying assumptions for the parameters. The PC-1D model, a one-dimensional semiconductor device modeling program developed by Paul Basore, was used. The basic cell configuration used in the model calculations was similar to a cell design used by the Spire Corporation. The carrier lifetime in the base material was increased up to 10 msec, consistent with the recent improvement in crystal growth technology. The effect of various trap levels was investigated by using this starting material lifetime as a reference. In addition, light trapping was introduced in an attempt to increase the cell efficiency to approximately 25%.

An attempt was made to bridge the gap between silicon vendors and cell manufacturers by providing guidelines for selecting the optimum resistivity without going through extensive experimentation and expense. In the PC-1D model, the lifetime in the material is controlled by a single defect level located at the center of the forbidden gap, in addition to the Auger and band-to-band effects. However, in an actual semiconductor, defects can produce a variety of different deep levels and, therefore, the lifetime will not only depend upon the number of traps present but also on the location of the trap level. A combination of trap sensitive carrier lifetime model and PC-1D has been employed to show that the optimum resistivity for a given cell design depends on (1) trap location, dictated by the impurities or defects in the material, (2) the starting lifetime of the material prior to any intentional doping (undoped), and (3) the relationship between the defect density and doping density in the material. The optimum resistivity was approximately 0.2 ohm-cm for low initial lifetime material independent of the trap location. For the higher initial lifetime material, the optimum resistivity changed from 0.2 to 200 ohm-cm as the trap location shifted from 0.5 eV to 0.2 eV.

In the PC-1D model, the generation profile is only applicable to flat surfaces. The angle of incidence and the incident intensity can be changed to produce different carrier generation profiles. Using a short program, developed by Basore, we have modeled cells with Lambertian texturing on the front surface. Model calculations show that a thickness of approximately 150 to 250 microns is optimal and that, as the lifetime of the material is increased, the importance of optimizing the thickness is reduced. To examine the effect of other surface geometries, a ray tracing program was written to determine new generation profiles. In the program, the normal of the surface is determined first and then the dot product of this and the incident ray is calculated to determine the new direction of the ray. The path of the ray is followed until the length traversed is greater than the absorption length, resulting in a generation profile. The resulting profile was matched to the generation profile from PC-1D by tailoring the flux and the angle of incidence and then the simulations were performed. Green has shown that both Lambertian and perpendicular

slats geometries are superior to regular pyramidal textured surface. Our calculations support his findings. In addition to that we have found: (1) the textured angle and the thickness of the cell with perpendicular slat influences the magnitude of the trapped flux, (2) there is a definite improvement in J_{sc} and efficiency in going from regular textured or Lambertian to perpendicular slats, however, the difference between Lambertian and perpendicular slats is not very significant (less than 0.5%).

Table 1 is a description of the cell characteristics used throughout the device simulations. Figure 1 shows that the material lifetime changes if the trap level is not constant. The decrease in lifetime at low resistivity is attributed to the Auger recombination effect. Calculated efficiencies, Figure 2, for the lifetimes in Figure 1 indicate that an optimum resistivity exists at 0.2 to 1 ohm-cm depending upon the trap level and for this starting lifetime. From Figure 3 it is observed that the starting lifetime can dictate which resistivity (0.2 to 2 ohm-cm) is optimum if the trap level is fixed. Yet, if the trap level is changed, Figure 4, the optimum resistivity changes (0.1 to 200 ohm-cm). By examining Figure 5, an optimum thickness of 150 to 300 microns is seen for high lifetime Lambertian textured cells. For the lower lifetime the optimum not obtained. Figure 6 indicates that the quality of the surface must be maintained to ensure high efficiency. Table 2 gives the calculated fluxes for Lambertian and perpendicular slats geometries at various cell thicknesses. For perpendicular slats, two texturing angles have been included.

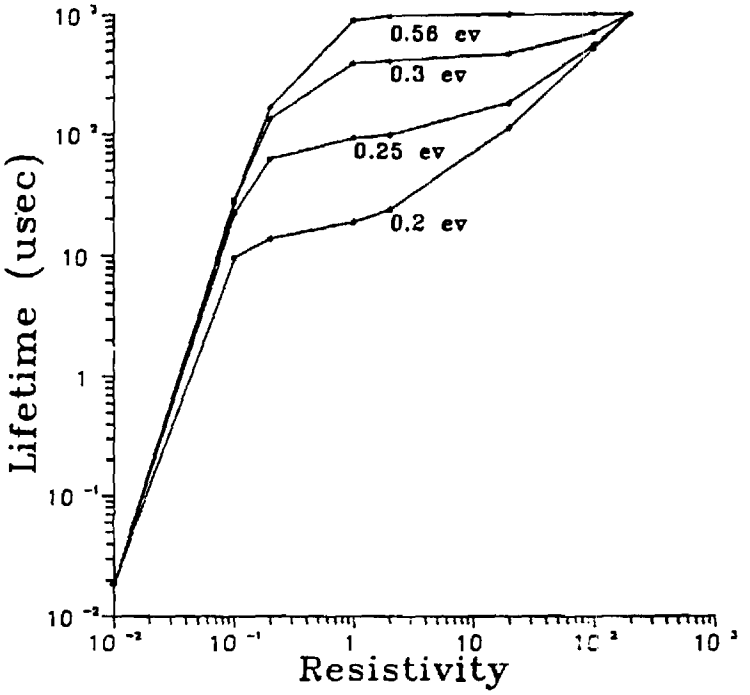

Figure 1. Lifetime of charge carriers as a function of resistivity for several different trap levels within the forbidden gap starting with 1 millisecond base material.

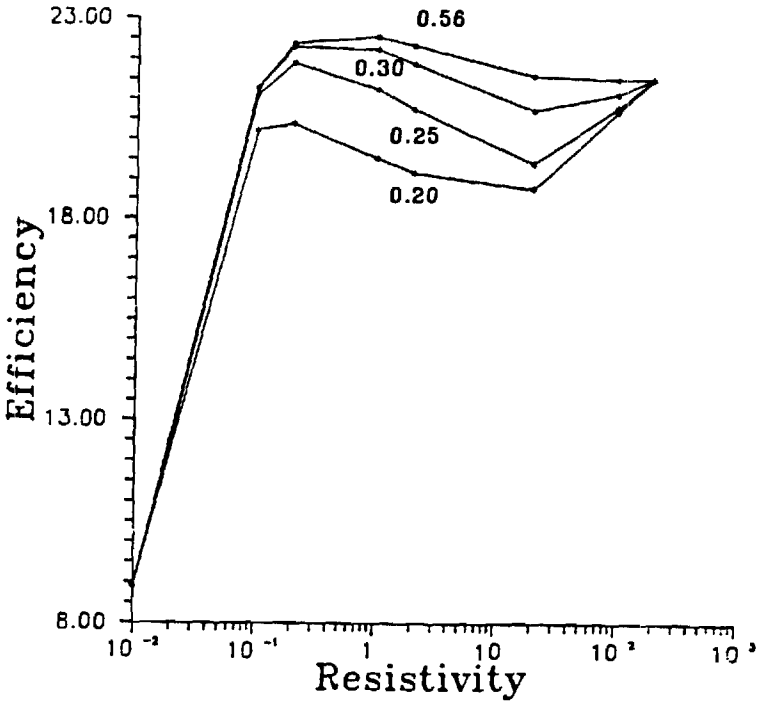

Figure 2. The calculated efficiency of cells with 1 millisecond lifetime base material when the trap level is located at different energy levels.

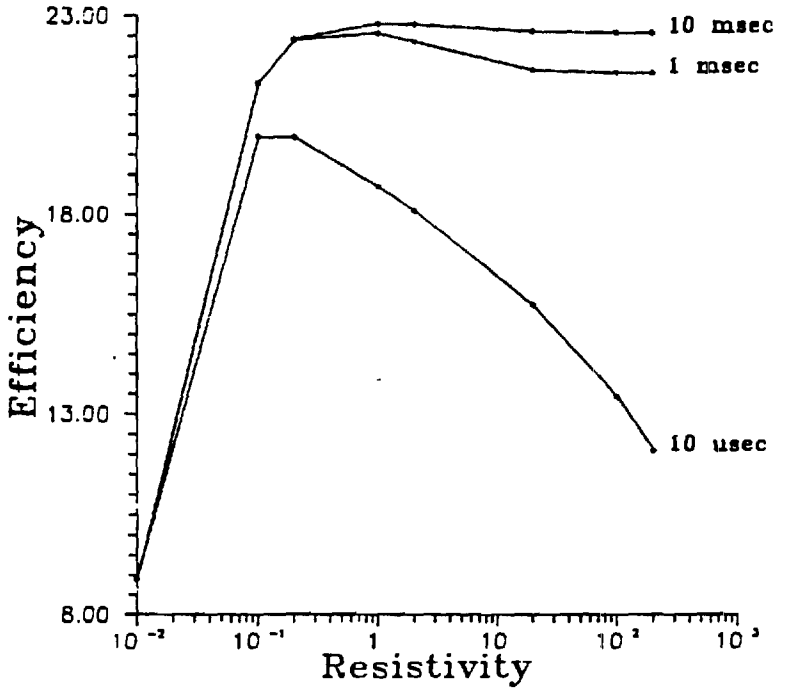

Figure 3. The calculated efficiency of cells with a variable starting lifetime base material but the trap is located at 0.56 eV.

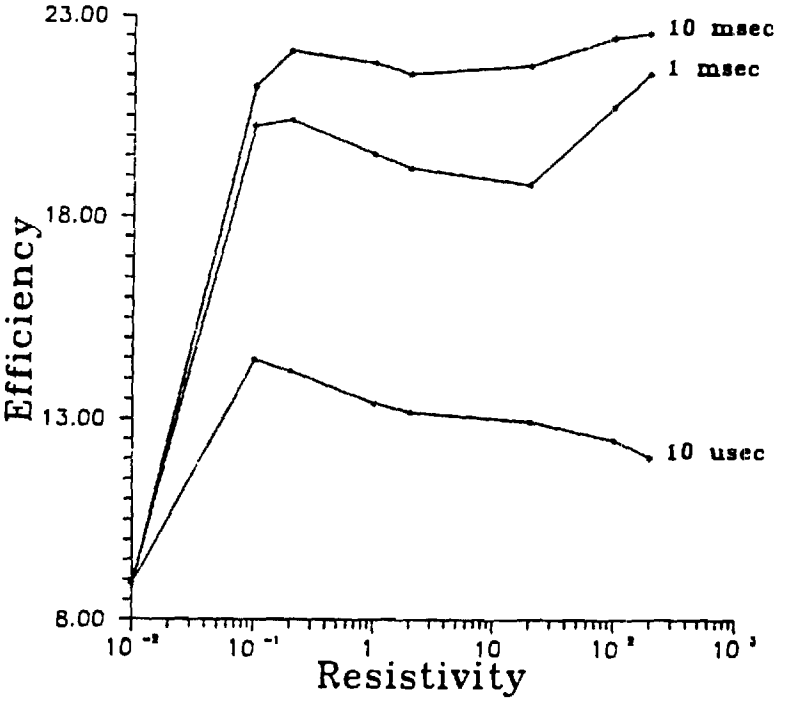

Figure 4. The calculated efficiency of cells with a variable starting lifetime base material but the trap is located at 0.20 eV.

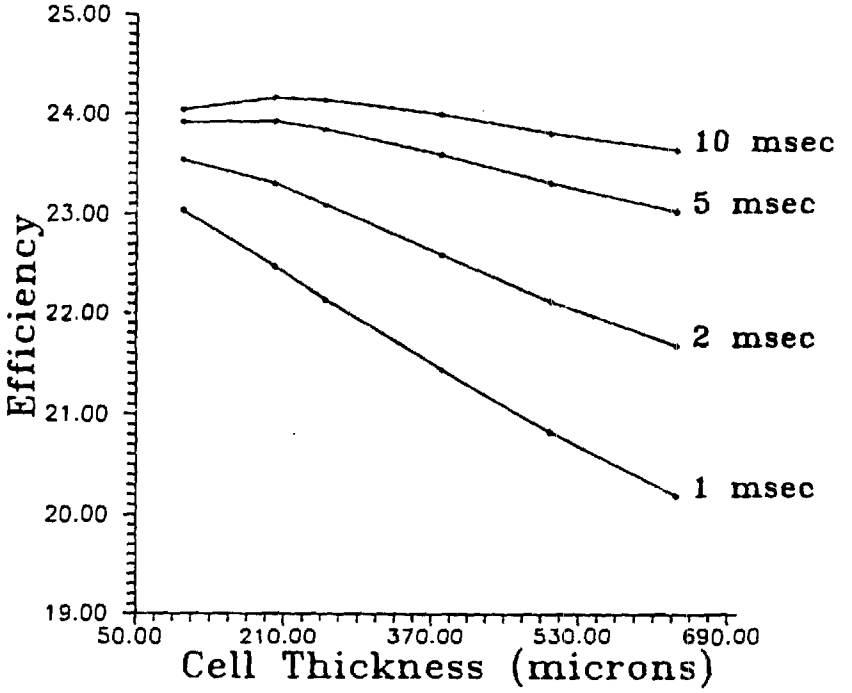

Figure 5. The calculated efficiency of Lambertian textured cells of varying thickness which have variable lifetime base material. The trap level for these cells is located at midgap.

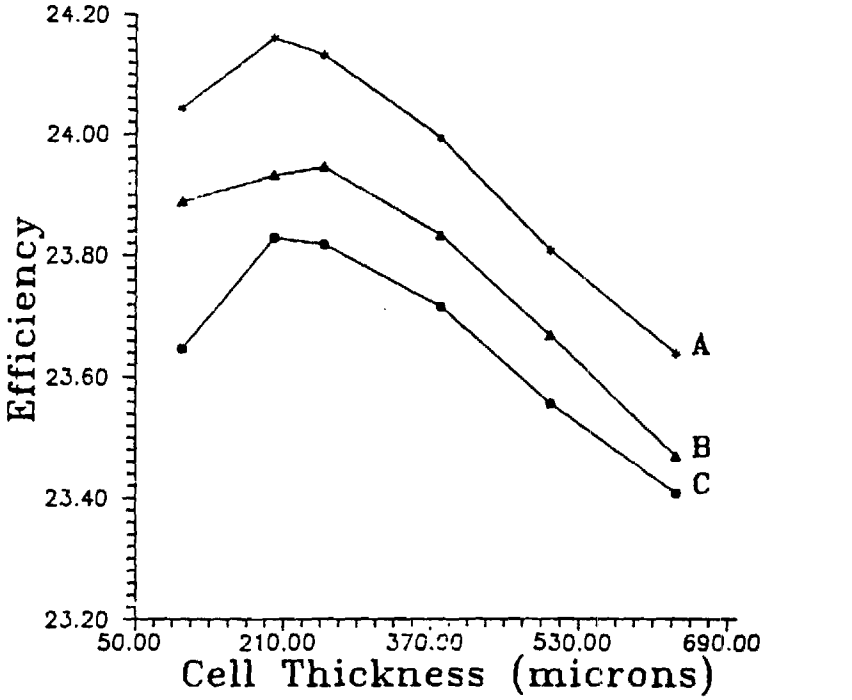

Figure 6. The calculated efficiency of Lambertian textured cells of varying thickness. The base lifetime was 10 milliseconds, but the quality of the surface was variable.
A. FSRV and BSRV of 100 cm/sec
B. FSRV of 100 cm/sec and BSRV of 500 cm/sec
C. FSRV and BSRV of 500 cm/sec.

Table 1. Cell design parameters used in the stimulation of high efficiency silicon solar cells.

1. Emitter width is 0.2 microns
2. Emitter doping is complementary error with doping of $2x10^{19}$
3. Front surface coverage of 4.5%
4. Front surface recombination velocity is variable
5. Back surface field width of 2 microns
6. Back surface doping of $2x10^{18}$ and complementary error
7. Back surface recombination velocity is variable
8. Series resistance was 0.4
9. Cell area of 1 cm^2
10. Back surface reflector of 98% effectiveness
11. Front surface internal reflector of 92% effectiveness
12. Latest values for the Auger coefficients of the carriers
13. n-type emitter
14. p-type base and buffer

For textured cells, the base resistivity was 200 ohm-cm. For deep level calculations, the thickness of the cell was 254 μm.

Table 2. Calculated flux for Lambertian and perpendicular slats geometry for various thickness of cells. In all cases, 4.5% front surface loss and 98% effective back surface reflector were considered. The perpendicular slat calculations are for two texturing angles.

	Flux ($\#/cm^2$)		
		Perpendicular Slats	
Cell Thickness (μm)	Lambertian	θ = 55	θ = 63
100	2.5072×10^{17}	---	2.5152×10^{17}
200	2.5454×10^{17}	---	2.5549×10^{17}
254	2.5546×10^{17}	2.5763×10^{17}	---
381	2.5697×10^{17}	---	2.5751×10^{17}
500	2.5774×10^{17}	2.5929×10^{17}	2.5915×10^{17}
635	2.5882×10^{17}	2.5981×10^{17}	2.5970×10^{17}

CONTRACTOR: Complete all spaces and the bottom block.

Sandia National Laboratories

PURCHASING ORGANIZATION Georgia Tech

ALBUQUERQUE, NEW MEXICO 87185
LIVERMORE, CALIFORNIA 94550

J. Gee
Sandia Contracting Representative

MONTHLY COST STATUS REPORT

CONTRACT NO. 57-6152

PERIOD ENDING (1) June 30, 1988

Contractor must forecast as a minimum the first three months, Balance of Fiscal Year, and Subsequent Fiscal Years when costs will be incurred in these months and years.

Contractor must forward this report to reach the Sandia Contracting Representative by the 15th of the month following the Report Period or at such other time as requested by the Sandia Contracting Representative.

TOTAL FUNDS AUTHORIZED		$ 72,448.00
ACTUAL COST INCURRED TO DATE(2)		9,797.49
ESTIMATED COST TO COMPLETE:(3)		
1st MONTH FOLLOWING "PERIOD ENDING" as specified above	6,961.17	
2nd MONTH	6,961.17	
3rd MONTH	6,961.17	
4th MONTH		
5th MONTH		
6th MONTH		
BALANCE OF FISCAL YEAR(4)		
SUBSEQUENT FISCAL YEARS	41,767.00	
TOTAL ESTIMATE TO COMPLETE		62,650.51
TOTAL ESTIMATED COST AT COMPLETION		$ 72,448.00

NOTES:
(1) Last full month for which actual costs are available.
(2) Cost includes applicable fee.
(3) Estimates for costs to be incurred (Do not include commitments), including applicable fee.
(4) Fiscal year is 10/1 through 9/30. Balance of fiscal year means all months remaining in the fiscal year following the 6th month shown on the line above. If the 6th month is September, then balance of fiscal year is 10/1 through 9/30 of the next fiscal year.

Contractor (name and address)	Signature of Contractor's Representative, Date and Phone
Georgia Tech Research Corporation School of Electrical Engineering Georgia Institute of Technology Atlanta, GA 30332	Pam Majors Pam Majors, Research Adm. 404-894-7337 7/22/88

BF6432-CS(1-85)

GEORGIA INSTITUTE OF TECHNOLOGY
SCHOOL OF ELECTRICAL ENGINEERING
ATLANTA, GEORGIA 30332

TELEPHONE: (404) 894-7337

August 11, 1988

Mr. J. Gee
Sandia National Laboratories
P. O. Box 5800
Albuquerque, NM 87185-5800

RE: Contract No. 57-6152
Project Director: A. Rohatgi

Dear Mr. Gee:

Enclosed please find copies of the Monthly Cost Status Report for the period 7/1/88-7/31/88 on the above referenced contract.

If you have any questions, please feel free to contact me.

Sincerely,

Pam Majors
Research Administrator

pm
Enclosure

CONTRACTOR: Complete all spaces and the bottom block.

Sandia National Laboratories

PURCHASING ORGANIZATION Georgia Tech

ALBUQUERQUE, NEW MEXICO 87185
LIVERMORE, CALIFORNIA 94550

J. Gee
Sandia Contracting Representative

MONTHLY COST STATUS REPORT

CONTRACT NO. 57-6152

PERIOD ENDING (1) July 31, 1988

Contractor must forecast as a minimum the first three months, Balance of Fiscal Year, and Subsequent Fiscal Years when costs will be incurred in these months and years.

Contractor must forward this report to reach the Sandia Contracting Representative by the 15th of the month following the Report Period or at such other time as requested by the Sandia Contracting Representative.

TOTAL FUNDS AUTHORIZED		$ 97,448.00
ACTUAL COST INCURRED TO DATE(2)		19,074.34
ESTIMATED COST TO COMPLETE:(3)		
1st MONTH FOLLOWING "PERIOD ENDING" as specified above	9,796.71	
2nd MONTH	9,796.71	
3rd MONTH		
4th MONTH		
5th MONTH		
6th MONTH		
BALANCE OF FISCAL YEAR(4)		
SUBSEQUENT FISCAL YEARS	58,780.24	
TOTAL ESTIMATE TO COMPLETE		78,373.66
TOTAL ESTIMATED COST AT COMPLETION		$ 97,448.00

NOTES:
(1) Last full month for which actual costs are available.
(2) Cost includes applicable fee.
(3) Estimates for costs to be incurred (Do not include commitments), including applicable fee.
(4) Fiscal year is 10/1 through 9/30. Balance of fiscal year means all months remaining in the fiscal year following the 6th month shown on the line above. If the 6th month is September, then balance of fiscal year is 10/1 through 9/30 of the next fiscal year.

Contractor (name and address)	Signature of Contractor's Representative, Date and Phone
Georgia Tech Research Corporation School of Electrical Engineering Georgia Institute of Technology Atlanta, GA 30332	Pam Majors Pam Majors, Research Adm. 404-894-7337 8/11/88

F6432-CS(1-85)

AN APPROACH TOWARD 25% EFFICIENT GaAs HETEROFACE SOLAR CELLS

S. A. Ringel and A. Rohatgi
School of Electrical Engineering
Microelectronics Research Center
Georgia Institute of Technology
Atlanta, Georgia 30332-0250

S. P. Tobin
Spire Corporation
Patriots Park
Bedford, MA 01730

ABSTRACT

In order to approach 25% efficiency in GaAs solar cells, it is necessary to improve the basic understanding of internal loss mechanisms by a combination of characterization techniques and computer models. A methodology is developed to measure and evaluate minority carrier transport properties such as lifetime and recombination velocity throughout the device structure in a 21.2% GaAs cell. It is found that this cell has a recombination velocity of 1.25×10^5 cm/s at the AlGaAs/GaAs interface and a base minority carrier lifetime of 8 ns. Guidelines are provided to increase the efficiency of this cell to 24% with slightly increased surface passivation and base lifetime using effective recombination velocity and device modeling computer programs. Further device modeling is performed to show that efficiencies of 25% can be obtained using a modified heteroface structure with a moderate surface recombination velocity of 1×10^4 cm/s if lifetime limiting mechanisms and their relation to device design are fully understood.

INTRODUCTION

As the conversion efficiencies of GaAs solar cells continue to increase, the ability to detect, analyze, and assess the importance of defects and other lifetime limiting mechanisms becomes critical to advance cell performance further. Most research to date has been devoted to the study of topics such as recombination centers in bulk GaAs [1,2] and at surfaces and interfaces using specialized test structures in which the interplay of interfacial effects with bulk properties such as minority carrier lifetime is not obvious [3-5]. Hence, it is important to develop measurement techniques in conjunction with device modeling to separate those material parameters that dictate the performance of solar cell and other GaAs devices in which the carrier transport mechanisms are not well understood. Recently, a few attempts have been made to address this issue for GaAs solar cells [6-9].

This paper presents a combination of characterization methodology and device modeling to improve solar cell design by detecting and evaluating important material parameters such as lifetime, interface recombination velocity, and deep levels within a state-of-the-art MOCVD grown GaAs p-n heteroface solar cell. First, a number of standard semiconductor characterization techniques, such as DLTS (Deep Level Transient Spectroscopy) and dark I-V (current-voltage) and I-V-T were used to determine the carrier recombination and generation lifetimes separately. Then dopant profile and depth-resolved surface photovoltage measurements were performed with the help of an electrochemical etching profiler to provide necessary inputs to the device modeling programs used in this investigation. A combination of a one-dimensional computer model and the experimental data obtained through the above techniques was used to reveal the variation in the effective

recombination velocity (S_e) throughout the device. S_e is indicative of net recombination anywhere within the device and can be used to guide the optimization of high efficiency cell design. A second device modeling program (PC-1D) was used to calculate cell parameters J_{sc}, V_{oc}, and efficiency along with the spectral response of the cell. The calculated values were correlated with the measured cell data to assess the accuracy of the characterization methodology to analyze the lifetime limiting mechanisms in the bulk and interfaces of GaAs structures. Finally, improved understanding of the loss mechanisms coupled with device modeling was used to provide guidelines for attaining GaAs cell efficiencies approaching 25% under AM 1.5 conditions.

EXPERIMENTAL METHODS

A. DEVICE STRUCTURE

Figure 1 shows the device structure of the MOCVD grown GaAs heteroface solar cell used in this study, along with the measured cell data. The GaAs layers were grown at 700°C using trimethyl gallium and arsine as reactants. The AlGaAs was grown at 800°C using trimethyl aluminum for the Al source. The mole fraction of Al in the AlGaAs window layer was 0.90. The heavily doped cap layer is for ohmic contact formation [9]. Zn and Si were the p-type and n-type dopants, respectively, used throughout the structure.

For DLTS, I-V, and I-V-T measurements, 50 mil diameter mesa dots were formed by evaporating Au/Zn ohmic contacts on the structure. The back surface was covered with evaporated Au/Ge ohmic contacts to facilitate the electrical measurements.

B. DEPTH-RESOLVED SPV/C-V MEASUREMENTS

Attempts were made to determine the carrier concentration profile and the spatial variation in the electro-optical response of the cell using a depth-resolved C-V and SPV (surface photovoltage) measurement. Both the measurements were performed in an automated electrochemical etching profiler in which an electrolyte is used to perform precise step-by-step etching coupled with I-V, C-V, and SPV measurements after each step [10]. A Schottky barrier formed between the electrolyte and the semiconductor facilitates both C-V and SPV measurements. The doping concentration is found from the C-V data at each depth. SPV measurements were performed in the wavelength range of 400 to 900 nm to accommodate both the GaAs and AlGaAs absorption edges. The SPV signal is measured at the surface under open circuit conditions to avoid electrochemical etching or deposition during the measurement. The choice of electrolyte is dictated by the properties of the semiconductor. For this study, a solution of 0.2 M NaOH + 0.1 M EDTA (ethylenediamminetetraacetic acid) was found to be an adequate electrolyte for Schottky barrier formation and electrochemical etching showed no signs of surface degradation.

C. DLTS STUDIES

A combination of DLTS and I-V-T measurements was used to determine the trap which controls the leakage current of the solar cell. The DLTS technique reveals all the detectable traps, regardless of their influence on the leakage current. DLTS measurements were made using an automated wafer analyzer system which obtains data via a modified lock-in amplifier type DLTS set-up. Nonuniformity in deep level distribution near the p-n junction of the solar cell was investigated by varying the steady reverse bias level from -5 volts

to -1 volt, but keeping the sum of the reverse bias and forward bias pulse height constant at -0.5 volts. In this way, the edge of the depletion region is steadily stepped toward the metallurgical junction as the reverse bias is decreased to provide a spatial trap profile in the depletion region. DLTS measurements were also performed in a forward bias mode (the sum of the steady reverse bias and the injection pulse height > the built-in voltage of the p-n junction) to detect both majority and minority carrier traps in the depletion region. The detection limit of our DLTS set-up is about 0.01% of the background doping concentration so defects with less than 2×10^{13} cm^{-3} concentration in the base region will not be detected.

D. I-V-T ANALYSIS

The I-V-T technique identifies only the activation energy of that deep level which limits the reverse leakage current if the leakage is trap dominated [11,12]. In addition, it does not suffer from the same doping dependent detection limit as DLTS, allowing information to be extracted from heavily doped device structures. The method is based on the assumption that the total reverse leakage current, J_0, is dominated by the space charge generation current and the diffusion component can be neglected under reverse bias. This is routinely observed in GaAs. From SRH (Schockly-Read-Hall) theory, the total carrier recombination rate, R, under steady state conditions is given by

$$R = \frac{np - n_i^2}{\tau_{p0}(n+n_1) + \tau_{n0}(p+p_1)} \tag{1}$$

where

$$\tau_{p0} = (\sigma_p N_T V_{TH})^{-1} \tag{2}$$

$$\tau_{n0} = (\sigma_n N_T V_{TH})^{-1} \tag{3}$$

$$n_1 = n_i \exp\left[\frac{(E_t - E_i)}{kT}\right] \tag{4}$$

$$p_1 = n_i \exp\left[\frac{-(E_t - E_i)}{kT}\right] \tag{5}$$

Under reverse bias conditions, the excess carrier concentration in the space charge region can be neglected so that Eq. (1) reduces to

$$R = -n_i/\tau_g \tag{6}$$

where τ_g, the generation lifetime, is defined as [10,11]

$$\tau_g = \tau_{p0} \exp\left[\frac{(E_t - E_i)}{kT}\right] + \tau_{n0} \exp\left[\frac{-(E_t - E_i)}{kT}\right] \tag{7}$$

and E_t is the energy level of the recombination center within the band gap and E_i is the position of the intrinsic Fermi level. If the capture cross sections for holes $(\sigma_p N_T V_{TH})^{-1}$ and electrons $(\sigma_p N_T V_{TH})^{-1}$ are comparable to each other, then τ_g reduces to

$$\tau_g = \tau_r \exp\left[\frac{|E_t - E_i|}{kT}\right] \tag{8}$$

where τ_r, the low level SRH recombination lifetime, is τ_{p0} for traps with $E_t > E_i$ and is τ_{n0} for traps with $E_t < E_i$. Using the definition of leakage current in a reverse-biased diode [13] and recalling the assumption which neglects the diffusion component of J_0,

$$J_{rev} \simeq \frac{qn_i w}{\tau_g} \tag{9}$$

where W is the width of the depletion region, then

$$J_{rev} \alpha \exp\left[\frac{-(E_t - E_v)}{kT}\right] \qquad \text{for } E_t > E_i \tag{10}$$

or

$$J_{rev} \alpha \exp\left[\frac{-(E_c - E_t)}{kT}\right] \qquad \text{for } E_t < E_i \tag{11}$$

Hence, the activation energy of the generation center which controls the leakage current can be determined from the slope of the $\ell n(J_{rev})$ vs 1000/T plot under constant applied reverse bias. It is important to note that the I-V-T method gives an activation energy of the trap which controls the leakage current, but it does reveal the band edge with respect to which that activation energy is measured, unless the trap location is known. Therefore, this method must be supplemented by other measurements such as DLTS which gives all the traps present, but does not really reveal which one controls the leakage current.

E. TRANSFORMED I-V ANALYSIS

The I-V characteristics of the mesa diode structure were measured in the dark and analyzed using an automated setup to separate the resistance, bulk, and junction region effects. The I-V characteristic of a solar cell is a composite of two exponential functions including series and shunt resistance effects. The transformed I-V program first measures and subtracts the resistance effects from the measured data and then fits the rest to a double exponential equation given by

$$J = J_1 + J_2 = J_{01}\left[e^{qV/kT} - 1\right] + J_{02}\left[e^{qV/nkT} - 1\right] \qquad (12)$$

where J_{01} and J_{02} are the saturation current densities for the diffusion (n = 1) and space charge generation (n = 2) current components, respectively. The computer program fits the data and provides values of J_{01} and J_{02}.

RESULTS AND DISCUSSION

The doping profile throughout the device structure, Figure 1, was confirmed by depth-resolved C-V measurements. Since the doping level in the AlGaAs window layer is similar to that of the emitter, the AlGaAs layer was not evident. Presence of the AlGaAs layer was confirmed by far infrared reflectance measurements which also revealed the mole fraction of Al to be 0.87, close to the target composition. The AlGaAs thickness was found to be 50 nm by reflectance measurements.

Spatial variations in the material properties were investigated by depth-resolved SPV measurements in an electrochemical profiler. Figure 2 shows photovoltage spectra taken at various etch depths. This data was not taken on the actual cell but on a piece adjacent to it, which has the p^+ GaAs cap layer intact. The initial (0.12-0.21 um) increase in the response with increasing etch depth is due to the succesive removal of the heavily doped cap layer which has high absorption and recombination. The two humps at 560 and 720 nm are the characteristic response of the SPV optics. The etch depths at which these measurements were made are indicated in the figure. Both the overall shape and magnitude of SPV response are related to the properties of the material being probed. As we etch through the emitter region (0.21-0.42 um), the response gradually drops. This does not necessarily indicate defects or

nonuniformity in the emitter region, but instead could be the result of enhanced competition from the p-n junction for the carriers generated within the emitter region. Notice that the overall open-circuit signal represents the spectrally resolved sum of the opposing photovoltages generated at the front electrolyte/GaAs Schottky barrier and at the p-n junction [10]. At present we are unable to quantitatively account for the effect of the p-n junction on the measured response.

A qualitative picture of material uniformity can be obtained from spectrally resolved divisions of consecutive SPV spectra. Figure 3 shows a series of ratios taken while the device is being etched through the emitter. SPV ratio curve "a" indicates that material quality is uniform between points 1 and 2 in the figure inset. The sign change in the SPV ratio curve "b" of Figure 3 taken just before the p-n interface indicates that for photons with wavelength greater than ~530 nm the p-n junction becomes the dominant carrier collecting junction. Up to this point, the effect of the presence of a defective region of material could be masked by the competition from the p-n junction. However, the SPV ratio curves "c" and "d", obtained by etching through the p-n junction and another slice 0.1 um later, respectively, do not suffer from this complication. The ratio curves "c" and "d" suggest that the near the p-n junction, the material quality improves in the base as we move away from the junction edge because the ratios are not only greater than one but gradually increase with depth, in spite of the constant base doping.

In order to further investigate the defect nonuniformity near the p-n junction, depth-resolved DLTS measurements were performed on the 50 mil diameter mesa diodes. The DLTS primarily probes the n-base side of the p^+-n junction. A deep level was detected only when the probed depletion region was

close to the p-n interface and is shown in Figure 4. This minority carrier trap has an activation energy of E_v + 0.912 eV and a concentration of 3.93 x 10^{14} cm^{-3}. The fact that this level was not detected for wider depletion widths supports the nonuniform defect distribution seen by the SPV response near the p-n junction. The ℓn(I) vs T plot from the I-V-T measurement, Figure 5, gave an activation energy of E_a = 0.45 eV for the J_{rev} leakage component. Since the sum of the DLTS and I-V-T activation energies is close to the bandgap of GaAs (0.45 + 0.91 = 1.36 eV), it is reasonable to conclude that the level detected by DLTS and I-V-T is the same and is also responsible for the excess leakage current.

While the DLTS and I-V-T measurements yield the characteristics of the space charge region, they offer no information about the bulk material properties. In order to assess the bulk properties the transformed I-V technique was used to separate the bulk and junction effects. Figure 6 shows the transformed I-V curve for this device measured at 25°C. J_{01} and J_{02} components were found to be 1.29 x 10^{-19} A/cm^2 and 8.33 x 10^{11} A/cm^2, respectively, while the corresponding n-factors were 1.00 and 1.97, consistent with theory.

Even though the trap detected by I-V-T and DLTS could not be seen deeper in the base, the leakage current produced in the depletion region of this cell degrades the cell performance because the J_{01} and J_{02} components are nearly equal at the cell operating point (~ 1 volt), Figure 6. Since the J_{02} component at the operating point represents the current that does not make it to the load, performance of this particular cell can be appreciably improved by eliminating the E_v + 0.912 eV trap.

COMPUTER MODELING

To test the experimental data and the validity of the above analyses, the solar cell was modeled with the help of two computer programs, one of which calculates the cell parameters V_{oc}, J_{sc}, efficiency, and spectral response, and the other which calculates an effective recombination velocity anywhere within the structure.

The PC-1D model, described elsewhere [14], was used first to model the spectral response. A net base lifetime of 8 ns with a front surface recombination velocity of 1.25×10^5 cm/s was required to obtain a good match between the model calculations and the experimental data, Figure 7. Back surface passivation was found to have negligible effect on the spectral response. The emitter and buffer lifetimes were determined from the SRH lifetime in the base according to

$$\frac{1}{\tau} = \frac{1}{\tau_{SRH}} + BN + CN^2 \qquad (13)$$

where B is the radiative recombination coefficient and C is the Auger recombination coefficient for GaAs. Using $B = 2.5 \times 10^{-11}$ cm^3 [15], $C = 1.60 \times 10^{-29}$ cm^6 [16], and $\tau = 8$ ns in the base, we obtain $\tau_{SRH} = 8.33$ ns. Assuming defect dominated τ_{SRH} to be constant throughout the device, Eq. (13) gave emitter and buffer lifetimes of 2.08 and 5.49 ns, respectively, by substituting the proper values for B and C in each region.

The modeled spectral response, Figure 7, was obtained from the calculated J_{sc} and measured reflectivity as a function of wavelength using the AM 1.5 energy content of the incident radiation. A shadow loss of 5% was used for the modeling. Figure 7 shows a good match between the calculated and measured values with only a slight difference in the short and long wavelengths. The

lower measured response in the short wavelength can be attributed to absorption in the AlGaAs passivation layer which is not considered in the model. The AlGaAs decreases the photon flux incident on the GaAs at the shorter wavelengths until the absorption edge of the AlGaAs at ~2 eV is reached. At long wavelengths (850 nm), the simulated response is somewhat lower than the actual, probably because of the increase in absorption coefficient due to doping near the band edge [17] which is not included in the PC-1D model. This additional absorption close to the junction will increase the collection efficiency or J_{sc} for long wavelength photons.

Since it is possible to match spectral response with a window of possible values for lifetime and surface recombination velocity, further verification of these parameters is necessary. Hence, J_{01} was modeled using the estimated lifetime profile (τ_e, τ_b, τ_{buff}) and recombination velocities which matched the spectral response through an effective recombination velocity (S_e) model, which calculated the reverse leakage current (J_{01}) for comparison with the measured value. S_e is a measure of the minority carrier losses in the various regions of the device from which J_{01} can be directly calculated. This model, which is described in detail elsewhere for silicon cell design and analysis [18], includes the effects of bandgap narrowing [19], Auger and radiative recombination, and recombination at surfaces and interfaces. The internal recombination velocity S_e throughout the cell is calculated using the front surface recombination velocity at the emitter/AlGaAs interface, FSRV, the back surface recombination velocity at the back of the buffer layer, BSRV, the diffusion length, doping profile, and cell dimensions as input parameters. Each region of the cell (buffer, base, and emitter) is subdivided into a number of elements, all of the same width. S_e is calculated iteratively from

FSRV and BSRV until the p-n junction edge is reached on each side. The recombination velocity S_{e2} at one boundary of any element is calculated in terms of velocity S_{e1} at the other boundary by

$$S_{e2} = \frac{N_2}{N_1}\frac{D}{L}\left[\frac{S_{e1}\frac{D}{L} + \tanh\left(\frac{W}{L}\right)}{1 + S_{e1}\frac{D}{L}\tanh\left(\frac{W}{L}\right)}\right] \exp\left[\frac{\Delta E_{g2} - \Delta E_{g1}}{kT}\right] \quad (14)$$

where

W = element width

D,L = diffusion coefficient and diffusion length of minority carriers within the element

$N_{1,2}$ = doping densities at boundaries of element

$\Delta E_{g1}, \Delta E_{g2}$ = bandgap narrowing due to doping densities N_1 and N_2.

The base and emitter components of the leakage current can then be determined from

$$J_{0B} = \frac{qn_i^2}{N_D} \cdot S_{ejb} \quad (15)$$

and

$$J_{0E} = \frac{qn_i^2}{N_A} \cdot S_{eje} \quad (16)$$

where S_{ejb} and S_{eje} are the recombination velocities at the base edge and emitter edge of the p-n junction, respectively.

Figure 8 shows plots of S_e versus depth for the GaAs heteroface cell for various values of FSRV and BSRV which support the spectral response conclusion that back surface passivation has little or no effect on J_{0B} in this cell. The model calculations reveal that recombination velocity at the base side of the p-n junction is pinned so that $J_{0B} = \sim 0.85 \times 10^{-19}$ A/cm^2 for all values of BSRV. For FSRV = 1.25×10^5 cm/s and τ_e = 2.08 ns, which gave the best match

for the spectral response, the S_e model gives $J_{0E} = 0.55 \times 10^{-19}$ A/cm^2 so that the simulated $J_{01} = J_{0E} + J_{0B} = 1.40 \times 10^{-19}$ A/cm^2. This is in good agreement with the measured J_{01} of 1.29×10^{-19} A/cm^2 which supports the selection of FSRV and lifetime for the simulated spectral response and confirms that J_{01} or V_{oc} of this cell is limited by both the base and emitter with the emitter contributing ~39% of J_{01}.

A few more revealing observations can be made from Figure 8. Contrary to the back surface, front surface passivation is critical for this cell because an FSRV of 1×10^7 cm/s, which is typical of the free GaAs surface, results in a large increase in J_{0E} and, hence, a lower V_{oc}. However, the AlGaAs passivation needs to limit FSRV only to ~1×10^4 cm/s since, in this particular cell, FSRV below this value has very little impact on S_{eje} or J_{0E}, Figure 8. Note also from this figure that the design rule for the emitter changes with the magnitude of FSRV. For devices with any reasonable amount of surface passivation, a lower J_{0E} is accomplished by thinning the emitter, but for unpassivated surfaces, emitter thinnning would actually increase J_{0E}. Thus, the AlGaAs passivation is most critical for thin emitters.

As a final confirmation of the lifetime profile and S value derived above, the cell J_{sc}, V_{oc}, and efficiency were calculated using PC-1D. Table 1 shows a very good agreement between the measured and modeled values confirming the validity of the above procedure. Having established the match, the PC-1D model was used to provide guidelines for improving the efficiency of this cell and to optimize the p-n heteroface cell design. Model calculations in Table 1 show that a significant improvement in cell efficiency (23%) can be realized by properly passivating the front surface of this cell so that the FSRV = 1×10^4 cm/s (note decrease in S_{eje} in Figure 8 for FSRV = 1×10^4 cm/s).

Only a slight improvement is found by back surface passivation for the lifetime profile of this device structure. However, if the effective base lifetime can be improved to 15 ns, the efficiency of this cell can reach ~24.17% with passivated front and back surfaces. This improvement is clearly understood upon inspection of Figure 9 which shows that longer lifetimes decrease the magnitudes of S_{eje} and S_{ejb} resulting in higher V_{oc}, in addition to raising J_{sc} via reduced recombination throughout the device. Further gain in efficiency can be obtained by optimizing the thickness and doping profile of the device. Since in n-type GaAs the net lifetime is dominated by defects up to a doping level of ~1 x 10^{18} cm^{-3} [7], an efficiency of ~24.40% can be obtained simply by changing the base doping to 5 x 10^{17} cm^{-3} and the buffer doping to 2.5 x 10^{18} cm^{-3}. These doping levels represent the optimum trade-off between an increase in V_{oc} due to the heavier base doping and a decrease in J_{sc} resulting from higher S_e in the base due to a reduced doping discontinuity (N_1/N_2) at the buffer/base interface. It should be recognized that these conclusions are easily deduced from S_e plots which signify the importance of such analysis. The cell efficiency tends to saturate near the 24.40% level unless the base material quality is improved further. Table 1 shows an efficiency of 24.76% can be obtained with a lifetime of 20 ns, which is still well below the intrinsic lifetime limit of GaAs at a doping level of 5 x 10^{17} cm^{-3}. This represents the highest efficiency found for our simulations of this particular p-n heteroface structure.

Further optimization is possible only by modifying the device structure. Table 1 shows that a 24.74% efficient cell can be achieved with only a 15 ns base lifetime by thinning the base to 1.2 um and buffer to 1.3 um. This improvement comes as a result of the trade-off between low S_e in the base and

increased photon absorption in the buffer. For this device structure, it is necessary to have a passivated back surface and reasonable lifetime in the buffer. The doping and thickness of the base and buffer layers become critical to the performance of such a device since there exists a sensitive trade-off between greatly increased carrier collection in the thinned base due to reduced recombination in the base resulting from the proximity of the base/buffer interface to the collecting junction, and the amount of carriers generated in the buffer layer that do not make it to the p-n junction. The V_{oc} is greatly increased due to the lower S_{ejb}, while the J_{sc} benefits from the higher collection efficiency of photogenerated carriers in the thin base. Model calculations in Table 1 also indicate efficiencies as high as ~25.04% are possible for a device with a base width of 1.2 um, buffer thickness of 1.3 um, base doping of 6×10^{17} cm^{-3}, buffer doping of 2.5×10^{18} cm^{-3}, base lifetime of 20 ns, FSRV = 1×10^{4} cm/s, and BSRV = 1×10^{3} cm/s. If an FSRV of 1×10^{3} cm/s can be attained, the efficiency can be increased to 25.15%. It should be noted that the buffer thickness now becomes important since the effectiveness of the back surface passivation would be reduced if the buffer were too thick. In essence, the buffer here acts as part of a two-step base layer which suggests that further gains in efficiency can be realized by multi-step or even graded base regions. These considerations, and the optimization of the thinned base structure will be presented elsewhere [20].

CONCLUSIONS

A high efficiency, MOCVD grown, GaAs p-n heteroface solar cell has been characterized to assess the loss mechanisms and its design optimized through

extensive computer modeling. Recombination mechanisms were studied using dark I-V, I-V-T, and DLTS measurements which revealed a hole trap at E_v + 0.912 eV as responsible for the space charge component of the leakage current. Depth-resolved DLTS and SPV measurements were performed to establish that this level was spatially localized near the p-n interface. Although the observed deep level does not affect J_{01}, it still degrades the cell performance by making the J_{02} component comparable to the J_{01} component at the cell operating point.

The internal recombination parameters (lifetime, J_{01}, FSRV, BSRV) were determined by simultaneously matching the measured and simulated spectral response, J_{01}, and cell data (J_{sc}, V_{oc}, efficiency) with the help of PC-1D and effective recombination velocity models. It was found that an FSRV of 1.25×10^5 cm/s and a net base lifetime of 8 ns were required to match the cell data. These values were further verified by a good match between the measured and calculated values of J_{01} using the above FSRV and lifetime profile as inputs to the effective recombination velocity model. This model also gave the emitter and base components of J_{01}, which showed that the base exerted primary control over the leakage current, accounting for ~67% of the total J_{01}.

Having matched the cell under investigation, guidelines were provided to optimize this structure. For the device studied here, the efficiency can be increased from 21.2% to over 24% by improved front surface passivation (FSRV ~ 1×10^4 cm/s) and base material quality (τ_b = 15 ns). Further efficiency improvement can be realized by thinning the base so that the buffer becomes an active part of the device, forming essentially a two-step base. This structure, however, requires back surface passivation to maximize cell

efficiency. This device structure, with a net base lifetime of 20 ns, can result in efficiencies in excess of 25%.

ACKNOWLEDGEMENT

The authors would like to acknowledge the assistance of A. Smith and J. D. Welch for assisting in the computer modeling. This work was supported by Sandia National Laboratories, Contract No. 02-2255.

FIGURE CAPTIONS

Figure 1. Device structure and measured cell data of the MOCVD GaAs heteroface cell used in this study.

Figure 2. Variation of SPV response as the device is etched through. The measurements were taken at etch depths of (a) 0.12 um, (b) 0.17 um, (c) 0.21 um, (d) 0.30 um, and (3) 0.42 um.

Figure 3. Ratios between SPV spectra taken at: (a) front of emitter; (b) just before p-n junction; (c) just after p-n junction; (d) 0.1 um after curve (c) as shown in inset.

Figure 4. DLTS scan and activation energy plot indicating the presence of a hole trap in the n-type base depletion region.

Figure 5. LN(J) vs T plot measured at 2 volts constant reverse bias. Trap activation energy is shown in the figure.

Figure 6. Transformed I-V characteristic for cell. J_1 (diffusion) and J_2 (space charge) current density components are indicated.

Figure 7. Comparison of actual spectral response (solid line) with modeled spectral response (blocks) as calculated from PC-1D for the given device structure.

Figure 8. Plot of effective recombination velocity, S_e, for various values of front and back surface recombination velocities. Emitter and base leakage current components are indicated for the cell-matching S_e plot.

Figure 9. Plot of effective recombination velocity, S_e, showing the influence of minority carrier lifetime on recombination throughout the device. The net lifetimes in each layer are indicated.

Table 1. Guideline for cell optimization using PC-1D and effective recombination velocity modeling. Actual cell data and best match are shown. Cells 6, 7, and 8 (starred entries) are thinned base and buffer structures.

REFERENCES

1. R. J. Nelson and R. G. Sobers, "Minority-carrier lifetime and internal quantum efficiency of surface-free GaAs," Appl. Phys., vol. 49, no. 12, pp. 6103-6108, 1978.
2. C. J. Hwang, "Doping dependence of hole lifetime in n-type GaAs," J. Appl. Phys., vol. 42, no. 11, pp. 4408-4413, 1971.
3. R. J. Nelson, "Interfacial recombination in GaAlAs-GaAs heterostructures," J. Vac. Sci. Technol., vol. 15, no. 4, pp. 1475-1477, 1978.
4. P. Dawson and K. Woodbridge, "Effects of prelayers on minority-carrier lifetime in GaAs/AlGaAs double heterostructures grown by molecular beam epitaxy," Appl. Phys. Lett., vol. 45, no. 11, pp. 1227-1229, 1984.
5. J. M. Woodall and J. L. Freeouf, "GaAs metallization: Some problems and trends," J. Vac. Sci. Technol., vol. 19, no. 3, pp. 794-798, 1981.
6. P. D. DeMoulin, C. S. Kyono, M. S. Lundstrom, and M. R. Melloch, "Dark I/V characterization of GaAs p/n heteroface cells," Proc. of the Nineteenth IEEE Photovoltaic Specialists Conf., pp. 93-97, 1987.
7. P. D. DeMoulin and M. S. Lundstrom, "Theoretical comparison of conventional and unconventional GaAs cell design," Proc. of Nineteenth IEEE Photovoltaic Specialists Conf., pp. 925-930, 1987.
8. M. S. Lundstrom, "Device physics of crystalline solar cells," Solar Cells, vol. 24, pp. 91-102, 1988.
9. S. P. Tobin, S. M. Vernon, C. Bajgar, L. M. Geoffroy, C. J. Keavney, M. M. Sanfacon, and V. E. Haven, "Device processing and analysis of high efficiency GaAs cells," Solar Cells, vol. 24, pp. 103-115, 1988.
10. P. Blood, "Measurement of optical absorption in epitaxial semiconductor layers by a photovoltage method," J. Appl. Phys., vol. 58, no. 6, pp. 2288-2295, 1985.

11. D. K. Schroder, "The concept of generation and recombination lifetimes in semiconductors," IEEE Trans. Electron Dev., vol. ED-29, no. 8, pp. 1336-1338, 1982.

12. K. W. Loh, D. K. Schroder, R. C. Clarke, A. Rohatgi, and G. W. Eldridge, "Low leakage current GaAs diodes," IEEE Trans. Electron Dev., vol. ED-28, no. 7, pp. 796-800, 1981.

13. A. S. Grove, Physics and Technology of Semiconductor Devices, Wiley, New York, 1967.

14. P. A. Basore, "Numerical analysis of semiconductor devices on personal computers," Proc. of the Sixth Biennial University/Government/Industry Microelectronics Symp., pp. 73-76, 1985.

15. C. J. Hwang, "Quantum efficiency and radiative lifetime of the band to band recombination in heavily doped n-type GaAs," Phys. Rev. B., vol. 6, pp. 1355-1359, 1972.

16. A. Huag, "Auger recombination in direct-gap semiconductors: band structure effects," J. Phys. C: Solid State Phys., vol. 16, pp. 4159-4172, 1983.

17. J. S. Blakemore, "Semiconducting and other major properties of gallium arsenide," J. Appl. Phys., vol. 53, no. 10, pp. R123-R181, 1982.

18. A. Rohatgi and P. Rai-Choudhury, "Design, fabrication and analysis of 17-18 percent efficient surface-passivated silicon solar cells," IEEE Trans. Electron Dev., vol. ED-31, no. 5, pp. 596-601, 1984.

19. H. Van Cong, "Impurity band structure in degenerate semiconductors for both dense donors and acceptors," Phys. Stat. Sol., vol. 56A, pp. 395-405, 1979.

20. S. A. Ringel and A. Rohatgi, to be presented at the Twentieth IEEE Photovoltaic Specialists Conf., Las Vegas, 1988.

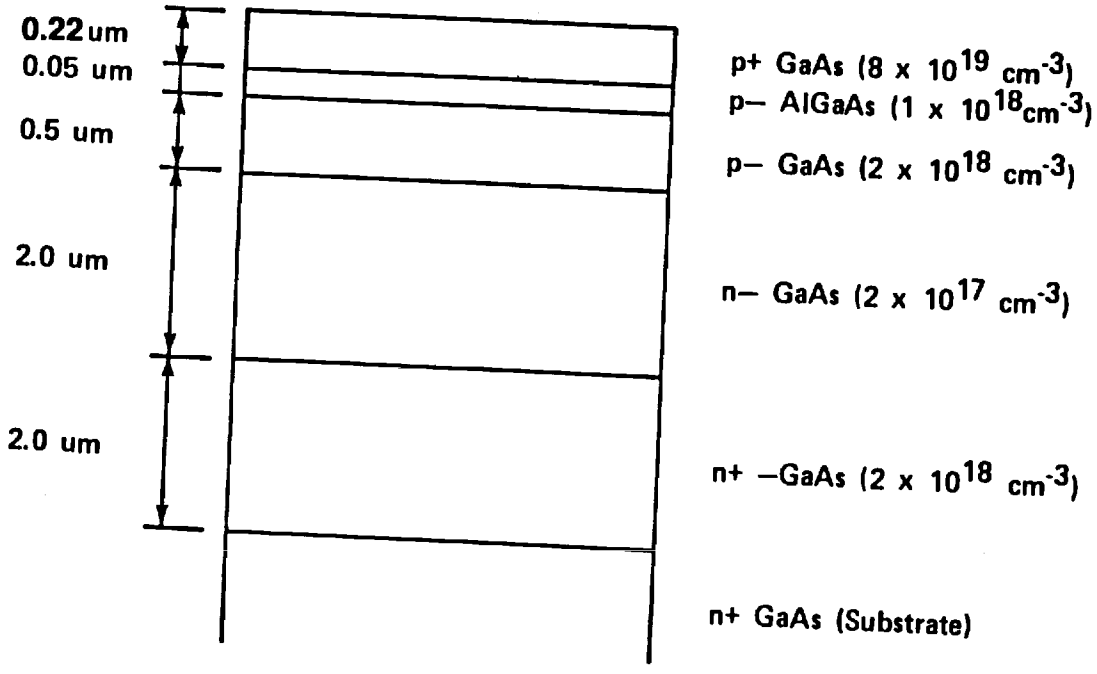

GaAs solar cell structure used in these experiments

V_{oc} = 1.013V J_{sc} = 24.5 mA/cm^2

F.F. = 0.855 Eff = 21.2%

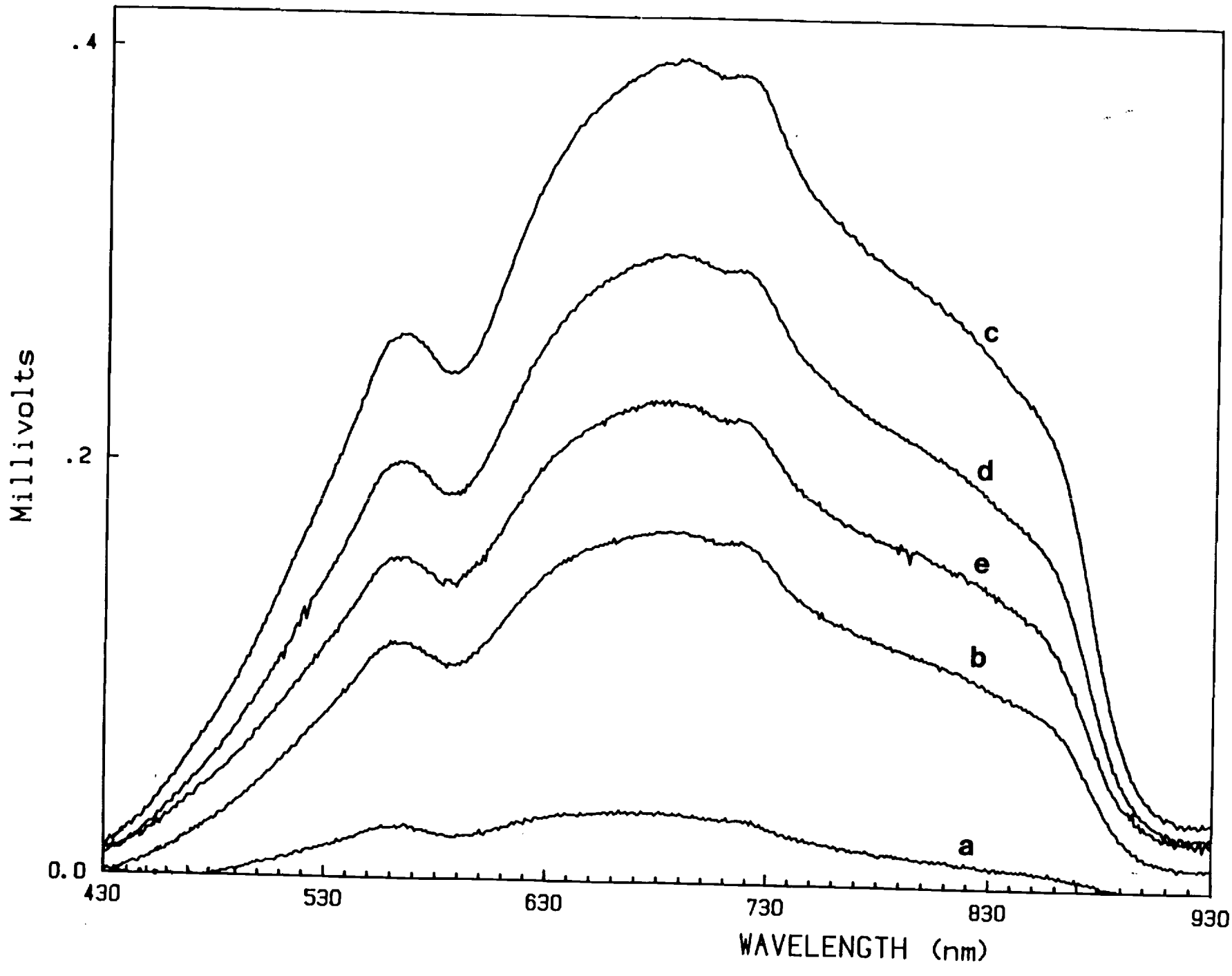
.4
.2
0.0
Millivolts
430
530
630
730
830
930
WAVELENGTH (nm)
a
b
c
d
e

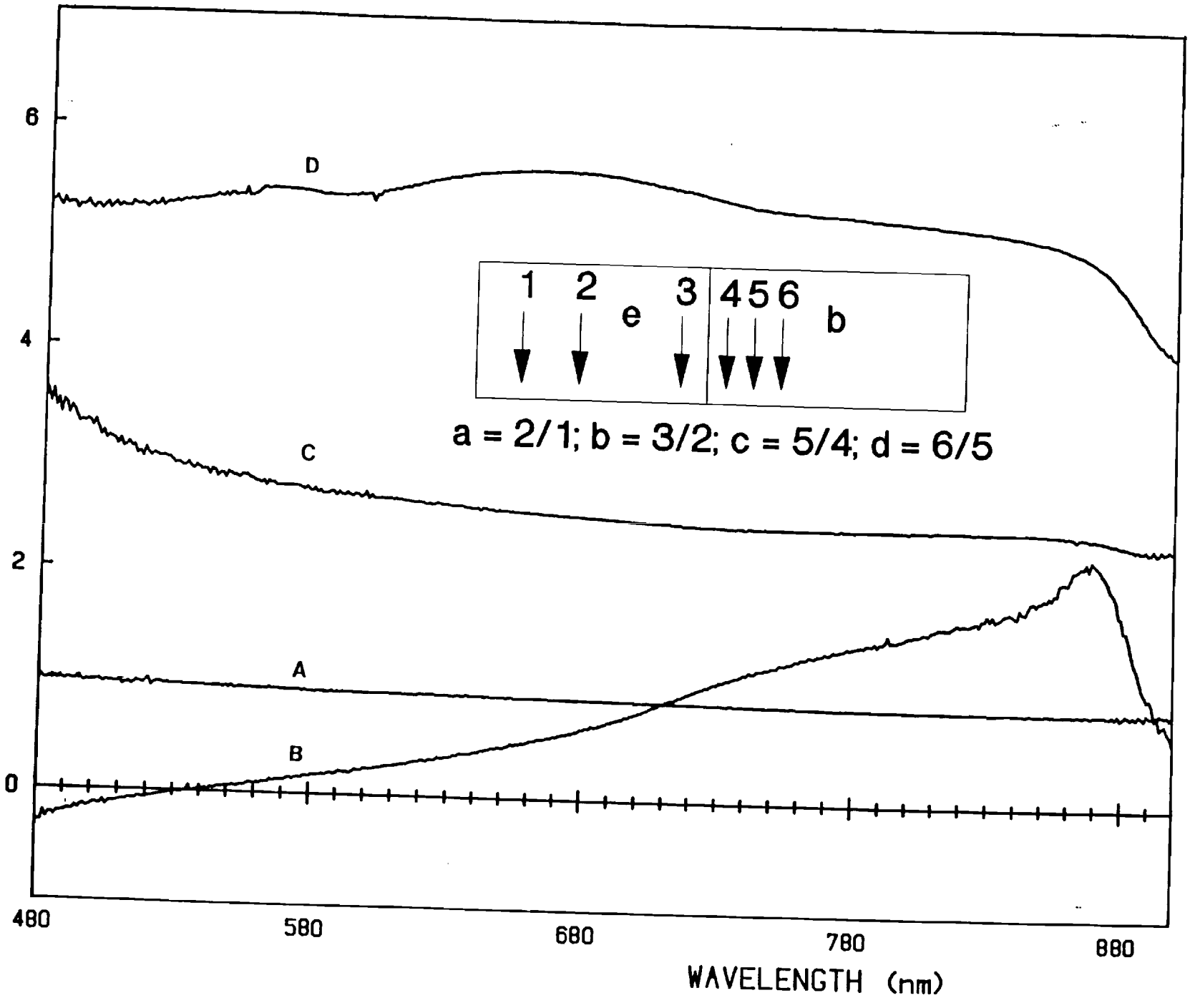
6
4
2
0
D
C
A
B
1 2 e 3 4 5 6 b
a = 2/1; b = 3/2; c = 5/4; d = 6/5
480
580
680
780
880
WAVELENGTH (nm)

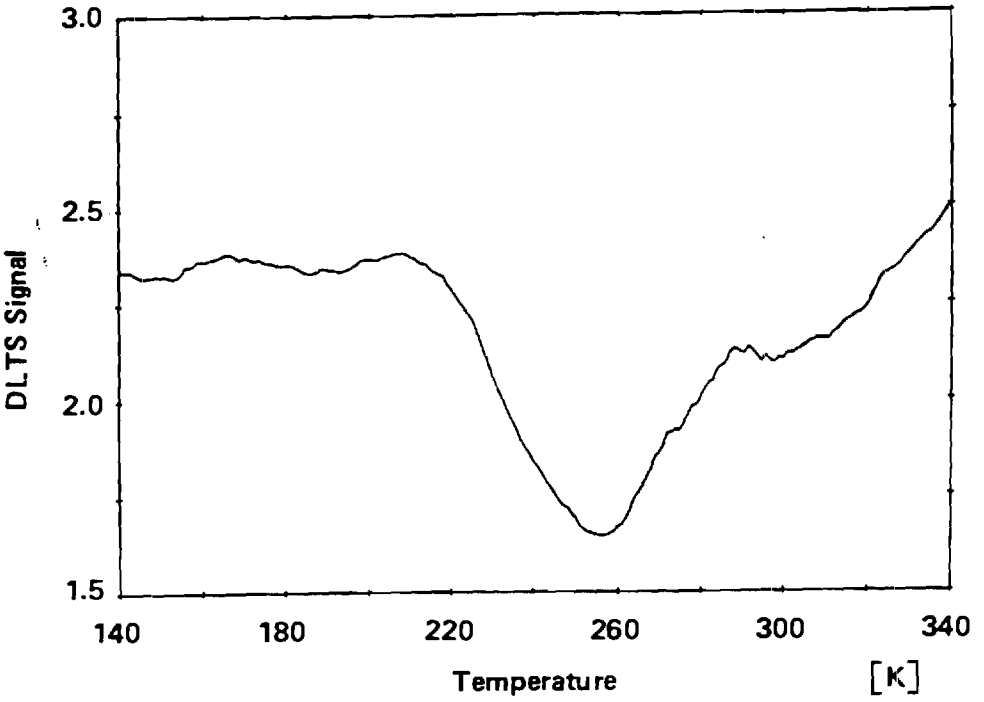
3.0
2.5
2.0
1.5
DLTS Signal
140
180
220
260
300
340
Temperature
[K]

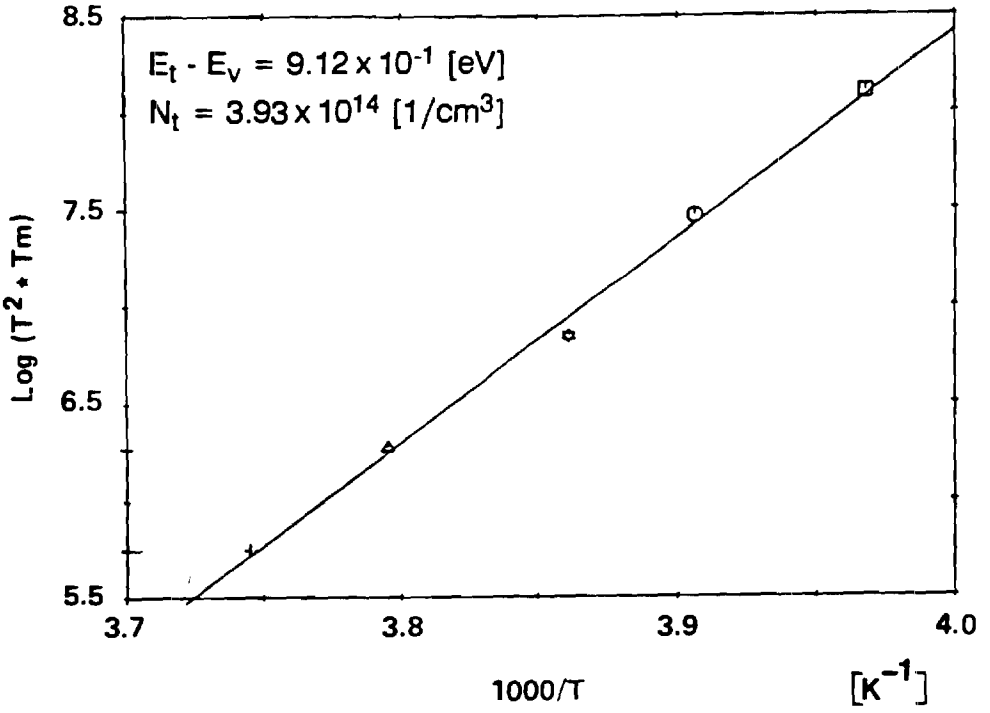
8.5
7.5
6.5
5.5
Log (T² * Tm)
Et - Ev = 9.12 x 10⁻¹ [eV]
Nt = 3.93 x 10¹⁴ [1/cm³]
3.7
3.8
3.9
4.0
1000/T
[K⁻¹]

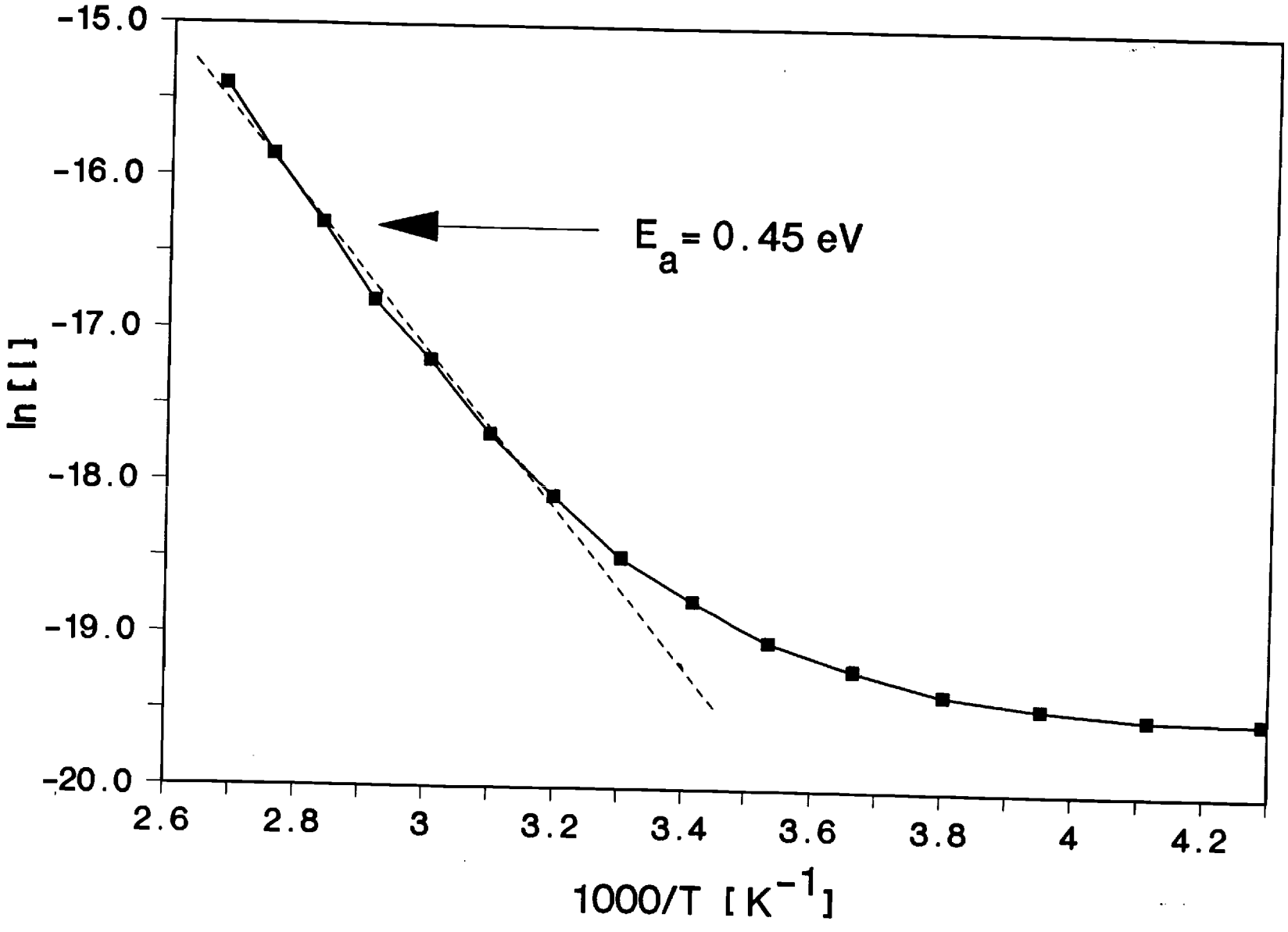
-15.0
-16.0
-17.0
-18.0
-19.0
-20.0
ln[I]
E_a = 0.45 eV
2.6
2.8
3
3.2
3.4
3.6
3.8
4
4.2
1000/T [K^{-1}]

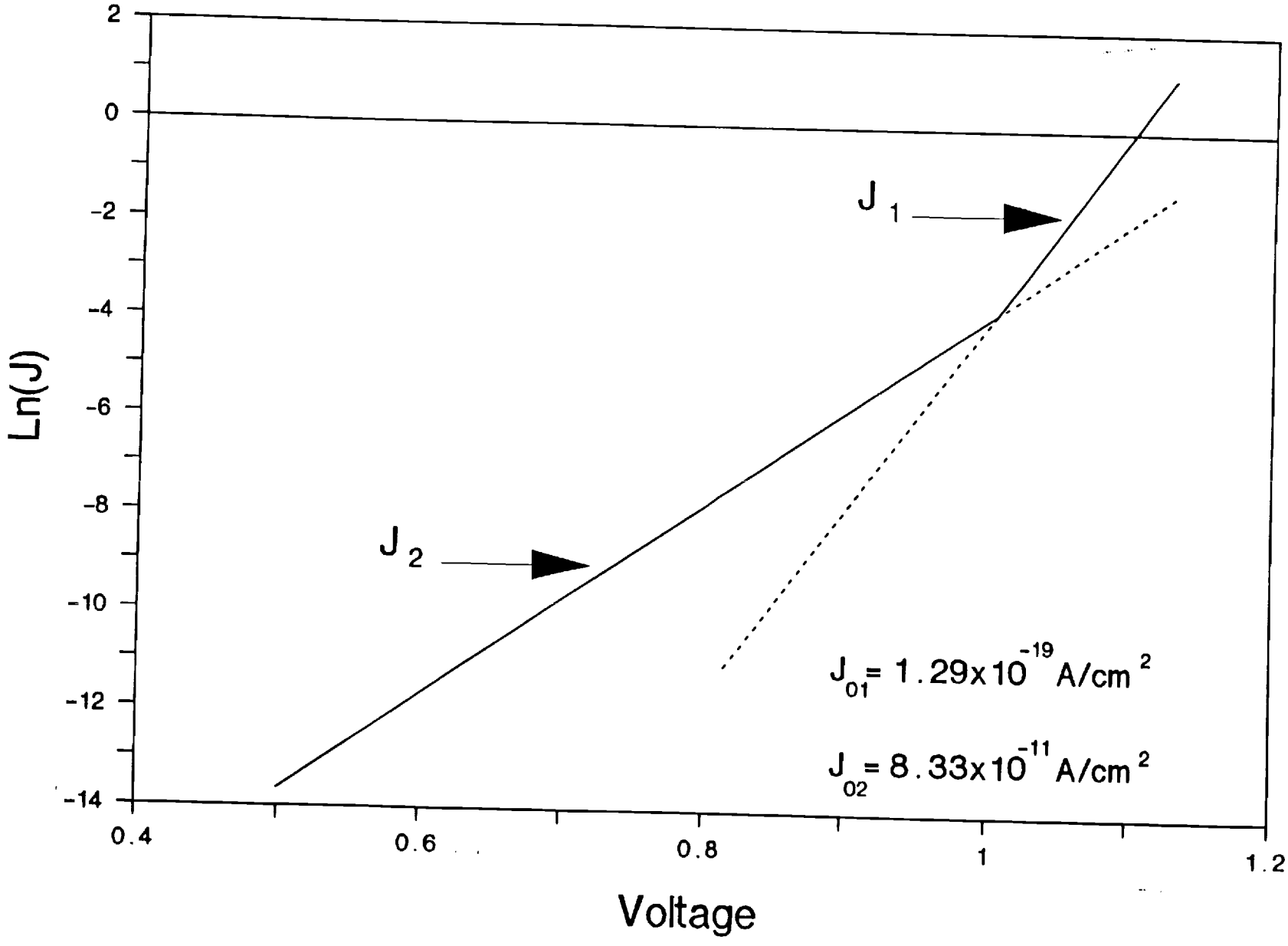
2
0
-2
-4
-6
-8
-10
-12
-14
Ln(J)
0.4
0.6
0.8
1
1.2
Voltage
J 1
J 2
J01= 1.29x10-19 A/cm 2
J02= 8.33x10-11 A/cm 2

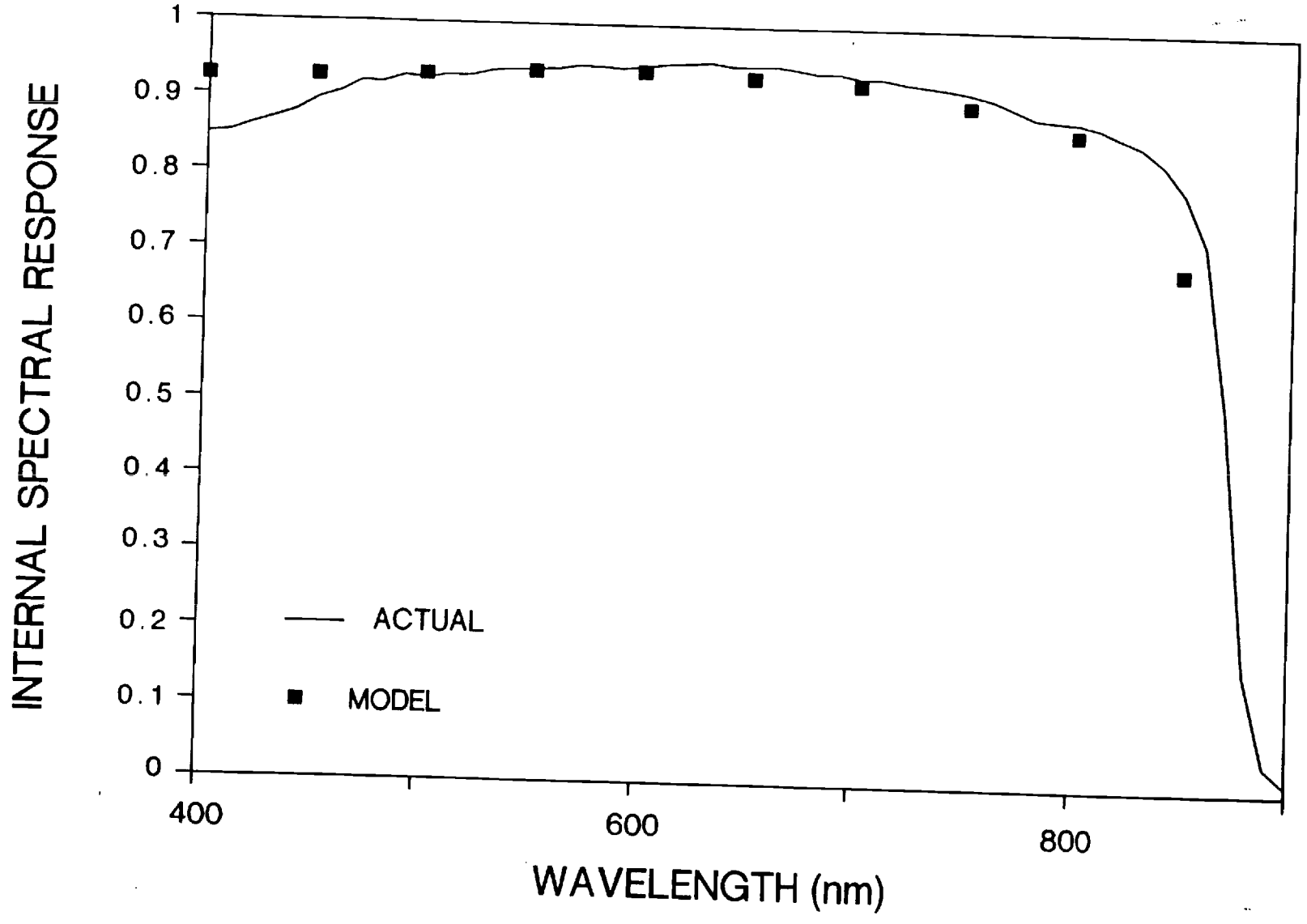
INTERNAL SPECTRAL RESPONSE
1
0.9
0.8
0.7
0.6
0.5
0.4
0.3
0.2
0.1
0
400
600
800
WAVELENGTH (nm)
ACTUAL
MODEL

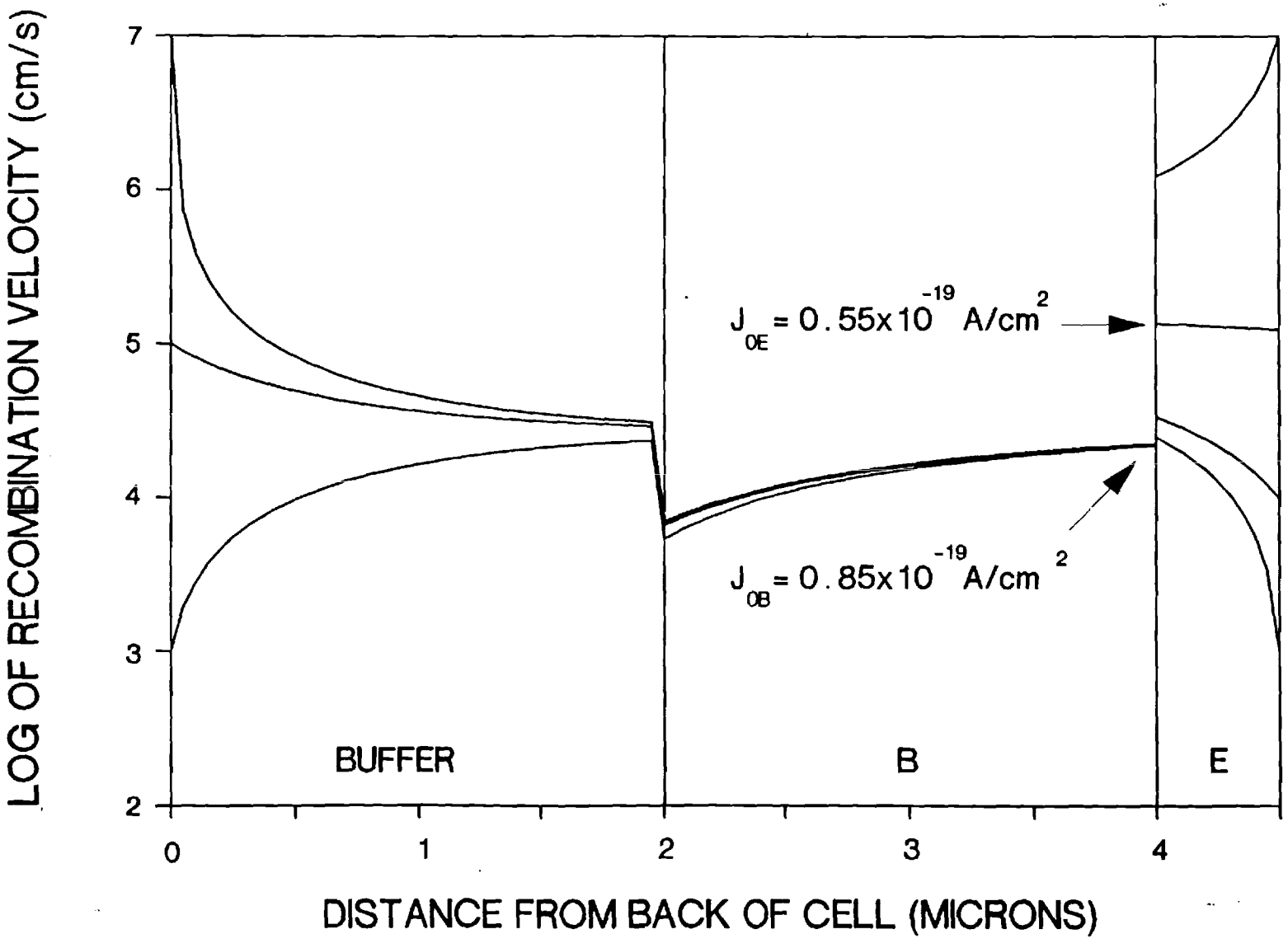
LOG OF RECOMBINATION VELOCITY (cm/s)
7
6
5
4
3
2
0
1
2
3
4
$J_{0E} = 0.55 \times 10^{-19}$ A/cm^2
$J_{0B} = 0.85 \times 10^{-19}$ A/cm^2
BUFFER
B
E
DISTANCE FROM BACK OF CELL (MICRONS)

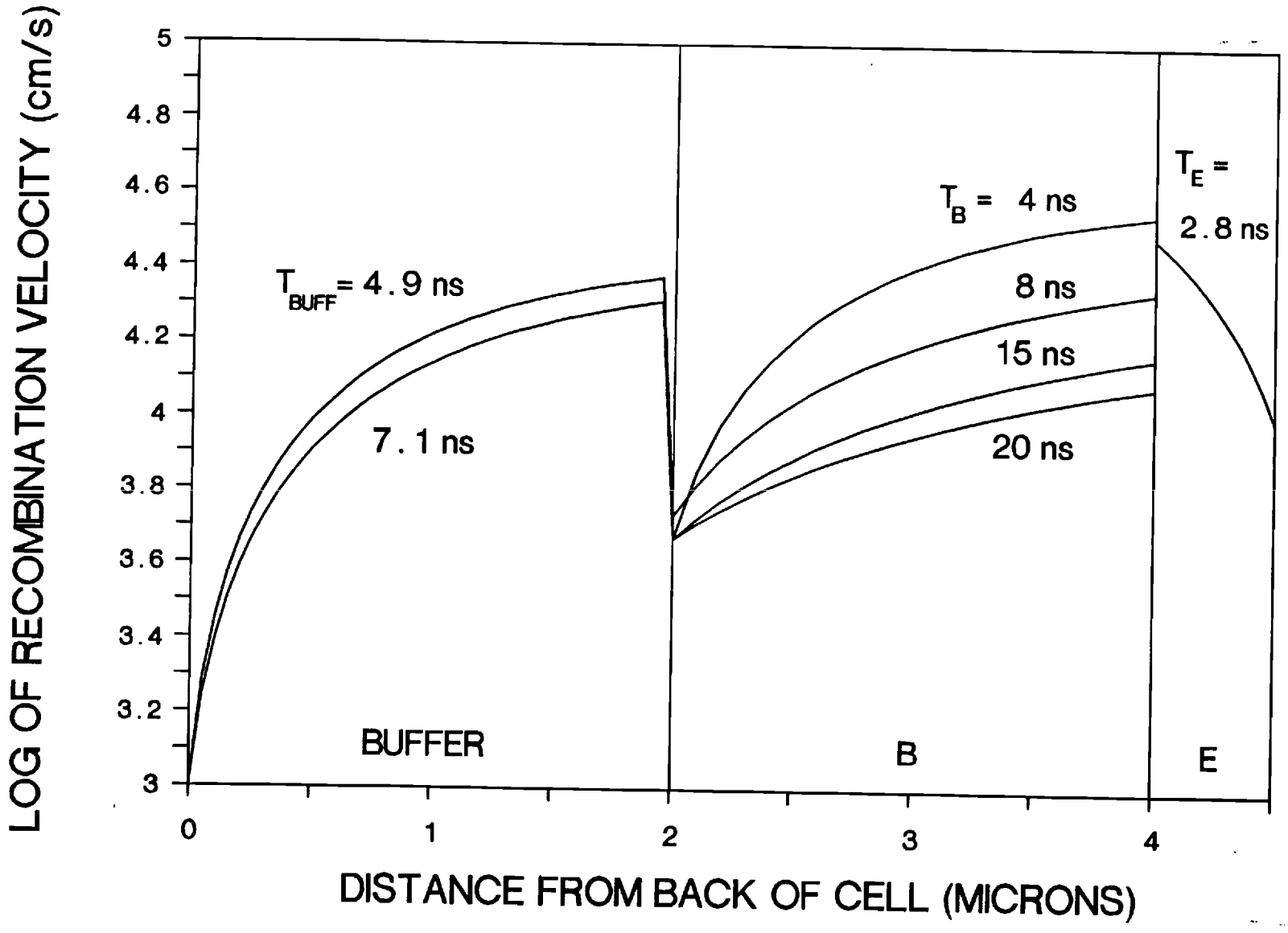
LOG OF RECOMBINATION VELOCITY (cm/s)
5
4.8
4.6
4.4
4.2
4
3.8
3.6
3.4
3.2
3
0
1
2
3
4
DISTANCE FROM BACK OF CELL (MICRONS)
T_{BUFF} = 4.9 ns
7.1 ns
BUFFER
T_B = 4 ns
8 ns
15 ns
20 ns
B
T_E =
2.8 ns
E

Cell ID	N_d (cm^{-3})	N_a (cm^{-3})	N_{buff} (cm^{-3})	FSRV (cm/s)	BSRV (cm/s)	T_b (ns)	V_{oc} (Volts)	J_{sc} (A/cm^2)	Eff (%)
Actual	$2.0x10^{17}$	$2.0x10^{18}$	$2.0x10^{18}$				1.013	24.5	21.2
Match	$2.0x10^{17}$	$2.0x10^{18}$	$2.0x10^{18}$	$1.25x10^{5}$	$1.0x10^{6}$	8	1.01	24.56	21.39
1	$2.0x10^{17}$	$2.0x10^{18}$	$2.0x10^{18}$	$1.0x10^{4}$	$1.0x10^{6}$	8	1.016	26.59	23.02
2	$2.0x10^{17}$	$2.0x10^{18}$	$2.0x10^{18}$	$1.0x10^{4}$	$1.0x10^{4}$	8	1.017	26.71	23.13
3	$2.0x10^{17}$	$2.0x10^{18}$	$2.0x10^{18}$	$1.0x10^{4}$	$1.0x10^{4}$	15	1.032	27.11	24.17
4	$5.0x10^{17}$	$2.0x10^{18}$	$2.5x10^{18}$	$1.0x10^{4}$	$1.0x10^{4}$	15	1.048	26.83	24.40
5	$5.0x10^{17}$	$2.0x10^{18}$	$2.5x10^{18}$	$1.0x10^{4}$	$1.0x10^{4}$	20	1.054	26.95	24.76
6*	$6.0x10^{17}$	$2.0x10^{18}$	$2.5x10^{18}$	$1.0x10^{4}$	$1.0x10^{3}$	15	1.055	27.04	24.74
7*	$6.0x10^{17}$	$2.0x10^{18}$	$2.5x10^{18}$	$1.0x10^{4}$	$1.0x10^{3}$	20	1.059	27.10	25.04
8*	$6.0x10^{17}$	$2.0x10^{18}$	$2.5x10^{18}$	$1.0x10^{3}$	$1.0x10^{3}$	20	1.062	27.17	25.15

EFFECT OF DEEP LEVEL POSITION AND SURFACE TEXTURING ON CELL PERFORMANCE

In order for all manufacturers to produce high efficiency cells optimum material characteristics must be formulated. An important characteristic is the trap level and its relationship to the lifetime in different resistivity material. This report shows that the optimum resistivity for a given cell design depends upon three factors: 1) The starting lifetime of the undoped material. 2) The location of the trap level in the forbidden band. 3) The trap density is independent of doping concentration.

Figure 1 shows the dependence of the lifetime on the trap level and resistivity for a 1 msec. starting lifetime undoped material. Figure 2 reflects the efficiency of cells using the lifetime in figure 1. For the instance in which the level is located in the middle of the gap the optimum resistivity is approximately 1 ohm-cm. Yet, for a level at 0.2 ev it would be benificial to remain at the higher resistivity. To examine the effect of the starting lifetime on the efficiency figures 3 and 4 were produced, by holding the trap level constant and varing the initial lifetime. For a trap at 0.56 ev, figure 3, a starting lifetime of 10 usec. and 1 msec produce the best efficiency cells on 0.2 to 1 ohm-cm substrates. 10 msec. starting material cells show little dependence upon the resistivity. When the trap level is shifted to 0.2 ev the optimum resistivity for low starting lifetime remains at 0.2 ohm-cm. For the higher quality starting material the optimum resistivity has shifted to the higher values of resistivity.

The second part of this report deals with texturing the surface of the cells to increase the short circuit current. To simulate this a ray tracing program was developed to produce generation profiles to be incorporated into PC-1D. Figure 5 illustrates the steps required to make the link between ray tracing and PC-1D. Figure 6 shows the surfaces which were simulated. The generation profiles of the pyramids and perpendicular slats geometries were produced by ray tracing, while the lambertian surface was approximated by another program. Table 1 lists the cumulative absorption for these geometries, the angle of the perpendicular slats was allowed to vary while the pyramid was fixed at 53 degrees. In order to use PC-1D the generation profile had to be changed to match the ray traced profile, figure 7, shows the reason for the need of change. After matching the profiles PC-1D simulations were performed, the results are given in Table 2. Figure 8 shows that for all thicknesses with the given cell design the perpendicular slats produces the highest efficiency cells. While it is seen that pyramids provide a substantial improvement over flat cells.

Since the cell design in used in simulations for the textured cells is not optimum, the cell parameters were changed to reflect the work in the previous section on traps. Simulations were performed on materials of varing lifetime with the optimum resistivity dictated by results from figures 3 through 5. Figure 9 shows the change in efficiency for varing lifetime with perpendicular slats and flat cells. The greatest

change in efficiency is for 100 usec. starting lifetime material, as reflected in figure 10.

Lifetime versus resistivity for various trap levels with one starting lifetime.

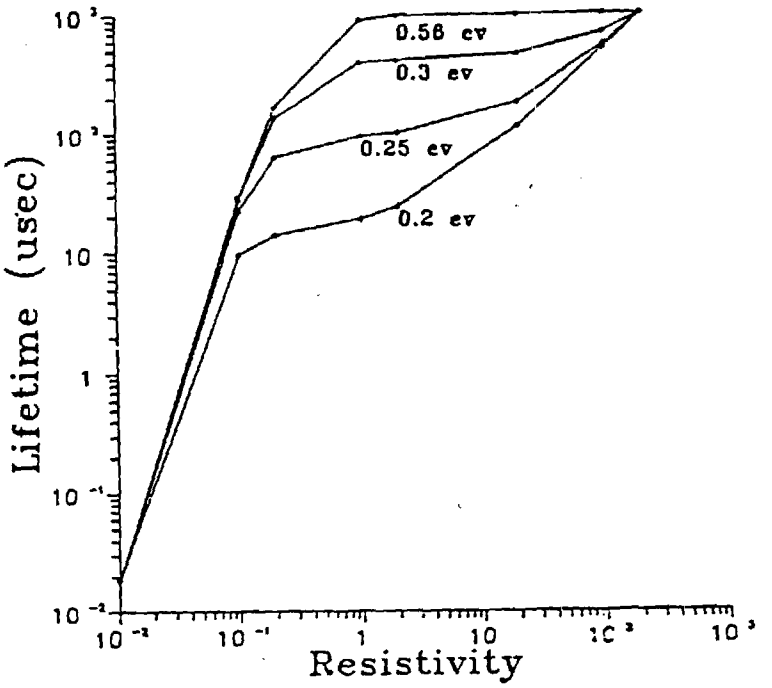

Efficiency versus resistivity for various trap levels with one starting lifetime.

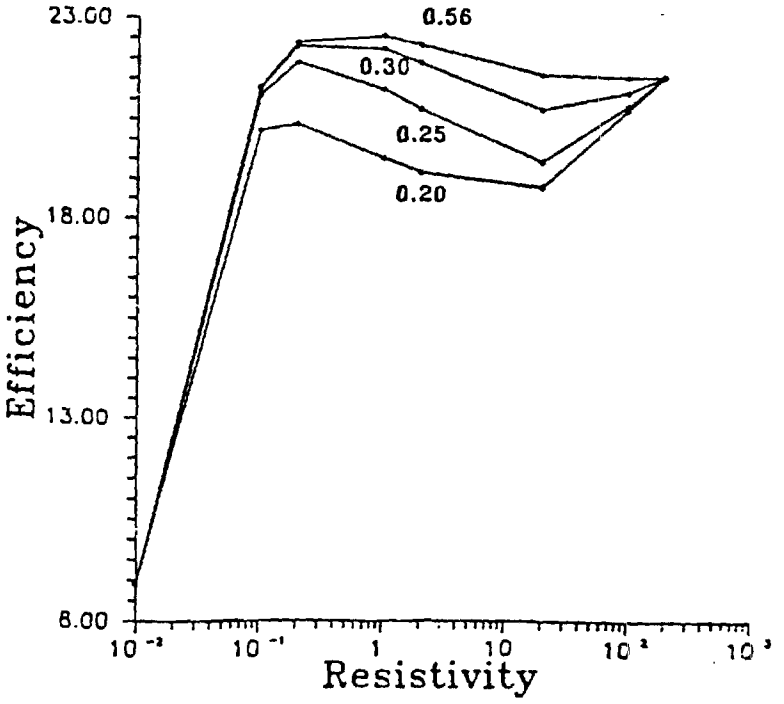

Efficiency versus resistivity for
a trap located at 0.56 ev.

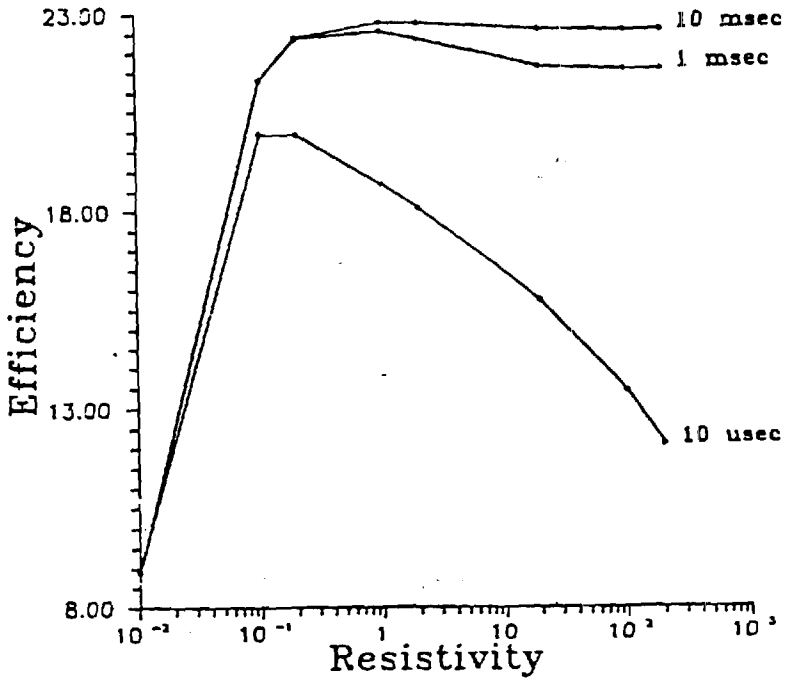

Efficiency versus resistivity for
a trap located at 0.2 ev.

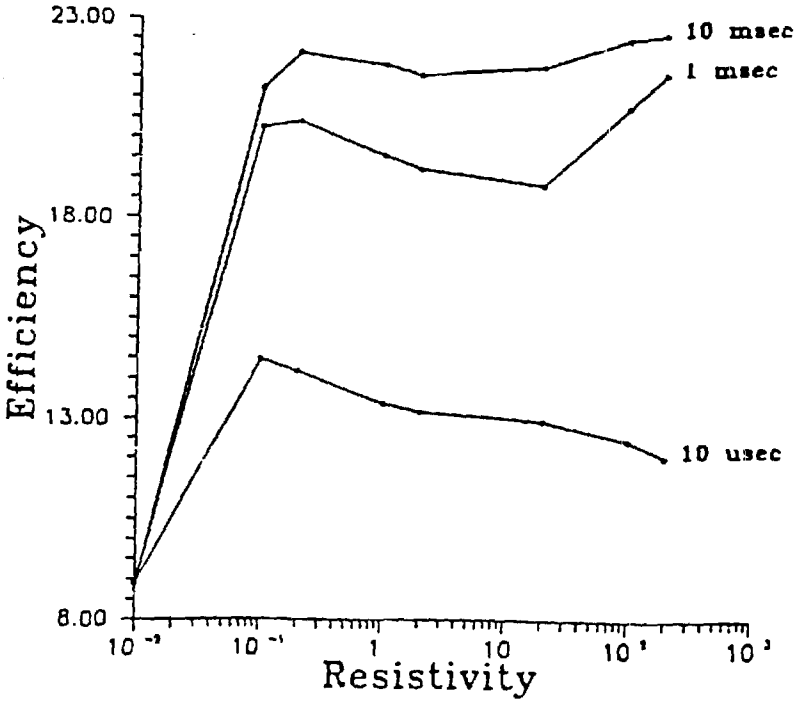

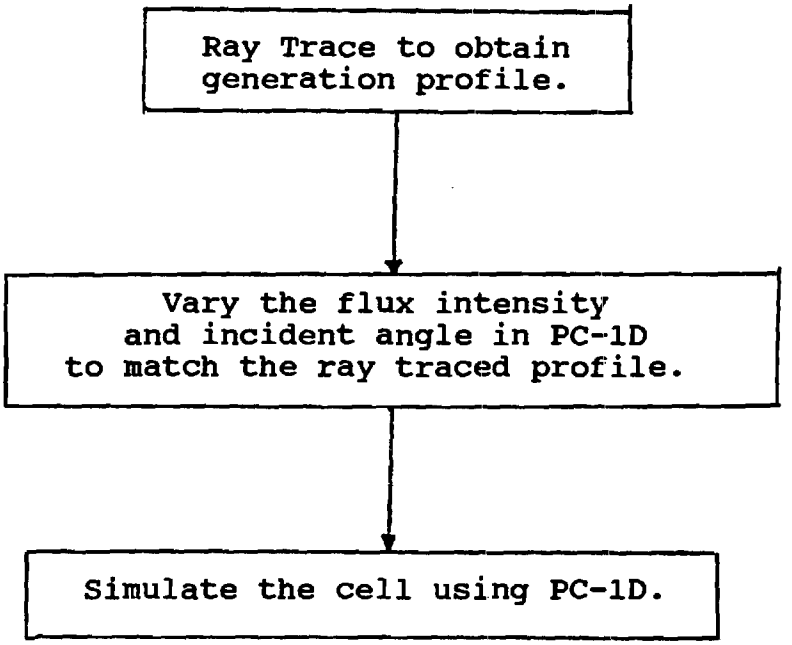
Ray Trace to obtain generation profile.
Vary the flux intensity and incident angle in PC-1D to match the ray traced profile.
Simulate the cell using PC-1D.

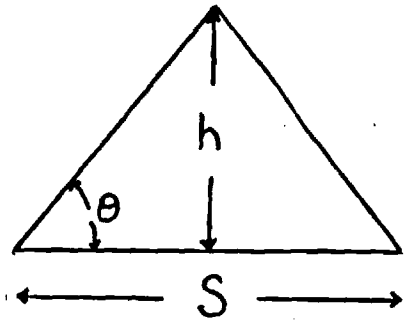

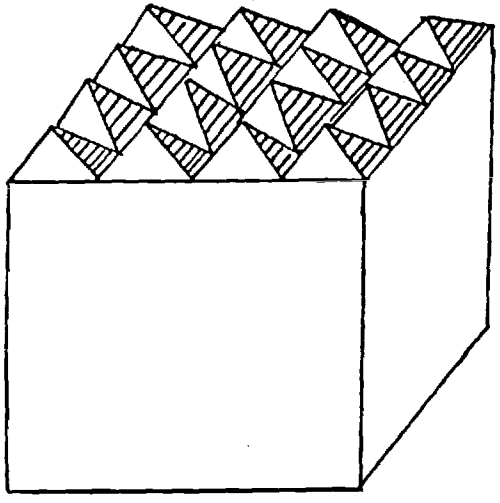

Pyramids

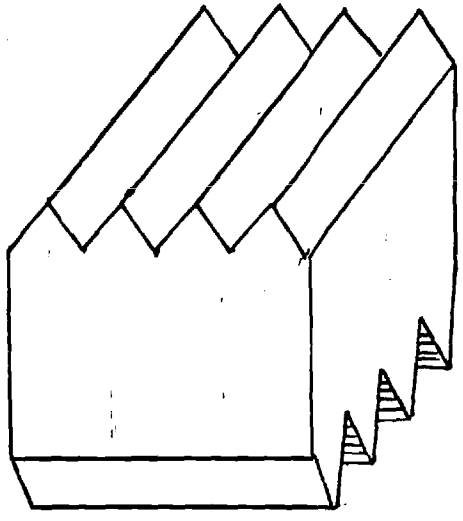

Perpendicular Slats

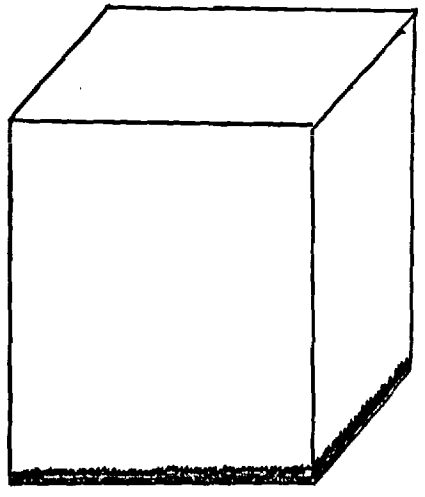

Lambertian

Cumulative absorption for various surface texturing and thicknesses, all fluxes are multiplied by 1.0 E17. Different angles are included for perpendicular slats.

Thickness	Perpendicular Slats				
(um)	45	53	55	63.4	75
100	2.3727	2.5144	2.5102	2.4908	2.3746
200	2.4319	2.5494	2.5446	2.5098	2.4318
254	2.4668	2.5593	2.5488	2.5176	2.4498
381	2.4964	2.5733	2.5721	2.5462	2.4774
500	2.503	2.5807	2.5782	2.5723	2.4941
635	2.5132	2.5951	2.5948	2.5832	2.505

Thickness (um)	Flat	Pyramid	Lambertian
100	2.3447	2.365	2.5072
200	2.4047	2.4446	2.5454
254	2.4259	2.4633	2.5546
381	2.455	2.4785	2.5697
500	2.4772	2.4963	2.5774
635	2.4938	2.5081	2.5882

Cumulative photon absorption for 381 um thick cell with various texturing.

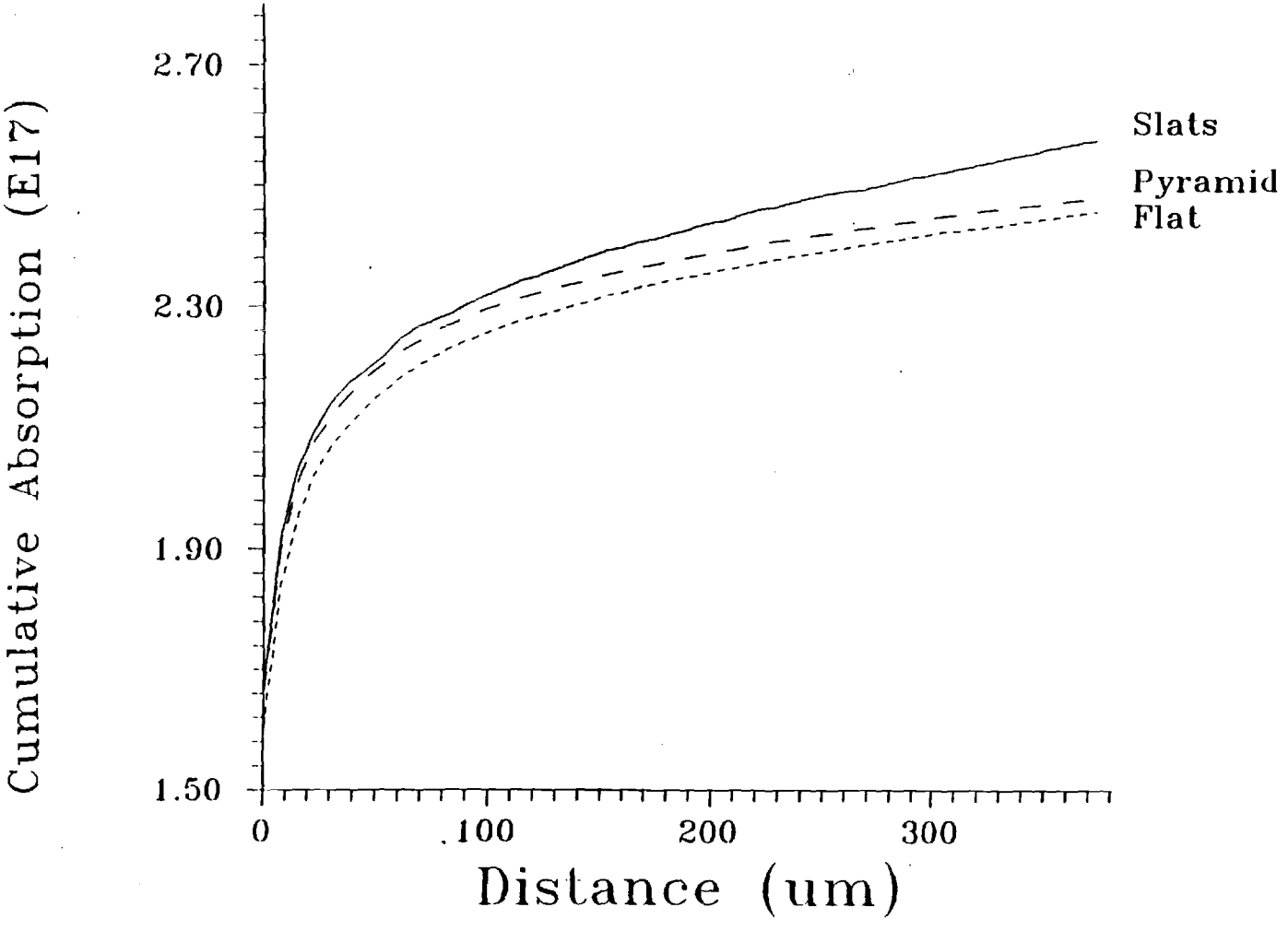

Tabulation of cell parameters for various surface texturing and cell thicknesses. Each cell has a series resistance of 0.2 ohms and FSRV and BSRV of 500 cm/sec.

Thickness (um)		Flat	Pyramid	Lambertian	Slats
100	Eff.	21.85165	22.00052	23.41613	23.45332
	Voc	0.69823	0.698328	0.699787	0.699875
	Jsc	0.037557	0.037821	0.040159	0.040229
200	Eff.	22.27526	22.62216	23.59323	23.6046
	Voc	0.69564	0.696037	0.696944	0.69701
	Jsc	0.038535	0.039121	0.040772	0.040824
254	Eff.	22.39572	22.75807	23.57452	23.5975
	Voc	0.69432	0.694778	0.695523	0.69559
	Jsc	0.038909	0.039524	0.040918	0.040989
381	Eff.	22.38395	22.62525	23.44705	23.5308
	Voc	0.69119	0.691444	0.692192	0.69228
	Jsc	0.039292	0.039715	0.041161	0.04124
500	Eff.	22.36546	22.57834	23.31279	23.373
	Voc	0.68864	0.688826	0.689485	0.68954
	Jsc	0.039646	0.040025	0.041282	0.041368
635	Eff.	22.30112	22.4234	23.14694	23.2514
	Voc	0.68608	0.686207	0.686873	0.68697
	Jsc	0.039952	0.040172	0.041447	0.041588

Efficiency versus cell thickness for various surface texturing.

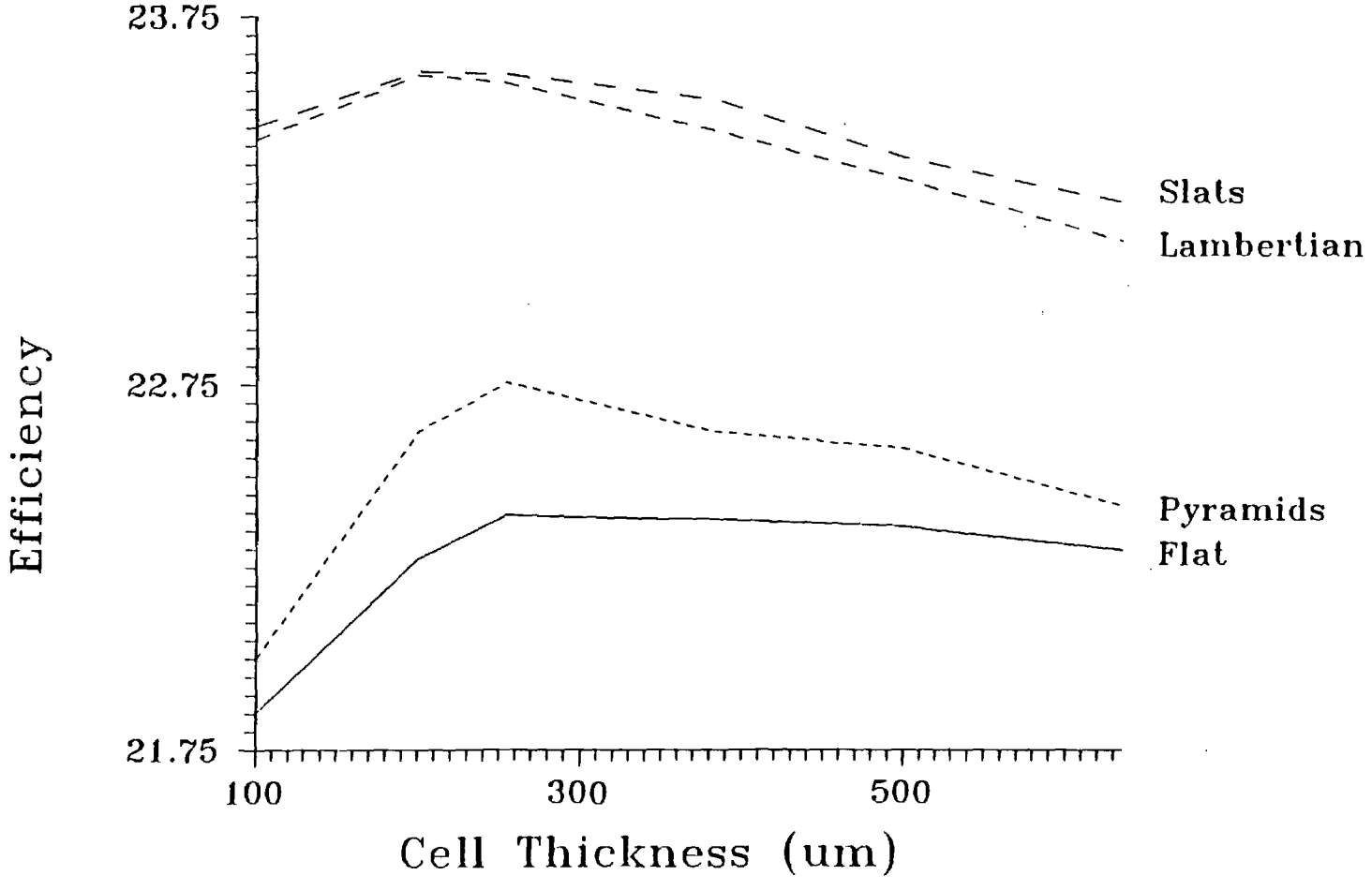

Comparison of efficiencies for flat and perpendicular slats, 100 um thick cells.

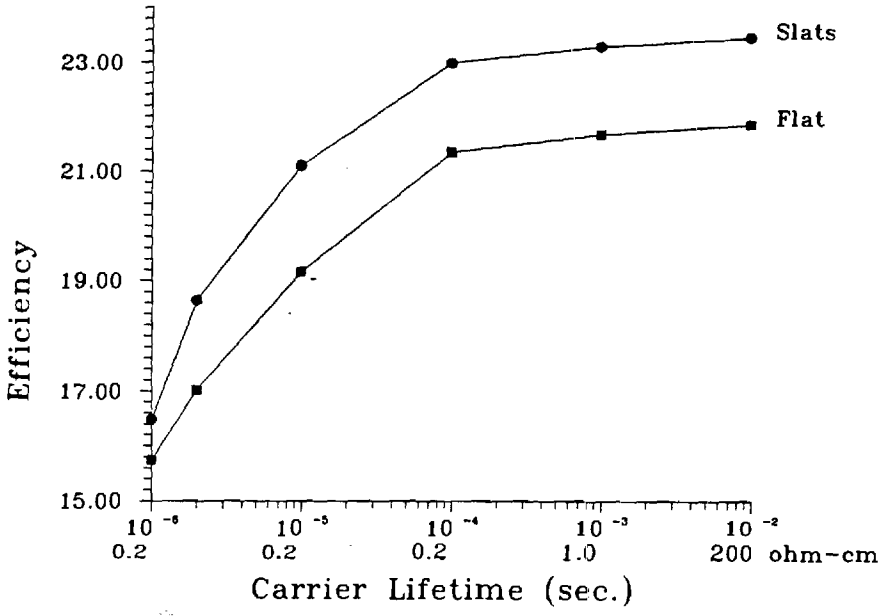

Percent change in efficiency between flat and perpendicular slats, 100 micron thick cells.

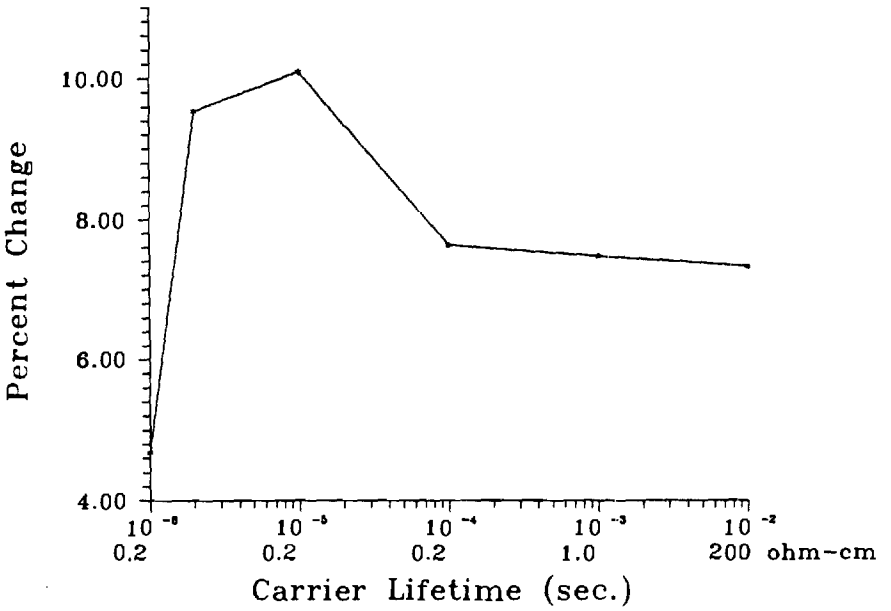

BOUNDARY CONDITIONS FOR HETEROJUNCTION SOLAR CELL MODELLING

This report deals with out first steps toward modeling heterojunction solar cells. The boundary conditions required to estimate the heterojunction are numerated. In future reports these must be converted into mathematical expressions which may be incorportated into the modeling program. In addition some of the effects leading to non-linear transport are discussed. Currently there appears to be no quick method of taking these effects into account in the program in use. Also some methods of incorporting these effects into the program are provided. These include a hybrid model between monte carlo and drift diffusion or an energy balence equation. At this time the incorporation of the energy balance equation appears to be the route of most interest. It will only add a small amount to the total computation time, as opposed to hugh amounts for the monte carlo approach, and yet take into account to a first approximation some of the non-linear effects of heterojunctions. A problem of the energy balance method is the material parameters of mobility and diffusivity need to be given as a function of carrier energy. This will require the use of monte carlo calculations to find these values for a specific material. Thereby, limiting the number of material systems the program can be applied to without going back to the monte carlo calculations.

The numerical solution of any differential equation is dependent upon the boundary conditions associated with the problem. In the numerical simulation of homojunction solar cells the boundary conditions were straight forward due to the continuity of material properties and lack of interfacial considerations, these must be taken into account in heterojunctions. Heterojunctions also pose problems of quantum mechanical phenomena which must be incorporated into the drift diffusion equations. All this must be accomplished without adding complexity to the problem, yet making sure that all contributions have been included. The following paragraphs are some of the boundary conditions which are important in the simulation of heterojunction solar cells.

The first condition is on the generation profile of the device. The absorption coefficient will experience a discontinuity at the metallurgical interface due to the change in material, yet the absorbed flux must be continuous across the junction. The importance of this result is characterized in two ways. First, this insures that all possible photons which may be absorbed, are absorbed and in the proper spatial location. This will lead to the proper current values. Second, the discontinuity of the generation profile would exhibit itself in the carrier density profile at the junction. The profile is important in both the Poisson equation of the electrostatic field and in the lifetime profile of the carriers. If these are not taken into account the built in

electric field values will be in error, and the incorrect lifetime will result in an erroneous open circuit voltage (as a result of an mistaken dark current in the depletion region).

Another condition on the electric field is the conservation of the electric flux density across the interface. This condition will also come into play in the solving of the Poisson equation. To be totally accurate the derivative of the permeativity with respect to position must also be included, for graded bandgap material. Again this condition will be hard to simulate in the finite difference technique unless a node is placed directly at the interface. The following equations show the relation of the electric displacement and the new Poisson equation

$$\epsilon_1 E = \epsilon_2 E$$

$$\frac{\partial^2 \psi}{\partial x^2} = \frac{q}{\epsilon_i}(p - n + N + N_i) - \frac{1}{\epsilon_i}\frac{\partial \psi}{\partial x}\frac{\partial \epsilon}{\partial x}$$

The last condition of the electric field is the use of interfacial charge in the solution of the Poisson equation. This charge arises due to dangling bonds at the interface. Their contribution will also appear as an effective surface recombination component at the junction. The charge will also have an effect on the band bending that is observed in both the conduction and valence bands. This bending will lead to some of the effective forces that the charge carriers will experience as they travel across the junction.

The amount of band bending is related to the distribution of charge carriers located at that particular position in space. Since the equilibrium fermi level must be constant across the entire device the carrier distribution must be such that this is satisfied. There is no criteria, except possibly piecewise continuity, on the quasi-fermi levels due to the interfacial charge and the band discontinuites. The continuity equations for both holes and electrons must still be satisfied so the flux of carriers into the junction plus the amount generated at the junction is the same as the amount that flow out plus the number that recombine.

In the calculation of the flux of the carriers, current density, across the junction the simplest equation is one in which the derivative of the quasi-fermi level is used, given below

$$J_n = q\mu_n n \frac{\partial \Phi_n}{\partial x} = \mu_n n\left[qE - \frac{\partial \chi}{\partial x} + \frac{KT}{n}\frac{\partial n}{\partial x} - \frac{KT}{N_c}\frac{\partial N_c}{\partial x} + \frac{q}{\mu_n n} D^T \frac{\partial T}{\partial x}\right]$$

$$J_p = q\mu_p p \frac{\partial \Phi_p}{\partial x} = \mu_p p\left[qE - \frac{\partial \chi}{\partial x} - \frac{\partial E_g}{\partial x} - \frac{KT}{p}\frac{\partial p}{\partial x} + \frac{KT}{N_v}\frac{\partial N_v}{\partial x} + \frac{q}{\mu_p p} D^T \frac{\partial T}{\partial x}\right]$$

This equation takes into account the electric field, the change in density of states, the carrier profile, temperature change, and the change in affinity with respect to position. This equation fails to account for such things as tunneling currents, quantum mechanical reflection at a discontinuity, and thermionic emission currents. These effects are consequences of the difference in the bandgaps of the materials and band bending leading to spikes and discontinuities in either or both

the conduction and valence band. The tunneling and thermionic currents are required when a spike occurs in either band. These currents will lead to additional current than would normally be expected, reflection must also be taken into account but is detrimental in nature. On the other hand the reflection is also in effect if the band discontinuity is adding to the current effect. The major problem with the contributions from these effects is the length of their influence on the charge. If the spike is high and narrow then tunneling is possible, but thermionic emission is negligable. In contrast if the peak is low and wide the thermionic emission is dominant while tunneling is non-existant. In both of the above cases the reflection of carriers from the potential must be taken into account. A discontinuity in a band orientated in a manner to be additive to the quasi-fermi level also produces a reflection of carriers, which decreases as the discontinuity is spread out over a larger distance. The manner in which these contributions can be easily incorporated into the finite difference technique is through quantum mechanical tunneling coefficients for the respective potentials. These would be involve terms in the current density equations as below,

$$J_n \frac{\partial \chi}{\partial x} \; ; \; J_n' \frac{KT}{N_c} \frac{\partial N_c}{\partial x}$$

$$J_p \left[\frac{\partial \chi}{\partial x} + \frac{\partial E_g}{\partial x}\right] ; \; J_p' \frac{KT}{N_v} \frac{\partial N_v}{\partial x}$$

The tunneling probalities would depend upon the height of the discontinuity, the energy of the carriers, and in the case of the electron affinity the width of the barrier. Quantum

mechanical reflection would also be taken into account by the same method for a discontinuity in the right orientation. For the case of the electron and hole affinity the tunneling probability would be in the form of tunneling through a triangular potential, for the finite difference a ratio of height to width would be used. In the case of the density of states a step potential would be employed.

The next boundary condition which must be addressed is the magnitude of the interface charge, its sign and magnitude. In most cases the trapped charge is assumed to be dependent upon the difference in the lattice constant of the two materials in contact as given by

$$N_i \approx \Delta a / a^3$$

This is just the density of availible traps. In most cases less than 100% of the traps are involved in the trapping process. Also the capture cross section of the trap must be estimated. Once this is done the amount of effective recombination due to the trapped charge is given by

$$S_i = v_{th} \sigma N_i \gamma$$

At this time it is believed that this is the final contribution of the trapped charge at the interface. An empirical parameter γ has been added to allow for user input into the amount of interface charge being active.

Boundary conditions for the electron/hole affinity and density of states are not required. The change in these parameters is incorporated into the quasi-fermi level. Again the major problem of simulating the abrupt change by the finite

difference technique may exist.

Continuity of momentum is the next condition which must be addressed. Using band structure the momentum is conserved across the interface by the equation

$$\hbar K_1 = \hbar K_2$$

Since these values are not used in finite difference calculations some other method must be considered. A macro estimate of the momentum would be given by

$$m_1^* V_1 = m_2^* V_2$$

It must be understood that this is only a "quasi" conservation of momentum since mV is not the true crystal momentum. This boundary condition will enter into the solution of the current density equations.

$$J_n|_{0-} = J_n|_{0+} \quad ; \quad J_p|_{0-} = J_p|_{0+}$$

Assuming that $\mu E = V_d$, the drift velocity, and $\frac{\partial \phi}{\partial x}$ is all of the potentials which make up the quasi-fermi levels. The condition for the "quasi" momentum is then given by

$$m_1^* \mu_1 \frac{\partial \phi_{n,p}}{\partial x} = m_2^* \mu_2 \frac{\partial \phi_{n,p}}{\partial x}$$

Since m_1^* and m_2^* are not input parameters they may be solved for by the use of the effective densiy of states, N_c and N_v. It must be strongly emphasized that the condition does not take into account all of the changes in momentum which occur at the interface.

The last condition of the heterojunction system is the conservation of energy. This condition assures that the solution of the device is not unrealistic. Yet, due to the need to balance the energy in the entire device it may not be

practical to implement. It will require an additional equation to be solved simultaneously at each node. At this time there is also some debate as to the form of the energy flux that is required in the equation.

$$(E-E_o)/\tau_e = \vec{J}\cdot\vec{\mathcal{E}} + U_t - \Delta\eta$$

Here E is the local carrier energy, E_o is the equilibrium energy distribution, U_t is the energy release by any recombination process, $\Delta\eta$ is the change in energy flux, and τ_e is the energy relaxation time.

Addressing the issue of the band bending model to be used for the heterojunction structure, the approach should be an Anderson modified band diagram. The modification would come in as the accounting of interfacial charge. At this time it is more complete than the Anderson model without the uncertainties associated with the interfacial dipole models suggested in the literature.

CONTRACTOR: Complete all spaces and the bottom block.

Sandia National Laboratories

PURCHASING ORGANIZATION Georgia Tech

ALBUQUERQUE, NEW MEXICO 87185
LIVERMORE, CALIFORNIA 94550

J. Gee
Sandia Contracting Representative

MONTHLY COST STATUS REPORT

CONTRACT NO. 57-6152

PERIOD ENDING (1) August 31, 1988

Contractor must forecast as a minimum the first three months, Balance of Fiscal Year, and Subsequent Fiscal Years when costs will be incurred in these months and years.

Contractor must forward this report to reach the Sandia Contracting Representative by the 15th of the month following the Report Period or at such other time as requested by the Sandia Contracting Representative.

TOTAL FUNDS AUTHORIZED		$ 97,448.00
ACTUAL COST INCURRED TO DATE(2)		26,135.68
ESTIMATED COST TO COMPLETE:(3)		
1st MONTH FOLLOWING "PERIOD ENDING" as specified above	10,187.47	
2nd MONTH		
3rd MONTH		
4th MONTH		
5th MONTH		
6th MONTH		
BALANCE OF FISCAL YEAR(4)		
SUBSEQUENT FISCAL YEARS	61,124.85	
TOTAL ESTIMATE TO COMPLETE		71,312.32
TOTAL ESTIMATED COST AT COMPLETION		$ 97,448.00

NOTES:
(1) Last full month for which actual costs are available.
(2) Cost includes applicable fee.
(3) Estimates for costs to be incurred (Do not include commitments), including applicable fee.
(4) Fiscal year is 10/1 through 9/30. Balance of fiscal year means all months remaining in the fiscal year following the 6th month shown on the line above. If the 6th month is September, then balance of fiscal year is 10/1 through 9/30 of the next fiscal year.

Contractor (name and address)	Signature of Contractor's Representative, Date and Phone
Georgia Tech Research Corporation School of Electrical Engineering Georgia Institute of Technology Atlanta, GA 30332	Pam Majors Pam Majors, Research Adm. 404-894-7337 9/19/88

SF6432-CS(1-85)

GEORGIA INSTITUTE OF TECHNOLOGY
SCHOOL OF ELECTRICAL ENGINEERING
ATLANTA, GEORGIA 30332

TELEPHONE: (404) 894-7337

October 12, 1988

Mr. J. Gee
Sandia National Laboratories
P. O. Box 5800
Albuquerque, NM 87185-5800

RE: Contract No. 57-6152
Project Director: A. Rohatgi

Dear Mr. Gee:

Enclosed please find copies of the Monthly Cost Status Report for the period 9/1/88-9/30/88 on the above referenced contract.

If you have any questions, please feel free to contact me.

Sincerely,

Pam Majors
Research Administrator

pm
Enclosure

CONTRACTOR: Complete all spaces and the bottom block.

Sandia National Laboratories

PURCHASING ORGANIZATION Georgia Tech

ALBUQUERQUE, NEW MEXICO 87185

LIVERMORE, CALIFORNIA 94550

J. Gee

Sandia Contracting Representative

MONTHLY COST STATUS REPORT

CONTRACT NO. 57-6152

PERIOD ENDING (1) 9/30/88

Contractor must forecast as a minimum the first three months, Balance of Fiscal Year, and Subsequent Fiscal Years when costs will be incurred in these months and years.

Contractor must forward this report to reach the Sandia Contracting Representative by the 15th of the month following the Report Period or at such other time as requested by the Sandia Contracting Representative.

TOTAL FUNDS AUTHORIZED		$ 97,448.00
ACTUAL COST INCURRED TO DATE(2)		32,872.78
ESTIMATED COST TO COMPLETE:(3)		
1st MONTH FOLLOWING "PERIOD ENDING" as specified above		
2nd MONTH		
3rd MONTH		
4th MONTH		
5th MONTH		
6th MONTH		
BALANCE OF FISCAL YEAR(4)		
SUBSEQUENT FISCAL YEARS	64,575.22	
TOTAL ESTIMATE TO COMPLETE		64,575.22
TOTAL ESTIMATED COST AT COMPLETION		$ 97,448.00

NOTES:

(1) Last full month for which actual costs are available.

(2) Cost includes applicable fee.

(3) Estimates for costs to be incurred (Do not include commitments), including applicable fee.

(4) Fiscal year is 10/1 through 9/30. Balance of fiscal year means all months remaining in the fiscal year following the 6th month shown on the line above. If the 6th month is September, then balance of fiscal year is 10/1 through 9/30 of the next fiscal year.

Contractor (name and address)	Signature of Contractor's Representative, Date and Phone
Georgia Tech Research Corporation School of Electrical Engineering Georgia Institute of Technology Atlanta, GA 30332	Pam Majors, Research Adm. 404-894-7337 10/12/88

This paper was presented at the 20th IEEE Photovoltaic Specialists Conference held in Las Vegas, NV, on September 26-30, 1988.

MATERIAL QUALITY AND DESIGN OPTIMIZATION FOR HIGH EFFICIENCY GaAs SOLAR CELLS

S. A. Ringel and A. Rohatgi

School of Electrical Engineering
Georgia Institute of Technology
Atlanta, Georgia 30332-0250

ABSTRACT

A methodology is developed to determine minority carrier lifetime and recombination velocity in high efficiency GaAs p/n heteroface solar cells. A combination of measurements and modeling is used to demonstrate that a base lifetime of 8 ns and a heteroface recombination velocity of 1.25×10^5 cm/s were necessary to simulate the spectral response, cell data, and leakage current in a 21.2% efficient GaAs cell. Optimization of the p/n heteroface structure shows that AM 1.5 one sun efficiencies of ~25% are achievable from a thin base/buffer design with a base lifetime of only 15 ns and a well-passivated back surface. In addition, it is shown that the doping dependence of the Shockley-Read-Hall lifetime is an important consideration in GaAs device modeling, especially if a shallow level ($\sim E_t = 0.2$ eV) limits the bulk lifetime.

1. INTRODUCTION

Minority carrier lifetimes and interface recombination rates are major factors in limiting GaAs solar cell performance [1,2]. To optimize cell characteristics, it is crucial to determine these parameters in existing devices. However, at present, no satisfactory method exists which accurately accomplishes this for GaAs solar cells. The best one can do is to find a window of possible lifetime and recombination velocity values which will satisfy measured cell data [3]. In this paper, we present a methodology to find unique values for lifetime and surface recombination velocity in a GaAs p/n heteroface solar cell by simultaneously matching computer simulated and measured spectral response, leakage current, and I-V characteristics of the cell. The design optimization is done first by improving bulk and interface quality and then the cell structure to show that ~25% one sun efficiency is possible for a cell with a base lifetime of 15 ns. Furthermore, increasing the lifetime to unrealistically high values (~50 ns at 6×10^{17} cm^{-3} doping level) does not produce significantly higher efficiencies. Since the lifetime in GaAs is controlled by Shockley-Read-Hall (SRH) recombination at the doping levels used in the base of GaAs cells, it is shown that location of deep levels could become important in optimizing the cell design and doping. GaAs heteroface solar cells were fabricated, characterized, and modeled to demonstrate the above effects.

2. EXPERIMENTAL

GaAs heteroface solar cells were fabricated by the MOCVD technique. A typical cell structure is shown in Fig. 1. Cell performance and spectral response were determined under AM 1.5 conditions at 300 K. The diffusion component of reverse leakage current (J_{01}) was measured by transformed dark I-V measurements [4]. The PC-1D model [5] was used to calculate the spectral response and cell data using the appropriate material and structural parameters. All PC-1D calculations were performed assuming a 5% loss due to shadow and reflection. The reverse leakage current was calculated with the help of an effective recombination velocity (S_e) model which includes the effects of: bandgap narrowing [6]; radiative, Auger, and SRH recombination; front and back surface recombination velocities (FRSV and BSRV, respectively); and device structure. The details of this model have been published elsewhere [4,7]. The output of this model is an internal recombination velocity plot through the device structure. The value of S_e at either side of the depletion region yields the emitter and base components (J_{oe} and J_{ob}, respectively) of J_{01} according to

$$J_{01} = J_{oe} + J_{ob} = (q/n_i^2)(N_a S_{eje} + N_d S_{ejb}) \quad (1)$$

which are summed to match the measured J_{01}.

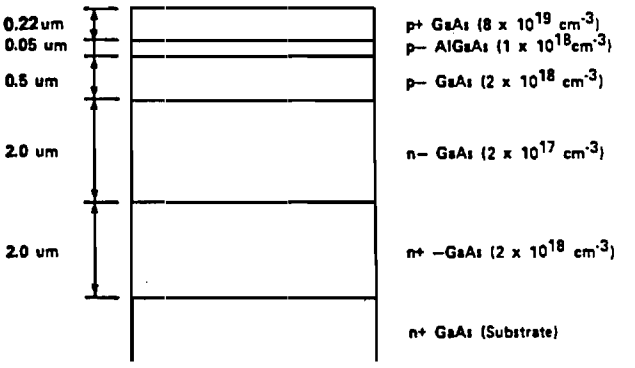

Fig. 1 GaAs p/n Heteroface Cell Structure Used In This Study. Measured Cell Data is Listed.

3. RESULTS AND DISCUSSION

3.1 Methodology for Determining Lifetime and Recombination Velocity

A threefold approach was established to accurately determine lifetime, FSRV, and BSRV for an MOCVD-grown GaAs p/n heteroface solar cell, Fig. 1, with a cell efficiency of 21.2%. The first step was to match the spectral response.

Figure 2 shows a good match between the simulated and measured spectral response for a net base lifetime of 8 ns and FSRV equal to 1.25×10^5 cm/s. BSRV was found to have no effect on the spectral response of this particular device structure. Lifetimes in the emitter and buffer were determined to be 2 and 5.5 ns, respectively, by using the SRH lifetime calculated from the net base lifetime and by properly accounting for the doping dependence of the Auger (C) and radiative (B) recombination terms in the equation

$$1/T = 1/\tau_{SRH} + BN + CN^2 \qquad (2)$$

as described previously [4]. The sligth mismatch at wavelengths below 450 nm is due to absorption in the AlGaAs window layer which was not accounted for in the modeling. It should be recognized that it is possible to match the spectral response with a range of lifetime and FSRV values [3], therefore, further modeling steps were necessary to determine the exact values.

The second step in the methodology was to model J_{01}. This was calculated using the lifetime profile (T_e, T_b, T_{buffer}) and recombination velocities which gave a good spectral response match. This simulation was done with the help of an effective recombination velocity model. Figure 2 shows a plot of S_e for various values of FSRV and BSRV. J_{ob} in this cell was found to be pinned at 0.85×10^{-19} A/cm^2 for all values of BSRV again supporting the fact that back surface passivation is not important for this design. In addition, it was found that $J_{oe}=0.55 \times 10^{-19}$ A/cm^2 for FSRV=1.25×10^5 cm/s, giving $J_{01}(=J_{oe}+J_{ob})=1.40 \times 10^{-19}$ A/cm^2, which is in good agreement with the measured J_{01} of 1.29×10^{-19} A/cm^2 and supports the choice of FSRV and base lifetime. Since $J_{ob} \sim 70\%$ of J_{01}, this cell is base/buffer dominated and not limited by the emitter side of the junction.

The third and final test of these values of FSRV and base lifetime is the match between the measured and calculated cell data. Table 1 shows excellent agreement between calculated and measured values of J_{sc}, V_{oc}, and efficiency for this cell.

3.2 Design Optimization for High Efficiency Cells

3.2.1 Effect of Material Quality and Interface Recombination Velocity. Having established the threefold match using a single set of parameters in Section 3.1, the cell design was optimized. Figure 3 shows that J_{oe} can be significantly lowered by improving the AlGaAs/GaAs heteroface quality so that FSRV=1×10^4 cm/s which is attainable for the $Al_{0.9}Ga_{0.1}As$/GaAs heteroface [8]. This will increase V_{oc} from 1.010 to 1.016 V by virtue of lower S_{eje} and J_{sc} from 26.56 to 26.59 mA/cm^2 due to reduced recombination in the emitter, raising cell efficiency to 23%. Figure 3 also shows that little would be gained for FSRV values below $\sim 1 \times 10^4$ cm/s, even if better passivation was possible. Since for this device design, J_{ob} is independent of BSRV and is set by the base diffusion velocity, D/L, the obvious way to gain higher performance is to improve the base material quality. If the base lifetime in this cell is increased from 8 to 15 ns, the efficiency will increase to 24.1%, Table 1. The efficiency can be

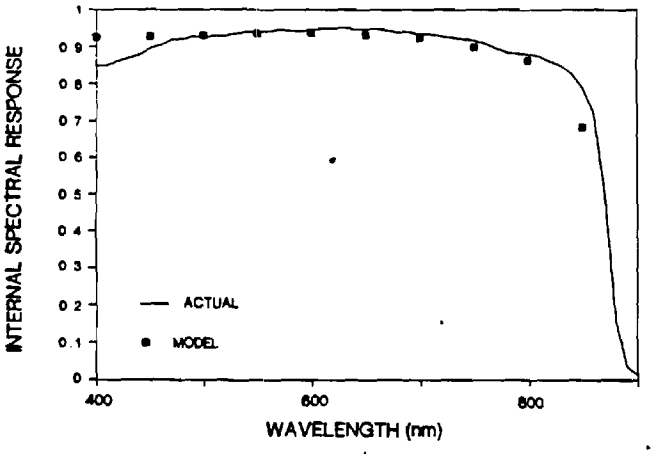

Fig. 2 Comparison of Actual Spectral Response (solid line) with Modeled Spectral Response (blocks) as Calculated from PC-1D.

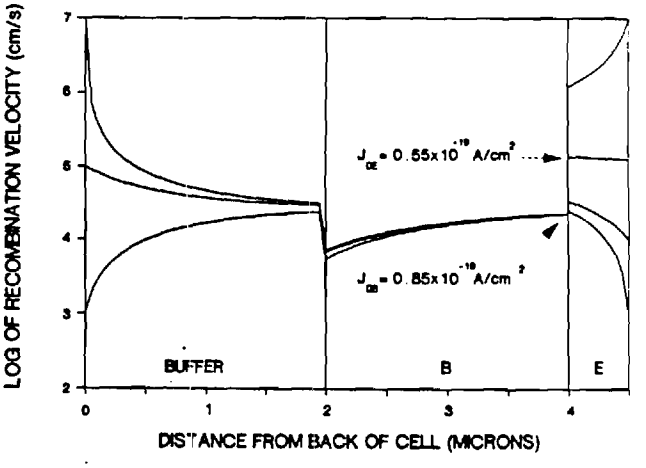

Fig. 3 Plot of Effective Recombination Velocity, S_e, for Various Values of FSRV and BSRV. Emitter and Base Leakage Current Components are Noted for the Cell-Matching S_e Plot.

Table 1. Cell Data Calculated Using PC-1D for the Device Structures Listed. An 0.5 um Emitter with $N_A = 2x10^{18}$ cm^{-3} was Used in Each Calcuation.

width (um) base	buffer	Doping (cm^{-3}) base	buffer	FSRV (cm/s)	BSRV (cm/s)	T_B (ns)	V_{oc} (volts)	J_{sc} (mA/cm^2)	Eff (%)
				Actual					
2.0	2.0	$2.0x10^{17}$	$2.0x10^{18}$				1.013	24.5	21.2
				Match					
2.0	2.0	$2.0x10^{17}$	$2.0x10^{18}$	$1.25x10^{5}$	$1.0x10^{6}$	8	1.01	24.56	21.39
				Material and interface optimization					
2.0	2.0	$2.0x10^{17}$	$2.0x10^{18}$	$1.0x10^{4}$	$1.0x10^{6}$	8	1.016	24.59	23.02
2.0	2.0	$2.0x10^{17}$	$2.0x10^{18}$	$1.0x10^{4}$	$1.0x10^{6}$	8	1.017	26.71	23.13
2.0	2.0	$2.0x10^{17}$	$2.0x10^{18}$	$1.0x10^{4}$	$1.0x10^{4}$	15	1.032	27.11	24.17
2.0	2.0	$5.0x10^{17}$	$2.5x10^{18}$	$1.0x10^{4}$	$1.0x10^{4}$	15	1.048	26.83	24.40
2.0	2.0	$5.0x10^{17}$	$2.5x10^{18}$	$1.0x10^{4}$	$1.0x10^{4}$	20	1.054	26.95	24.76
				Design optimization					
1.2	1.2	$6.0x10^{17}$	$2.5x10^{18}$	$1.0x10^{4}$	$1.0x10^{3}$	15	1.055	27.04	24.75
1.3	1.1	$6.0x10^{17}$	$2.5x10^{18}$	$1.0x10^{4}$	$1.0x10^{3}$	20	1.059	27.10	25.05
1.5	1.1	$6.0x10^{17}$	$2.5x10^{18}$	$1.0x10^{4}$	$1.0x10^{3}$	30	1.063	27.19	25.31
1.9	1.1	$6.0x10^{17}$	$2.5x10^{18}$	$1.0x10^{4}$	$1.0x10^{3}$	55	1.068	27.31	25.62

raised to ~24.4% by increasing the base doping to $5x10^{17}$ cm^{-3} and buffer doping to $2.5x10^{18}$ cm^{-3} which primarily increases V_{oc} without sacrificing J_{sc}, assuming the lifetime is independent of doping in the base, Table 1 [9,10]. If the base lifetime is increased further to 20 ns, the efficiency climbs to only ~24.76%, indicating it has apparently reached a plateau. Further increase in efficiency, without going to unreasonably high lifetime, can only come from optimizing the base and buffer regions since the emitter design is already near optimum.

3.2.2 Optimized Device Structures for High Efficiency. The next step toward increasing cell performance was to optimize the base and buffer region. Optimum thicknesses of the base and buffer are dictated by the lifetime. A tradeoff exists between high carrier collection efficiency in the base and the photon absorption in the lower lifetime, heavily doped buffer. To reduce the latter effect, the base width must be increased. However, the minority carrier diffusion length then limits the collection of carriers generated deep in the base which is compounded by the reduced effectiveness of the back surface field. In order to absorb ~97% of the incident photons in the base, a base width of ~3 um is necessary with an emitter thickness of 0.5 um. However, to collect nearly all the photogenerated carriers from the base, it was found that a diffusion length of about three times the base thickness (~9 um) was necessary. This would require a base lifetime greater than the fundamental limit at the doping levels used in GaAs solar cells. One way to circumvent this limitation is to employ a thin base to maximize collection by allowing the diffusion length to be much greater than the base thickness, while maintaining good material quality in the active buffer which would now required good back surface passivation. For a thin base cell, the buffer thickness should also be reduced because S_{ejb} depends upon S_e at the base/buffer interface which, in turn, depends on the buffer thickness and BSRV, Fig. 4.

Based on the above considerations, optimized device structures and the corresponding cell efficiencies for base lifetimes of 15, 20, 30, and 55 ns are shown in Table 1. A p-type emitter with a thickness of 0.5 um, doping of $2x10^{18}$ cm^{-3}, a lifetime of 2 ns, and an FSRV of $1x10^{4}$ cm/s was used in all designs. Bandgap narrowing [6] in this emitter was found to lower V_{oc} by 14 mV without affecting the J_{sc}. Optimum values for base and buffer doping were found to be $6x10^{17}$ and $2.5x10^{18}$ cm^{-3}, respectively, for each lifetime case, assuming base lifetime is independent of doping [9,10]. The base width for each lifetime was optimized for maximum efficiency. Figure 5 shows that the optimum base width increases from 1.1 um for a 15 ns base to 1.9 um for a 55 ns base. The optimized buffer thickness for each case is listed in Table 1. An FSRV of $1x10^{4}$ cm/s

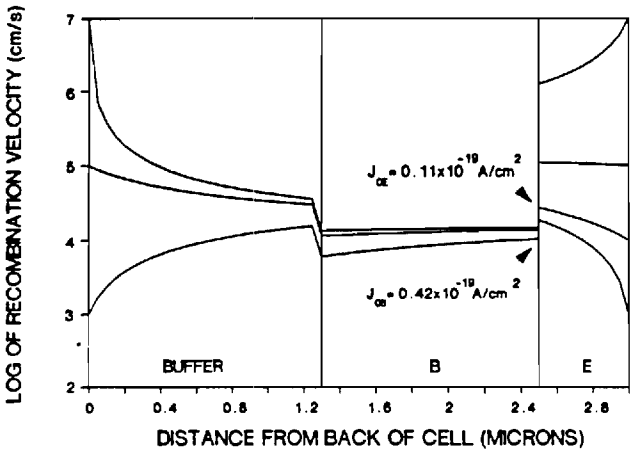

Fig. 4 Plot of Effective Recombination Velocity, S_e, for Thinned Device Structure Indicating the Importance of BSRV and Buffer Thickness.

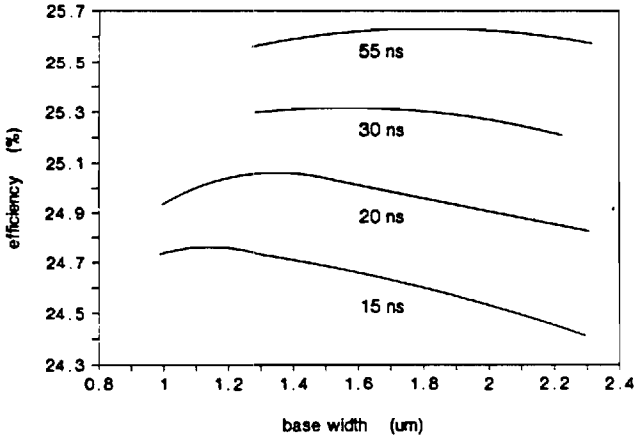

Fig. 5 Variation of Cell Efficiency versus Base Thickness for Base Lifetimes of 15, 20, 30, and 55 ns at the Optimized Designs Listed in Table 1.

and BSRV of $1x10^3$ cm/s (achievable from an $Al_{0.3}Ga_{0.7}As/GaAs$ heterojunction [11]) was found to be necessary to obtain maximum efficiency for each lifetime, Fig. 6. Model calculations indicate that a maximum efficiency of ~25.6% can be realized for a base lifetime of 55 ns (fundamental lifetime limit at $6x10^{17}$ cm^{-3} doping), Fig. 5 and Table 1. This is less than one absolute percent higher than the maximum efficiency of ~24.75% obtained from the 15 ns base. Hence, there is apparently little point in improving base material quality beyond 15-20 ns if the proper device design is employed.

It is also noteworthy that the maximum efficiency (~24.75%) for the 15 ns base design (base width of

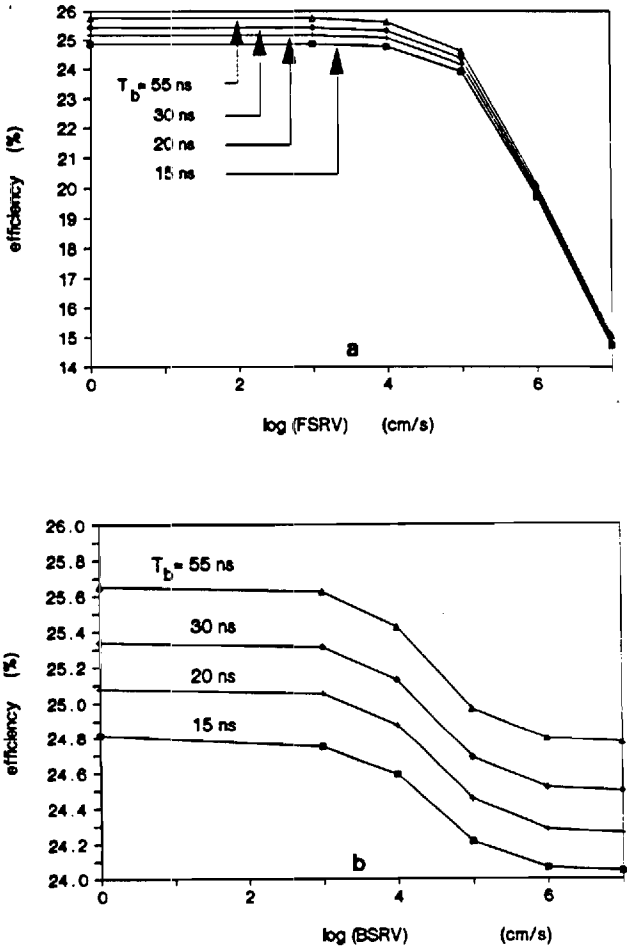

Fig. 6 Variation of Cell Efficiency versus (a) FSRV and (b) BSRV for 15, 20, 30, and 55 ns Thin Base Designs.

1.1 um) is ~0.4% absolute higher than the "optimized" thicker device design (base + buffer thickness = 4 um) in Section b.1. This increase occurs in spite of the fact that 5.5% of the incident light is not absorbed at all in this 2.9 um device, whereas all but ~1% of the incident light is absorbed in the 4.5 um device. Thus we run into a base lifetime dependent tradeoff between the increase in carrier collection for thinner structures and a decrease in total amount of photons absorbed within the device, Fig. 5, which limits the practically achievable one sun efficiencies to less than 26%. Further increase in cell performance can only come from surface texturing or light trapping techniques to increase the photon absorption in the base without increasing the base width.

3.3 Effect of Deep Level Position on Cell Optimization

All of the preceding model calculations assumed that the base lifetime, which is largely

controlled by SRH recombination via deep levels, is independent of doping. This assumption is valid only if the lifetime limiting deep level is at or near the midgap region. While this has been found to be the case for melt-grown GaAs [10], this may not be necessarily true for all types of GaAs, especially expitaxially grown GaAs, where some deep levels have been found to reside as close as 0.17 eV below the conduction band edge [12] and 0.27 eV above the valence bandedge [13], respectively. To investigate what effects this has on the material lifetime as well as cell performance, the net lifetime was modeled according to

$$\frac{1}{\tau} = \frac{1}{\tau_{SRH}} + BN + CN^2 \qquad (3)$$

where

$$\tau_{SRH} = \left[\frac{1}{n_o+p_o+\delta_n}\right]\left[\tau_{po}(n_o+\delta_n+n_1)+\tau_{no}(p_o+\delta_n+p_1)\right] \qquad (4)$$

and n_1, p_1, τ_{no}, and τ_{po} are given their usual meanings as in [14], and B and C are the radiative and Auger recombination coefficients, respectively, as calculated from [9]. Assuming low level injection conditions and $\tau_{no}=\tau_{po}$, Eq. (3) has been plotted for n-type GaAs as a function of doping level for different deep levels, Fig. 7. Indeed we see that the lifetime does not depend on doping in the range of interest here ($1x10^{17}$-$1x10^{18}$ cm^{-3}) and tails off above ~$1x10^{18}$ cm^{-3} due to Auger recombination [9]. Deep levels apparently affect the lifetime only for doping levels below $1x10^{16}$ cm^{-3} in both n-type and p-type GaAs.

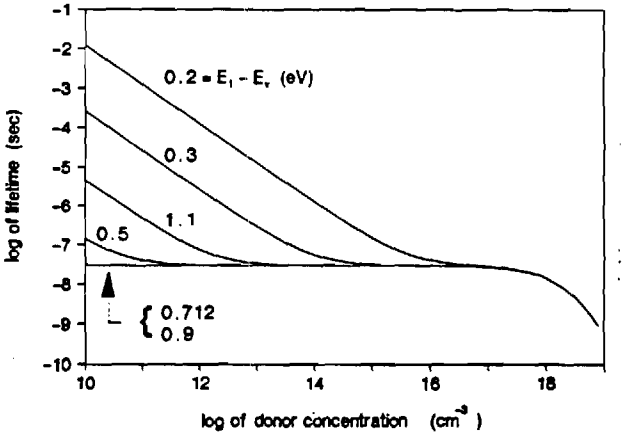

Fig. 7 Total Minority Carrier Lifetime as a Function of Doping Density in n-type GaAs Including Doping Dependent SRH Lifetime and Radiative and Auger Lifetimes for Various Trap Levels as Measured with Respect to the Valence Band Edge.

In the above example, we assumed $\tau_{no}=\tau_{po}$ = a constant for each deep level which changed the initial value of the lifetimes. However, if the technology or the quality of the GaAs layer is defined by a fixed lifetime at some lower doping level ($1x10^{16}$ cm^{-3}), then the position of the deep level can influence the device design and cell performance. This case is plotted for n-type GaAs with a starting lifetime of 20 ns at $1x10^{16}$ cm^{-3} doping (Fig. 8a) and for p-type GaAs with a starting lifetime of 10 ns at $1x10^{16}$ cm^{-3} doping (Fig. 8b). Here we see a strong doping dependence of lifetime dictated by deep level position in the doping concentration range of interest. N-type GaAs doped to $6x10^{17}$ cm^{-3} now shows a decrease in lifetime from 15 to 11 ns if the deep level is shifted from midgap to Ev+0.2 eV. This results in a decrease of ~0.5 um in minority carrier diffusion length causing a reduction in cell efficiency from 24.75% to 24.50% for the thin base 15 ns optimized design in Table 1. A larger effect was observed for the original 4.5 um design, where efficiency dropped from 24.4% to 24.0% indicating that the thin base design, as would be expected, is more forgiving to lifetime variations. P-type GaAs shows similar behavior in Fig. 8b. In both cases, we see that deep levels which are closest to the valence band severely limit the lifetime

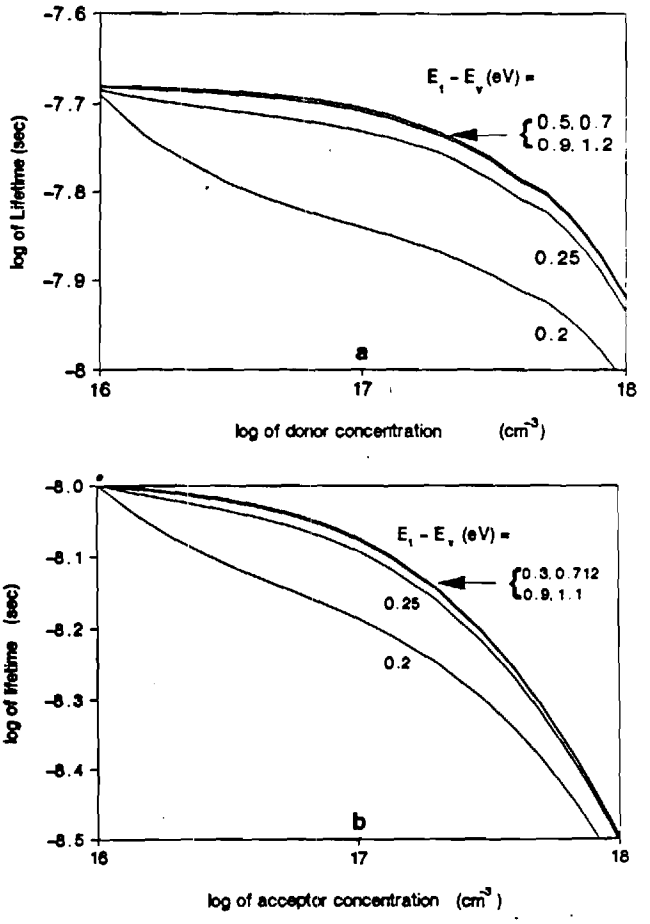

Fig. 8 Total Minority Carrier Lifetime as a Function of Doping for Various Deep Levels Assuming a Constant Starting Lifetime of (a) 20 ns at $1x10^{16}$ cm^{-3} for n-GaAs and (b) 10 ns at $1x10^{16}$ cm^{-3} for p-GaAs.

for both p and n-type GaAs, while those closer to the conduction band have little effect on the lifetime. This is a result of the large density of states in the valence band (N_v=9.5x10^{18} cm^{-3} at 300 K) [15] compared with the density of states in the conduction band (N_c=4.2x10^{17} cm^{-3} at 300 K) [15] which allows the p_1 term to dominate over the n_1 term in the SRH lifetime equation, even for traps which are very close to the conduction band. Hence, we see that this lifetime dependence on deep level position can influence optimized cell design by affecting the diffusion length. Future work will involve a more quantitative treatment of this observation and effect on GaAs devices.

4. CONCLUSIONS

In conclusion, we have developed a threefold methodology which consists of simultaneously matching simulated and measured spectral response, leakage current, and cell data to determine minority carrier lifetime, FSRV, and BSRV. For a 21.2% p/n heteroface cell studied here, a net base lifetime of 8 ns and an FSRV of 1.25x10^5 cm/s was necessary to obtain the match. The cell performance was then optimized first by improving the material and interface quality without altering the cell structure which resulted in efficiencies of 24.4% for a 15 ns base. Further improvements were realized by thinning the base so that the buffer becomes an active part of the device, forming essentially a two-step base. This structure, however, requires back surface passivation and a thinner buffer to maximize cell efficiency. Optimized cell designs with efficiencies of 24.8% and 25.1% were established for 15 and 20 ns base lifetimes, respectively. Even if the lifetime is increased to the fundamental limit, efficiencies of only ~25.6% can be obtained for realistic values of recombination velocities, reflection losses, and AlGaAs absorption.

The influence of a doping dependent SRH lifetime was investigated and it was found that deep levels near the valence band edge in GaAs can significantly lower the lifetime at doping levels commonly used in GaAs solar cells. This can have an impact on the cell performance and optimized cell design.

ACKNOWLEDGEMENTS

This work was supported by Sandia National Laboratories, Contract No. 57-6152.

REFERENCES

1. H.J. Hovel, "Solar Cells," in Semiconductors and Semimetals, R.K. Willardson and A.C. Beer (Eds.), vol. 11, Academic Press, New York, 1975.

2. R.C. Knechtli, R.Y. Loo, and G.S. Kamath, "High Efficiency GaAs Solar Cells," IEEE Trans. Electron. Dev., vol. ED-31, no. 5, pp. 577-588, 1984.

3. S.P. Tobin, S.M. Vernon, C. Bajgar, L.M. Geoffrey, C.J. Keavney, M.M. Sanfacon, and V.E. Haven, "Device Processing and Analysis of High Efficiency GaAs Cells," Solar Cells, vol. 24, p. 103-115, 1988.

4. S.A. Ringel, A. Rohatgi, and S.P. Tobin, "An Approach Toward 25% Efficient GaAs Heteroface Solar Cells," submitted to IEEE Trans. Electron. Dev., August 1988.

5. P.A. Basore, "Numerical Analysis of Semiconductor Devices on Personal Computers," Proc. of the Sixth Biennial University/Government/Industry Microelectronics Symp., p. 73-76, 1985.

6. H. Van Cong, "Impurity Band Structure in Degenerate Semiconductors for Both Dense Donors and Acceptors," Phys. Stat. Sol., vol. 56A, pp. 395-405, 1979.

7. A. Rohatgi and P. Rai-Choudhury, "Design, Fabrication, and Analysis of 17-18 Percent Efficient Surface-Passivated Silicon Solar Cells," IEEE Trans. Electron. Dev., vol. ED-31, no. 5, pp. 596-601, 1984.

8. L.D. Partain, M.S. Kuryla, L.M. Fraas, P.S. McLeod, and J.A. Cape, " A New Sequentially Etched Quantum-Yield Technique for Measuring Surface Recombination Velocity and Diffusion Lengths of Solar cells," J. Appl. Phys., vol. 61, pp. 5150-..., 1987.

9. P.D. DeMoulin and M.S. Lundstrom, "Theoretical Comparison of Conventional and Unconventional GaAs Cell Design," 19th IEEE Photovoltaic Specialists Conf., pp. 925-930, 1987.

10. C.J. Hwang, "Doping Dependence of Hole Lifetime in n-type GaAs," J. Appl. Phys., vol. 42, no. 11, 1971.

11. R.J. Nelson, "Interfacial Recombination in GaAlAs-GaAs Heterostructures," J. Vac. Sci. Technol., vol. 15, no. 4, 1978.

12. G.M. Martin, A. Mitonneau, and A. Mircea, "Electron Traps in Bulk and Epitaxial GaAs Crystals," Electron. Lett., vol. 13, no. 22, pp. 191-192, 1977.

13. A. Mitonneau, G.M. Martin, and A. Mircea, "Hole Traps in Bulk and Epitaxial GaAs Crystals," Electron. Lett., vol. 13, no. 22, 1977.

14. W. Shockley and W.T. Read, "Statistics of the Recombination of Holes and Electrons," Phys. Rev., vol. 87, no. 5, 1952.

15. J.S. Blakemore, "Semiconducting and Other Major Properties of Gallium Arsenide," J. Appl. Phys., vol. 53, no. 10, pp. R123-R181, 1982.

GEORGIA INSTITUTE OF TECHNOLOGY
SCHOOL OF ELECTRICAL ENGINEERING
ATLANTA, GEORGIA 30332

TELEPHONE: (404) 894-7337

November 30, 1988

Mr. J. Gee
Sandia National Laboratories
P. O. Box 5800
Albuquerque, NM 87185-5800

Re: Contract No. 57-6152
Project Director: A. Rohatgi

Dear Mr. Gee:

Enclosed please find the Monthly Technical Progress Report for the periods 8/17/88-9/16/88 and 9/17/88-10/16/88 on the above referenced contract.

If you have any questions, please feel free to contact me.

Sincerely,

Pam Majors
Research Administrator

pm
Enclosure

TECHNICAL REPORT

1. POTASSIUM HYDROXIDE (KOH) THINNING

A quartz beaker and a teflon beaker were used for the KOH thinning. Wafer preclean was done before the thinning process.

The KOH etches the quartz beaker badly and is very corrosive on the hood and nearby equipment. Therefore any equipment used for KOH needs to be carefully isolated from the other processes.

The wafer used for texturing had following characteristics : n-type, 3 inch
(100) direction
50-60 [Ohm-cm]
675 µm (~ 27 mil)

Thinning Procedure :

1. Etch in hot (110-115 °C) KOH solution (quartz beaker)
2. DI rinse : spray and dump for 5 minutes (teflon boat)
3. Dry with N_2 blower and measure thickness.
   Repeat 1-3 to obtain desired thickness.

We have done this procedure for 10 min, 20 min, and 30 min to determine the etching rate. Figure 1 shows that the etch rate is about 6µm/min. We intend to apply this process when we need to thin the wafer.

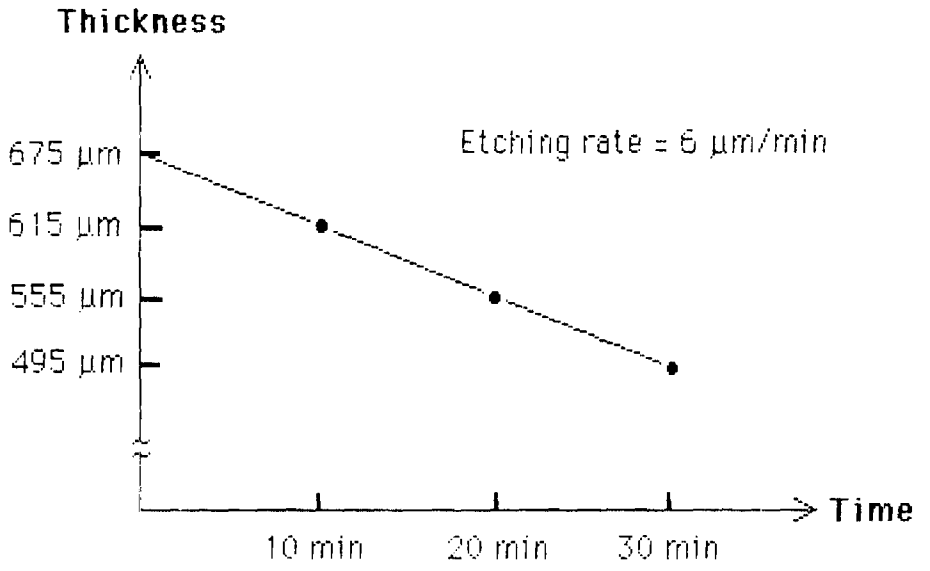

Fig. 1 Etching rate of KOH thinning

2. TEXTURING

1) Both sides of the samples were texture-etched in a potassium hydroxide (KOH) solution. Wafer preclean was done before the texturing. Texturing procedure is as follows.

A) Preparing the texture solution :

1. Add 500 ml DI water to the quartz bowl.
2. Add 7.65 ml KOH to the water.
3. Stir the KOH into the water.
4. Set the hot plate temperature control to high.
5. Cover the bowl with the quartz sheet.
6. Check the temperature after 30 minutes and thereafter until the temperature reaches 65°C.
7. Remove the bowl cover, add 37.5 ml IPA and use a boat of dummy wafers to stir in the IPA.
8. Leave the boat in the texture solution for about 45 minutes with the lid covering the bowl. Set the temperature control to keep the solution at 85°C.
9. Remove the boat of dummy wafers and recover the bowl. The solution temperature should remain ready for use all day at 85°C.

B) Using the texture solution :

1. The solution temperature must be 85 +/- 3 degrees C.
2. Remove the bowl lid.
3. Insert the boat of wafers without agitation.
4. Remove the boat handle and cover the bowl.
5. Set the clock for a 45 minute cycle.

C) Post-texture cleaning :

a) Prepare the cleaning solutions :

1. Bring a quartz bowl with H_2SO_4 to a temperature of about 75 °C then add H_2O_2. (H_2SO_4 : H_2O_2 = 9 : 1)
2. Bring a separate teflon bowl filled with DI to a temperature of over 90 °C.
3. Bring another quartz bowl filled with DI and HCL to a teperature near 80 °C then add H_2O_2. (DI : HCL : H_2O_2 = 6.5 : 1 : 1)

b) Post-texture cleaning procedure :

1. Just before using the solutions add 0.6 ratio of H_2O_2 to the H_2SO_4 : H_2O_2 (bring the teperature to 110 -130 °C) and add 1 ratio of H_2O_2 to the DI : H_2O_2 : HCL (bring the temperature to 90 -50 °C).
2. Immerse the boat slowly into the H_2SO_4 : H_2O_2 - 10 minutes.
3. Immerse the boat slowly into the DI rinser - 4 minutes.
4. Immerse the boat slowly into the hot DI - 2 minutes.
5. Immerse the boat slowly into the DI rinser - 4 minutes.
6. Immerse the boat slowly into the DI : H_2O_2 : HCL - 10 minutes.
7. Immerse the boat slowly into the DI rinser - 4 minutes.
8. Immerse the boat slowly into the spin dry - 5 minutes.

The following picture is obtained by the Scanning Auger Microscopy(SAM).

TEXTURED Si
25000X

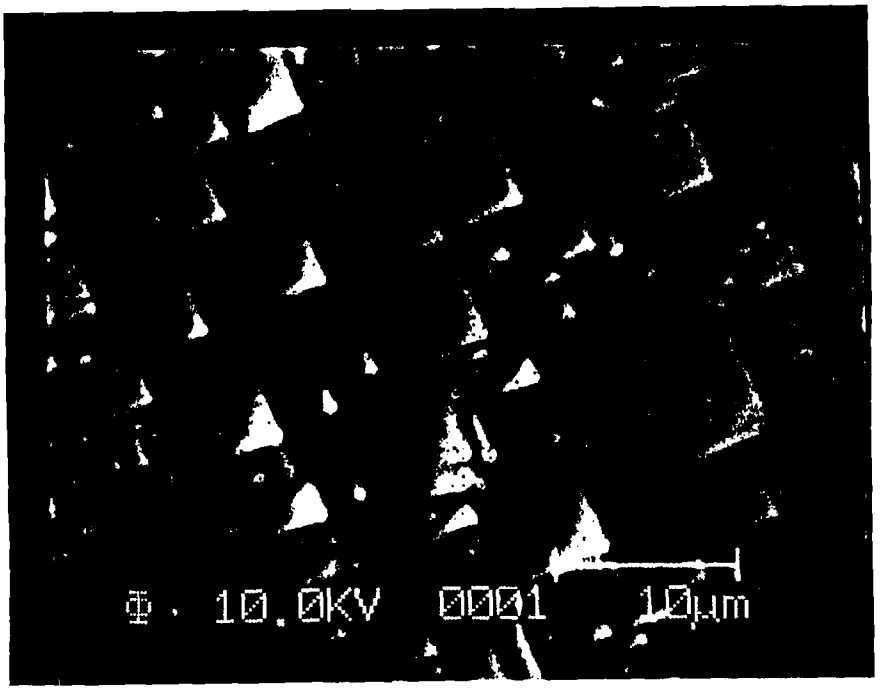

2) Oxidized samples (both side : 850°C, 50 min, dry O_2 ambient) were also texture-etched in a potassium hydroxide (KOH) solution by the same procedures. We found that there was no sign of texturing. Therefore we can use this oxidized layer as a protect masking when we want one side texturing only.

3) Reflectance test was also performed to compare the textured surface and untextured one (same wefer characteristics), and the results of this are attached.
We are measuring somewhat lower reflectance than expected from the textured surface because we do not have the integrating sphere and we may be loosing some of the scattered light.

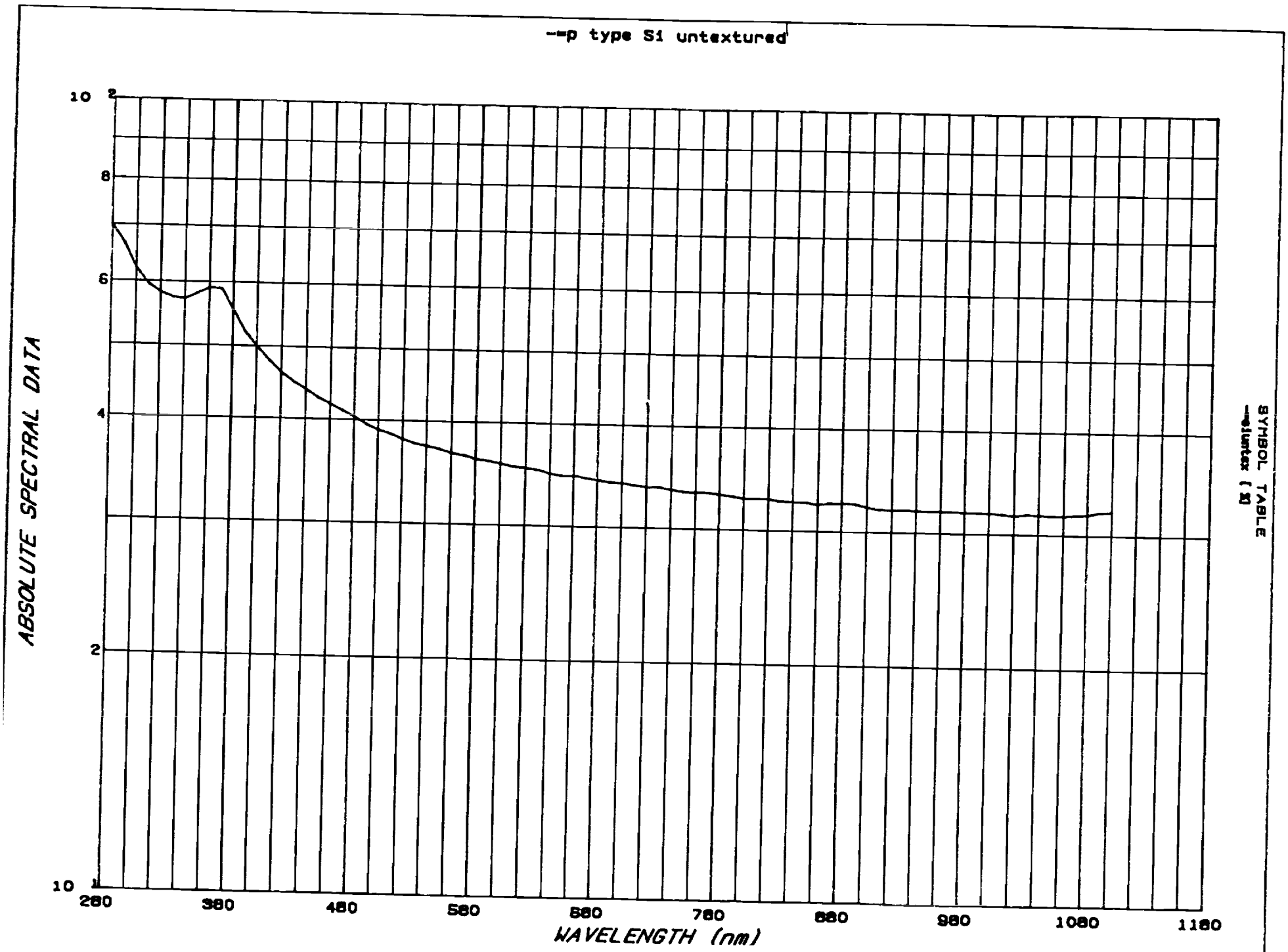
--p type Si untextured
ABSOLUTE SPECTRAL DATA
10 2
8
6
4
2
10 1
280
380
480
580
680
780
880
980
1080
1180
WAVELENGTH (nm)
SYMBOL TABLE
--Symbol [X]

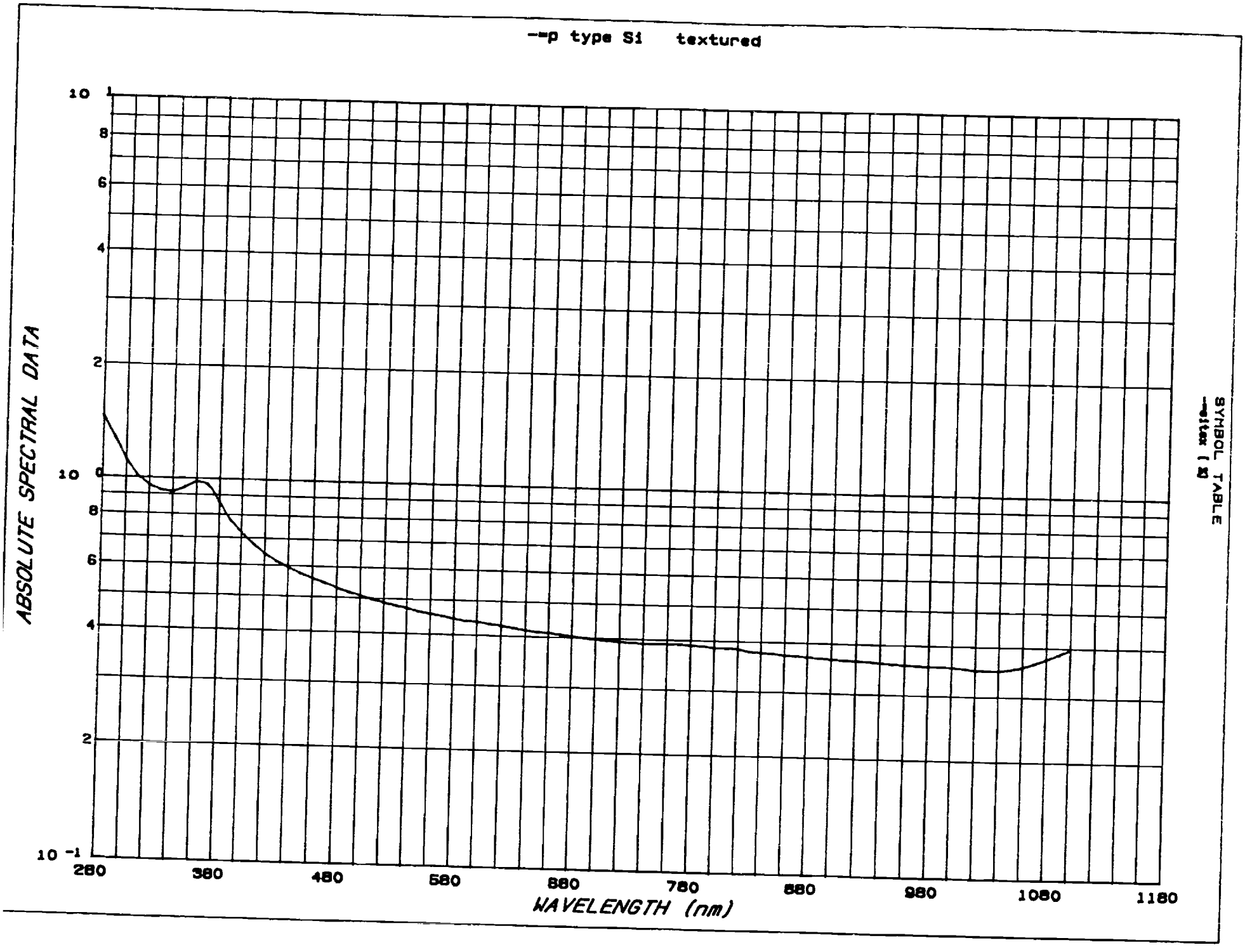
--p type Si textured
ABSOLUTE SPECTRAL DATA
10 1
8
6
4
2
10 0
8
6
4
2
10 -1
280
380
480
580
680
780
880
980
1080
1180
WAVELENGTH (nm)
SYMBOL TABLE

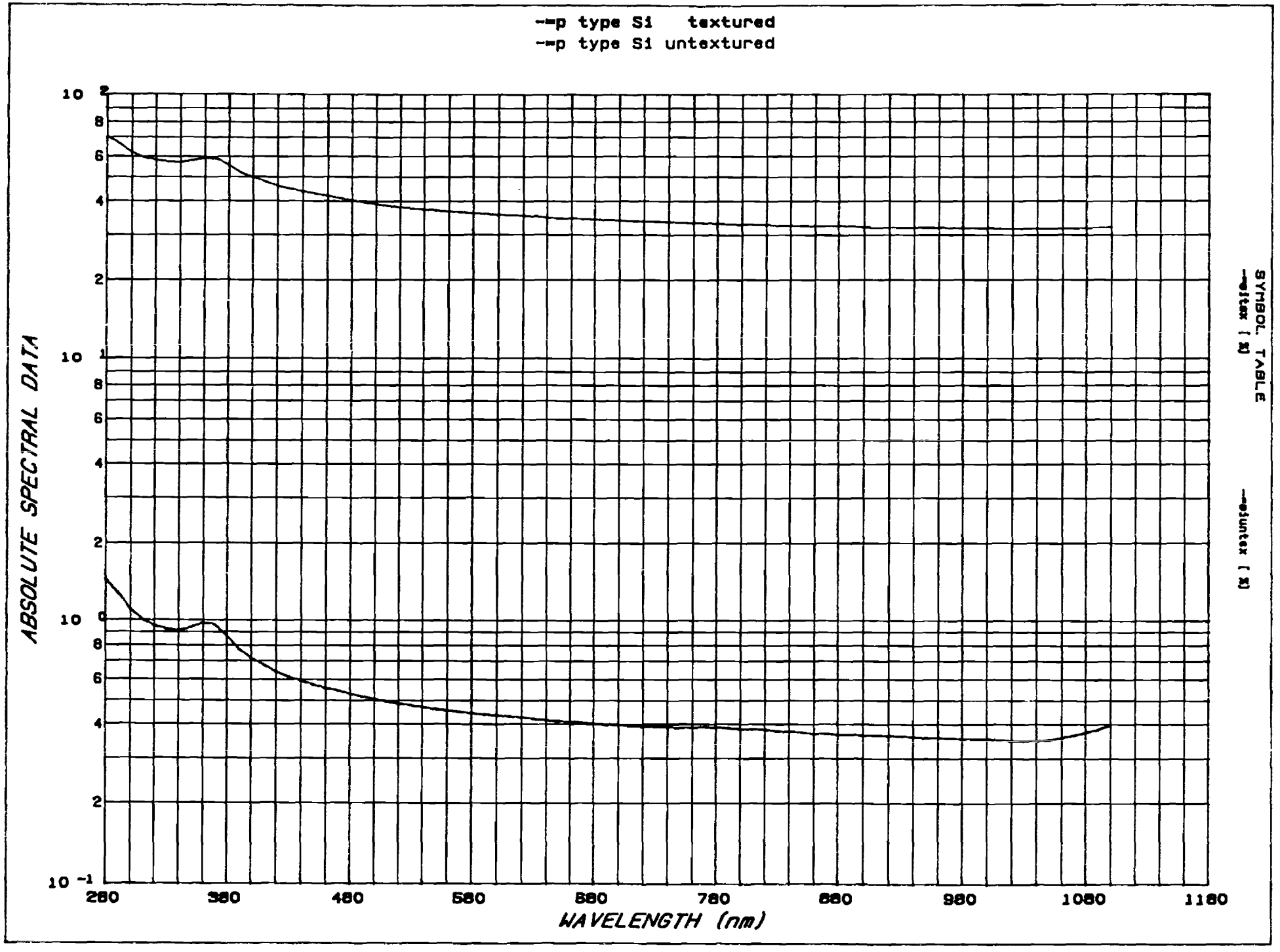
--=p type Si textured
--=p type Si untextured
ABSOLUTE SPECTRAL DATA
10 2
8
6
4
2
10 1
8
6
4
2
10 0
8
6
4
2
10 -1
280
380
480
580
680
780
880
980
1080
1180
WAVELENGTH (nm)
SYMBOL TABLE
--=tex [%]
--=untex [%]

TECHNICAL REPORT

PHOSPHORUS DIFFUSION

Phosphorus diffusion using the solid source has been performed (source type: TP 360, source size: 3"x.06"). Wafer preclean was done before this diffusion. Sheet resistivities of the diffused samples were measured by 4 point probe measurement and the junction depths were calculated using the Irvin's curve (Table 1). Because we are still trying to make our electrochemical etching profiler work on silicon. In the mean time selected samples were sent to Westinghouse for spreading resistance measurements.

The wafer used had the following characteristics : P-type, 3 inch
(100) direction
0.27 [ohms-cm]
15 mil

Process sequence for diffusion are as follows:

step	Rate/time	Temp	Gas
Insert	4"/min	750 C	N2 ambient (flow rate :3 lpm)
Stabilize	5 min	750 C	"
Ramp	10 C/min	850 C	"
Hold	50 min	850 C	"
Ramp	10 C/min	750 C	"
Pull	4"/min	750 C	"

Diffusion Temp. T_D (° C)	Time t_D (min)	Measured Sheet Resistivity (Ohms/□)	Calculated Surface Concentration (cm^{-3})	Calculated Junction Depth (μm)
850	50	50 - 55	4×10^{20}	0.2 - 0.25
900	50	13 - 15	6×10^{20}	0.65 - 0.75

Table 1 Measured sheet resistivities and calculated junction depthes.

DIFFUSION PROFILE MEASUREMENT

There is a need to be able to measure dopant and carrier concentration profiles in silicon after each diffusion during the solar cell fabrication cycle. Two techniques which are currently being used to determine carrier concentration profiles in silicon, are spreading resistance (SR) which has been used for last twenty years, and electrochemical CV (ECV) etching profiler, which has been used for the last ten years with great success on III-V semiconductors. During the last few years, developments in ECV have made it possible to extended the applicability of this technique to silicon.

We have used spreading resistance measurement at Westinghouse to get the junction depth and diffusion profile ,figure 1 and 2.We are trying to do the same measurement with ECV in our facility.This technique is briefly described below:

To measure carrier concentration profiles and junction depth after diffusion electrochemical cv profiling(Polarn PN4200) is being used.

Polarn PN4200 is a computer controlled electrochemical carrier concentration profiling system for obtaining electrically active carrier concentration profiles vs. depth into the semiconductor surfaces .

The system operates by placing the sample in contact with a defined area of electrolyte and applying a small biasing voltage across the semiconductor and electrolyte interface. This contact is basically equivalent to a metal schottky contact. Majority carrier concentration can be obtained by analyzing capacitance voltage data from the depleted region.

By designing the electrolyte in such a way that a well defined electrochemical dissolution reaction can be induced,the area of silicon material in contact with the electrolyte can be gradually dissolved and carrier concentration vs. depth profiles can be calculated.

Successful results depends upon availability of an electrolyte which supports

1)A well defined electrochemical dissolution process.

2)Formation of a near-ideal schottky contact.

The above criteria is not easily met for silicon.

The basic equations used in the system are :

1) The Schottky equation for capacitance of a "one-sided" junction

$$C^2 = \frac{Aq\varepsilon_o\varepsilon_r N}{2(\psi - V)}$$

which is differentiated and rewritten

$$\text{Carrier Concentration } N = \frac{1}{q\varepsilon_o\varepsilon_r A^2} \quad \frac{C^3}{dc/dv}$$

2) The equation for a parallel plate capacitor

$$\text{depletion depth } Wd = \frac{\varepsilon_o\varepsilon_r A}{C}$$

3) Faraday's Law of electrolysis

$$\text{Etch Depth } Wr = \frac{M}{ZFDA} \int I dt$$

Where A = area of specimen

q = electronic charge

$\varepsilon_o \varepsilon_r$ = permittivity of semiconductor material

ψ = barrier potential of interface

V = applied potential

I = current drawn

t = time

N = carrier concentration

C = capacitance of interface

M = molecular weight of semiconductor

D = density of semiconductor

F = the Faraday constant

Z = valency of the semiconductor

The following solution has been used as the electrolyte solution :

1 molar NAF solution with .05 molar H_2SO_4 as the solvent is the stock solution. We have found that 1:1 dilution of the stock solution gives very fast etch while 1:2 dilution gives a smooth etch and quality of the etch improves with more dilution.

Right now there is a problem with gas formation at Si/electrolyte interface and we are trying to solve this problem. Further improvement in this area will be reported in future reports.

WESTINGHOUSE ELECTRIC CORPORATION RESEARCH AND DEVELOPMENT CENTER
Solid State Division
Spreading Resistance Measurement Laboratory

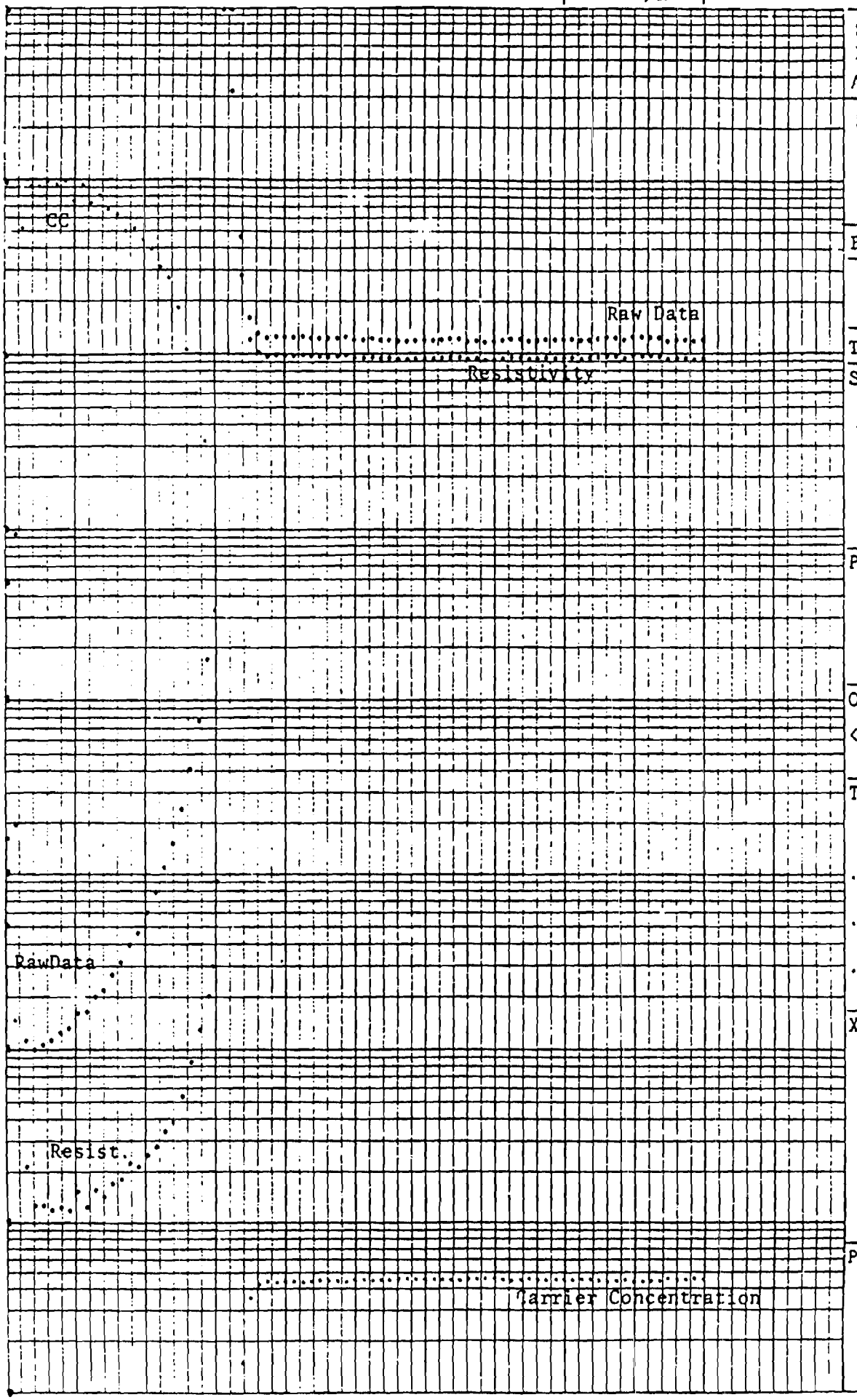

Sample Submitt
By
A. Pohatgi

SAMPLE ID
B003

BLOCK 17 min.#

Technician PAP

Surface Fini

Diamond	1
2	3
4	5

Probe Load, g

	10
20	45

Orientation

<100>.	<111

Tan α

	0
.005	.01
.02	.05
.10	.20

X-Step, μm

	.5
1	2.5
5	10
25	100

Probe Sep., μ

	25
100	600

CR-113

WESTINGHOUSE ELECTRIC CORPORATION RESEARCH AND DEVELOPMENT CENTER
Solid State Division
Spreading Resistance Measurement Laboratory

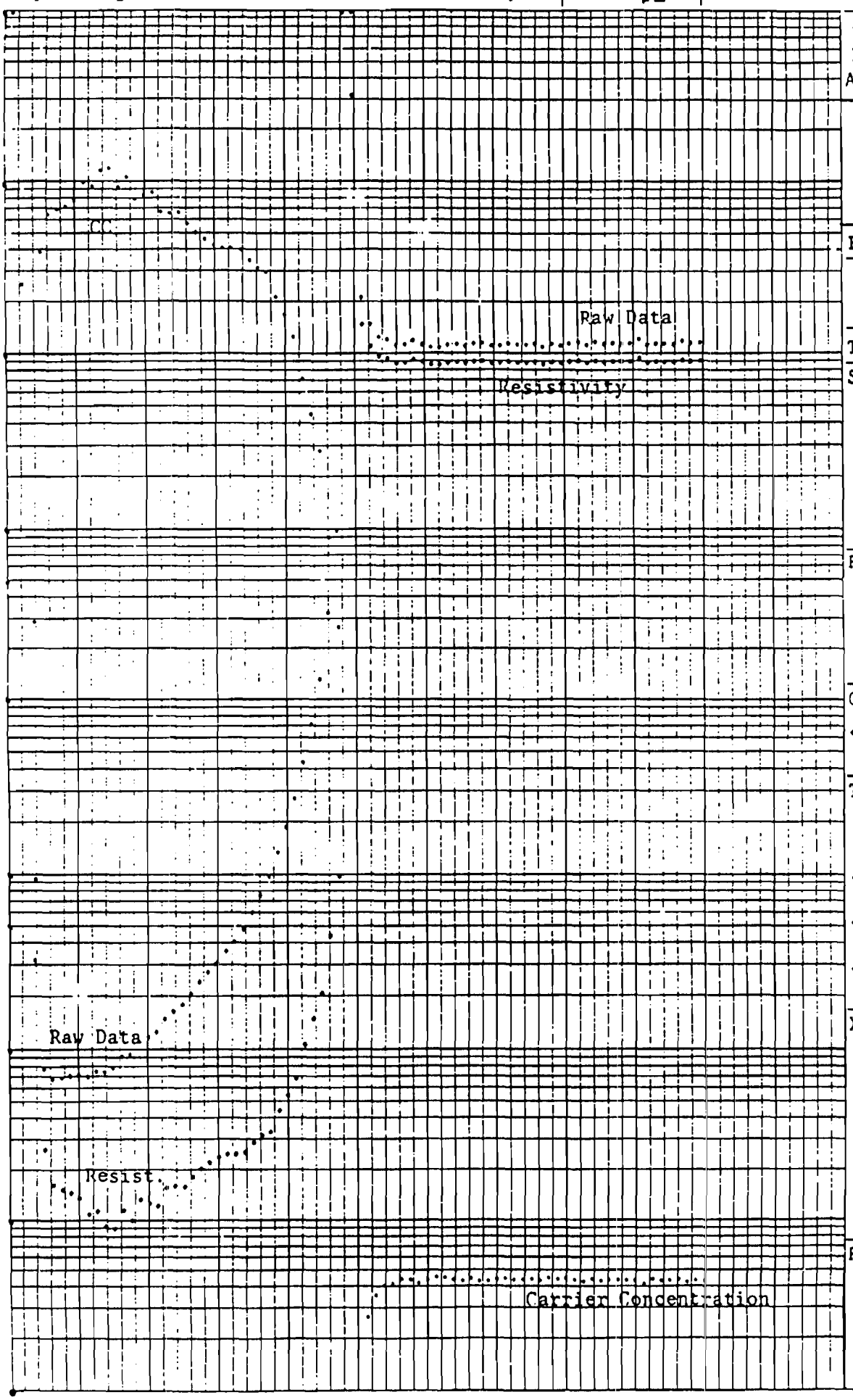

Sample Submitted By
A. Rohatgi

SAMPLE ID
B006

BLOCK 17 min.#2

Technician PAP

Surface Finis

Diamond	1
2	3
4	5

Probe Load, gm

	10
20	45

Orientation

<100>	<111>

Tan α

	0
.005	.01
.02	.05
.10	.20

X-Step, µm

	.5
1	2.5
5	10
25	100

Probe Sep., µ

	25
100	600

GP-113

GEORGIA INSTITUTE OF TECHNOLOGY
SCHOOL OF ELECTRICAL ENGINEERING
ATLANTA, GEORGIA 30332

TELEPHONE: (404) 894- 7337

December 12, 1988

Mr. J. Gee
Sandia National Laboratories
P. O. Box 5800
Albuquerque, NM 87185-5800

RE: Contract No. 57-6152
Project Director: A. Rohatgi

Dear Mr. Gee:

Enclosed please find copies of the Monthly Cost Status Report for the period 11/1/88-11/30/88 on the above referenced contract.

If you have any questions, please feel free to contact me.

Sincerely,

Pam Majors
Research Administrator

pm
Enclosure

CONTRACTOR: Complete all spaces and the bottom block.

Sandia National Laboratories

PURCHASING ORGANIZATION Georgia Tech

ALBUQUERQUE, NEW MEXICO 87185

LIVERMORE, CALIFORNIA 94550

J. Gee

Sandia Contracting Representative

MONTHLY COST STATUS REPORT

CONTRACT NO. 57-6152

PERIOD ENDING (1) November 30, 1988

Contractor must forecast as a minimum the first three months, Balance of Fiscal Year, and Subsequent Fiscal Years when costs will be incurred in these months and years.

Contractor must forward this report to reach the Sandia Contracting Representative by the 15th of the month following the Report Period or at such other time as requested by the Sandia Contracting Representative.

TOTAL FUNDS AUTHORIZED		$ 97,448.00
ACTUAL COST INCURRED TO DATE(2)		38,840.34
ESTIMATED COST TO COMPLETE:(3)		
1st MONTH FOLLOWING "PERIOD ENDING" as specified above	11,721.53	
2nd MONTH	11,721.53	
3rd MONTH	11,721.53	
4th MONTH	11,721.53	
5th MONTH	11,721.54	
6th MONTH		
BALANCE OF FISCAL YEAR(4)		
SUBSEQUENT FISCAL YEARS		
TOTAL ESTIMATE TO COMPLETE		58,607.66
TOTAL ESTIMATED COST AT COMPLETION		$ 97,448.00

NOTES:

1) Last full month for which actual costs are available.
2) Cost includes applicable fee.
3) Estimates for costs to be incurred (Do not include commitments), including applicable fee.
4) Fiscal year is 10/1 through 9/30. Balance of fiscal year means all months remaining in the fiscal year following the 6th month shown on the line above. If the 6th month is September, then balance of fiscal year is 10/1 through 9/30 of the next fiscal year.

Contractor (name and address)	Signature of Contractor's Representative, Date and Phone
Georgia Tech Research Corporation School of Electrical Engineering Georgia Institute of Technology Atlanta, GA 30332	Pam Majors, Research Adm. 404-894-7337 12/12/88

3432-CS(1-85)

GEORGIA INSTITUTE OF TECHNOLOGY
SCHOOL OF ELECTRICAL ENGINEERING
ATLANTA, GEORGIA 30332

TELEPHONE: (404) 894.7337

January 16, 1989

Mr. J. Gee
Sandia National Laboratories
P. O. Box 5800
Albuquerque, NM 87185-5800

RE: Contract No. 57-6152
Project Director: A. Rohatgi

Dear Mr. Gee:

Enclosed please find copies of the Monthly Cost Status Report for the period 12/1/88-12/31/88 on the above referenced contract.

If you have any questions, please feel free to contact me.

Sincerely,

Pam Majors
Research Administrator

pm
Enclosure

CONTRACTOR: Complete all spaces and the bottom block.

Sandia National Laboratories

PURCHASING ORGANIZATION Georgia Tech

ALBUQUERQUE, NEW MEXICO 87185
LIVERMORE, CALIFORNIA 94550

James Gee
Sandia Contracting Representative

MONTHLY COST STATUS REPORT

CONTRACT NO. 57-6152

PERIOD ENDING (1) December 31, 1988

Contractor must forecast as a minimum the first three months, Balance of Fiscal Year, and Subsequent Fiscal Years when costs will be incurred in these months and years.

Contractor must forward this report to reach the Sandia Contracting Representative by the 15th of the month following the Report Period or at such other time as requested by the Sandia Contracting Representative.

TOTAL FUNDS AUTHORIZED		$ 97,448.00
ACTUAL COST INCURRED TO DATE(2)		41,415.30
ESTIMATED COST TO COMPLETE:(3)		
1st MONTH FOLLOWING "PERIOD ENDING" as specified above	18,677.56	
2nd MONTH	18,657.57	
3rd MONTH	18,677.57	
4th MONTH		
5th MONTH		
6th MONTH		
BALANCE OF FISCAL YEAR(4)		
SUBSEQUENT FISCAL YEARS		
TOTAL ESTIMATE TO COMPLETE		56,032.70
TOTAL ESTIMATED COST AT COMPLETION		$ 97,448.00

NOTES:
(1) Last full month for which actual costs are available.
(2) Cost includes applicable fee.
(3) Estimates for costs to be incurred (Do not include commitments), including applicable fee.
(4) Fiscal year is 10/1 through 9/30. Balance of fiscal year means all months remaining in the fiscal year following the 6th month shown on the line above. If the 6th month is September, then balance of fiscal year is 10/1 through 9/30 of the next fiscal year.

Contractor (name and address)	Signature of Contractor's Representative, Date and Phone
Georgia Tech Research Corporation School of Electrical Engineering Georgia Institute of Technology Atlanta, GA 30332	Pam Majors, Research Adm. 404-894-7337 1/12/89

SF6432-CS(1-85)

GEORGIA INSTITUTE OF TECHNOLOGY
SCHOOL OF ELECTRICAL ENGINEERING
ATLANTA, GEORGIA 30332

TELEPHONE: (404) 894-7337

January 31, 1989

Mr. J. Gee
Sandia National Laboratories
P. O. Box 5800
Albuquerque, NM 87185-5800

Re: Contract No. 57-6152
Project Director: A. Rohatgi

Dear Mr. Gee:

Enclosed please find the Monthly Technical Progress Report for the period 10/17/88-11/16/88 on the above referenced contract.

If you have any questions, please feel free to contact me.

Sincerely,

Pam Majors
Research Administrator

pm
Enclosure

TECHNICAL REPORT

We made the N^+/P standard solar cells by using two different isolation methods; mesa etch isolation and oxide isolation. Device fabrication and characterization are described below.

I. The wafer used had following characteristics: p-type, 3 inch
(100) direction
0.27 [ohms-cm]
15 mils

II. The process flow applied was as follows:

1. Process flow using mesa etch isolation method

1) Wafer clean
2) Phosphorus diffusion
3) Oxide etch
4) Premetal clean
5) Metallize front side
6) Lap back
7) Wafer clean
8) Photolithography with contact grid mask
9) Etch metal
10) Strip PR
11) Premetal clean
12) Metallize back side
13) Photolithography with mesa mask
14) Etch silicon
15) Strip PR both sides

2. Process flow using oxide isolation method

1) Wafer clean
2) Thermal oxide both side
3) Photolitohgraphy with mesa mask
4) Strip front side oxide for diffusion pattern
5) Strip PR both sides
6) Wafer clean
7) Phosphorus diffusion front side
8) Etch phosphorus glass
9) Premetal clean
10) Metallize front and back
11) Photolithography with contact grid mask
12) Etch metal front side
13) Strip PR both sides

A. Detailed process flow using mesa etch isolation method

1) Wafer clean:

[1] Boil out tweezers and boat in DI water for 15 minutes
[2] Boil quartz beaker in 5:2:1 H_2O:H_2O_2:HCl for 2 hours for use in step [7]
[3] Etch the wafer in a 15:1 Nitric:HF solution for 30-40 seconds.(etch rate: about 3 microns/min)
[4] DI rinse for 3 minutes.(Avoid unnecessary exposure to air and 10 cycles in a dump rinsed)
[5] Dip wafer in a 1:10 HF:H_2O for 1 minute. Avoid exposure to light during this step (plate out metals)
[6] Rinse as in step [4]
[7] Boil the wafer in 5:2:1 H_2O:H_2O_2:HCl for 10 minutes.

2) Phosphorus diffusion: 850 C, 50 minutes
measure sheet resistance: 55-65 [ohms/sq]
calculated junction depth:0.25-0.35 [um]

3) Oxide etch: dip 1:10 HF:H_2O until oxide removed

4) Premetal clean:

[1] H_2SO_4:H_2O_2, 87 C, 5 minutes
[2] 1:10 HF:H_2O, 10 seconds

5) Metallize front side: thermal evaporation at $2x10^{-6}$ torr
Aluminum
1200 [A]

6) Lap back: after lapping process: thickness: 13 mils
conductivity: p-type
resistivity: 0.27 [ohms-cm]

7) Wafer clean: same as in step A. 1)

8) Photolithography with contact grid mask:

[1] Clean: 1 min in boiled TCE
methanol rinse
DI rinse and blow dry
[2] Prebake 120 C, 10 min
[3] Prime: HMDS coat

spin 4000 rpm, 25 sec
dry 30 sec

[4] PR coat: negative photoresist (Waycoat IC)
[5] Spin: 4000 rpm, 25 sec
[6] Softbake: 85 C, 10-20 min
[7] Expose: 5 sec
[8] Develop: IC developer 1 min
N-butyl acetate 1 min
methanol 1 min
DI rinse and blow dry
[9] Post bake: 120 C, 10 min

9) Etch metal: 1:4:4:1 HNO_3:CH_3COOH:H_3PO_4:H_2O (= Al etchant)
etch rate: 350 A/min

10) Strip PR: microstrip 60 C, 5 min
methanol rinse
DI rinse and blow dry

11) Premetal clean: same as in step A. 4)

12) Metallize back side: same as in step A. 5)

13) Photolithography with mesa mask:

[1] Clean
[2] Prebake
[3] Prime (front side)
[4] PR coat (front side)
[5] Spin
[6] Softbake
[7] Expose with mesa mask
[8] Develop
[9] Postbake
[10] Prime (backside)
[11] PR coat (backside)
[12] Spin
[13] Softbake
[14] Expose with no mask
[15] Postbake

14) Etch silicon: 44:26:29 HF:HNO3:CH3COOH (= silicon etchant)
5 C
etch time: 5-10 sec
etch rate: about 0.4 um/sec

15) Strip PR both sides: same as in step A. 10)

B. Detailed process flow using oxide isolation method

1) Wafer clean: same as in step A. 1)

2) Thermal oxide both side: 1100 C, 5 hrs and 30 min
Ambient: argon, oxygen and TCA
thickness: 0.45 [um]

3) Photolithography with mesa mask: same as in step A. 13)

4) Strip front side oxide for diffusion pattern: 1:1 HF:H_2O

5) Strip PR both sides: same as in step A. 15)

6) Wafer clean: 5:1:1 Hot H_2O:H_2O_2:HCl - 5 min
rinse and blow dry

7) Phosphorus diffusion front side: same as in step A. 2)

8) Etch phosphorus glass: dip 1:10 HF: H_2O for 5-10 sec

9) Premetal clean: same as in step A. 4)

10) Metallize front and back : same as A. 5) & 12)

11) Photolithography with contact grid mask: same as in step A. 13)

12) Etch metal front side: same as in step A. 9)

13) Strip PR both sides: same as in step A. 15)

III. Measurement of I-V

1. N^+/P standard solar cell using mesa etch isolation:

1) Cell area: 1 [cm^2]
2) Normalized series resistance (Rs) : 9.4 [ohm-cm^2]
3) Normalized shunt resistance (Rsh) : 21.15 [kohm-cm^2]
4) Short circuit current density (Jsc) : 21.85 [mA/cm^2]
5) Open circuit voltage (Voc) : 0.611 [V]
6) Fill factor : 0.4657
7) Efficiency : 6.22 [%]
8) Figure 1.

2. N^+/P standard solar cell using oxide isolation:

1) Cell area: 1 [cm^2]
2) Normalized series resistance (Rs) : 6.79 [ohm-cm^2]
3) Normalized shunt resistance (Rsh) : 53.28 [kohm-cm^2]
4) Short circuit current density (Jsc) : 22.26 [mA/cm^2]
5) Open Circuit voltage (Voc) : 0.562 [V]
6) Fill factor : 0.5512
7) Efficiency : 6.89 [%]
8) figure 2.

Among the above parameters the series resistance, shunt resistance and fill factor was very bad. We think these come from the metal contact of front and back sides. We could not calibrate the thickness of metal when we metallized the Aluminum. Therefore the thickness of Al was only 0.12 um for front and 0.4 for back side. If we deposit proper thickness and proper metals for solar cells (i.e. Ti:1500 A, Pd:500 A, Ag:2 um) much higher efficiency is anticipated.

This technical report was written by K. Lee, J. Salami.

C. Final Structure of Both Cells

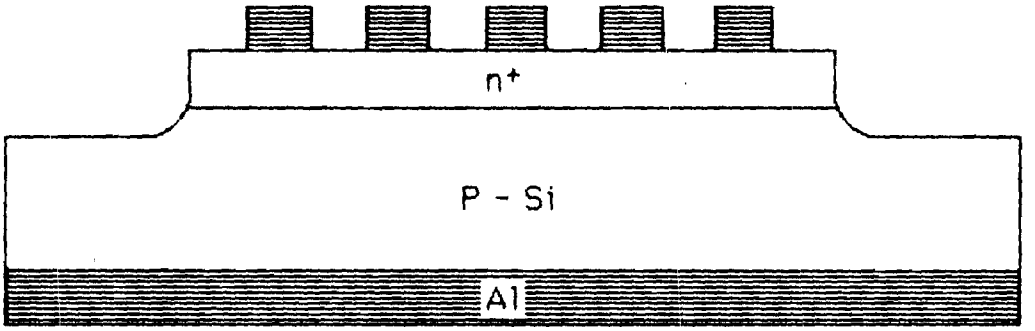

Fig. 1 N^+/P standard cell using mesa etch isolation.

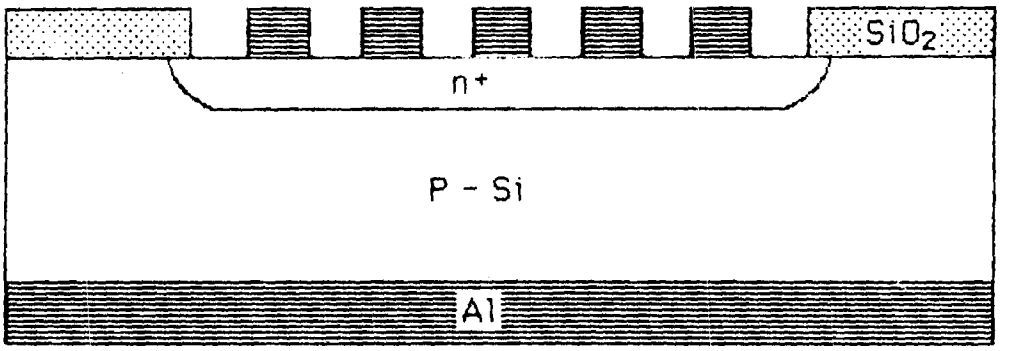

Fig. 2 N^+/P standard solar cell using oxide isolation.

L 21-6-88

CERTIFICATE OF SERVICES/RESEARCH
CONTRACT NO. F33615-83-D-0601
GEORGIA TECH PROJECT NO. A3529-320

Period Covered: MARCH 1, 1987 through JANUARY 31, 1989* Delivery Order 0032

I. DIRECT COSTS:

	CURRENT	CUMULATIVE
Subcontracts (Univ. of Texas Health Science Ctr.)	1,476.99	45,621.62
Management Fee(5% of Total Costs)	7.77	2,215.00
TOTAL	1,484.76	47,836.62

"I certify that the above is a true and correct statement of efforts performed under Contract No. F33615-83-D-0601 by the Georgia Institute of Technology, contracting through the Georgia Tech Research Corporation for the subject time period."

James C. Toler, Project Director

The above statement is approved for payment by the Government.

Lt. Col. S. L. Hartgraves

Cruz Cantu

Please remit approved "Certificate" to: GEORGIA INSTITUTE OF TECHNOLOGY
ATLANTA, GEORGIA 30332
ATTN: Julie Blankenship
GTRI Acctg. & Budgets

*NOTES: Dates represent a billing period only. All charges were incurred prior to contract termination, 4-15-87.

GEORGIA INSTITUTE OF TECHNOLOGY
SCHOOL OF ELECTRICAL ENGINEERING
ATLANTA, GEORGIA 30332

TELEPHONE: (404) 894-7337

February 14, 1989

Mr. J. Gee
Sandia National Laboratories
P. O. Box 5800
Albuquerque, NM 87185-5800

Re: Contract No. 57-6152
Project Director: A. Rohatgi

Dear Mr. Gee:

Enclosed please find the Monthly Technical Progress Report for the period 11/17/88-12/16/88 on the above referenced contract.

If you have any questions, please feel free to contact me.

Sincerely,

Pam Majors
Research Administrator

pm
Enclosure

IMPACT OF DEEP LEVEL POSITION AND LIGHT TRAPPING ON SILICON CELL PERFORMANCE

A. Rohatgi, A. W. Smith, and S. K. Pang
School of Electrical Engineering
Georgia Institute of Technology
Atlanta, Georgia 30332-0250

and

P. A. Basore
Sandia National Laboratories
Albuquerque, NM 87185-5800

ABSTRACT

In spite of recent improvements in silicon quality, a considerable gap still remains between theoretically possible and experimentally achieved lifetimes in silicion due to defects induced traps. Model calculations in this paper reveal and quantify the influence of trap location and light trapping on the cell performance and optimum base resistivity for cells fabricated on high and low quality silicon.

1. INTRODUCTION

The right combination of material quality, cell design, and light trapping is the key to achieving high efficiency cells. The objective of the paper is twofold. First, to bridge the gap between silicon vendors and cell manufacturers by providing guidelines for selecting the right combination of carrier lifetime and resistivity for a conventional high efficiency n^+-p-p^+ cell design. Secondly, to quantity the effect of various surface texturing schemes on not only the increased photon absorption but also on the performance of cells with base minority carrier lifetime ranging from 1 μs to 10 ms.

Even the best silicon available today suffers from defects that lead to trap induced recombination. This paper shows that the optimum resistivity and performance for a given cell design depends on (1) trap location, (2) starting minority carrier lifetime, prior to intentional doping, and (3) injected carrier concentration in the cell. It is shown that starting with a high lifetime material alone is not sufficient because certain trap locations can severely limit the performance if the base doping is inappropriate or the cell goes into high level injection. The model calculations have been done for one sun AM 1.5 conditions but the results may have implications for concentrator cells.

2. MODELING

2.1 Light Trapping

In the PC-1D device model [1] used in this paper, the generation profile is only applicable to flat surfaces, however, the angle of incidence and incident flux can be changed to produce different carrier generation profiles. To quantify the importance of light trapping, a ray tracing program was developed

to obtain generation profiles for different surfaces: regular pyramid-like, Lambertian, and perpendicular slats. In this program, the incoming flux is divided into a large number of rays and the path of each ray is followed until the ray is completely absorbed, resulting in a generation profile. It is important to realize that relative improvement in cell performance from increased photon absorption depends on the base quality and collection efficiency. In an attempt to quantify this effect, generation profiles in PC-1D were created and matched with the generation profiles from the ray tracing program by tailoring the flux and angle of incidence, prior to performing the solar cell simulations for base material with lifetimes ranging from 1 μs to 10 ms. It should be noted that in these preliminary calculations we have ignored the effects of two-dimensional carrier flow and increased emitter area due to the textured surfaces.

2.2 Carrier Lifetime and Device Modeling

In an earlier paper [2], we made an attempt to investigate some of these effects, using a combination of the semiconductor device modeling program PC-1D and an independent lifetime model. Since PC-1D was configured for only midgap traps, artificially higher values of τ_{no} and τ_{po} were introduced to give the correct recombination rate for shallow traps. This resulted in somewhat inaccurate or higher V_{oc} values for shallow traps when the cell went into high level injection. The latest version of PC-1D has been modified to account for the effect of trap location. In order to understand the physics behind the calculated results by PC-1D, we have utilized analytical expressions for V_{oc}, Shockley-Read-Hall lifetime, and net lifetime. These equations utilize injection level calculated by PC-1D. The equations are listed below for p-base solar cells:

- Open circuit voltage for all levels of injection in a cell is given by

$$V_{oc} = \frac{kT}{q} \ell n\left(\frac{np}{ni^2}\right) \tag{1}$$

provided quasi-Fermi levels are flat.

- The net lifetime in the base is given by

$$\frac{1}{\tau_{net}} = \frac{1}{\tau_{SRH}} + \frac{1}{\tau_{Auger}} + \frac{1}{\tau_r}$$

$$\frac{1}{\tau_{net}} = \frac{1}{\tau_{SRH}} + C_p p^2 + C_n n^2 + B(p+n) \tag{2}$$

where C_p and C_n are the Auger coefficients, n and p are total electron and hole concentrations in the base of the cell, B is the radiative band to band coefficient, and

$$\tau_{SRH} = \frac{\tau_{no}(p_o+p_1+\Delta n) + \tau_{po}(n_o+n_1+\Delta n)}{p_o + n_o + \Delta n} \tag{3}$$

where Δn is the injected carrier concentration, n_o and p_o are equilibrium carrier concentrations,

$$n_1 = N_c \exp\left(-\frac{E_c - E_t}{kT}\right) \quad \text{and} \quad p_1 = N_v \exp\left(-\frac{E_t - E_v}{kT}\right)$$

where E_t is the energy level of the trap.

3. RESULTS AND DISCUSSION

3.1 Effect of Trap Location on Lifetime

Model calculations in Figure 1 show that, for a given quality of undoped starting material, minority carrier lifetime under low level injection decreases with increasing doping density and the doping dependence is dictated by the trap location within the bandgap. For a silicon technology that can produce 200 ohm-cm wafers with 10 ms lifetime, a midgap trap shows essentially no doping dependence until $N_a \sim 2 \times 10^{15}$ cm^{-3}. Beyond this doping the lifetime drops sharply due to Auger recombination. Shallow traps show a much stronger and undesirable doping dependence. This is because in order to keep the same starting lifetime, the τ_{no} and τ_{po} values for the shallow traps are smaller than for a midgap trap. These calculations assume $\tau_{no} = \tau_{po}$.

Figure 2 shows the effect of injection level on lifetime for two different trap locations in a 200 ohm-cm silicon with a starting lifetime of 10 ms. This figure shows both SRH lifetime and net lifetime. It is interesting to note that as the material begins to go into high level injection ($\Delta n > N_a$), the lifetime increases for the midgap trap, but it decreases for the shallow trap. Once it gets into very high injection ($\Delta N >> 10\ N_a$), SRH lifetime becomes constant: $\tau_{SRH} = \tau_{no} + \tau_{po}$. Net lifetime, shown by the solid line, indicates that for the midgap trap lifetime continues to rise from 10 ms to ~18 ms before Auger recombination takes over at $\Delta n \approx 10^{15}$ cm^{-3} and after that, the lifetime drops rapidly. For the shallow trap (E_v + 0.2 eV), both net and SRH lifetimes continue to fall from 10 ms to about 200 μs until $\Delta n \approx 10^{16}$,

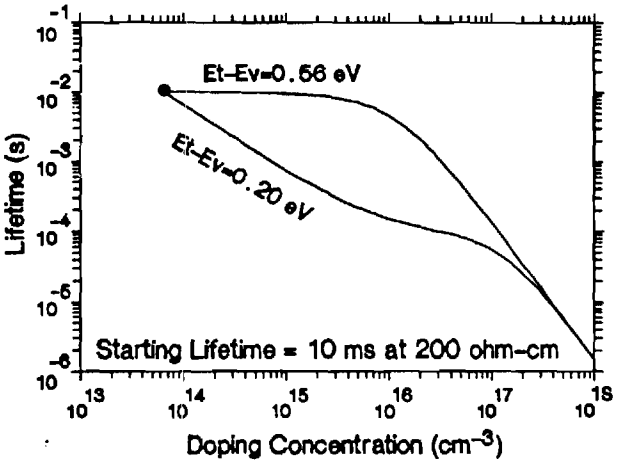

Figure 1. Lifetime versus doping concentration for a midgap trap and a shallow trap in a material with 10 ms starting lifetime at 200 Ω-cm.

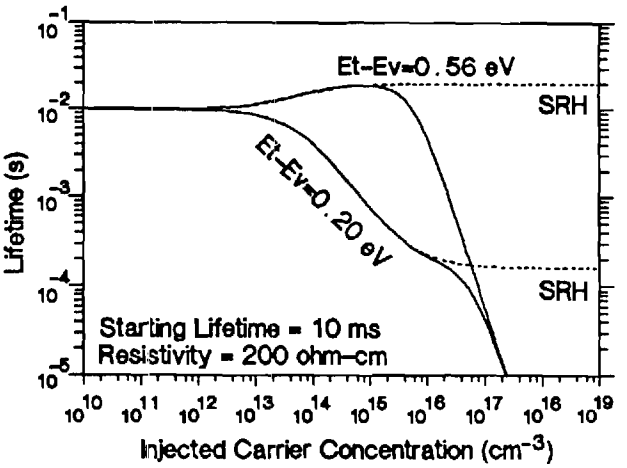

Figure 2. Lifetime versus injection level for a shallow and deep trap in 200 Ω-cm silicon with 10 ms lifetime at low level injection.

beyond which Auger recombination takes over. These trap induced lifetime behaviors (Figures 1 and 2) can significantly effect the performance of cells which are dominated by base recombination.

3.2 Effect of Trap Location on Cell Performance

Figures 3 and 4 show the effect of base doping concentration and trap level location on the performance of cells fabricated on a very high quality (τ = 10 ms at 200 ohm-cm) material, as well as on a low quality (τ = 10 μs at 200 ohm-cm) silicon. The cell design is shown in Table 1. Emitter and BSF recombinations were kept small to emphasize the effect of base lifetime. Model calculations indicate that for high quality material the optimum choice of resistivity will shift from high (> 200 ohm-cm) to low (~0.2 ohm-cm) if the trap is located at E_v + 0.20 eV instead of midgap. On the other hand, optimum resistivity for the low quality material remains at ~0.1-0.2 ohm-cm regardless of the trap location. It should be noted that here we have assumed trap density to be independent of doping density. We have shown elsewhere [2] that if trap density increases with doping concentration, then the optimum resistivity for low quality silicon tends to increase.

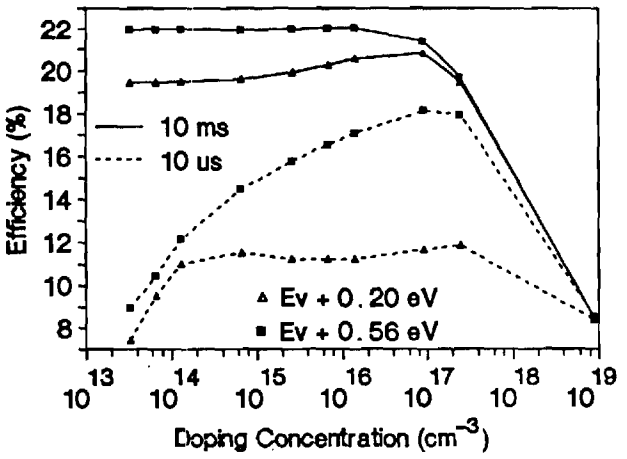

Figure 3. Effect of base quality (τ = 10 μs and 10 ms), base doping, and trap location on cell performance.

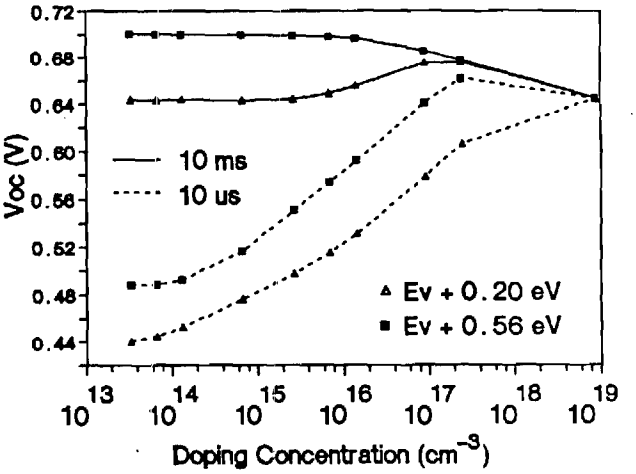

Figure 4. Effect of base quality, base doping, and trap location on V_{oc}.

TABLE 1. Configuration of N^+-P-P^+ Cells Used in Numerical Simulations

1. Cell area of 1 cm^2
2. Series resistance of 0.2 ohm
3. Uniform emitter doping of 2.0×10^{19} cm^{-3}
4. Emitter thickness of 0.2 microns
5. Cell thickness of 254 microns
6. Uniform BSF doping of 2.0×10^{18}
7. BSF thickness of 2 microns
8. 5% shadow and reflective loss
9. 98% effective back surface reflector
10. FSRV and BSRV of 0 cm/sec

In order to explain the interesting observations in Figure 3, lifetime calculations were performed as a function of base resistivity and injection level. Figures 5 and 6 represent high quality material with a midgap trap and a shallow trap, respectively. Both SRH lifetime, indicated by dotted lines, as well as net lifetime, indicated by solid lines, are plotted to delineate which recombination mechanism dominates. A point is shown on each curve indicating the conditions present when the cell is open circuited under illumination.

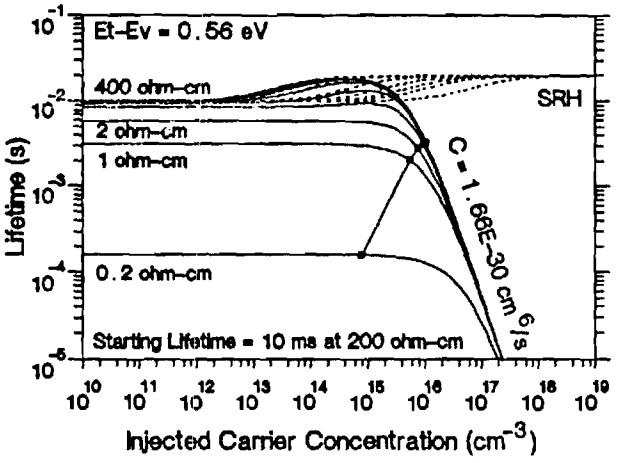

Figure 5. Net lifetime (solid lines) and SRH lifetime (dotted lines) as a function of injection level and base doping in a high quality silicon with a midgap trap.

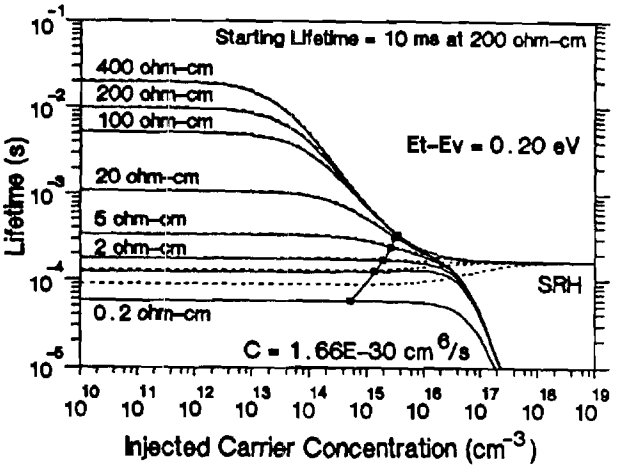

Figure 6. Net lifetime and SRH lifetime in a high quality silicon with a shallow (0.20 eV) trap. Points designate lifetime and injection level at V_{oc}.

Figure 5 demonstrates that for high quality silicon with a midgap trap, the lifetime at open circuit is limited by the Auger process. The cells remain under high level injection ($\Delta n > 10\ N_a$) down to a base resistivity of 20 ohm-cm. In this high injection range, Auger recombination limits V_{oc}, and cell performance remains essentially unaffected by resistivity. For cells with base resistivity less than 5 ohm-cm, Figure 5, the lifetime at V_{oc} decreases. However, the injection level at V_{oc} drops faster than the rise in N_a, resulting in a net decrease in np product and V_{oc}. Below 0.1 ohm-cm, V_{oc} decreases sharply due to a combination of Auger recombination and bandgap narrowing. Thus, high base resistivity is optimum for high quality material with midgap trap.

Figure 6 shows that for E_v + 0.2 eV trap, low level injection lifetime decreases with increased doping density, even for very lightly doped material. In addition, when the cell goes into high injection level ($\Delta n > N_a$), the lifetime begins to fall again due to a decrease in SRH lifetime until Auger recombination takes over. It is interesting to note that in this case lifetime at V_{oc} is limited by τ_{SRH}, and not by Auger recombination. Compared to the midgap trap case, lifetime, injection level, and np product are all smaller, resulting in lower V_{oc} and cell efficiency. Cell efficiency peaks around 0.2 ohm-cm for a shallow trap because V_{oc} reaches a maximum at ~0.1-0.2 ohm-cm, and below that resistivity V_{oc} and J_{sc} begin to drop due to Auger recombination.

In the case of technology that produces low quality silicon (τ = 10 µs at 200 ohm-cm), similar analysis, Figure 7, showed that the lifetime and injection level is dictated by SRH lifetime for both midgap and shallow traps. Cell performance peaks at 0.2 ohm-cm, regardless of the trap position, because Δn is small and np/n_i^2 product is dominated by the doping density. Below 0.1-0.2 ohm-cm, doping induced Auger recombination and bandgap narrowing begin to lower J_{sc} and cell performance rapidly, Figure 3. Again, V_{oc} and cell performance at the optimum resistivity is higher for the midgap trap because τ_{SRH} and injection levels are higher under illumination, Figure 7.

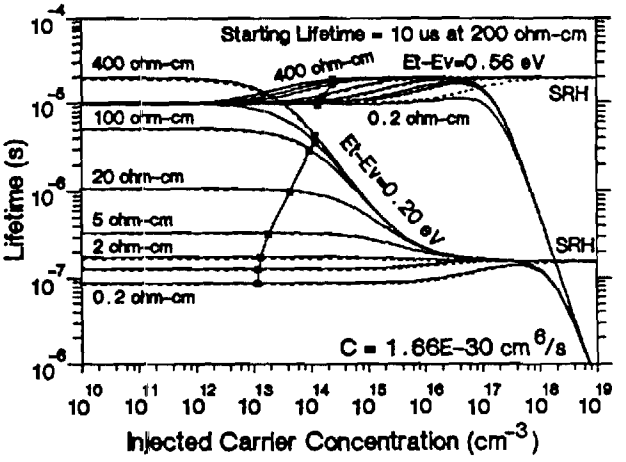

Figure 7. Net lifetime and SRH lifetime in a low quality silicon (τ = 10 µs at 200 Ω-cm) with a midgap trap as well as E_v+0.20eV trap.

3.4 Light Trapping Induced Improvement in Cell Performance

Preliminary calculations were performed to determine the effect of light trapping on efficiency of cells with base lifetime ranging from 1 µs to 10 ms. Consistent with Green et al. [3], we also found, Figure 8, that perpendicular slats, Lambertian, and pyramid-like surface texturing are superior to a flat surface. Perpendicular slat geometry, in which grooves at the top and bottom surfaces run perpendicular to each other, produce maximum improvement in the trapped flux. Slat spacing used was 10 µm and the angle of slats was 53° with respect to horizontal. Figure 9 shows that in spite of the same improvement in the trapped flux, actual increase in cell performance is dictated by the base lifetime. Light trapping in 100 micron thick cells produces significant increases in cell efficiency if the base lifetime is greater than 100 µs. Equally important is the fact that appreciable improvement is observed even in the cells with lifetime as low as 1 µs. Notice that, in Figure 9, base resistivity and cell performance were optimized for each lifetime. The cell design used was similar to that of Table 1 with the exception of complementary error doping profiles and FSRV = BSRV = 500 cm/sec.

4. CONCLUSIONS

The importance of trap location and light trapping has been investigated for various qualities of silicon. It is shown that optimum resistivity depends upon the lifetime prior to doping and the trap location. For a high quality silicon (τ = 10 ms at 200 ohm-cm), high resistivity (> 200 ohm-cm) is optimum if the trap is at midgap, but if the trap is shallow, then the optimum resistivity shifts to about 0.2 ohm-cm. For low quality silicon (10 µs at 200 ohm-cm) optimum resistivity was found to be ~0.1-0.2 ohm-cm, regardless of the trap location. Thus, before buying silicon for a given cell design, one needs to know the starting lifetime and trap location in order to specify resistivity to achieve best cell performance. For the same resistivity and

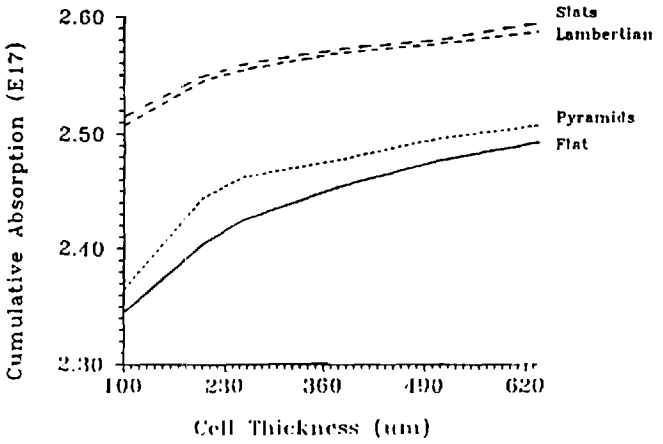

Figure 8. Increased photon absorption due to various light trapping schemes.

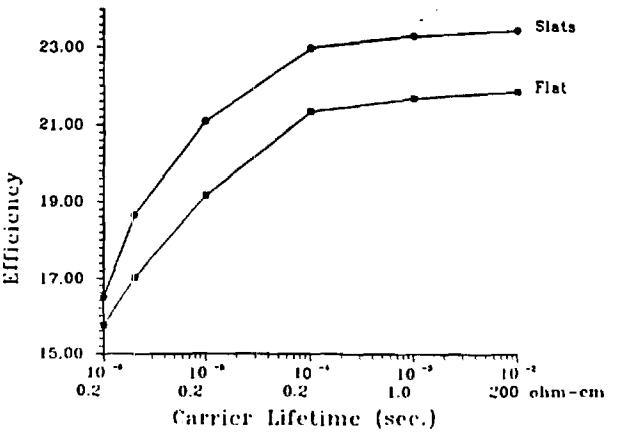

Figure 9. Effect of light trapping on efficiency of 100 μm thick cells with base lifetimes of 1 μs to 10 ms.

lifetime in silicon prior to illumination, shallow traps result in lower efficiency cells because of lower lifetime and injection level at the cell operating point. We have shown elsewhere [2] that a low quality material (τ = 100 μs at 200 ohm-cm) with midgap trap can give higher optimized cell efficiency than a somewhat higher quality material (τ = 1 ms at 200 ohm-cm) with a shallow trap.

Finally, we have shown that perpendicular slat type surface texturing can provide appreciable improvement in cell performance even when the base lifetime is in the range of 1-10 μs. Absolute improvement in cell performance due to light trapping increases with base lifetime.

5. ACKNOWLEDGEMENTS

The lifetime modeling and trap location part of this work was supported by EPRI, Contract No. RP8001-4, while the devcie modeling and light trapping was supported by Sandia/DOE, Contract No. 57-6152.

6. REFERENCES

[1] D. T. Rover, P. A. Basore, and G. M. Thorson, "Solar Cell Modeling on Personal Computers," Proc. 18th IEEE Photovoltaic Specialists Conf., pp. 703-709, 1985.

[2] A. W. Smith and A. Rohatgi, "Modeling the Effect of Trap Levels on the Optimum Resistivity of Silicon Solar Cells," to be published in 21st Photovoltaic Specialists Conf., Las Vegas, October 1988.

[3] M. A. Green and P. Campbell, "Light Trapping Properties of Pyramidally Textured and Grooved Surfaces," Proc. 19th IEEE Photovoltaic Specialists Conf., pp. 912-917, 1987.

GEORGIA INSTITUTE OF TECHNOLOGY
SCHOOL OF ELECTRICAL ENGINEERING
ATLANTA, GEORGIA 30332

TELEPHONE: (404) 894-7337

February 16, 1989

Mr. J. Gee
Sandia National Laboratories
P. O. Box 5800
Albuquerque, NM 87185-5800

RE: Contract No. 57-6152
Project Director: A. Rohatgi

Dear Mr. Gee:

Enclosed please find copies of the Monthly Cost Status Report for the period 1/1/89-1/31/89 on the above referenced contract.

If you have any questions, please feel free to contact me.

Sincerely,

Pam Majors
Research Administrator

pm
Enclosure

CONTRACTOR: Complete all spaces and the bottom block.

Sandia National Laboratories

PURCHASING ORGANIZATION Georgia Tech

ALBUQUERQUE, NEW MEXICO 87185
LIVERMORE, CALIFORNIA 94550

James Gee
Sandia Contracting Representative

MONTHLY COST STATUS REPORT

CONTRACT NO. 57-6152

PERIOD ENDING (1) January 31, 1989

Contractor must forecast as a minimum the first three months, Balance of Fiscal Year, and Subsequent Fiscal Years when costs will be incurred in these months and years.

Contractor must forward this report to reach the Sandia Contracting Representative by the 15th of the month following the Report Period or at such other time as requested by the Sandia Contracting Representative.

TOTAL FUNDS AUTHORIZED		$ 97,448.00
ACTUAL COST INCURRED TO DATE(2)		54,652.52
ESTIMATED COST TO COMPLETE:(3)		
1st MONTH FOLLOWING "PERIOD ENDING" as specified above	21,397.74	
2nd MONTH	21,397.74	
3rd MONTH		
4th MONTH		
5th MONTH		
6th MONTH		
BALANCE OF FISCAL YEAR(4)		
SUBSEQUENT FISCAL YEARS		
TOTAL ESTIMATE TO COMPLETE		42,795.48
TOTAL ESTIMATED COST AT COMPLETION		$ 97,448.00

NOTES:
(1) Last full month for which actual costs are available.
(2) Cost includes applicable fee.
(3) Estimates for costs to be incurred (Do not include commitments), including applicable fee.
(4) Fiscal year is 10/1 through 9/30. Balance of fiscal year means all months remaining in the fiscal year following the 6th month shown on the line above. If the 6th month is September, then balance of fiscal year is 10/1 through 9/30 of the next fiscal year.

Contractor (name and address)	Signature of Contractor's Representative, Date and Phone
Georgia Tech Research Corporation School of Electrical Engineering Georgia Institute of Technology Atlanta, GA 30332	Pam Majors, Research Adm. 404-894-7337 2/14/89

SF6432-CS(1-85)

GEORGIA INSTITUTE OF TECHNOLOGY
SCHOOL OF ELECTRICAL ENGINEERING
ATLANTA, GEORGIA 30332

TELEPHONE: (404) 894-

March 15, 1989

Mr. J. Gee
Sandia National Laboratories
P. O. Box 5800
Albuquerque, NM 87185-5800

RE: Contract No. 57-6152
Project Director: A. Rohatgi

Dear Mr. Gee:

Enclosed please find copies of the Monthly Cost Status Report for the period 2/1/89-2/28/89 on the above referenced contract.

If you have any questions, please feel free to contact me.

Sincerely,

Pam Majors
Research Administrator

pm
Enclosure

CONTRACTOR: Complete all space and the bottom block.

Sandia National Laboratories

PURCHASING ORGANIZATION Georgia Tech

ALBUQUERQUE, NEW MEXICO 87185
LIVERMORE, CALIFORNIA 94550

Mr. James Gee
Sandia Contracting Representative

MONTHLY COST STATUS REPORT

CONTRACT NO. 57-6152

PERIOD ENDING (1) 2/28/89

Contractor must forecast as a minimum the first three months, Balance of Fiscal Year, and Subsequent Fiscal Years when costs will be incurred in these months and years.

Contractor must forward this report to reach the Sandia Contracting Representative by the 15th of the month following the Report Period or at such other time as requested by the Sandia Contracting Representative.

TOTAL FUNDS AUTHORIZED	$ 97,448.00
ACTUAL COST INCURRED TO DATE(2)	72,313.73
ESTIMATED COST TO COMPLETE:(3)	
1st MONTH FOLLOWING "PERIOD ENDING" as specified above	25,134.27
2nd MONTH	
3rd MONTH	
4th MONTH	
5th MONTH	
6th MONTH	
BALANCE OF FISCAL YEAR(4)	
SUBSEQUENT FISCAL YEARS	
TOTAL ESTIMATE TO COMPLETE	25,134.27
TOTAL ESTIMATED COST AT COMPLETION	$ 97,448.00

NOTES:
(1) Last full month for which actual costs are available.
(2) Cost includes applicable fee.
(3) Estimates for costs to be incurred (Do not include commitments), including applicable fee.
(4) Fiscal year is 10/1 through 9/30. Balance of fiscal year means all months remaining in the fiscal year following the 6th month shown on the line above. If the 6th month is September, then balance of fiscal year is 10/1 through 9/30 of the next fiscal year.

Contractor (name and address)	Signature of Contractor's Representative, Date and Phone
Georgia Tech Research Corp. School of Electrical Engineering Georgia Institute of Technology Atlanta, GA 30332	Pam Majors, Research Adm. 404-894-7337 3/15/89

F6432-CS(1-85)

GEORGIA INSTITUTE OF TECHNOLOGY
SCHOOL OF ELECTRICAL ENGINEERING
ATLANTA, GEORGIA 30332

TELEPHONE: (404) 894-

April 15, 1989

Mr. J. Gee
Sandia National Laboratories
P. O. Box 5800
Albuquerque, NM 87185-5800

RE: Contract No. 57-6152
Project Director: A. Rohatgi

Dear Mr. Gee:

Enclosed please find copies of the Monthly Cost Status Report for the period 3/1/89-3/17/89 on the above referenced contract.

If you have any questions, please feel free to contact me.

Sincerely,

Pam Majors
Research Administrator

pm
Enclosure

CONTRACTOR: Complete all spaces and the bottom block.

Sandia National Laboratories

PURCHASING ORGANIZATION Georgia Tech

ALBUQUERQUE, NEW MEXICO 87185

LIVERMORE, CALIFORNIA 94550

James Gee
Sandia Contracting Representative

MONTHLY COST STATUS REPORT

CONTRACT NO. 57-6152

PERIOD ENDING (1) 3-16-89

Contractor must forecast as a minimum the first three months, Balance of Fiscal Year, and Subsequent Fiscal Years when costs will be incurred in these months and years.

Contractor must forward this report to reach the Sandia Contracting Representative by the 15th of the month following the Report Period or at such other time as requested by the Sandia Contracting Representative.

TOTAL FUNDS AUTHORIZED	$ 97,448.00
ACTUAL COST INCURRED TO DATE(2)	97.448.00
ESTIMATED COST TO COMPLETE:(3)	
1st MONTH FOLLOWING "PERIOD ENDING" as specified above	
2nd MONTH	
3rd MONTH	
4th MONTH	
5th MONTH	
6th MONTH	
BALANCE OF FISCAL YEAR(4)	
SUBSEQUENT FISCAL YEARS	
TOTAL ESTIMATE TO COMPLETE	
TOTAL ESTIMATED COST AT COMPLETION	$ 97,448.00

NOTES:

1) Last full month for which actual costs are available.

2) Cost includes applicable fee.

3) Estimates for costs to be incurred (Do not include commitments), including applicable fee.

4) Fiscal year is 10/1 through 9/30. Balance of fiscal year means all months remaining in the fiscal year following the 6th month shown on the line above. If the 6th month is September, then balance of fiscal year is 10/1 through 9/30 of the next fiscal year.

Contractor (name and address)	Signature of Contractor's Representative, Date and Phone
Georgia Tech Research Corporation School of Electrical Engineering Georgia Institute of Technology Atlanta, GA 30332	Pam Majors, Research Adm. 404-894-7337 4/15/89

5432-CS(1-85)

GEORGIA INSTITUTE OF TECHNOLOGY
SCHOOL OF ELECTRICAL ENGINEERING
ATLANTA, GEORGIA 30332

TELEPHONE: (404) 894-

May 9, 1989

Mr. J. Gee
Sandia National Laboratories
P. O. Box 5800
Albuquerque, NM 87185-5800

Re: Contract No. 57-6152
Project Director: A. Rohatgi

Dear Mr. Gee:

Enclosed please find the Monthly Technical Progress Reports for the periods 12/17/88-1/16/89 and 1/17-89-2/16/89 on the above referenced contract.

If you have any questions, please feel free to contact me.

Sincerely,

Pam Majors
Research Administrator

pm
Enclosure

Texture

Texture is a 3 dimensional ray tracing program designed to provide the solar cell community with a method to quantitiatively describe the enhancement in absorbed flux for various surface texturing. The program is designed to run on an IBM-pc compatible computer, an optional co-processor is recommended. The program is intended to be a companion to PC-1D version 2. A one dimensional generation profile can be output in the proper format to be easily incorportated into PC-1D, this will only be valid if the surface texturing is small. In addition, Texture uses the same absorption or material files as PC-1D version 2. Options within the program allow for three modes of operation. The first is a full 3 dimensional response to the incoming light. The second is again a 3 dimensional response to the light but a reduction to a one dimensional generation profile. The last option is a qualitative mode which provides characterizing information. Output from Texture includes a generation profile, all of the material information entered (for cataloging), and the amount of photons lost due to all surfaces and structures. In the qualitative mode the output includes the average path length, the number of rays remaining after each pass, the number of rays that re-enter, and other information.

At the start of each run you will be asked a number of questions concerning the mode of operation, typical options are

as follows; material parameters, cell structure, grid lines, angle of incidence of the light, files for index of refraction and reflection as a function of wavelength, and the number of photon packets to be followed. Each of the options will be explained in detail in the following paragraphs. First an explanation of how the program works is in order.

The incoming light is broken up into different wavelengths and energy, these are determined from the spectrum and incident energy that you have chosen. The number of photons is determined from this information. The number is then divided by the number of rays that you would like to trace. The more rays traced the longer the execution time, but the more accurate the answer. When these rays are incident upon a surface some photons are reflected while others penetrate. Those that enter the structure are broken down further into an exponentially decreasing profile which is followed until all of the photons are absorbed or lost out the front or sides of the structure. Those photons which are reflected are followed until they strike a surface or it is determined that they will never enter the cell. Those photons which are refracted from within the cell in an outward direction are followed in the same manner as a reflected ray.

The angle of incidence is an input variable which the user is allowed to specify. Two random numbers are generated to determine where on a plane located just above the cell structure the ray strikes. If a cover glass option is chosen the top of the glass is the plane. If no cover glass is in place the plane is located at the thickness of the cell plus the height of the

front structure, figure 1. If the front surface is a flat plane then no further modification is required. If the surface is textured then a routine is called which will determine exactly where the ray strikes the surface. When more rays are traced in this manner then more of the cell surface is sampled to determine its effect on the incoming light.

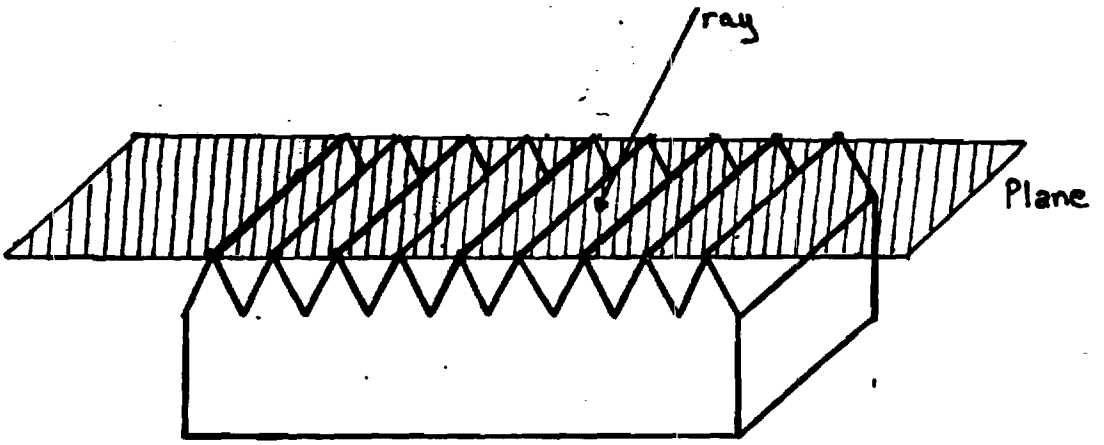

The incoming ray which contains x#-photons, is now broken up into two distinct rays. The first carries FSR*x#-photons, where FSR is the front surface reflection factor for the wavelength in question. This ray will be reflected from the surface and followed until a surface is encountered or it escapes completely from the cell structure. The second ray carries (1 - FSR)*x#-photons and is intended to enter the cell. This ray will be refracted upon entering the cell. The angle of refraction will depend upon the incident angle, the wavelength of the radiation, the index of refraction of the first material, and the index of refraction of the second material. The absorption coefficienct of the material at the wavelength in question will be obtained from a separate routine. A distance of 30* will be used as a

stopping criteria for the rays. The distance $30*1/\alpha$ will allow for absorption of virtually all of the photons. If the number of photons in a ray is less the exp(30) then the distance is truncated to a smaller value. If the incident flux is so high that the number of photons associated with a ray is greater than exp(30) then a slight error will be introduced into the calculations. This can be remedied by tracing more incoming rays with less intensity associated with each ray.

Once the ray has entered the cell and the direction is determined, the point where the ray hits the structure again is found. This is done by first checking to see if the ray rehits the front surface. If it does not rehit the front, it must be going towards the back. But before it hits the back there is the possiblity that it could hit the side of the cell, and this is also checked. If it does not hit the side then the point where it hits the back is found. Now two points are available, the point of incidence and the new point. The distance between the two points is found and checked to see if any of the photons could have been absorbed in this distance. If any are absorbed, the the position along the axes where absorption takes place is recorded along with the number absorbed. This is how the generation profiles are obtained. The ray is then reflected and its next intersection with a surface is found.

The process will continue until all of the photons are absorbed or leave the structure and can not re-enter. At this time a new ray is started and the whole process is repeated until all packets are traced. Then the next wavelength is

treated in the same manner.

Input Values

This section will describe the input values and options for the user. The questions in the program are fairly self-explanatory.

The first input encountered will be for the option of a cover glass. Since most cells today incorporate some sort of encapsulant material this is a necessary option for real cell simulation. If a cover glass is chosen then the program will prompt for the file containing the index of refraction as a function of wavelength. If a static index of refraction is to be used then no file need be given. The next prompt will be for cover glass texturing. This option is mainly for thin cells deposited on glass substrates where the front surface has been mechanically textured, it may also be useful for other applications. The back surface of the cell will be assumed to be flat, but an encapsulating material will be assumed to fill the spaces between the plate and the cell. The final input for the cover glass will be its thickness.

The second input is the front structure of the cell. Currently there are 4 available choices:

1) flat
2) slats in the x direction
3) pyramids (four sided figures, fifth side down)

4) tetrahedrons (three sides, fourth side down)

The basic structures and distances which can be specified are shown in figure 2. Notice that none of the characteristics imply any dimensions. These will be determined at a later time. A structure is determined by inputing the integer preceding the description. A note must be placed here concerning certain structures. In most cases a choice of front structure will have no bearing on the choices or dimensions of the back structure. Only in the case when the back structure is chosen to be positive slats in the x direction and the thickness of the cell is less than the height of the slat, will there be a problem. This situation will not be allowed, and the user will be prompted for new values of the dimension of the structure.

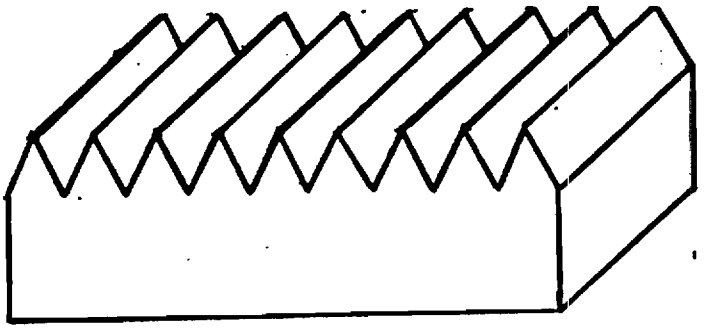

Orthographic projection of a surface textured with slats.

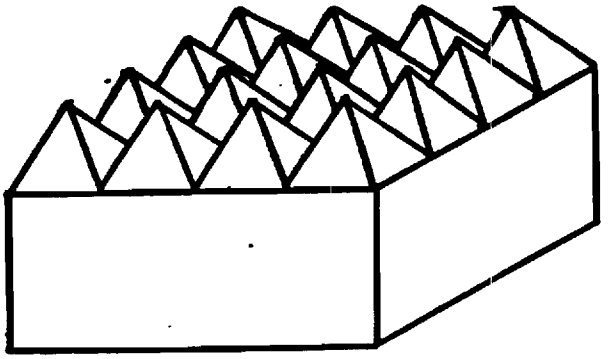

Orthographic projection of a surface textured with pyramids.

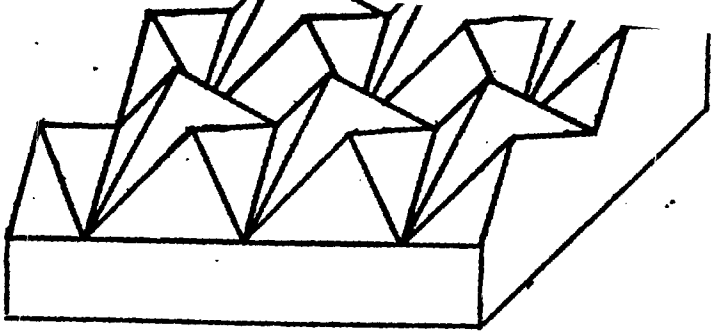

Orthographic projection of a surface
textured with tetrahedrons.

Once the strucure is chosen, questions will be asked concerning the dimensions of the sturcture. Enter all values in microns and as positive values!! Figure 3 contains diagrams concerning all the data tha can be entered for each structure. Different values can be entered at any point allowing for an infinite number of structures to be modeled.

See next page

The next input will control the structure of the back surface. As in the structure of the front surface the choice is made by selecting the appropriate integer. Currently these are the back sturctures supported:

1) flat
2) slats in the x direction
3) slats in the y direction

4) pyramids

5) positive slats in the x direction

6) tetrahedrons

Figure 4 shows the possible configurations. Again note that no dimensions are given, these will occur in the next question. Remember the choice of the back structure is independent of the choice of the front structure.

Similar to Front

Once the back structure has been determined the program will ask for the important dimensions of the structure. Input the dimensions in microns and as positive values, the program will do any interpretation of the values!!

The next input is for the thickness of the cell. Do not include the thicknesses of the front or back structure, these are already taken into account. The values of various thicknesses is shown in figure 5. At this point the structure dependence will take effect. If the back structure is positive slats in the x direction and the height is greater than the thickness then an error will occur for any front structure other than slats in the x direction. Even so, if the lengths of the front and back structure are not the same an error will occur and you will be returned to the front structure input menu. A very thin cell

will produce a longer execution time because of the amount of time to produce refraction routines and check all of the possible combinations of where the ray could go. The ray will tend to leave the cell more often and therefore produce more reflected rays which must be traced.

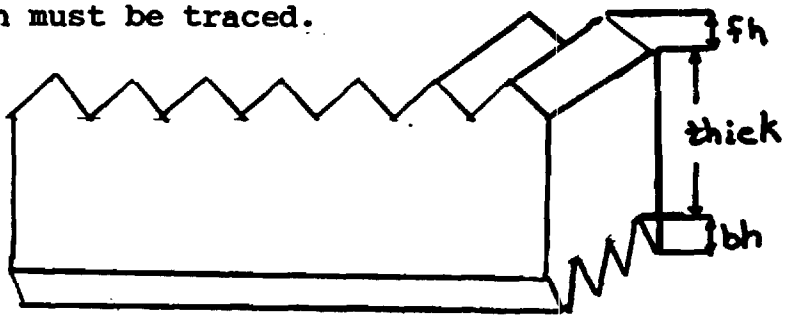

The next input is for the number of rays to be traced at each wavelength. A large number here will produce a long execution time due to the amount of work in tracing each ray. The number of photons traced in each ray will be given by the formula

$$X\#\text{-photons} = (\text{energy}*\text{lamda})/(q*1.2399*\text{number of rays})$$

It can be clearly seen that the more rays traced, the closer the solution is to the exact solution, therefore; there is a compromise between the speed of solution and the accuracy. Only for cells with both flat front and back structures will it be appropriate to follow only one ray at each wavelength.

The next input is to chose whether to use a file which contains the reflection and index of refraction data. If a file is used then the program will read the file and use the data. The file should contain values for the whole range of wavelengths

in the spectrum to be used. The wavelengths do not have to match exactly with the spectrum file. Interpolation using cubic splines will be used to determine values at the wavelengths required. If no file is given then the program will prompt the user for the front surface reflection factor, the static index of refraction of the semiconductor, and the static index of refraction of the outer medium, a value of 1.0 implies no bonding material.

The grid line option is the next input. If no grid lines are required then input "no". If grid lines are needed then the number of lines required is asked first. Then the program will prompt for the (X,Y) coordinate of the lower left corner of the grid line. The program will then prompt for the (X,Y) coordinate of the upper right corner of the grid line. This will produce a grid line similar to figure 7. At this time only grid lines parallel to the axes are supported. If a ray strikes a grid line from the inside of the cell then it will be internally reflected, with some loss in intensity regardless of the angle of incidence. If a grid line is struck on the outside of the cell then the ray is treated as if it were a reflected ray, again with some loss in intensity. The absorption which takes place at a grid line depends upon the metal forming the grid. The next two inputs are for the effectiveness of reflection from the grid lines. The first is for the ray that is external, this value will usually be close to one since silver is used as the top of

the grid line. The second input is for rays internal to the cell. This value will be closer to 0.8, because the reflectivity of titanium is lower than for some other metals.

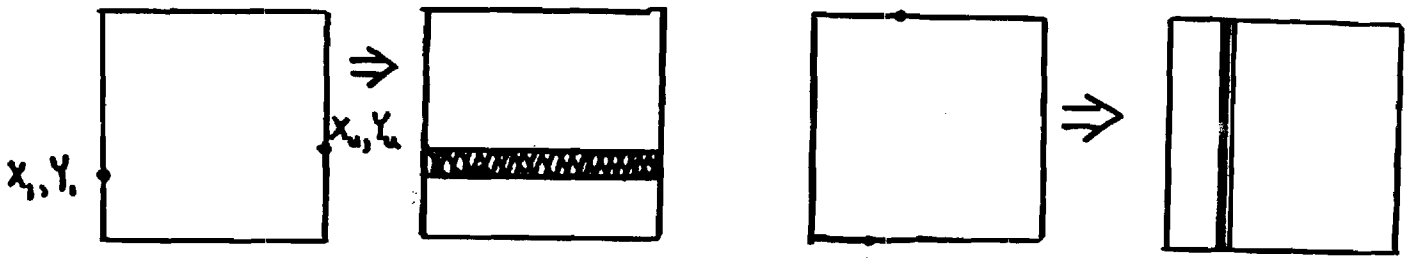

The angle of incidence of the incoming light is specified with the next input. Changing from normal incidence will produce a longer execution time because the initial contact point of the ray and the structure must be calculated. This option allows the user to determine the degradation/enhancement of the cell in question due to tracking errors or stationary configurations. The angle of incidence must be given in direction cosines of the angle. That is normalized to one as will be explained later.

The next input is for the spectrum to be used. Since these cells may be used in any application most common spectrums are supported. The spectrum files from PC-1D version 2 are the best examples. Or the user can create orginal spectrum to match specific applications.

The energy density of the incoming ray is the next consideration. The user is allowed to specify the exact energy

distribution for the spectrum. This will allow for concentration systems to be modelled or attenuation of energy due to atmospheric conditions to be modelled.

The final input is the material file which will contain either the absorption as a function of wavelength or the values for the internal model absoprtion for the material in question. Again a PC-1D version 2 material file is supported or the user can make a custom file.

Theory of Operation

The formulas used in the derivation are as follows.

The equation of a line is given by

$$\frac{X1 - X0}{CALF} = \frac{Y1 - Y0}{CBET} = \frac{Z1 - Z0}{CGAM}$$

Where X1, Y1, and Z1 are the coordinates of the new point and X0, Y0, and Z0 are the coordinates of the inital point. Calf, Cbet, and Cgam are the direction cosines of the line.

The equation of a plane is given by

$$\frac{X}{a} + \frac{Y}{b} + \frac{Z}{c} = 1$$

Where a, b, and c are the intercepts of the x,y, and z axes respectively. The direction cosines of the normal of the plane would be given by

$$\text{Calfn} = \frac{a}{\sqrt{a^2+b^2+c^2}}$$

$$\text{Cbetn} = \frac{b}{\sqrt{a^2+b^2+c^2}}$$

$$\text{Cgamn} = \frac{c}{\sqrt{a^2+b^2+c^2}}$$

The main idea of the program is to find the intersection of the line (ray) and the plane of the cell structure.

The first step is to constrain the ray into a fixed area. In this fixed area the only planes the ray may hit are determined by the structure of the cell. This is called normalization. The point of intersection is found and translated into normalized coordinates and then translated back to the structure. The following example and figure 8 should help the explanation. If the ray is traveling from the front of the cell towards the back then the point of intersection of the line and the x-y plane located at z = 0 is found. Then using the coordinates of the point and the characterizing distances of the back structure the point is translated to a new coordinate system. This new coordinate system will have its origin located at the peak of the structure, and all other points will be referenced to this point. The following formulas are for slats running in the x direction.

The value of XN is between -bl(1) and bl(2), with XOFFSET given by an integer multiple of (bl(1) + bl(2)). For slats running in the y direction the results would be similar with just a replacement of y for x. The normalzation of the pyramid structure on the back surface would be given by

The normalized structures are diagramed below.

These structures will be used to find the point where the ray strikes. This is done by checking all of the distinct planes in

the structure. To ensure that the program does not repeat calling the same plane over and over, and to save time, the routine does not consider the plane of origin. This can be done because a ray cannot rehit the same plane without hitting another plane first. If the ray does not strike any of the planes in the region given by the normalized contraints then it must be heading towards the opposite surface.

If the ray is heading towards the opposite surface then there is the possibility that it will strike a side before arriving. This alternative is accounted for. If the ray does strike the side and the angle of incidence is such that the ray is coupled out of the cell then this energy is lost. If the ray is reflected the new direction is found and tracing continues.

Once the new point is found the angle of reflection or refraction must be found for the ray to continue. The normal of the surface is found from the side of the structure that the ray strikes. Then the direction numbers of a line perpendicular to both the surface normal and incident ray is found. This is done by taking the cross product of the direction cosines, between the surface normal and incident ray.

incident ray surface normal = abc-line

aa = Cbet*Cgamn - Cbetn*Cgam

bb = Calfn*Cgam - Cgamn*Calf

cc = Calf*Cbetn - Calfn*Cbet

The reflected/refracted ray will also be perpendicular to this line. This will produce the first condition on the reflected/refracted ray. This condition is given by the dot

product of the reflected/refracted ray and the line given by aa, bb, and cc. Because the lines are perpendicular, their dot product is zero.

$$0.0 = aa*Calfr + bb*Cbetr + cc*Cgamr$$

It is also known that since the surface normal and the incident ray are unit vectors then the dot product of the two vectors is the cosine of the angle between them (angle of incidence)

$$Cos(\Theta_i) = Calf*Calfn + Cbet*Cbetn + Cgam*Cgamn$$

For the case of a reflected ray and the surface normal this expression is also valid since the angle of reflection is equal to the angle of incidence.

$$Cos(\Theta_r) = Cos(\Theta_i)$$
$$Cos(\Theta_i) = Calfr*Calfn + Cbetr*Cbetn + Cgamr*Cgamn$$

This is the scond condition on the reflected ray. The third and final condition is also given by the knowledge that the angle of incidence is equal to the angle of reflection. Then the angle between the incident and refected ray is twice this angle.

$$Cos(\Theta_{i+r}) = Cos(2\Theta_i)$$
$$Cos(2\Theta_i) = Calfr*Calf + Cbetr*Cbet + Cgamr*Cgam$$

This leads to a system of three equations with 3 unknowns, (Calfr, Cbetr, and Cgamr), which must be solved simultaneously.

$$0.0 = aa*Calfr + bb*Cbetr + cc*Cgamr$$

$$\cos(\Theta_r) = Calfr*Calfn + Cbetr*Cbetn + Cgamr*Cgamn$$

$$\cos(2\Theta_i) = Calfr*Calf + Cbetr*Cbet + Cgamr*Cgam$$

In the case of the refracted ray the first condition is the same. For the second condition the knowledge of Snell's refraction law must be employed.

$$\frac{\sin(\Theta_i)}{\sin(\Theta_r)} = \frac{\eta_r}{\eta_i}$$

$$\cos(\Theta_r) = \cos\left(\arcsin\left(\sin(\Theta_i)* \frac{\eta_r}{\eta_i}\right)\right)$$

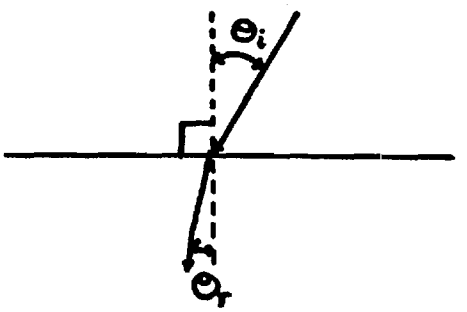

Then the second condition would be given by

$$\cos(\Theta_r) = Calfr*Calfn + Cbetr*Cbetn + Cgamr*Cgamn$$

Which is the dot product between the normal and the refracted ray. The third condition is the angle between the incident ray and the refracted ray. This would be given by

$$\cos(\theta_{r1}) = \cos(\arccos(\theta_r) + \arccos(\theta_1))$$

Where

$$\cos(\theta_1) = Calf*Calfn + Cbet*Cbetn + Cgam*Cgamn$$

These three conditions lead to the following 3 equations in Calfr, Cbetr, and Cgamr. (In this case these are refacted angles)

$$0.0 = aa*Calfr + bb*Cbetr + cc*Cgamr$$
$$\cos(\theta_r) = Calfr*Calfn + Cbetr*Cbetn + Cgamr*Cgamn$$
$$\cos(\theta_{r1}) = Calfr*Calf + Cbetr*Cbet + Cgamr*Cgam$$

Solving the appropriate system for the ray in question gives the new direction for the ray to follow.

The absorption coefficient is found in the same manner as in PC-1D. As either a function of the wavelength or an interpolation between two input values. The maximum possible distance the ray can be followed is $30*(1/\alpha)$ in microns. This would lead to a reduction in the photon number by approximately 10^{-15}, as given by

$$I = I_o*\exp(-30)$$

If the simulation is to model a concentrator design then sufficient rays must be input so that the starting intensity of

each ray is less than 10^{15}. Otherwise a significant portion of the light might not be accounted for. The distance 30*(1/€) is used only as a stopping criteria, so the ray is not followed to long. The number absorbed is found at each node by calculating the number of photons that could be absorbed between it and the next lower node. The intensity is then lowered by this amount and the absorption at the next node is calculated. This is continued from the incident point to the new point of intersection. Then by knowning the distance the ray has traveled, given by the distance formula

$$\text{distance} = \sqrt{(X0 - X1)^2 + (Y0 - Y1)^2 + (Z0 - Z1)^2}$$

and the incremental distances, if the distance is greater than the incremental distance then a portion of the ray is absorbed. The coordinate of absorption is noted and the absorbed intensity in the incremental volume is increased by the amount absorbed.

If a ray strikes a grid line or a non-perfect rear surface reflector then the intensity of the light remaining in the ray is decreased by the loss due to the metal absorption. This is similar to the treatment the ray receives when it is coupled out of the side of the cell. In that case though, all of the remaining intensity is lost. In all the cases, counters are incremented to tell the user exactly how much energy is lost due to each phenomena. This is done to aid in the design of even better cells by pointing out areas where the most improvement may be obtained.

Program Output

The output of the program will depend upon which mode of operation was selected by the user. The basic output will contain the cell structure used, with the dimensions, the files or static numbers for material parameters, the spectrum chosen, and the mode dependent data.

The cell structure will be listed from the top to the bottom of the cell. If the cover glass was present then the structure, thickness and the other dimensions will be output first. Then if a file was chosen for the index of refraction and reflection its name will be output, otherwise the static number will be ouput. The structure and its parameters for the front surface will come next in the output. To be followed by the back surface numbers. Then the file or static numbers for the semiconductor will be presented.

If the grid option was chosen the beginning and ending points of the grid will be ouput in the following form

X_{ll} Y_{ll} X_{ur} Y_{ur}

Then the outer reflectivity will be given along with the number of photons which were absorbed due to this grid. The inner reflectivity values will be given in a similar manner.

The name of the spectrum file will be given next in the output file with the energy density that the user requested. If the program was run in the distance mode then the energy density will not be given. If the program was not run in the distance mode then the next values output will be the cumulative number of

photons absorbed and the maximum number that could be absorbed. This maximum number is calculated by finding the number of photons available at each wavelength where is absorption coefficient is non-zero.

If the program has been run in the distance mode then the next ouput is the percent rays remaining as a function of the number of passes through the cell. Two sets values will be given, the first is for rays that are counted only until they exit the cell. The second set of numbers is for rays that have exited the cell but by either reflection or refraction re-enter the cell. These numbers will be higher because they include the rays from the first case. The last two values will be the total average distance the ray traced before exiting the cell. These values divided by the thickness of the cell give the relative impovement of the cell structure over a flat cell of the same dimensions. The last output value for this case is the average reflectivity of the surface. This value is found by R^n where n is the number of bounces, the number of times a refected ray can strike the surface before it is lost out of the cell.

If a one dimensional profile mode was the option chosen then the output will consist of the cumulative and actual absorption which takes place at each node. In addition the ouput will contain the number of photons lost due to refraction out the sides of the cell, the front of the cell, and the number lost out the back of the cell.

In a three dimensional mode the ouput will consist of cumulative absorption on a small normalized X-Y plane at a

constant Z value. Since these are really a four dimensional plots there will be values at each value of Z where a node was placed.

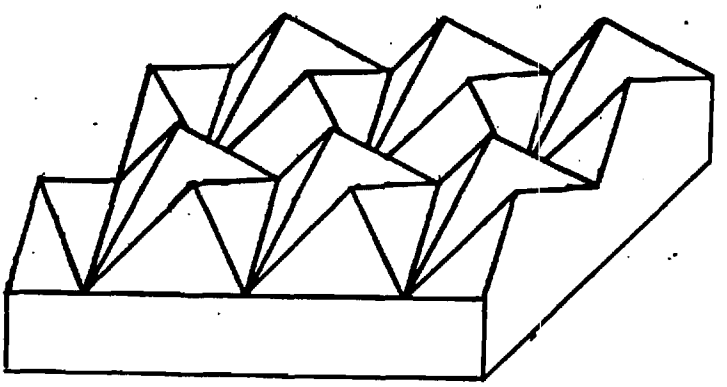

Orthographic projection of a surface textured with tetrahedrons.

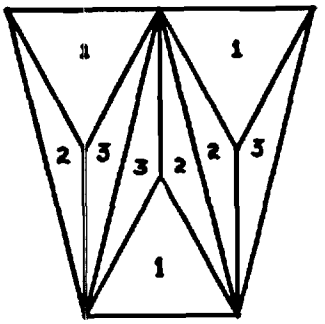

X-Y trace of several tetrahedronds with the distinct planes numbered.

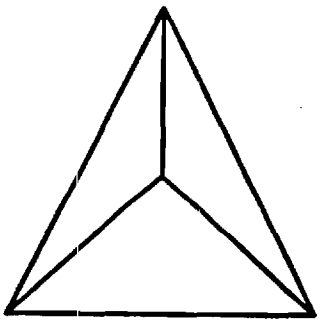

X-Y trace of a single tetrahedron, with the distinct sides shown.

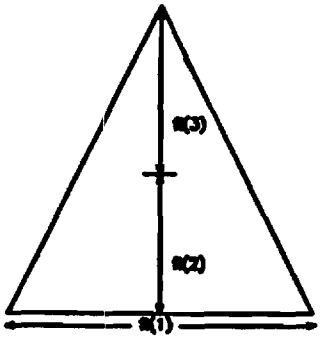

Plot of X-Y plane for a single tetrahedron with three of the user adjustable dimensions shown. Note: peak center located at f1(1)/2.

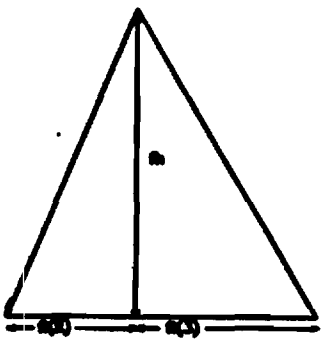

X-Z trace of the tetrahedron showing the relationship between the two user adjustable X dimensions and the height.

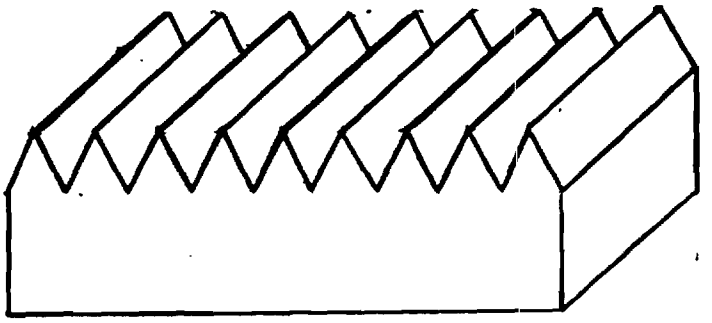

Orthographic projection of a surface textured with slats.

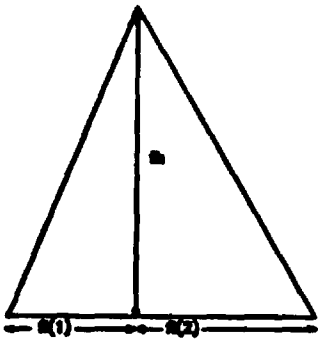

Plot of an X-Y plane trace of a slat. The three user adjustable parameters are clearly shown.

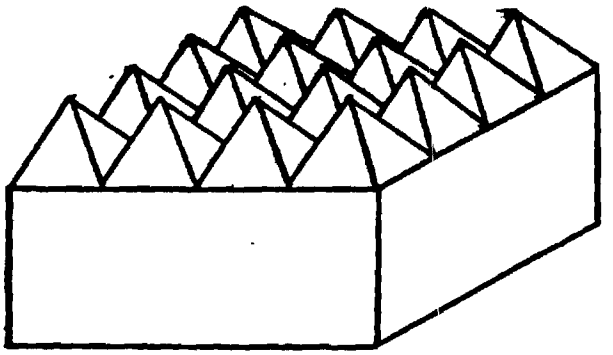

Orthographic projection of a surface textured with pyramids.

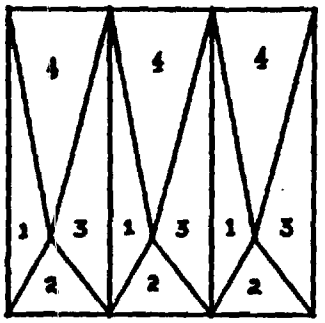

Looking down on X-Y plane of a surface textured with pyramids. Distinct sides are numbered.

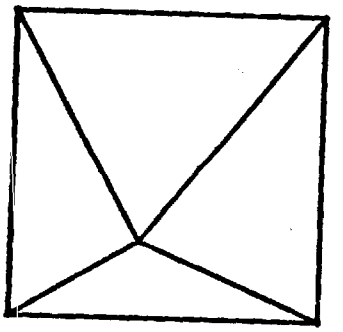

Plot of X-Y plane of a single pyramid with the four distinct planes shown.

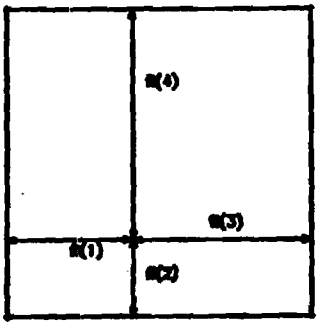

Plot of X-Y plane of a single pyramid showing the four dimensions that are user adjustable.

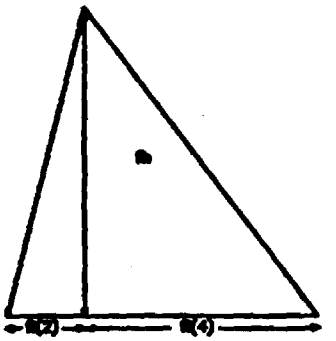

Y-Z trace of a pyramid showing the relationship between the height and the Y variables.

GEORGIA INSTITUTE OF TECHNOLOGY
SCHOOL OF ELECTRICAL ENGINEERING
ATLANTA, GEORGIA 30332

TELEPHONE: (404) 894-

May 9, 1989

Mr. J. Gee
Sandia National Laboratories
P. O. Box 5800
Albuquerque, NM 87185-5800

Re: Contract No. 57-6152
Project Director: A. Rohatgi

Dear Mr. Gee:

Enclosed please find the Monthly Technical Progress Reports for the periods 12/17/88-1/16/89 and 1/17-89-2/16/89 on the above referenced contract.

If you have any questions, please feel free to contact me.

Sincerely,

Pam Majors
Research Administrator

pm
Enclosure

The Effect of Deep Levels on Minority Carrier Lifetime in n-Type GaAs and Their Influence on Solar Cell Design

S. A. Ringel and A. Rohatgi
School of Electrical Engineering
Microelectronics Research Center
Georgia Institute of Technology
Atlanta, Georgia 30332-0250

ABSTRACT

In most n-type GaAs grown today, Shockley-Read-Hall recombination controls the minority carrier lifetime at doping levels below ~1 x 10^{18} cm^{-3} and is commonly assumed to be independent of trap characteristics and doping concentration. It is shown here that various realistic combinations of deep level location and cross section can result in orders of magnitude fluctuations in lifetime values. In addition, deep levels which reside within 0.4 eV from the valence band edge and 0.3 eV from the conduction band edge can make the lifetime a strong function of doping concentration in the material resulting in large variations in lifetime values as a function of deep level position within the GaAs bandgap. This has important ramifications for GaAs devices such as solar cells where optimized design and performance depends on assumed lifetime values. It is demonstrated experimentally that a trap located at E_v + 0.25 eV in a p/n GaAs heteroface cell reduced the AM 1.5 one sun cell efficiency from a projected value of ~24.5% to an observed value of 20.9%. An alternative design is proposed which utilizes a thin base, thin buffer, and back surface passivation and makes the cell performance relatively insensitive to the trap. Furthermore, this modified cell design can also result in one sun efficiencies over 25% for moderate lifetime values (20 ns) reducing the need for very high quality GaAs for high efficiency devices.

1. INTRODUCTION

The bulk minority carrier lifetime in compound semiconductors such as GaAs is a crucial parameter for obtaining optimum performance in optoelectronic devices such as solar cells, lasers, and LEDs. The optimum design of such devices requires a knowledge of the minority carrier lifetime dependence on deep level position and dopant concentration. While the effects of Auger[1,2] and radiative[3,4] recombination on the minority carrier lifetime have been well documented both experimentally and theoretically in the literature, relatively little has been done concerning the influence of the defect-specific Shockley-Read-Hall (SRH) lifetime on the overall minority carrier lifetime and device performance. This is in part due to earlier published experimental data which showed that the minority carrier lifetime in GaAs was constant below a doping concentration of ~1 x 10^{18} cm^{-3} for n-type material[5] and below ~ mid 10^{17}'s for p-type material[6]. However, other published experimental data showed a strong doping dependence of minority carrier lifetime down to a doping level of ~2 x 10^{15} cm^{-3} in LPE-grown GaAs where only defect induced (SRH) recombination is important[7]. This scatter in the reported lifetime values for different growth and preparation techniques can only be attributed to different defects and possible domination of SRH recombination because intrinsic recombination mechanisms such as Auger and radiative processes are independent of growth technique. This paper shows that exact knowledge of lifetime variation with deep level position and doping concentration is critical for optimum device design since much of the design criteria is centered about assumed lifetime behavior.

In this paper, GaAs heteroface solar cells are used as an example to show the impact of the SRH lifetime on device performance and design optimization

for various deep level positions and trap parameters. First, a theoretical calculation of the doping dependence of the SRH lifetime in n-type GaAs is performed for different quality GaAs as a function of the position of deep levels within the bandgap. Then the effects of the deep level position and cross-section on the performance of p/n heteroface GaAs solar cells are revealed with the help of the PC-1D device modeling program.[8] It is shown how cell efficiency can be severely miscalculated, and device structures erroneously designed if certain deep levels are present and not properly accounted for. Some of these effects were also experimentally validated by performing Deep Level Transient Spectroscopy (DLTS) measurements on GaAs heteroface solar cells whose efficiency was found to be limited by the observed deep level. Finally, some novel heteroface cell designs are proposed, utilizing a thin base and thin passivated buffer, which not only make the cell performance relatively insensitive to deep level position but also result in somewhat higher efficiencies than the conventional thick base (2-3 μm) designs.[9,10] It is shown that only when the lifetime reaches its intrinsic (fundamental) limit does the conventional thick base cell efficiency surpass the thin base cell efficiency.

2. LIFETIME CALCULATIONS

The minority carrier lifetime in GaAs was calculated as a function of doping concentration according to

$$\frac{1}{\tau} = \frac{1}{\tau_{SRH}} + BN + CN^2 \qquad (1)$$

where C is the Auger recombination coefficient and B is the radiative recombination coefficient. Calculations were made for both n and p-type GaAs, however, only the n-type case is considered here since the heteroface solar cell structures to be discussed later utilizes an n-type base. For n-type GaAs, $C = 1.60 \times 10^{-29}$ cm^6/sec over the entire doping range.[1] However, B is not constant due to the Burstein shift[3,11] in n-type GaAs. This doping dependence of B[3,11] was accounted for in our model calculations. The SRH lifetime under low level injection, and with the trap concentration much smaller than the doping concentration, can be expressed as[12]

$$\tau_{SRH} = \frac{\tau_{no}(p_o+p_1) + \tau_{po}(n_o+n_1)}{n_o + p_o} \tag{2}$$

where

$$\tau_{no} = (\sigma_n N_T v_{TH})^{-1} \tag{3}$$

$$\tau_{po} = (\sigma_p N_T v_{TH})^{-1} \tag{4}$$

$$n_1 = N_c \exp\left[\frac{(E_T-E_c)}{kT}\right] \tag{5}$$

$$p_1 = N_v \exp\left[\frac{(E_v-E_T)}{kT}\right] \tag{6}$$

The total minority carrier lifetime was calculated as a function of doping concentration from Eq. (1) for different deep levels specified by their characteristic values of τ_{no}, τ_{po}, and E_t. The values used for these parameters were chosen within the observed range of values reported in the literature[13,14] for both n and p-type GaAs.

3. DEVICE MODELING

In order to reveal the impact of deep levels on device performance, solar cell characteristics were calculated using the PC-1D device modeling program, described elsewhere,[9,10] with appropriate material and cell dimensional parameters. The effects of deep levels were taken into account by modifying the lifetime profile throughout the device structure according to the doping dependence of lifetime determined from Eq. (1) assuming that the particular deep level under consideration exists uniformly in the base and buffer regions. All simulations were performed under one sun AM 1.5 conditions.

4. EXPERIMENTAL

To support some of the theoretical findings by experimental results, p on n heteroface solar cells (Figure 1) were fabricated by the MOCVD technique and only those devices with poor performance (18-20% efficiency rather than ~23%) were selected for analysis. The minority carrier diffusion length and lifetime in the n-base of these low efficiency cells was estimated from the measured internal quantum efficiency.[15]

In order to reveal the traps which limit the lifetime in the selected low efficiency devices, DLTS measurements were performed. Fifty mil diameter mesa dots were formed using Au/Zn for ohmic contacts on the p-type front surface, and Au/Ge ohmic contacts on the back. DLTS measurements were made using an automated wafer analyzer system which obtains data via a lock-in amplifier type setup. The output signal was integrated and analyzed using five different weighting functions. The activation energy of the trap, ΔE, was found from the slope of the Arrhenius plot of $\log(T^2/e_m)$ vs $1000/T$ where the trap emission rate, e_m, is given by

$$e_m = N_v \sigma v_{TH} \exp\left[\frac{-\Delta E}{kT}\right] \quad (7)$$

and the terms in Eq. (7) have their usual meaning.[16]

5. RESULTS AND DISCUSSION

5.1 Effects of Deep Levels on Lifetime Vs Doping Behavior in n-Type GaAs

An assessment of the effects of deep level position on the minority carrier lifetime was made by plotting Eq. (1) for various deep levels. Selected examples in Figure 2 show lifetime vs doping plots for four possible scenarios depending upon starting material quality and position of the deep level. Figure 2a represents the doping dependence for GaAs technologies that can produce starting lifetimes in the range of 46 ns to 1 μs at a doping concentration of 1×10^{14} cm^{-3}, regardless of the deep level position. The former represents commonly observed lifetime values for n-type GaAs,[5-7] while the latter represents the highest lifetime for GaAs reported in the literature.[17] Model calculations in Figure 2b represent another scenario in which the lifetime ranges from 4 ns to 230 ns but at a starting donor concentration of 1×10^{16} cm^{-3} instead of 1×10^{14} cm^{-3} (Figure 2a). Each curve describes the net lifetime for a material which has a given trap location within the bandgap and constant values of τ_{no} and τ_{po} (which are assumed to be equal and will be referred to as τ_o) over the entire doping range. It is important to realize that, in Figures 2a and 2b, the value of τ_o was calculated from Eqs. (1) and (2) for each curve from the assumed deep level, and the lifetime and doping concentration at the starting point.

In most n-type GaAs available today, the radiative and Auger lifetimes do not appreciably limit the net lifetime below ~1 x 10^{18} cm^{-3} because the combined contribution of the Auger and band-to-band recombination processes to the lifetime is much greater than the total lifetime. Hence, SRH recombination generally dictates the lifetime behavior. Model calculations in Figure 2 indicate that the lifetime is very sensitive to small changes in deep level position for traps residing less than ~0.4 eV from the valence band edge and ~0.3 eV from the conduction band edge. Between these values, the lifetime behaved as if the trap was located at midgap, i.e. independent of doping concentration and equal to τ_o, until the onset of intrinsic (Auger and radiative) recombination processes. The observed kink in the lifetime curves near 5 x 10^{17} cm^{-3} for the highest lifetime curves is due to the Burstein shift effect in the radiative lifetime which partially limits the net lifetime in the high quality materials. If the trap position is now moved to 0.25 eV above the valence band edge, the lifetime shows a strong initial doping dependence up to a doping concentration of ~1 x 10^{16} cm^{-3} and then flattens out at the value of τ_o when the denominator of Eq. (1) offsets the increase in the numerator due to p_1, Figure 2a. Finally, at higher doping, the lifetime begins to decrease again due to the Auger limit. Notice that the influence of trap location is much less pronounced for the cases shown in Figure 2b because the starting point is shifted to N_d = 1 x 10^{16} cm^{-3}.

Thus the knowledge of trap location induced doping dependence could be very important for the design of lightly doped devices (< 1 x 10^{16} cm^{-3}). Even more significant is the fact that the absolute value of lifetime at any given doping concentration (Figure 2) can be orders of magnitude different depending upon the combination of the trap location and the nature of the trap

dictated by $\tau_o = (\sigma N_T v_{TH})$. This will influence the optimum design of both lightly and heavily doped devices. The effect of trap location on deviced performance is quantitatively demonstrated in the following section by fabricating and carefully analyzing selected GaAs solar cells.

5.2 Effect of Deep Levels on the Performance of Conventional Thick Base Cell Designs

Figure 1 shows the device structure of a conventional GaAs p/n heteroface cell fabricated by the MOCVD technique. Based on our model calculations, this design was expected to yield high cell efficiencies (23-24%) assuming base lifetimes of 15-20 ns, but the selected experimental device showed a one sun efficiency of only 18.9%, J_{sc} = 22.11 mA/cm^2, and V_{oc} = 1.006 V. The minority carrier lifetime was estimated to be ~3 ns from the measured internal quantum efficiency and using D_p = 4.5 cm^2/s.[18] Using this lifetime in conjunction with an FSRV (front surface recombination velocity at the $Al_{.9}Ga_{.1}As$/p-emitter interface) of ~1.0 x 10^5 cm/s and a BSRV (back surface recombination velocity at the n-base/$Al_{.2}Ga_{.8}As$ interface) of ~1 x 10^3 cm/s, we were able to match the measured and calculated cell data. The calculated efficiency from the PC-1D model was 18.8% with a J_{sc} of 22.11 mA/cm^2 and a V_{oc} of 1.010. Even by lowering the observed high surface reflectance (~20%) to 5% in this cell, and further passivating the heteroface so that FSRV = 1 x 10^4 cm/s, the calculated efficiency for this cell could reach only 20.90%, which is well below the expected performance of 23-24%. This indicates that the low base lifetime is limiting this cell efficiency.

To determine the cause of the 3 ns lifetime, DLTS measurements were performed on this 18.9% cell. Figure 3 shows the DLTS spectrum along with the

associated Arrhenius plot. A hole trap located at E_v + 0.25 eV with a trap density of 4 x 10^{13} cm^{-3} was detected within the n-type base. Model calculations in Figure 2a show that an E_v + 0.25 eV trap can result in a 3 ns lifetime at N_d = 8 x 10^{17} cm^{-3} if the starting lifetime is 46 ns at a doping of 1 x 10^{14} cm^{-3}, curve 1. Alternatively, Figure 2b reveals that a material with a starting lifetime of 4 ns at a doping of 1 x 10^{14} cm^{-3} and an E_v + 0.25 eV trap can also result in a 3 ns lifetime at N_d = 8 x 10^{17} cm^{-3}, curve 3 (other possibilities exist as well). From curves 1 and 3, it can be seen that for this shallow trap little or no increase in lifetime (hence cell improvement) can be gained by lowering the base doping concentration to as low as ~1x 10^{15} cm^{-3}. Hence, this cell performance can only be improved by changing the cell design. However, if the material had a midgap trap and belonged to the family of curves 1 and 2, then the lifetime would have been 21 ns instead of 3 ns at N_d = 8 x 10^{17} cm^{-3}, resulting in the expected cell efficiency of 24.7%.

Thus, the dependence of cell efficiency on deep levels can be significant over a wide doping range for the conventional thick base design. Hence, to design an optimized thick base solar cell, it is necessary to know in advance the location and nature of the deep level in the material available. One way to circumvent this difficulty is to employ a design which is relatively insensitive to deep level position and lifetime. This is demonstrated in the following section.

5.3 Relatively Defect Insensitive Thin Base GaAs Heteroface Cell Designs

The base thickness is a critical parameter for high efficiency cells. Typically, the base thickness is chosen so that most or all of the incident photons are absorbed within this region. For the 3 μm base design discussed

earlier, ~97% of the photons are absorbed in the emitter and base regions. However, it was found that a diffusion length of 2-3 times the base thickness is necessary to collect nearly all of the photogenerated carriers in the base which requires minority carrier lifetimes near the fundamental radiative and Auger limit. This is why the thick base cell efficiency is severely reduced when deep levels exist in the material which degrade the lifetime. Therefore, we propose and demonstrate by model calculations an alternative solution which employs a thinner base to relax the constraint on the diffusion length requirements without diminishing the cell performance. In fact, as shown below, it gives slightly higher efficiencies than the thicker base design unless the lifetime becomes very high.

We have previously shown by device simulation that a GaAs p/n heteroface cell design utilizing a thin base and buffer can attain one sun efficiencies over 25% with a moderate base lifetime of 20 ns and a 5% shadow + reflection loss.[9,10] An example of such a design is shown in Figure 4 which is optimized for a 20 ns base lifetime. The premise for this design is to maximize the collection efficiency of photogenerated carriers within the base by forcing the diffusion length to be greater than the base width and by bringing the buffer/base doping discontinuity step closer to the collecting junction. Detailed calculations show that high efficiency is achieved even though ~10% of the light is absorbed in the heavily doped buffer and an additional ~4.5% of the light is not absorbed anywhere within the active regions of the device. It should be noted that a thinner buffer, along with a BSF layer, is necessary to minimize the losses in the thin cell design, Figure 4.

To demonstrate the relative insensitivity of the thin base cell performance to the lifetime limiting deep levels, the performance of the thin

base device in Figure 4 was calculated using the same trap (E_v + 0.25 eV) detected in the thick base experimental cell with an efficiency of 18.9% (20.9% with 5% surface reflection). Model calculations in Figure 5 show that even with such poor material (3 ns lifetime), an efficiency of 22.92% is achievable with the thin base device (as compared to 20.9% for the thick base device), assuming a 5% shadow + reflection loss, an FSRV of 1 x 10^4 cm/s and a BSRV of 1 x 10^3 cm/s. Figure 5 exemplifies the superiority and relative insensitivity of the thin base structure to lifetime variation as compared to the thicker base structure for a starting material quality of 46 ns at N_d = 1 x 10^{14} cm^{-3}. Figure 5 also shows that traps located close to the band edges result in the largest degradation in cell efficiency for either design. However, for the thicker base, an absolute efficiency loss of ~4% results if a trap is moved from midgap to 0.25 eV while a drop of only 2% occurs for the thin base design.

The efficiency difference between the two designs is most striking for very low base lifetimes (shallow traps), where the diffusion length is 2-3 times less than the thicker base width, and becomes less significant for midgap traps where the lifetimes are significantly improved. However, even when the trap is at midgap, the thin base cell efficiency still remains higher than that of the thick base design (Figure 5) since the lifetime is now limited by the τ_o term in the SRH lifetime. It was found that most of the efficiency difference results from improved J_{sc}, due to higher diffusion length to base width ratio. Further model calculations show that only if the lifetime reaches the intrinsic (fundamental) limit for GaAs at the designed base doping levels does the thicker base design attain a higher efficiency (25.50%) than the thin base cell (25.30%) because of the improved collection

efficiency at long wavelengths. Thus the thin base design is predicted to result in higher cell efficiencies for practically achievable base lifetimes today and is much less sensitive to material quality variations than the standard thicker base (2-3 μm) GaAs p/n solar cells.

6. CONCLUSIONS

We have calculated the trap and doping dependence of lifetime in n-type GaAs and have shown that various realistic combinations of trap location and cross-section can result in orders of magnitude variation in lifetime at all doping levels below ~1x 10^{18} cm^{-3}. In addition, traps that are located within ~0.4 eV of the valence band edge and ~0.3 eV of the conduction band edge show the strongest doping dependence of lifetime below a doping level of ~1x 10^{16} cm^{-3}. It is also shown by device modeling that this has a large effect on the optimum design and performance of GaAs devices such as solar cells. It is experimentally demonstrted that a cell design which should have an efficiency over 24% (for a midgap trap, τ = 20 ns) using a 3 μm thick base resulted in a 20.9% efficiency due to an E_v + 0.25 eV trap. To minimize the influence of traps (and lifetime), which can only be found by difficult and time consuming DLTS-type measurements, an alternative design is proposed which employs thin base and buffer layers in addition to a heterojunction BSF to lower BSRV. This design minimizes the high lifetime requirement for high performance cells. It has been shown that this design is much less sensitive to deep level position than the conventional thicker base design. It is also shown that the thin cell design is slightly superior to the thick base design for most GaAs p/n heteroface cells in which the base lifetime is limited by defects. Only when the lifetime is limited by intrinsic (fundamental)

recombination mechanisms (i.e. independent of defects) does the thick base cell efficiency slightly surpass that of the thin base cell design because of more absorption and carrier collection.

ACKNOWLEDGEMENTS

This work was sponsored by Sandia National Laboratories, contract no. 02-2255. Computer model for lifetime versus trap and doping concentration were developed under EPRI contract no. RP 8001-4. The authors are thankful to Dr. S. P. Tobin for providing the GaAs cells and cell data, and S. K. Pang for help in the lifetime modeling.

REFERENCES

[1] A. Haug, J. Phys. C. 16, 4159 (1983).

[2] M. Takeshima, J. Appl. Phys. 58, 3846 (1985).

[3] C. J. Hwang, Phys. Rev. B 6, 1355 (1972).

[4] H. Van Cong, J. Phys. Chem. Solids 42, 95 (1981).

[5] C. J. Hwang, J. Appl. Phys. 42, 4408 (1971).

[6] H. C. Casey and M. B. Panish, in Heterostructure Lasers, Academic Press, 1978, New York.

[7] R. J. Nelson and R. G. Sobers, J. Appl. Phys. 49, 6103 (1978).

[8] P. A. Basore, Proc. of Sixth Biennial University/Government Industry Microelectronics Symp., 73 (1985).

[9] S. A. Ringel and A. Rohatgi, submitted to IEEE Trans. El. Dev. (1988).

[10] S. A. Ringel and A. Rohatgi, Proc. of 20th IEEE Photovoltaic Spec. Conf., in print (1988).

[11] P. D. Demoulin and M. S. Lundstrom, Proc. of 19th IEEE Photovoltaic Spec. Conf., 925 (1987).

[12] W. Shockley and W. T. Read, Jr., Phys. Rev. 87, 835 (1952).

[13] G. M. Martin, A. Mitonneau, and A. Mircea, Electron. Lett. 13, 191 (1977).

[14] A. Mitonneau, G. M. Martin, and A. Mircea, Electron. Lett. 13, 666 (1977).

[15] N. D. Arora, S. G. Chamberlain, and D. J. Roulston, Appl. Phys. Lett. 37, 325 (1980).

[16] A. Rohatgi, J. R. Davis, R. H. Hopkins, and P. G. McMullin, Solid State Electron. 23, 1039 (1983).

[17] E. Yablonovitch, R. Bhat, J. P. Harbison, and R. A. Logan, Appl. Phys. Lett. 50, 1197 (1987).

[18] S. M. Sze, in Physics of Semiconductor Devices, John Wiley and Sons, 1981, New York, p. 29.

FIGURE CAPTIONS

Figure 1. GaAs p/n heteroface solar cell structure used in this study. The cell data listed was measured under one sun AM 1.5 conditions.

Figure 2. Minority carrier lifetime as a function of doping in n-type GaAs for materials with starting lifetimes of (a) 1000 and 46 ns at $N_d = 1 \times 10^{14}$ cm^{-3}, and (b) 230 and 4 ns at $N_d = 1 \times 10^{16}$ cm^{-3} for different trap levels as indicated. Curves 1, 2, 3, and 4 are as referred in the text.

Figure 3. DLTS scan for the GaAs device shown in Figure 1 using five different weighting functions from 4 to 64 msec. Trap parameters calculated from the associated Arrhenius plot are shown.

Figure 4. Example device structure for thin base design. The dimensions shown are optimized for a 20 ns base lifetime. The simulated cell data for this lifetime are shown assuming a 5% loss to shadow plus reflection, an FSRV of 1×10^4 cm/s, a BSRV of 1×10^3 cm/s, and one sun AM 1.5 conditions.

Figure 5. Cell efficiencies calculated by PC-1D are shown for the device designs of Figure 1 (conventional) and Figure 4 (thin base) as a function of trap level (indicated with respect to the valence band edge). All calculations assume a 5% total surface loss, an FSRV of 1×10^4 cm/s, a BSRV of 1×10^3 cm/s, and one sun AM 1.5 conditions.

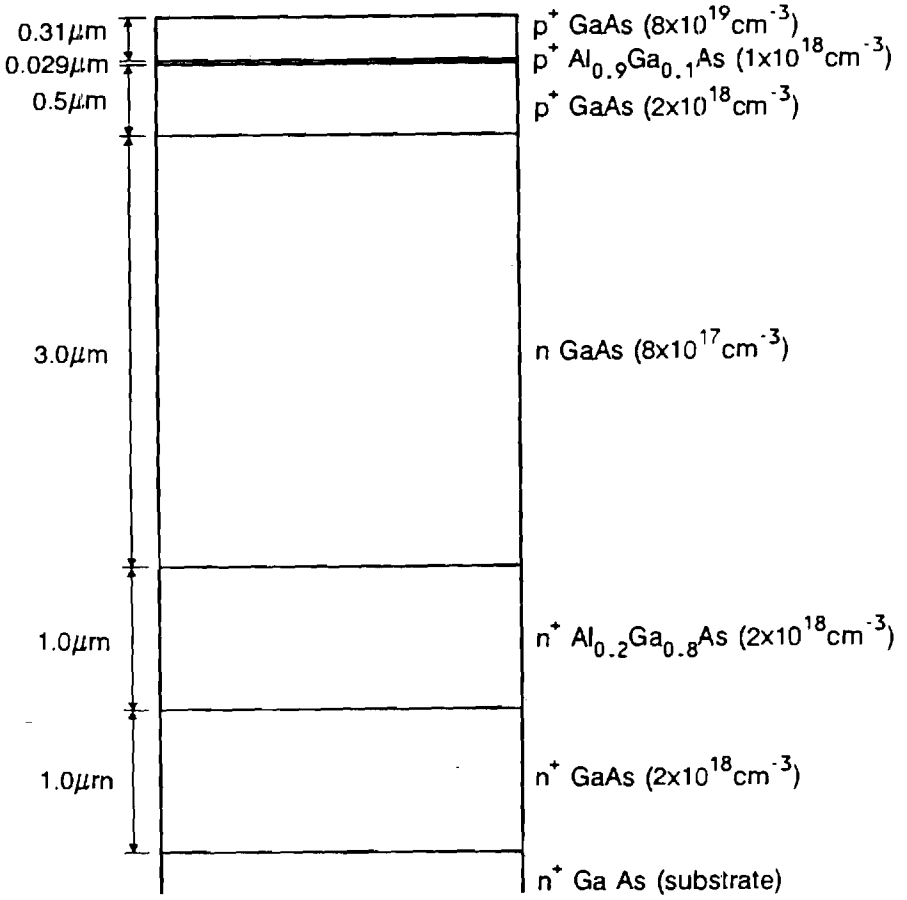

V_{oc} = 1.006 V J_{sc} = 22.11 mA/cm^2

F.F. = 0.848 Eff = 18.9%

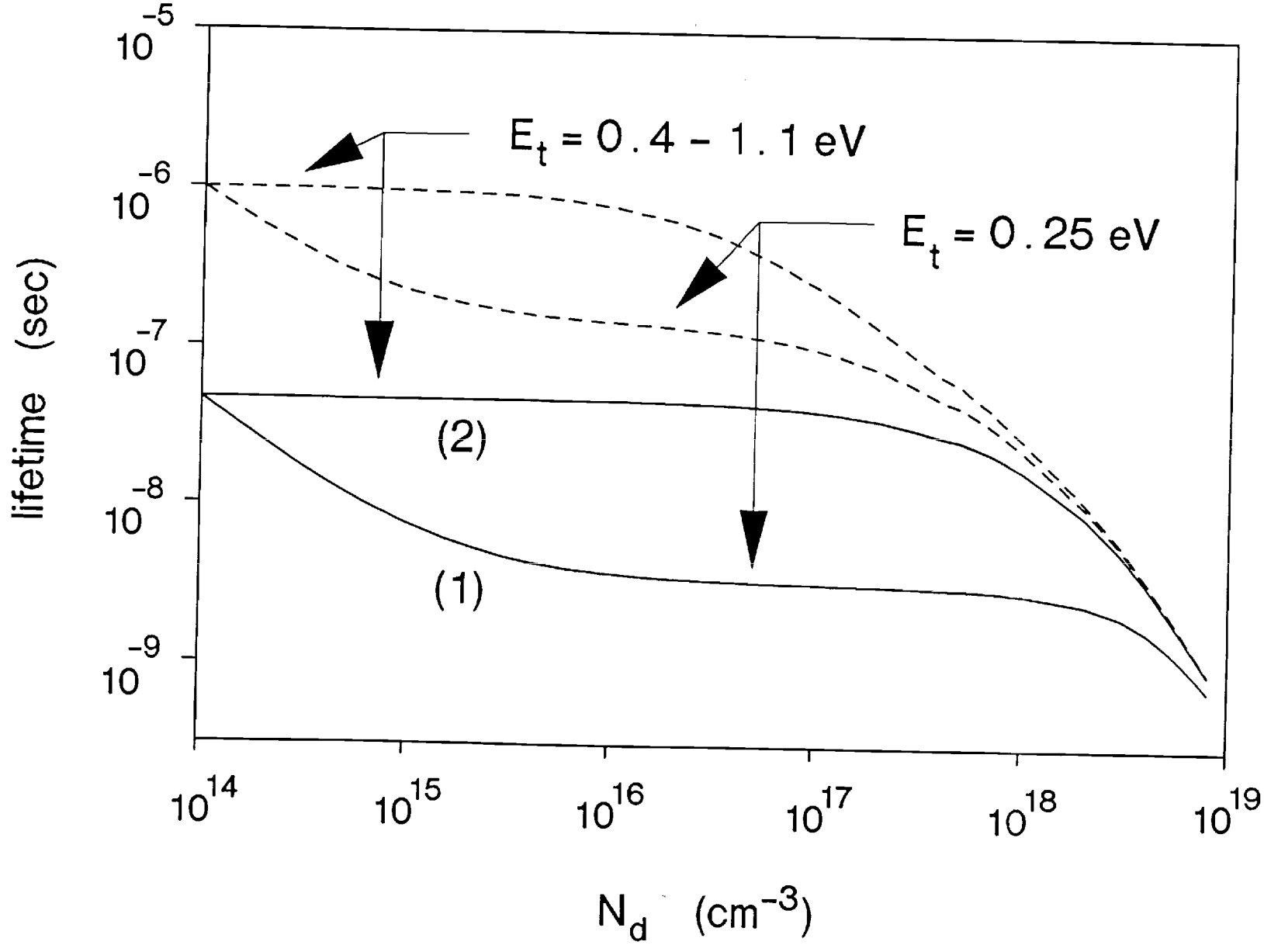
lifetime (sec)
10^{-5}
10^{-6}
10^{-7}
10^{-8}
10^{-9}
E_t = 0.4 - 1.1 eV
E_t = 0.25 eV
(2)
(1)
10^{14}
10^{15}
10^{16}
10^{17}
10^{18}
10^{19}
N_d (cm^{-3})

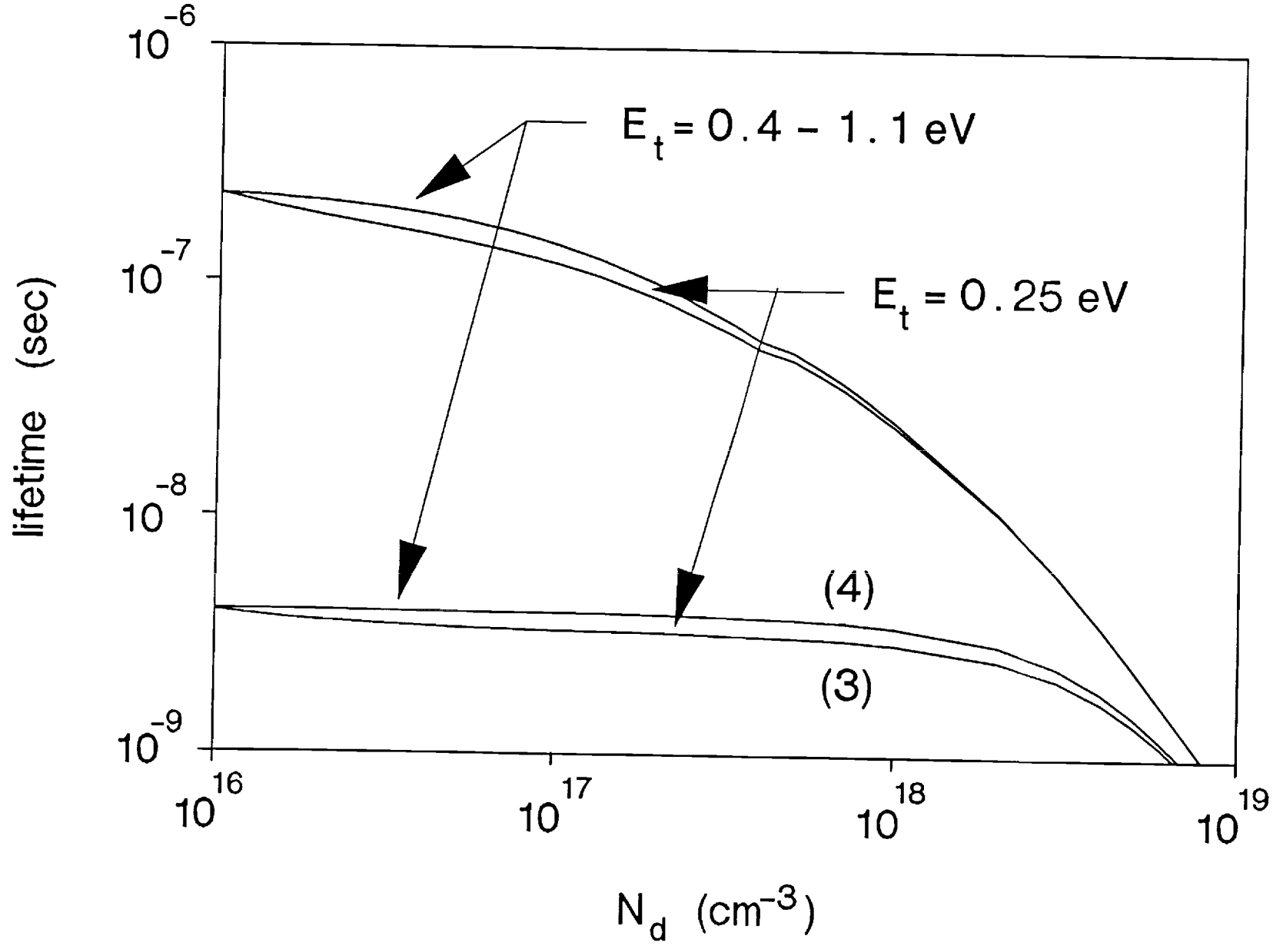
10^{-6}
10^{-7}
10^{-8}
10^{-9}
lifetime (sec)
$E_t = 0.4 - 1.1$ eV
$E_t = 0.25$ eV
(4)
(3)
10^{16}
10^{17}
10^{18}
10^{19}
N_d (cm^{-3})

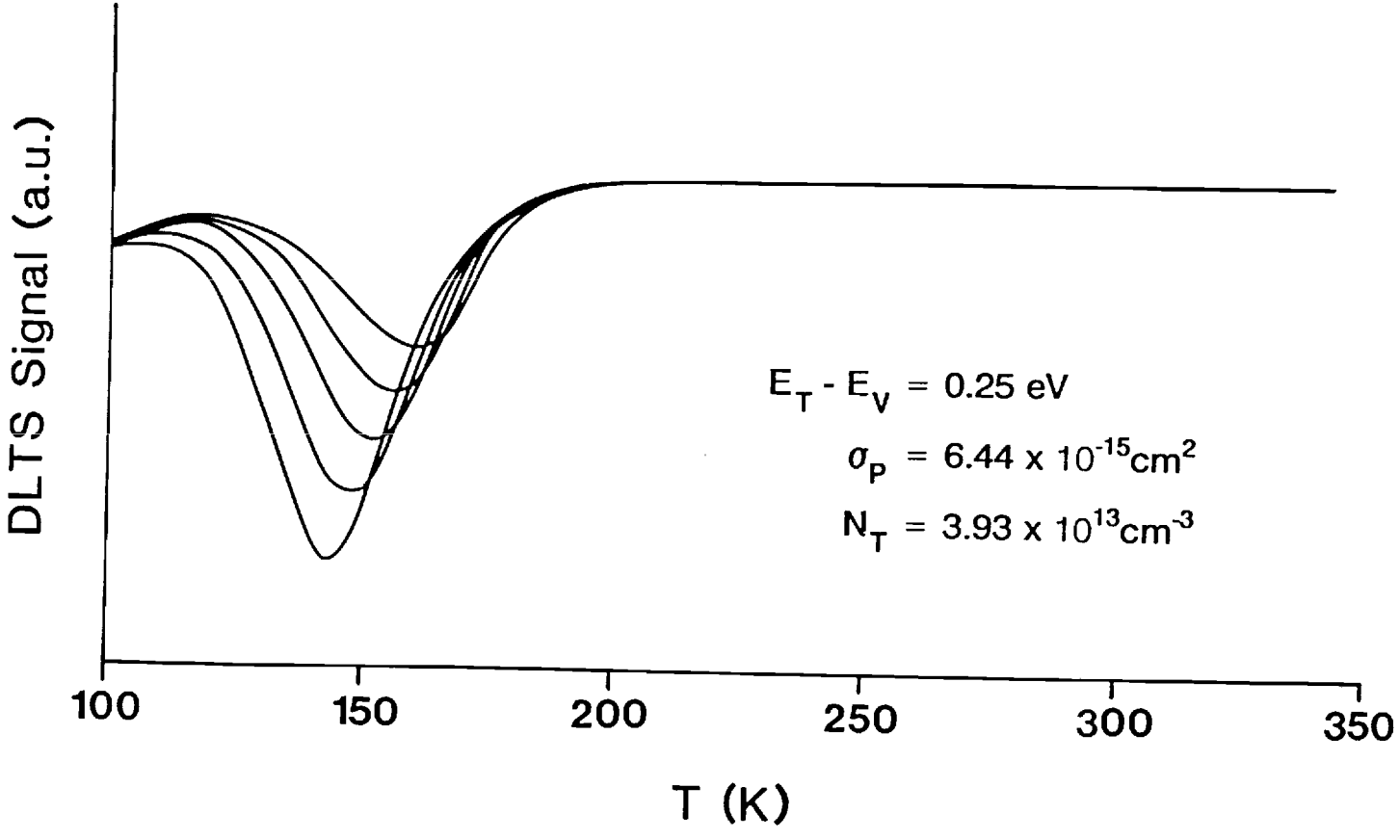
DLTS Signal (a.u.)
$E_T - E_V$ = 0.25 eV
σ_P = 6.44 x 10^{-15}cm^2
N_T = 3.93 x 10^{13}cm^{-3}
100
150
200
250
300
350
T (K)

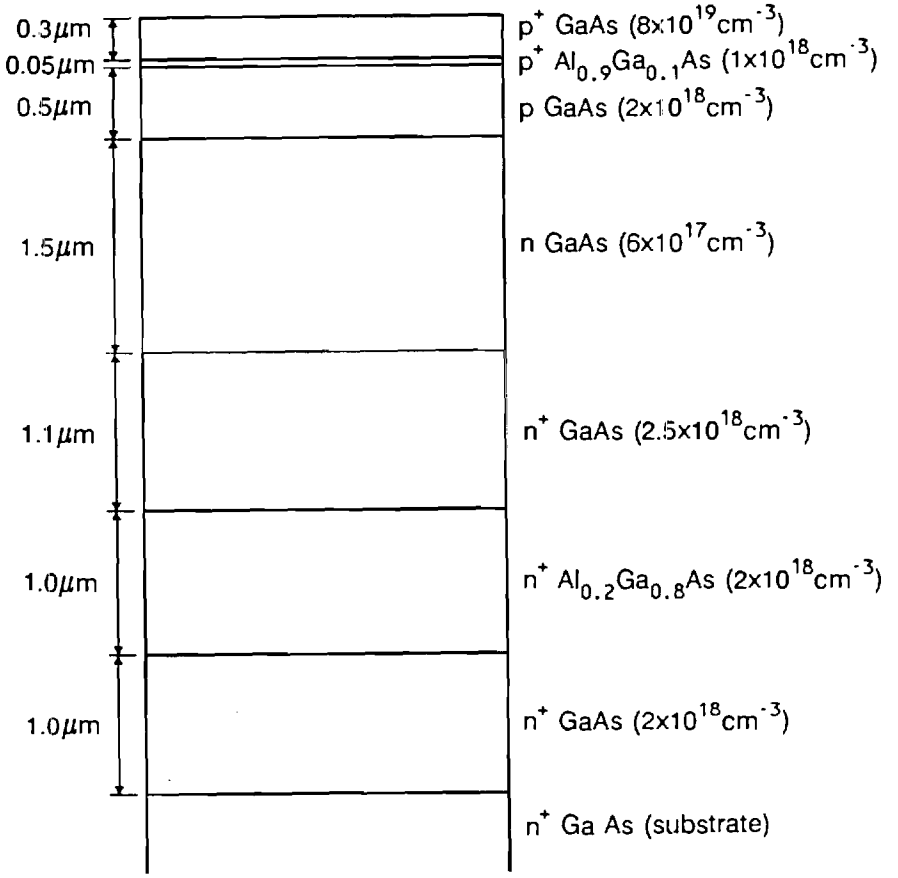
0.3μm
0.05μm
0.5μm
1.5μm
1.1μm
1.0μm
1.0μm
p+ GaAs (8x10^19cm^-3)
p+ Al0.9Ga0.1As (1x10^18cm^-3)
p GaAs (2x10^18cm^-3)
n GaAs (6x10^17cm^-3)
n+ GaAs (2.5x10^18cm^-3)
n+ Al0.2Ga0.8As (2x10^18cm^-3)
n+ GaAs (2x10^18cm^-3)
n+ Ga As (substrate)

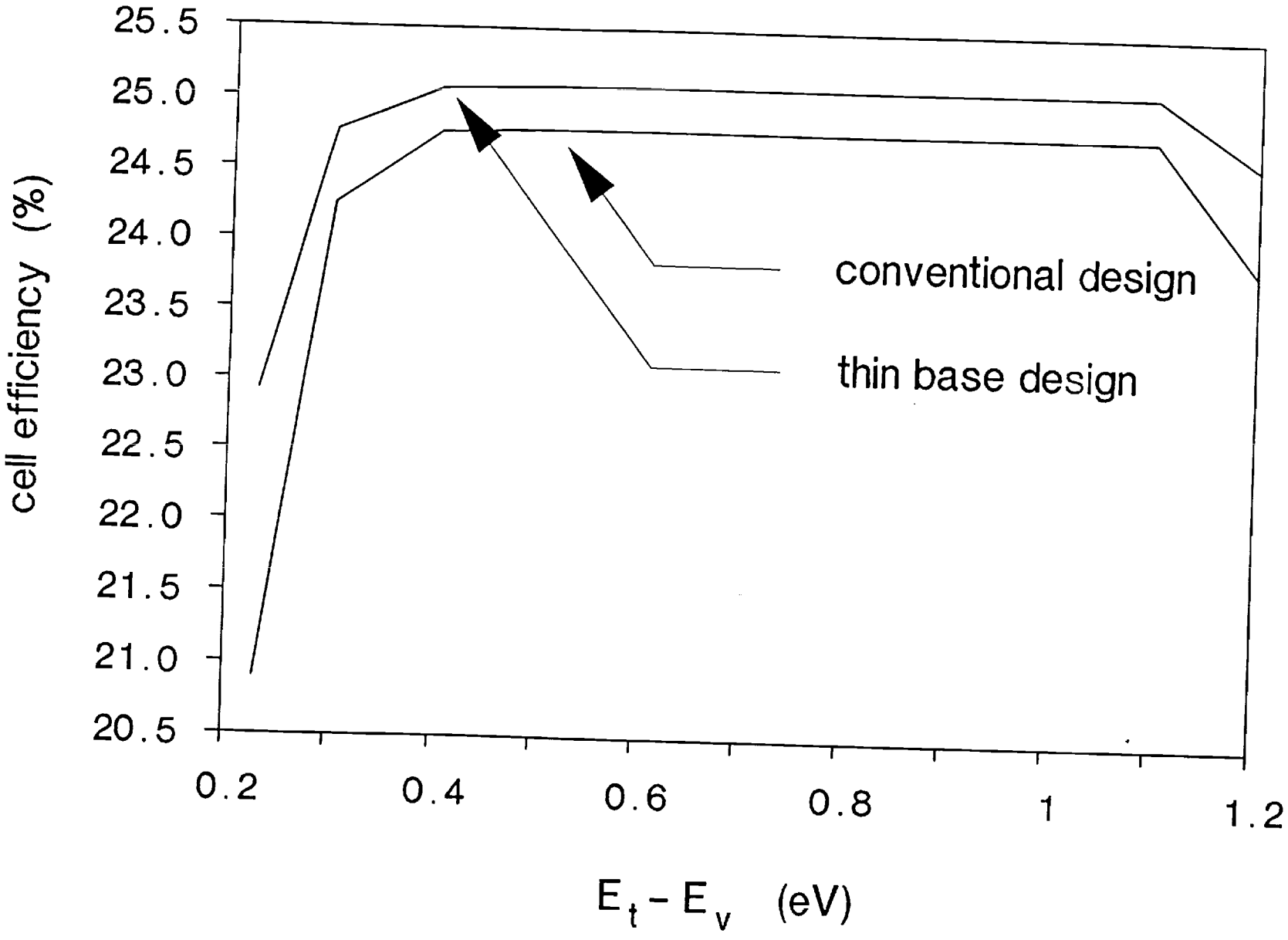
25.5
25.0
24.5
24.0
23.5
23.0
22.5
22.0
21.5
21.0
20.5
cell efficiency (%)
conventional design
thin base design
0.2
0.4
0.6
0.8
1
1.2
$E_t - E_v$ (eV)

GEORGIA INSTITUTE OF TECHNOLOGY
SCHOOL OF ELECTRICAL ENGINEERING
ATLANTA, GEORGIA 30332

TELEPHONE: (404) 894-

September 15, 1989

Mr. J. Gee
Sandia National Laboratories
P. O. Box 5800
Albuquerque, NM 87185-5800

Re: Contract No. 57-6152
Project Director: A. Rohatgi

Dear Mr. Gee:

Enclosed please find a draft of the Final Report on "Research on Design and Fabrication of High Efficiency Solar Cells," for the period 1/16/87-3/17/89 on the above referenced contract.

If you have any questions, please feel free to contact me.

Sincerely,

Ajeet Rohatgi
Professor

AJ/pm
Enclosure

TABLE OF CONTENTS

LIST OF FIGURES

APPENDIX FIGURES

1. INTRODUCTION

The overall objective of this program was to understand the loss mechanisms in Si and GaAs solar cells and provide guidelines for improving the cell performance. Major emphasis was placed on modelling and quantifying the effect of trap location and light trapping, in addition to determining the loss mechanisms by a combination of characterization and modelling the devices. Attempts were made to develop silicon cell fabrication facility from scratch and fabricate some solar cells.

The understanding of the role of deep level on solar cells performance is critical for obtaining high efficiency in both Si and GaAs based solar cells. However, the characteristics of the trap has been in general neglected in optimizing solar cell designs in current literature. It is shown that by not incorporating the proper deep level characteristics, the cell can be erroneously designed since optimal performance depends upon assumed lifetime values. Furthermore, the doping dependence of the (τ) lifetime plays an important role in the design criteria for both GaAs and Si solar cells. In the case of Si, high level injection introduces other design constraints.

The objective of this research in the Si area was to understand the reason for the gap between theoretical and experimental one sun cell efficiencies. Numerical studies were performed to determine the effect of different trap levels on the optimum resistivity. Originally, work was carried out using PC-1D version 1. This program only accounted for levels at midgap, which led to erroneous trends for shallow traps under high level injection conditions. Further work was carried out when PC-1D version II became available, which correctly accounts for trap location.

Light trapping is the key to high efficiency silicon cells. A ray tracing program is being written to account for various surface texturing and design parameters. This user friendly and PC compatible three dimensional ray tracing program includes the effects that are currently neglected in other ray tracing and analytical models.

In GaAs solar cells, minority carrier lifetimes and interface recombination rates are major factors in limiting cell performance. To obtain high efficiency, the determination and understanding of the loss mechanisms is critical if theoretical performance limits are to be reached. In particular,

the understanding of the role of defects in limiting lifetime must be better understood. Lifetime calculations and PC-1D cell modeling has been used to show how deep levels can significantly alter optimized cell designs. A three fold approach has been developed to determine bulk lifetime and interface recombination velocities in GaAs heteroface solar cells. A novel "thin-base" design is proposed which not only gives more efficient GaAs cells but is also less sensitive to defects or deep level location.

2. TECHNICAL PROGRESS

This chapter describes the technical progress and accomplishments. Sections 2.1 to 2.6 represent six technical papers that were published during the one year period of this program. Section 2.7 describes the development of the silicon fabrication facility including process development and some initial solar cell runs.

2.1 MODELING THE EFFECT OF TRAP LEVELS ON THE OPTIMUM RESISTIVITY OF SILICON SOLAR CELLS

2.1.1 Introduction

Material quality and cell design both are critical for high efficiency cells. Even in the best silicon available today, minority carrier lifetime is limited by defect-induced deep levels. The objective of this paper is to reveal the impact of various defect levels in dictating the optimum resistivity for high efficiency silicon solar cells. An attempt has been made to bridge the information gap between silicon vendors and cell manufacturers by providing guidelines for selecting the optimum resistivity without going through extensive experimentation and large expense. The PC-1D model (1), a one-dimensional semiconductor device modeling program developed by Paul Basore, was used to simulate cell performance. In the PC-1D model, the lifetime in the material is controlled by a single defect level located at the center of the forbidden gap, in addition to the Auger and band-to-band effects. In an actual semiconductor, defects can produce a variety of deep levels and, therefore, the lifetime will not only depend upon the manner of traps but also on the location of the trap level. The starting material lifetime (prior to any intentional doping) was varied in the range of 10 μsec to 10 msec. Increasing the carrier lifetime to 10 msec is consistent with the recent improvement in crystal growth technology. A combination of a trap sensitive carrier lifetime model and PC-1D has been employed to show that the optimum resistivity for a given cell design depends on the (1) trap location, (2) starting lifetime of the material prior to any intentional doping (undoped), (3) relationship between the defect density and doping density in the material, and (4) the injected carrier concentration in the cell under operation.

2.1.1a. Carrier Lifetime and Device Modeling

To determine the effect of the resistivity, trap level, and initial lifetime on the cell efficiency, numerical simulations were performed using PC-1D model. In PC-1D, the lifetime model is only valid for a trap located at the midgap. In order to examine the effect of various trap levels, the SRH lifetime at low injection was calculated according to equation (2,3)

$$\tau_{SRH} = \tau_{no}(P_0 + P_1) + \tau_{PO}(N_0 + N_1) \tag{1}$$

Where N_0 and P_0 are the equilibrium concentration of carriers and N_1 and P_1 are given below:

$$N_1 = n_{ie} \exp(E_t/(kT)) , \qquad P_1 = n_{ie} \exp(-E_t/(kT))$$

The net lifetime was obtained from

$$1/\tau_{net} = 1/\tau_{SRH} + CN^2 + BN . \tag{2}$$

Where B is the band-to-band coefficient and C is the Auger coefficient. The SRH lifetime was used to input into PC-1D and the substrate lifetime was checked to be sure it was the same as our calculated net lifetime. This insured that doping effects have been properly accounted for in the emitter and buffer regions of the cell. As a first approximation, the trap density was assumed to be independent of the doping density for the SRH contribution in most calculations. Only in selected cases was this assumption later relaxed by assuming that the trap density changes with the doping density according to

$$N_T = N_{TO}[1 + N_a/N_{REF}]$$

which leads to a Kendall-like (4) modification of the SRH lifetime

$$\tau'_{SRH} = \tau_{SRH}/[1 + N_a/N_{ref}] \tag{3}$$

where $N_{ref} = 7.0\ 10^{15}$ is used as a reference doping threshold.

As we go to higher resistivity, the doping dependence of lifetime and the increased injected carrier density could switch the cell operating point from low level to high level injection. The PC-1D model used in this paper can account for such a switch. Some of the key equations to understand the impact of injection level on V_{oc} are listed below.

2.1.1b. Low Level Injection ($\Delta n < N_a$)

At all levels of injection, the open circuit voltage, V_{oc}, is given by

$$V_{oc} = kT/q\ \ell n\ (np/n_i^2)\ . \tag{4}$$

Under low level injection conditions, this reduces to

$$V_{oc} = kT/q\ \ell n(J_{sc}/J_o + 1) \tag{5}$$

where J_o is the dark current density. A reduction in the dark current without a loss in J_{sc} would result in a higher open circuit voltage and thereby increase the efficiency. A fundamental equation for J_o is given below (5)

$$J_o = [(qD_e n_i^2/(L_n N_d))^* F_N] \tag{6}$$

If the surfaces are well passivated, then this equation would reduce to

$$J_o = [(qD_e n_i^2/(L_e N_a))^* \tanh(W_p/L_e) + (qD_h n_i^2/(L_h N_d))^* \tanh(W_n/L_h)] \tag{7}$$

Now is the base contribution dominates the dark current, Eq. (7) can be written

$$J_o = (qD_b n_i^2/(L_b N_b))^* \tanh(W_b/L_b) \tag{8}$$

J_o will be minimum when the product L_bN_b is maximum. Equation (1) points out that in this case the SRH contribution to the lifetime will depend on both the trap level and the doping concentration.

2.1.1c. Higher Level Injection

As the material lifetime and cell resistivity increases, the injected carrier concentration can exceed the doping concentration driving the cell into higher level injection. In higher level injection, Eq. (6) for J_o is no longer valid and V_{oc} is given by

$$V_{oc}\,(kT/q)\,\ell n(np/n_i^2) = (kT/q)\,\ell n((\Delta n N_a + \Delta n^2)/n_i^2) \qquad (9)$$

The SRH lifetime in this case would be a function of doping density, Δn, and deep level position.

$$\tau_{SRH} = \tau_{no}(P_o + P_1 + \Delta n) + \tau_{po}(N_o + N_1 + \Delta n) \qquad (10)$$

2.1.1d. High Level Injection $\Delta n >> 10\ N_a$

Once the high level of injection ($\Delta n >> 10\ N_a$) sets in, Eq. (10) indicates that the SRH lifetime becomes constant ($\tau = \tau_{no} + \tau_{po}$) and independent of trap level or injection level. Using the basic equation for V_{oc} and substituting $N = P = \Delta n >> N_a$, the equation for V_{oc} under high level injection reduces to

$$V_{oc} = (kT/q)\,\ell n(NP/n_i^2) = (kT/q)\,\ell n(\Delta n^2/n_i^2) = (2kT/q)\,\ell n(\Delta n/n_i) \qquad (11)$$

These equations and the regions in which they are valid will be discussed later in this paper.

The basic cell design used in this paper is given in Table 1. To determine if cell design had a significant effect upon the results, simulations were also performed on cells with slightly different designs compared to the standard cell. Modifications included higher values of front and back surface recombination velocities and a decrease in BSF thickness and emitter doping. The results of these changes are also briefly discussed.

TABLE 1. Configuration of N^+-P-P^+ Cells Used in Numerical Simulations.

1. Cell area of 1 cm^2
2. Emitter resistance of 0.2 ohm-cm
3. Emitter doping of 2.0 x $10^{19}cm^{-3}$
4. Complementary error doping profile in emitter
5. Emitter thickness of 0.2 microns
6. Cell thickness of 254 microns
7. BSF doping of 2.0 x 10^{18}
8. Complementary error doping profile in BSF
9. BSF thickness of 2 microns
10. 5% shadow and reflective loss
11. 98% effective back surface reflector
12. FSRV and BSRV of 100 cm/sec

2.1.2 Results and Discussion

The lifetimes were calculated with the help of a computer program which took into account the trap level, trap density, doping density, and band-to-band and Auger recombination effects. Figure 1 displays the calculated lifetime profiles as a function of doping density and trap level for a material with starting lifetime of 10 msec at 200 ohm-cm resistivity. Using the lifetime profiles for traps located at 0.56 and 0.20 eV. PC-1D simulations were performed for the standard cell configuration. The efficiencies are shown in Fig. 2. For the trap at midgap, bulk lifetime is independent of doping density and the cell remains under high level injection all the way down to 5 ohm-cm. As a result, the V_{oc}, J_{sc}, and efficiently remain essentially constant. As we go from 5 to 0.2 ohm-cm, the injection level drops to low level, lowering the V_{oc} and the cell efficiency slightly. Below 0.2 ohm-cm, Auger recombination sharply lowers τ, V_{oc}, J_{sc}, and the efficiency. However, in the case of a trap located at 0.20 eV, the efficiency begins to drop because the lifetime

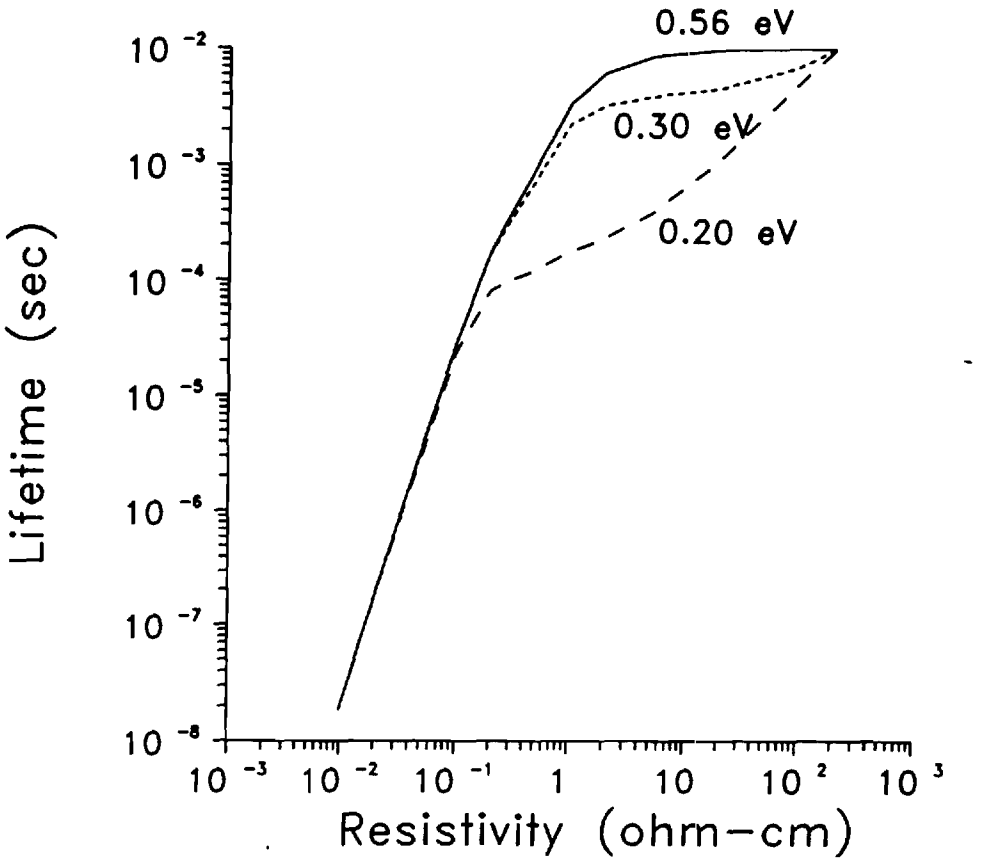

Figure 1. Net Lifetime as a Function of Doping Density for Deep Levels.

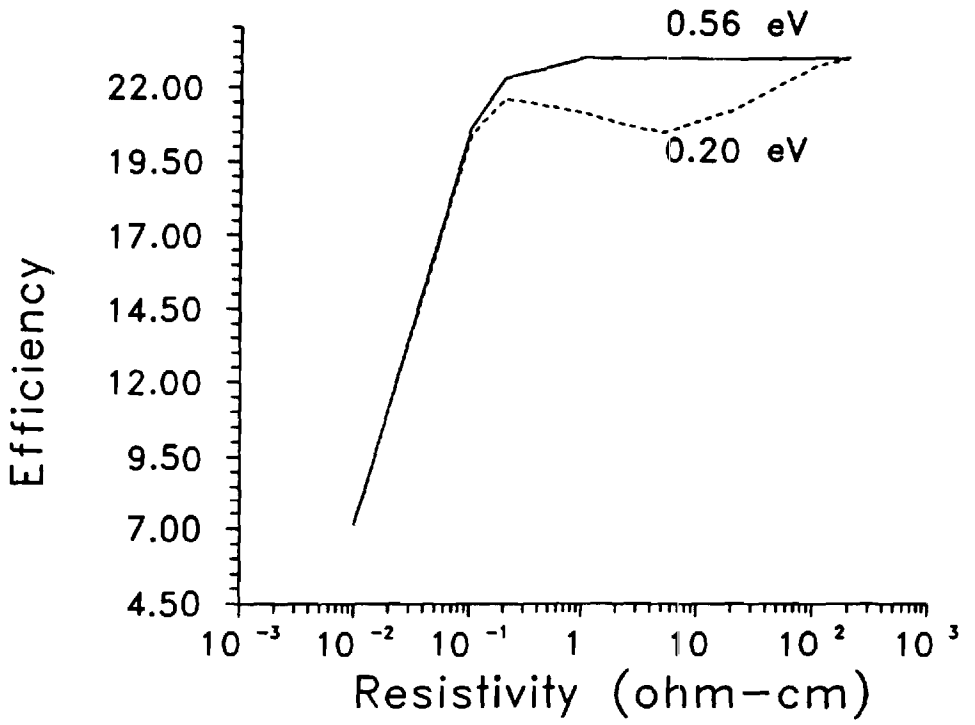

Figure 2. Efficiency as a Function of Doping Density for Material with 10 msec. Starting Lifetime at 200 ohm-cm. Dotted Line Indicates a Shallow Trap, Solid Line Indicates a Midgap Trap.

in this case drops fast enough with resistivity so that the cell can no longer sustain as high an injection level as in the case of a midgap trap. Below 5 ohm-cm, the efficiency starts to rise and peaks around 0.2 ohm-cm, Fig. 2. The rise in efficiency is due to the reduction in the dark current which is inversely related to the doping density and under low level injection affects the open circuit voltage, Fig. 3. Even with this increase in the voltage, the efficiency does not reach the value obtained for the high level injection at high resistivity, Fig. 2. The sharp drop in efficiency below 0.2 ohm-cm resistivity is again due to the drop in lifetime caused by Auger recombination. Figure 4 shows that the increase in efficiency is not due to the short circuit current since the J_{sc} for the high quality material is essentially the same for both trap levels. Therefore, for a high lifetime starting material (τ = 10 msec, W = 254 microns), the best cells will come from high resistivity no matter where the trap is located, provided high level injection can be maintained. For trap levels between 0.56 and 0.20 eV, the behavior is similar, being bounded by these two trap levels.

As the initial lifetime decreases, the location of the trap becomes even more important. Figure 5 shows that unlike the high lifetime case, materials with moderate lifetimes (100 μsec - 1 msec) and midgap trap, show optimum resistivity of 0.2 ohm-cm. Because of the midgap trap, the lifetime remains unchanged with increased doping, resulting in higher V_{oc}, Eq. (9), without sacrificing J_{sc}. This results in a gradual rise in efficiency down to 0.2 ohm-cm. On the other hand, as we lower the resistivity from 200 ohm-cm, the trap located at 0.20 eV first produces a drop in efficiency by lowering the lifetime or Δn, Fig. 5. As we approach low level injection and beyond, the lifetime decrease is offset by the increased doping resulting in lowering the dark current, $I_o \alpha 1/N_a\tau$, associated with a rise in efficiency. Figure 5 clearly shows that, unlike the midgap trap case, the optimum shifts to low resistivity when the trap is located at 0.2 eV. It is interesting to note in Fig. 5 that a cell produced on 100 microsecond initial lifetime material with a midgap trap and optimum resistivity of 0.2 ohm-cm gives higher efficiency than the optimum cell produced from 1 millisecond starting material with a trap located at 0.20 eV. This trend is repeated for all starting lifetimes in the range of 100 μsec to 1 msec.

In the case of poor quality material with starting lifetime of $\leq$ 10 μsec, Fig. 6, the highest efficiency is obtained at 0.2 ohm-cm no matter which trap level is present. This is primarily due to the reduction in the dark current which reaches a minimum at 0.2 ohm-cm when the product L_bN_a

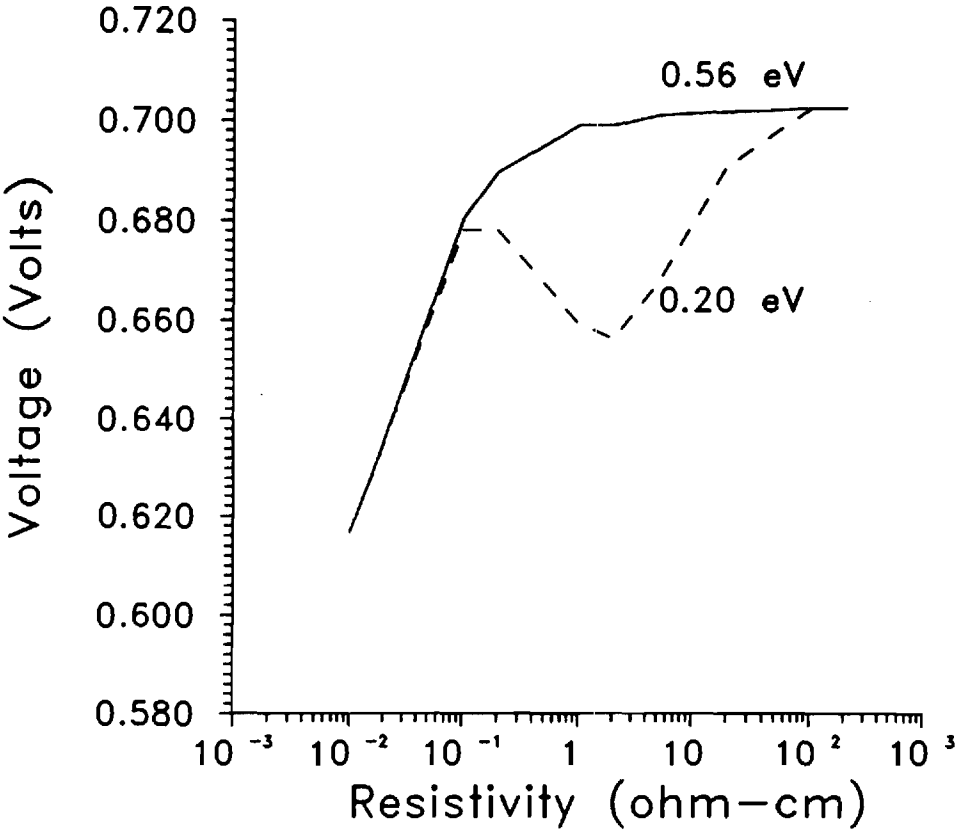

Figure 3. Open Circuit Voltage Values Corresponding to Efficiency Values in Fig. 2. The Dotted Line is the Shallow Trap Level, while the Solid Line is a Midgap Trap.

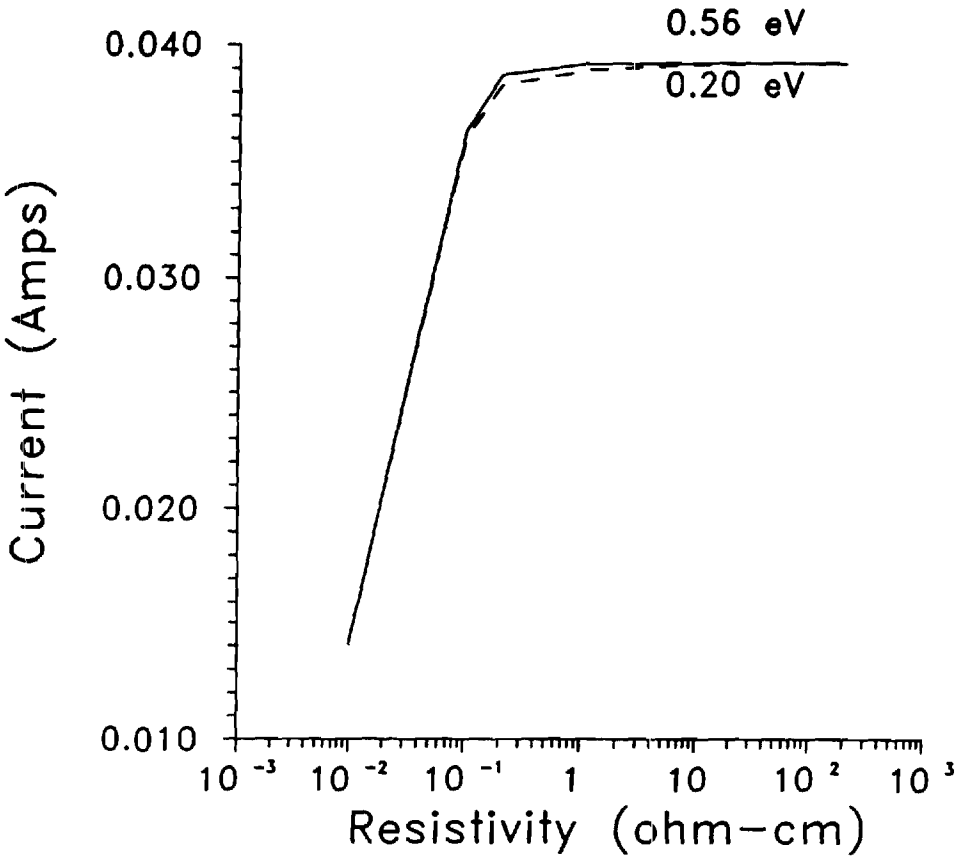

Figure 4. Short Circuit Current for 200 ohm-cm Starting Material with a Lifetime of 10 msec. The Dotted Line is the Shallow Level, Solid is a Midgap Level.

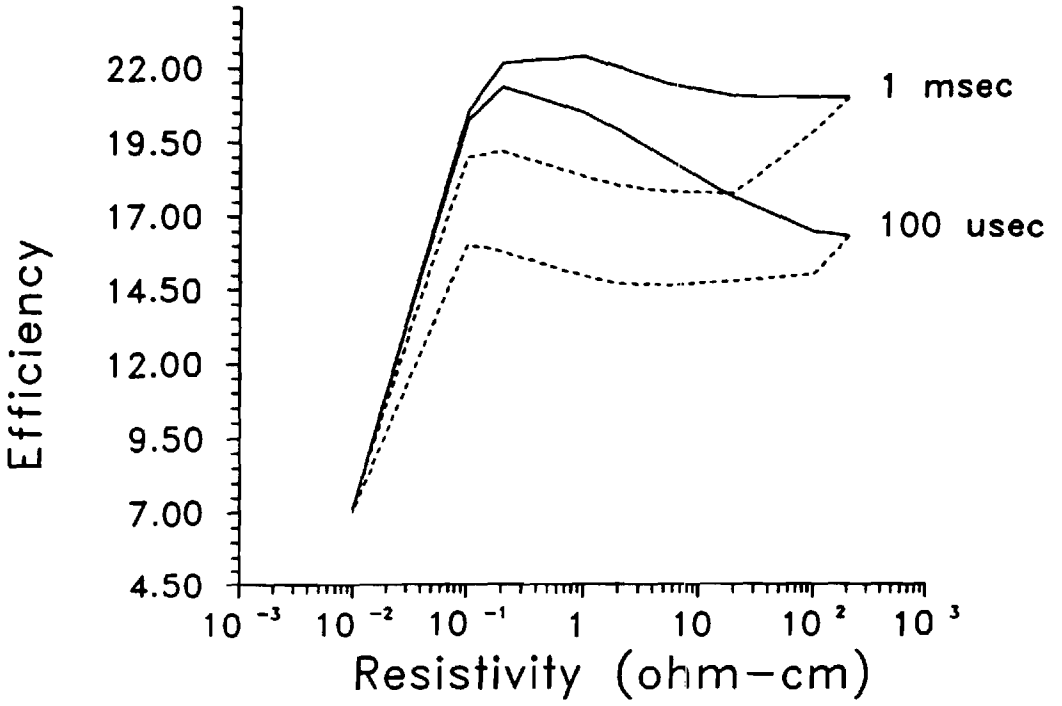

Figure 5. Efficiency as a Function of Doping Density for Intermediate Starting Lifetime in 200 ohm-cm Material. Dotted Line Indicates Shallow Levels, Solid Indicate Midgap Traps.

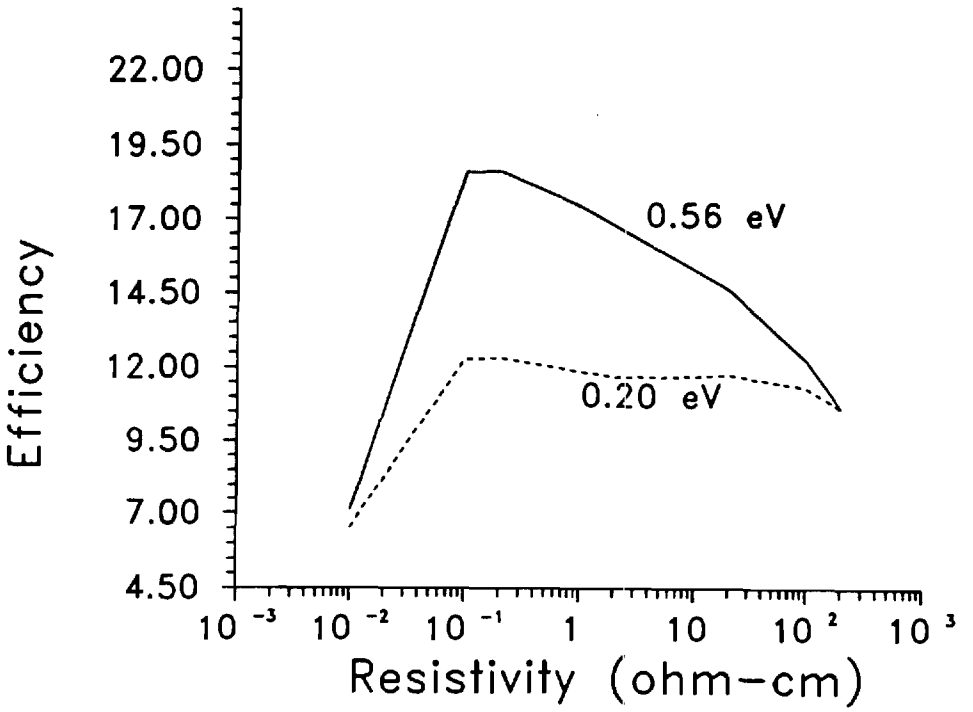

Figure 6. Efficiency as a Function of Doping Density for Low Quality Starting Material (10 μsec).

peaks. The cell always remains in low level injection because the generated carriers recombine too fast.

To illustrate the effect of the starting lifetime more clearly, the efficiency was calculated and plotted for various starting lifetimes in the range of 10 μsec - 10 msec, Figs. 7 and 8. For a trap level located at 0.56 eV, it was found that the efficiency is nearly independent of the resistivity for the high lifetime material (>1 msec). However, for the lower lifetime material, the optimum resistivity is approximately 0.2 ohm-cm. This is because the lifetime is fairly independent of resistivity, thereby allowing only the highest lifetime material to go into high level injection.

Figure 8 shows that for the trap at 0.20 eV, the optimum resistivity choice for low lifetime material still remains 0.2 ohm-cm but for the higher lifetime materials, the lifetime choice decidedly shifts to high resistivity ($\geq$200 ohm-cm).

The effect of the relationship between trap density and doping density was investigated. Lifetime profiles change when the trap density is allowed to vary according to a Kendall-like equation, Fig. 9. For this case, the lifetime in the low resistivity material drops off much faster because of the increase in the trap density. Figure 10 shows a comparison between the efficiencies of cells simulated with 1 millisecond starting lifetime material with and without the change in trap density. The trap density in both cases was assumed to be identical in 200 ohm-cm. The efficiencies at higher resistivities are comparable because the trap density is not changing appreciably, Eq. (3), to affect the lifetime. As we move toward lower resistivity, the efficiency for the $N_t = f(N_d)$ case drops off more rapidly, especially when the trap is located at 0.20 eV. The net result is that the optimum shifts toward higher resistivity material.

It should be noted that these calculations were performed for a one sun cell design with flat surfaces. Therefore, these results may not be valid for textured or concentrator cells where high level injection may be achieved at other resistivities. These results do help explain why the best sun cells with conventional N^+-P-P^+ cell designs and lifetime of <100 μsec have been achieved on 0.2 ohm-cm material. Changing the cell design slightly from that used in the above calculations does not change the conclusions. Raising the FSRV or BSRV results in a small loss in V_{oc}, but the conclusions remain the same for all resistivities. A decrease in the BSF thickness increases the V_{oc} uniformly over most of the resistivity range. Decreasing the emitter doping had the same effect of raising the

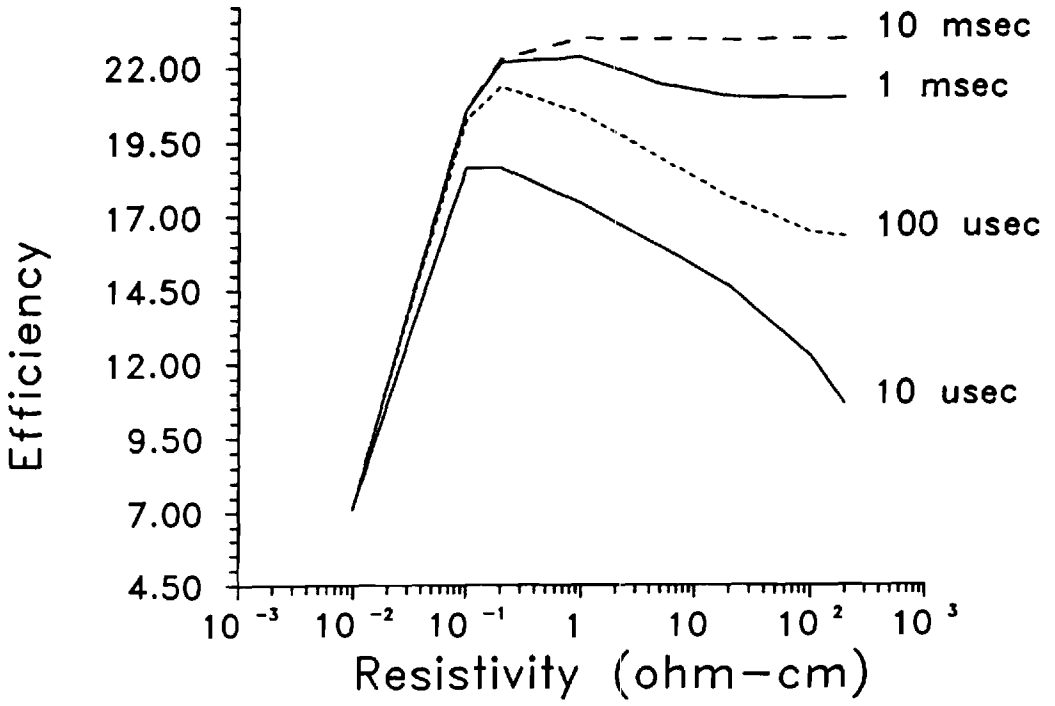

Figure 7. Efficiency for Various Initial Lifetimes in the 200 ohm-cm Material. The Trap Level is Located at Midgap.

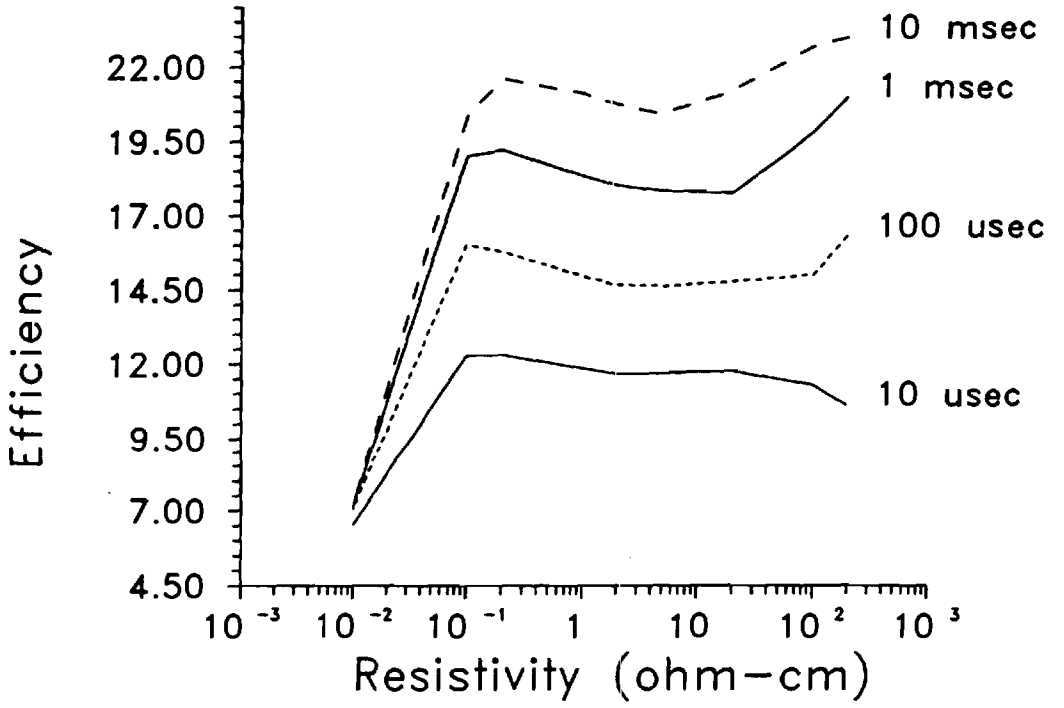

Figure 8. **Efficiency for Various Initial Lifetimes in the 200 ohm-cm Material when the Trap is at 0.20 eV.**

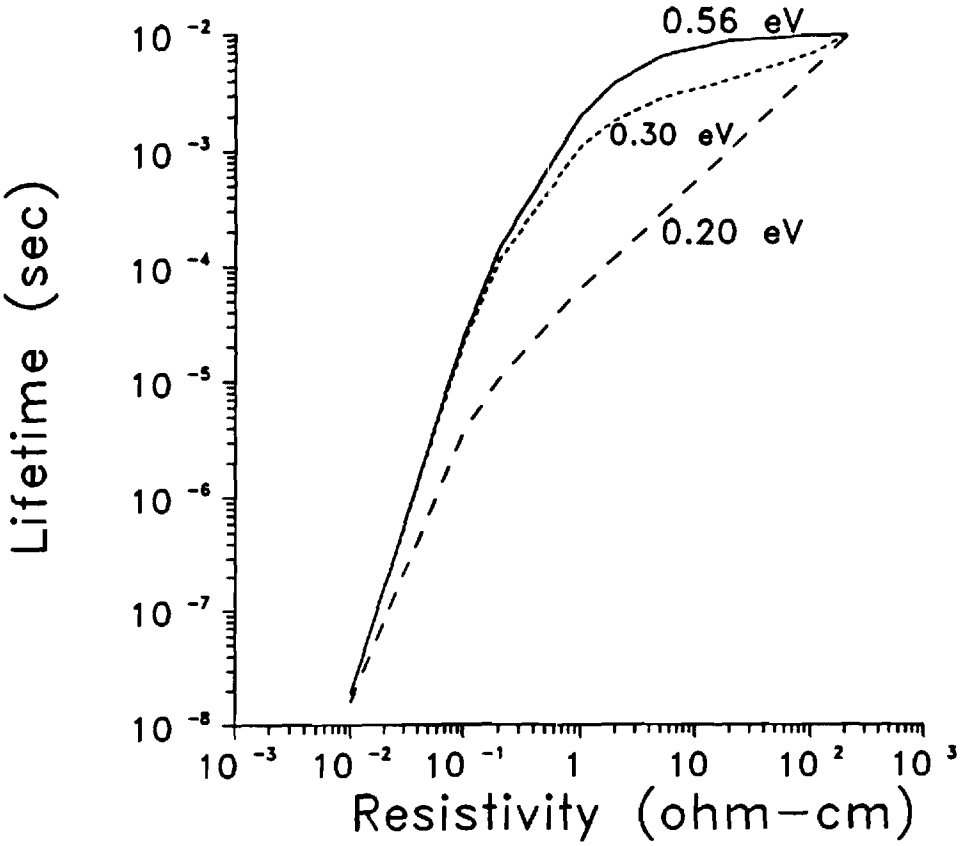

Figure 9. Lifetime as a Function of Resistivity when the Trap Density Depends upon the Doping Density in a Kendall-Like Manner.

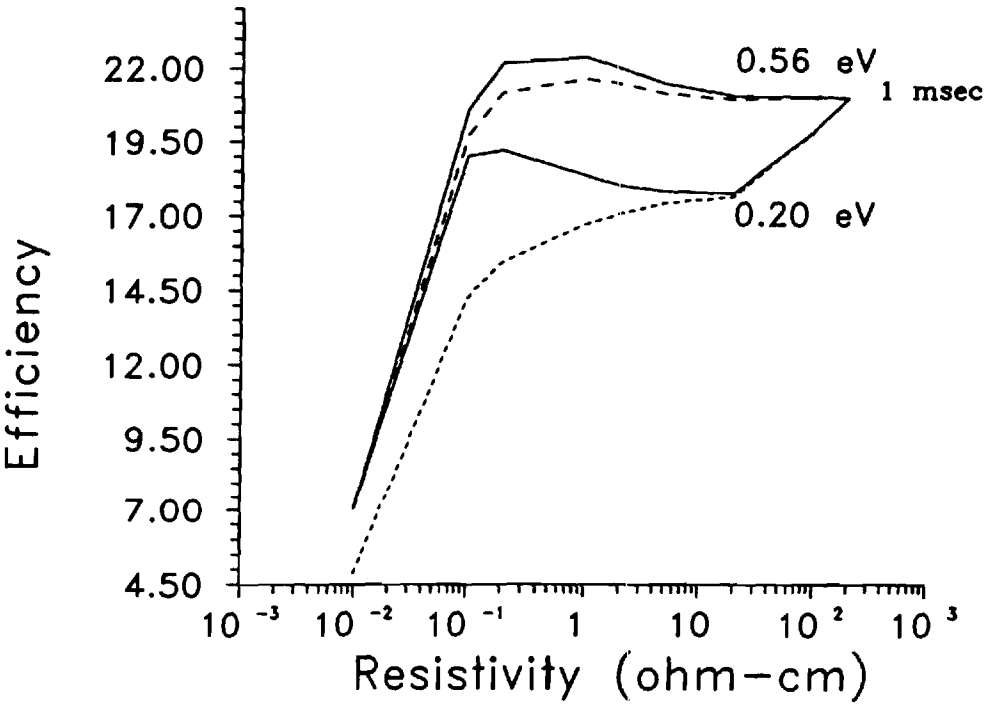

Figure 10. Comparison of Efficiency for Material with 1 msec Lifetime in the Undoped Material when the Trap Density is allowed to vary in a Kendall-Like Manner. The Trap Levels are Located at 0.56 and 0.20 eV. The Dotted Lines are for Constant Trap Density.

open circuit voltage and efficiency, and was more effective in the lower resistivity cells. This is because the emitter starts to play a bigger role in controlling V_{oc}. The effect was still not big enough to alter the trends.

2.1.3 Conclusion

Guidelines are provided for selecting the material for high efficiency solar cells. It is shown that the position of the deep level can change the lifetime and, consequently, the injection level at any given doping density. A combination of lifetime and device modeling indicates that in order to select the optimum resistivity at least three parameters need to be specified: (1) location of lifetime limiting deep level, (2) starting lifetime of the material, prior to any doping, and (3) dependence of the trap density on the doping density in the material. These factors at any given resistivity dictate whether the cell will be operating under high or low level injection, which in turn, affects the cell efficiency. Modeling calculations reveal that high resistivity is optimum for very high lifetime (>1 msec) materials independent of the trap location. If the lifetime is very low (<10 μsec), then a low resistivity, 0.2 ohm-cm, is optimum for the best cells regardless of the trap location. For intermediate starting lifetimes (100 μsec - 1 msec), with a midgap trap, low resistivity (0.2 to 1 ohm-cm) is preferred, but if the trap is located at 0.20 eV, the choice shifts to high resistivity.

2.2 IMPACT OF DEEP LEVEL POSITION AND LIGHT TRAPPING ON SILICON CELL PERFORMANCE

2.2.1 Introduction

The right combination of material quality, cell design, and light trapping is the key to achieving high efficiency cells. The objective of the section is twofold. First, to bridge the gap between silicon vendors and cell manufacturers by providing guidelines for selecting the right combination of carrier lifetime and resistivity for a conventional high efficiency n^+-p-p^+ cell design. Secondly, to quantity the effect of various surface texturing schemes on not only the increased photon absorption but also on the performance of cells with base minority carrier lifetime ranging from 1 μs to 10 ms.

Even the best silicon available today suffers from defects that lead to trap induced recombination. This paper shows that the optimum resistivity and performance for a given cell design depends on (1) trap location, (2) starting minority carrier lifetime, prior to intentional doping, and (3) injected carrier concentration in the cell. It is shown that getting started with a high lifetime material alone is not sufficient because certain trap locations can severely limit the performance if the base doping is inappropriate or the cell goes into high level injection. The model calculations have been done for one sun AM 1.5 conditions but the results have implications for concentrator cells.

2.2.2 Modeling

2.2.2a. Light Trapping

In the PC-1D device model [1] used in this paper, the generation profile is only applicable to flat surfaces, however, the angle of incidence and incident flux can be changed to produce different carrier generation profiles. To quantify the importance of light trapping, a ray tracing program was developed to obtain generation profiles for different surfaces: regular pyramid-like, Lambertian, and perpendicular slats. In this program, the incoming flux is divided into a large number of rays and the path of each ray is followed until the ray is completely absorbed, resulting in a generation profile. It is important to realize that relative improvement in cell performance from increased photon absorption depends on the base quality and collection efficiency. In a preliminary attempt to

quantify this effect, generation profiles in PC-1D were created and matched with the generation profiles from the ray tracing program by tailoring the flux and angle of incidence, prior to performing the solar cell simulations for base material with lifetimes ranging from 1 μs to 10 ms. It should be noted that in these initial calculations we have ignored the effects of two-dimensional carrier flow and increased emitter area due to the textured surfaces.

2.2.2b. Carrier Lifetime and Device Modeling

In an earlier paper [2], we made an attempt to investigate some of these effects, using a combination of the semiconductor device modeling program PC-1D and an independent lifetime model. Since PC-1D was configured for only midgap traps, artificially higher values of τ_{no} and τ_{po} were introduced to give the correct recombination rate for shallow traps when the cell went into high level injection. The latest version of PC-1D has been modified to account for the effect of trap location. In order to understand the physics behind the calculated results by PC-1D, we have utilized analytical expressions for V_{oc}, Shockley-Read-Hall lifetime, and net lifetime. These equations utilize injection level calculated by PC-1D. The equations are listed below for p-base solar cells:

- Open circuit voltage for all levels of injection in a cell is given by

$$V_{oc} = (kT/q)\, \ell n(np/n_i^2) \tag{12}$$

  provided quasi-Fermi levels are flat.

- The net lifetime in the base is given by

$$1/\tau_{NET} = 1/\tau_{SRH} + C_p p^2 + C_n n^2 + B(p+n) \tag{13}$$

  where C_p and C_n are the Auger coefficients, n and p are total electron and hole concentrations in the base of the cell, B is the radiative band to band coefficient, and

$$\tau_{SRH} = \tau_{no}(p_o + P_1 + \Delta n) + \tau_{po}(n_o + n_1 + \Delta n) \tag{14}$$

where Δn is the injected carrier concentration, n_o and p_o are equilibrium carrier concentrations,

$$n_1 = n_{ie} \exp(E_t/(kT)) , \quad p_1 = n_{ie} \exp(-E_t/(kT)) \tag{16}$$

where E_t is the energy level of the trap.

2.2.3 Results and Discussion

2.2.3a. Effect of Trap Location on Lifetime

Model calculations in Figure 11 show that, for a given quality of undoped starting material, minority carrier lifetime under low level injection decreases with increasing doping density and the doping dependence is dictated by the trap location within the bandgap. For a silicon technology that can produce 10 ms lifetime 200 ohm-cm wafers, a midgap trap shows essentially no doping dependence until $N_a \sim 2 \times 10^{15} cm^{-3}$. Beyond this the doping lifetime drops sharply due to Auger recombination. Shallow traps show a much stronger and undesirable doping dependence. This is because in order to keep the same starting lifetime, the τ_{no} and τ_{po} values for the shallow traps are smaller for a midgap trap. These calculations assume $\tau_{no} = \tau_{po}$.

Figure 12 shows the effect of injection level on lifetime for two different trap locations in a 200 ohm-cm silicon with a starting lifetime of 10 ms. This figure shows both SRH lifetime and net lifetime. It is interesting to note that as the material begins to go into high level injection ($\Delta n > N_a$), the lifetime increases for the midgap trap, but it decreases for the shallow trap. Once it gets into very high injection ($\Delta N >> 10\ N_a$), SRH lifetime become constant: $\tau_{SRH} = \tau_{no} + \tau_{po}$. Net lifetime, shown by the solid line, indicates that for the midgap trap lifetime continues to rise from 10 ms to ~18 ms before Auger recombination takes over at $\Delta n \approx 10^{15} cm^{-3}$ and after that, the lifetime drops rapidly. For the shallow trap ($E_v + 0.2$ eV), both net and SRH lifetimes continue to fall from 10 ms to about 200 μs until $\Delta n \simeq 10^{16}$, beyond which Auger recombination takes over. These trap induced lifetime behaviors (Figures 11 and 12) can significantly effect the performance of cells which are dominated by base recombination as discussed in the following section.

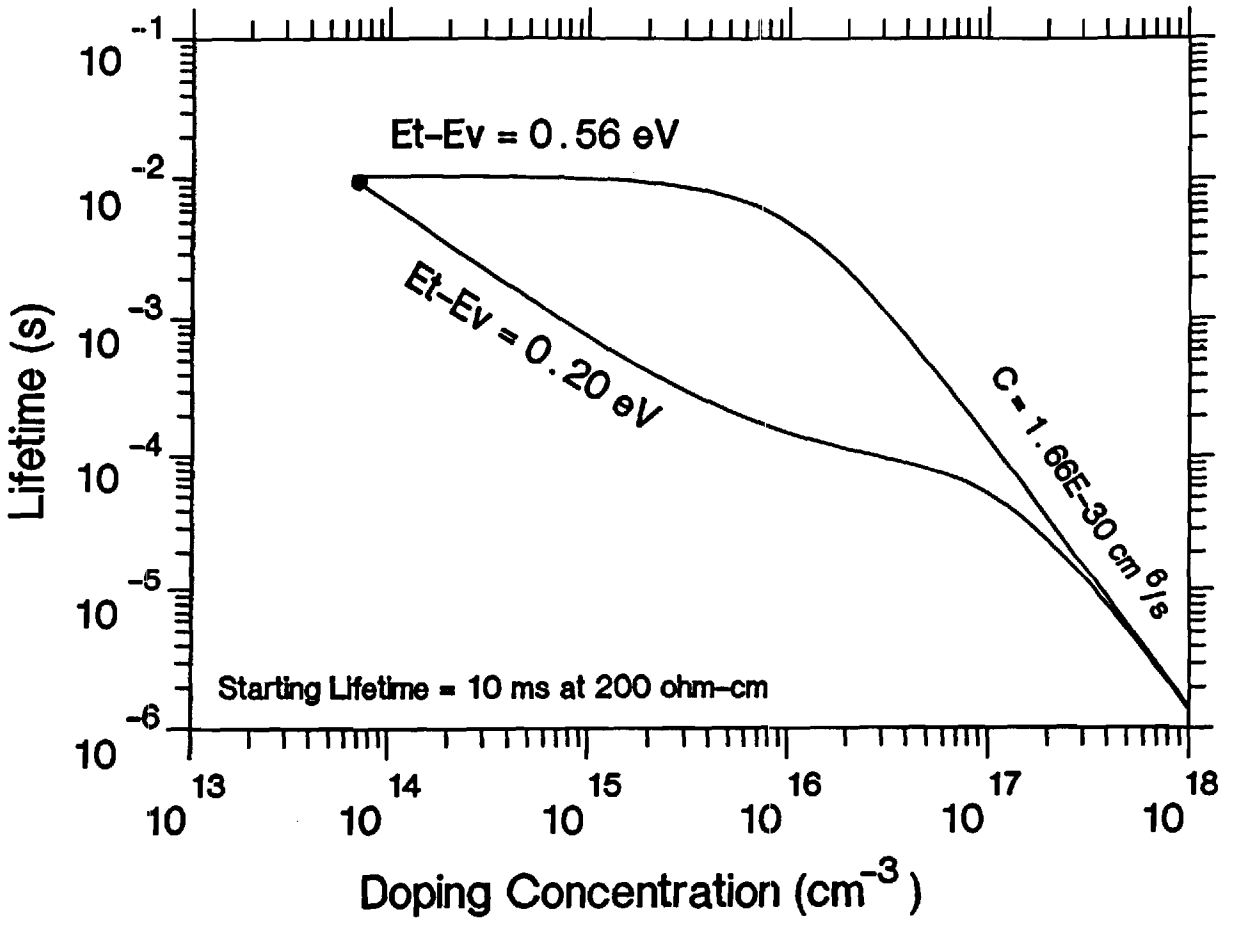

Figure 11. Lifetime Versus Doping Concentration for a Midgap Trap and a Shallow Trap in a Material with 10 msec Starting Lifetime at 200 ohm-cm.

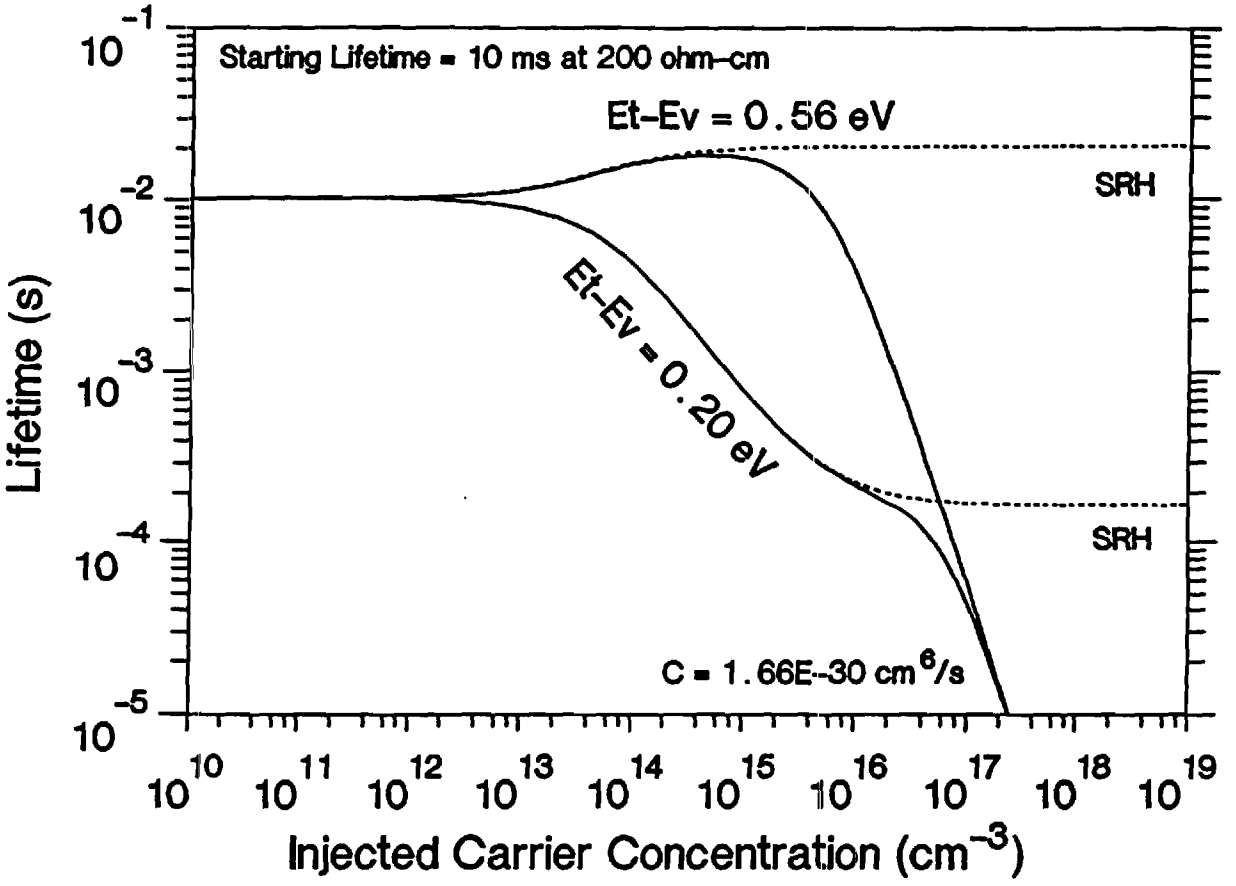

Figure 12. Lifetime Versus Injection Level for a Shallow and Deep Trap in 200 ohm-cm Silicon with 10 msec Lifetime at Low Level Injection.

2.2.3b. Effect of Trap Location on Cell Performance

Figures 13 and 14 show the effect of base doping concentration and trap level location on the performance of cells fabricated on a very high quality (τ = 10 ms at 200 ohm-cm) material, as well as on a low quality (τ = 10 μs at 200 ohm-cm) silicon. The cell design is shown in Table 2. Emitter and BSF recombinations were kept small, J_c = 0.01 pA/cm^2, to emphasize the effect of base lifetime. Model calculations indicate that for high quality material the optimum choice of resistivity will shift from high ($\geq$ 200 ohm-cm) to low (~0.2 ohm-cm) if the trap is located at E_v + 0.20 eV instead of midgap. on the other hand, optimum resistivity for the low quality material remains at ~0.1-0.2 ohm-cm regardless of the trap location. It should be noted that here we have assumed trap density to be independent of doping density. We have shown elsewhere [2] that if trap density increases with doping, then the optimum resistivity for low quality silicon tends to increase.

TABLE 2. Configuration of N^+-P-P^+ Cells Used in Numerical Simulations

1. Cell area of 1 cm^2
2. Series resistance of 0.2 ohm
3. Uniform emitter doping of 2.0 x 10^{19}cm^{-3}
4. Emitter thickness of 0.2 microns
5. Cell thickness of 254 microns
6. Uniform BSF doping of 2.0 x 10^{18}
7. BSF thickness of 2 microns
8. 5% shadow and reflective loss
9. 98% effective back surface reflector
10. FSRV and BSRV of 0 cm/sec

In order to explain the interesting observations in Figure 13, lifetime calculations were performed as a function of base resistivity and injection level. Figures 15 and 16 represent high quality material with a midgap trap and a shallow trap, respectively. Both SRH lifetime, indicated

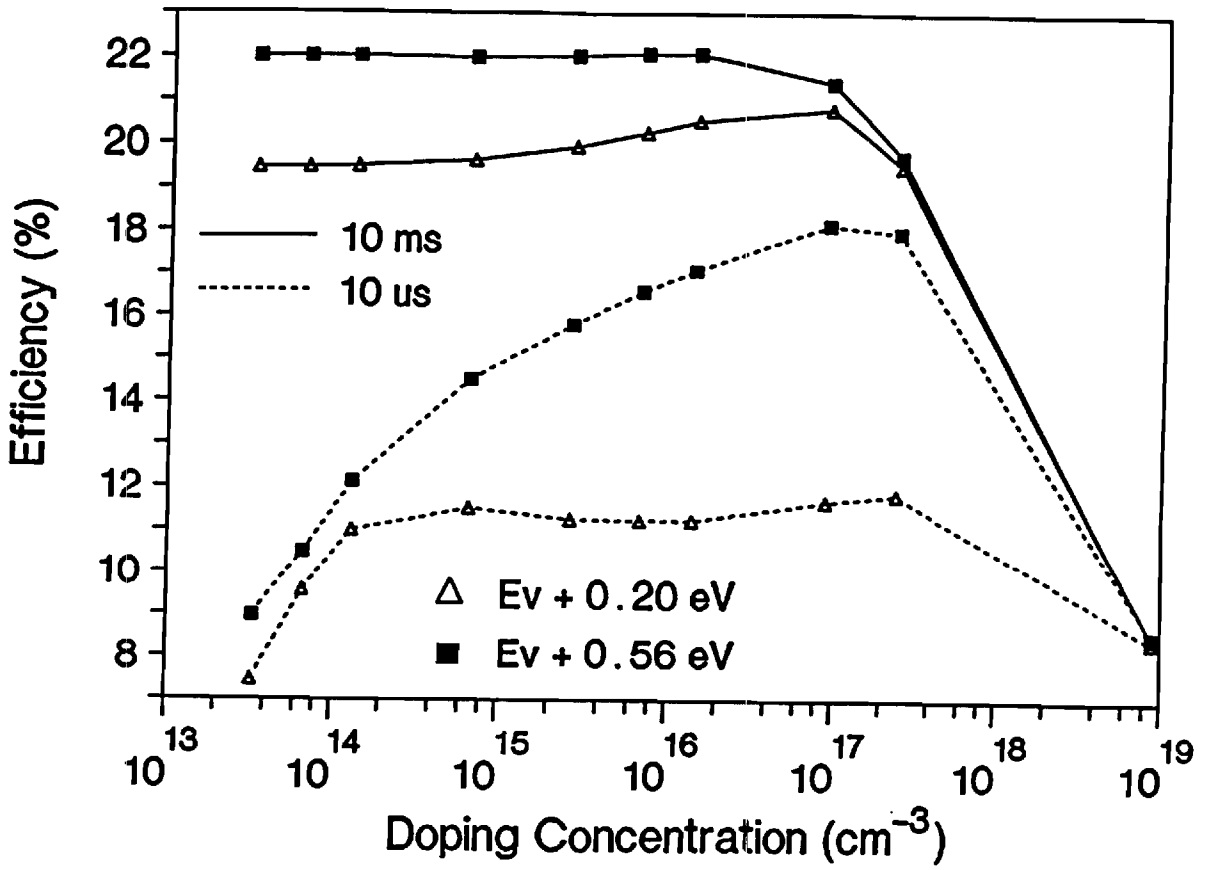

Figure 13. Effect of Base Quality (τ = 10 μsec and 10 msec), Base Doping, and Trap Location on Cell Performance.

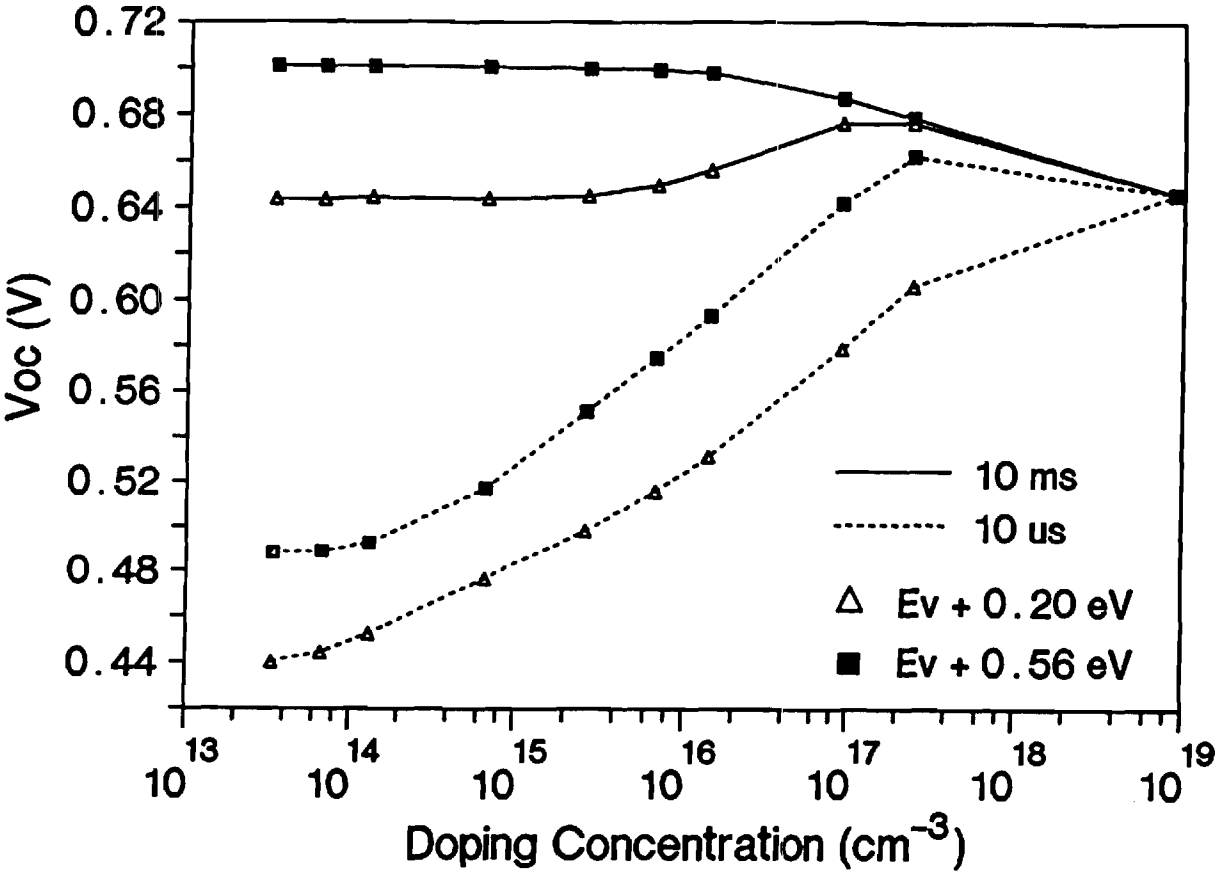

Figure 14. Effect of Base Quality, Base Doping, and Trap Location on V_{oc}.

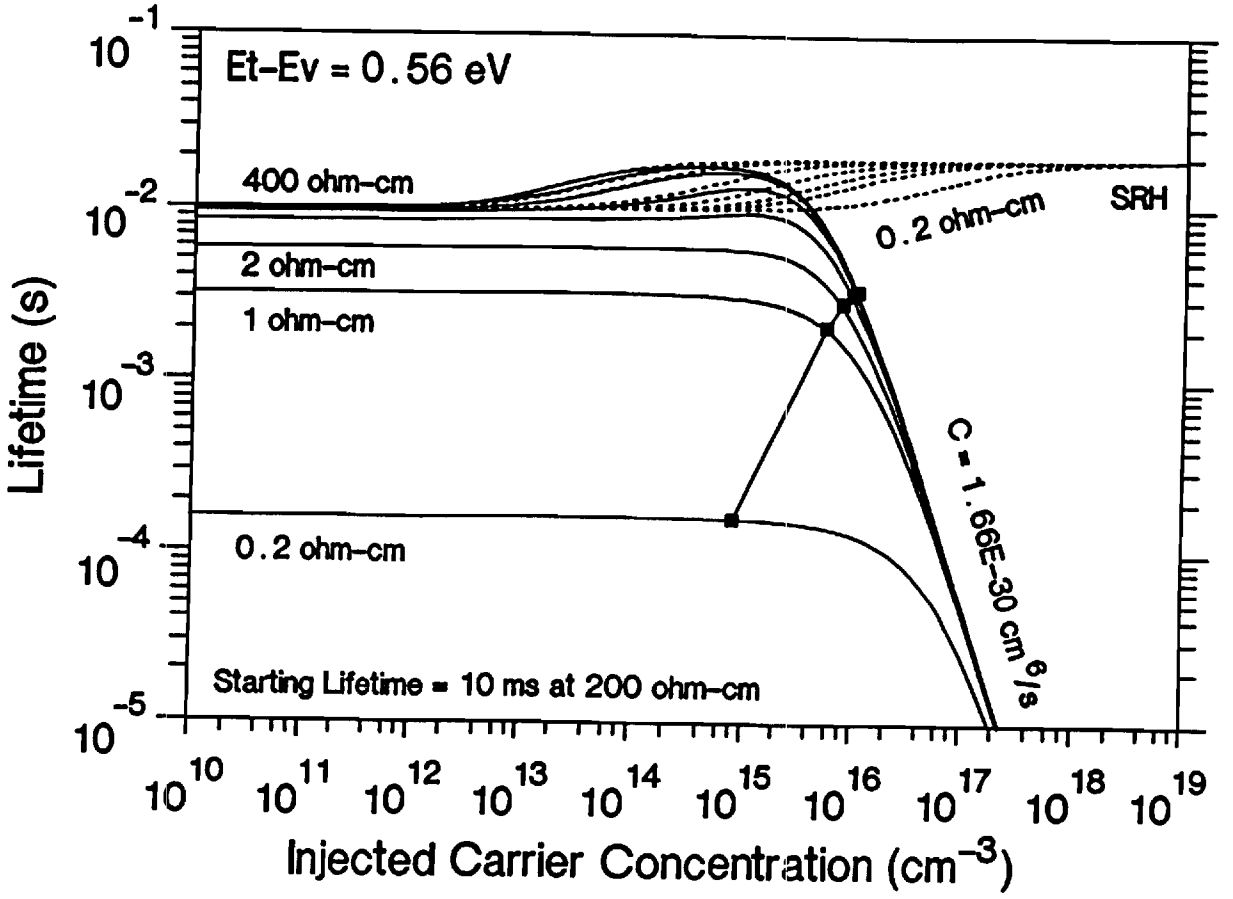

Figure 15. Net Lifetime (Solid Lines) and SRH Lifetime (Dotted Lines) as a Function of Injection Level, Base Doping and Trap Location in a High Quality Silicon (τ = 10 μsec at 200 ohm-cm) with a Midgap Trap. Points Designated Lifetime and Injection Level ag V_{oc}.

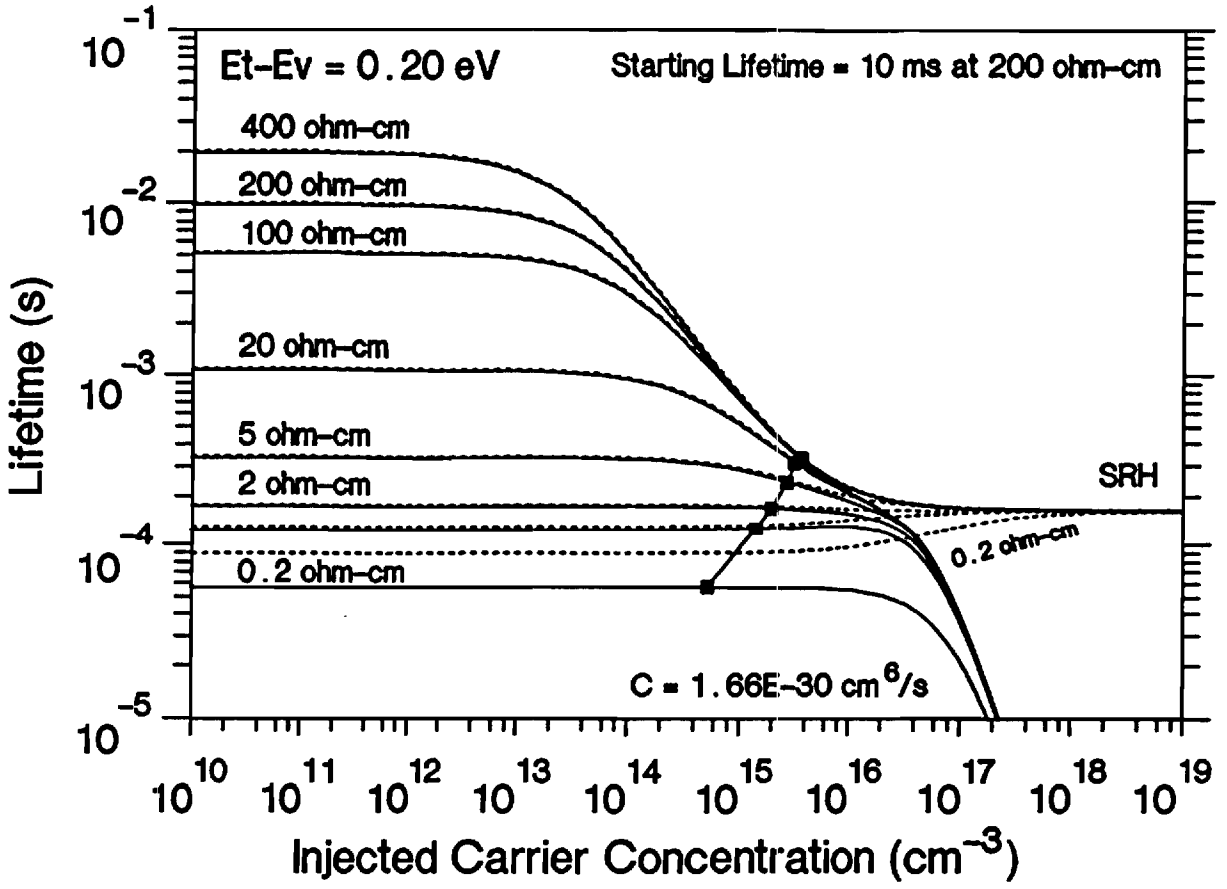

Figure 16. Net Lifetime and SRH Lifetime in a High Quality Silicon (τ = 10 msec at 200 ohm-cm) with a Shallow (0.20 eV) Trap.

by dotted lines, as well as net lifetime, indicated by solid lines, are plotted to delineate which recombination mechanism dominates. A point is shown on each curve indicating the conditions present when the cell is open circuited under illumination.

Figure 15 demonstrates that for high quality silicon with a midgap trap, the lifetime at open circuit is limited by the Auger process. The cells remain under high level injection ($\Delta n > 10\ N_a$) down to a base resistivity of 20 ohm-cm. In this high injection range, Auger recombination limits V_{oc}, and cell performance remains essentially unaffected by resistivity. For cells with base resistivity less than 5 ohm-cm, Figure 15, the lifetime at V_{oc} decreases sharply due to a combination of Auger recombination and bandgap narrowing. Thus, high base resistivity is optimum for high quality material with midgap trap.

Figure 16 shows that for $E_v + 0.2$ eV trap, low level injection lifetime decreases with increased doping density, even for very lightly doped material. In addition, when the cell goes into high injection level ($\Delta n > N_a$), the lifetime begins to fall again due to a decrease in SRH lifetime until Auger recombination takes over. It is interesting to note that in this case lifetime at V_{oc} is limited by τ_{SRH}, and not by Auger recombination. Compared to the midgap trap case, lifetime, injection level, and np product are all smaller, resulting in lower V_{oc} and cell efficiency. Cell efficiency peaks around 0.2 ohm-cm for a shallow trap because V_{oc} reaches a maximum at ~0.1-0.2 ohm-cm, and below that resistivity V_{oc} and J_{sc} begin to drop due to Auger recombination.

In the case of technology that produces low quality silicon (10 μs at 200 ohm-cm), similar analysis, Figure 17, showed that the lifetime and injection level is dictated by SRH lifetime for both midgap and shallow traps. Cell performance peaks at 0.2 ohm-cm, regardless of the trap position, because Δn is small and np/n^2_i product is dominated by the doping density. Below 0.1-0.2 ohm-cm, doping induced Auger recombination and bandgap narrowing begins to lower J_{sc} and cell performance rapidly. Again, V_{oc} and cell performance at the optimum resistivity is higher for the midgap trap because τ_{SRH} and injection levels are higher under illumination, Figure 17.

2.2.3c. Light Trapping Induced Improvement in Cell Performance

Preliminary calculations were performed to determine the effect of light trapping on efficiency of cells with base lifetime ranging from 1 μs to 10 ms. Consistent with Green et al. [3], we also

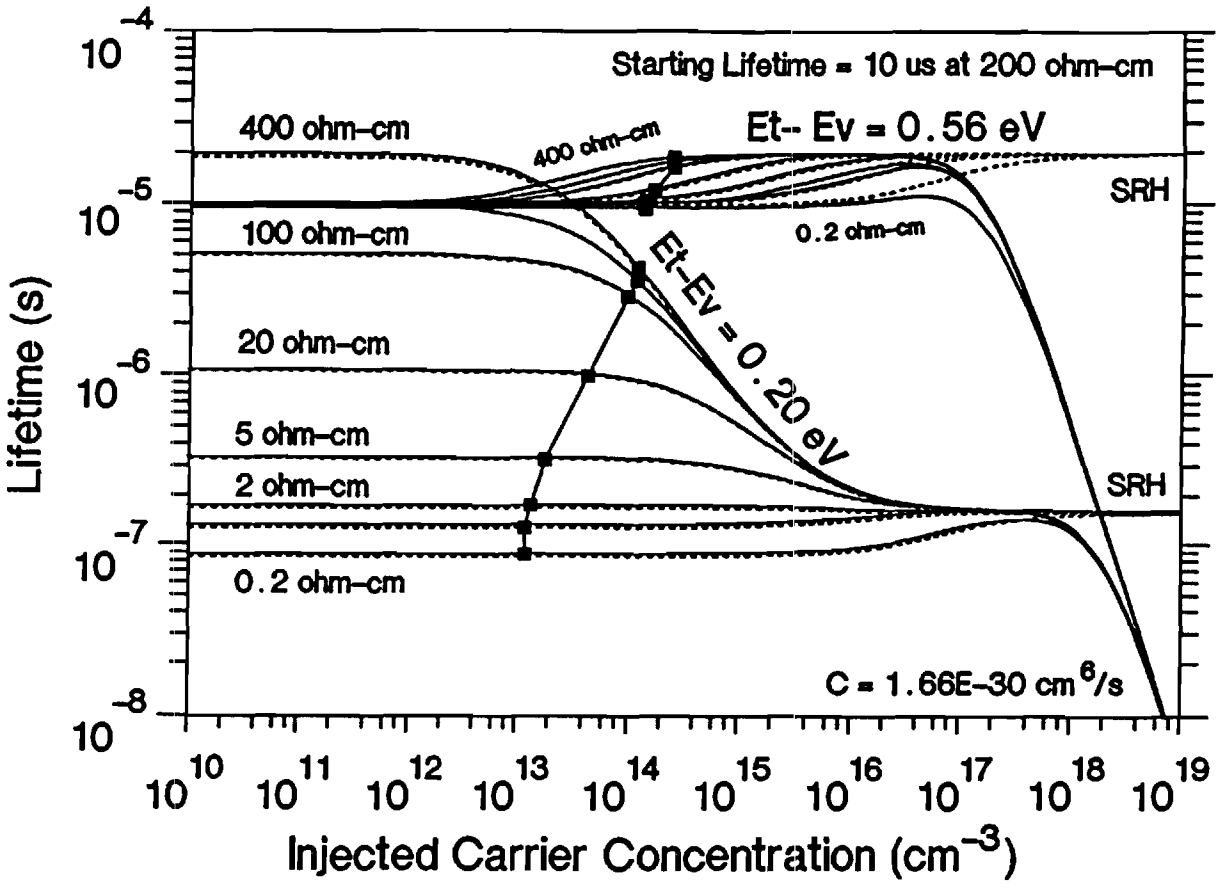

Figure 17. Net Lifetime and SRH Lifetime in a Low Quality Silicon (τ = 10 μsec at 200 ohm-cm) with a Midgap Trap as well as a Shallow Trap.

found, Figure 18, that perpendicular slats, Lambertian, and pyramid-like surface texturing are superior to a flat surface. Perpendicular slat geometry, in which grooves at the top and bottom surfaces run perpendicular to each other, produce maximum improvement in the trapped flux. Slat spacing used as 10 μm and the angle of slats was 53° with respect to horizontal. Figure 19 showed that in spite of the same improvement in the trapped flux, actual increase in cell performance is dictated by the base lifetime. Light trapping in 100 micron thick cells produces significant increases in cell efficiency if the base lifetime is greater than 100 μs. Equally important is the fact that appreciable improvement is observed even in the cells with lifetime as low as 10 μs. Notice that, in Figure 19, base resistivity and cell performance were optimized for each lifetime. The cell design used was similar to that of Table 2 with each lifetime. The cell design used was similar to that of Table 2 with the exception of complementary error doping profiles and FSRV = BSRV = 500 cm/sec.

2.2.4 Conclusions

The importance of trap location and light trapping has been investigated for various qualities of silicon. It is shown that optimum resistivity depends upon the lifetime prior to doping and the trap level location. For a high quality silicon (τ = 10 ms at 200 ohm-cm), high resistivity (> 200 ohm-cm) is optimum if the trap is at midgap, but if the trap is shallow, then the optimum resistivity shifts to about 0.2 ohm-cm. For low quality silicon (10 ms at 200 ohm-cm) optimum resistivity was found to be ~0.1-0.2 ohm-cm, regardless of the trap location. Thus, before buying silicon for a given cell design, one needs to know the starting lifetime and trap location in order to specify resistivity to achieve best cell performance. For the same resistivity and lifetime in silicon prior to illumination, give lower efficiency cells because of lower lifetime and injection level at the cell operating point. We have shown elsewhere [2] that a low quality material (τ = 100 μs at 200 ohm-cm) with midgap trap can give higher optimum efficiency than a somewhat higher quality material (τ = 1 ms at 200 ohm-cm) with a shallow trap.

Finally, we have shown that perpendicular slat type surface texturing can provide appreciable improvement in cell performance even when the base lifetime is in the range of 1-10 μs. Absolute improvement in cell performance due to light trapping increases with lifetime.

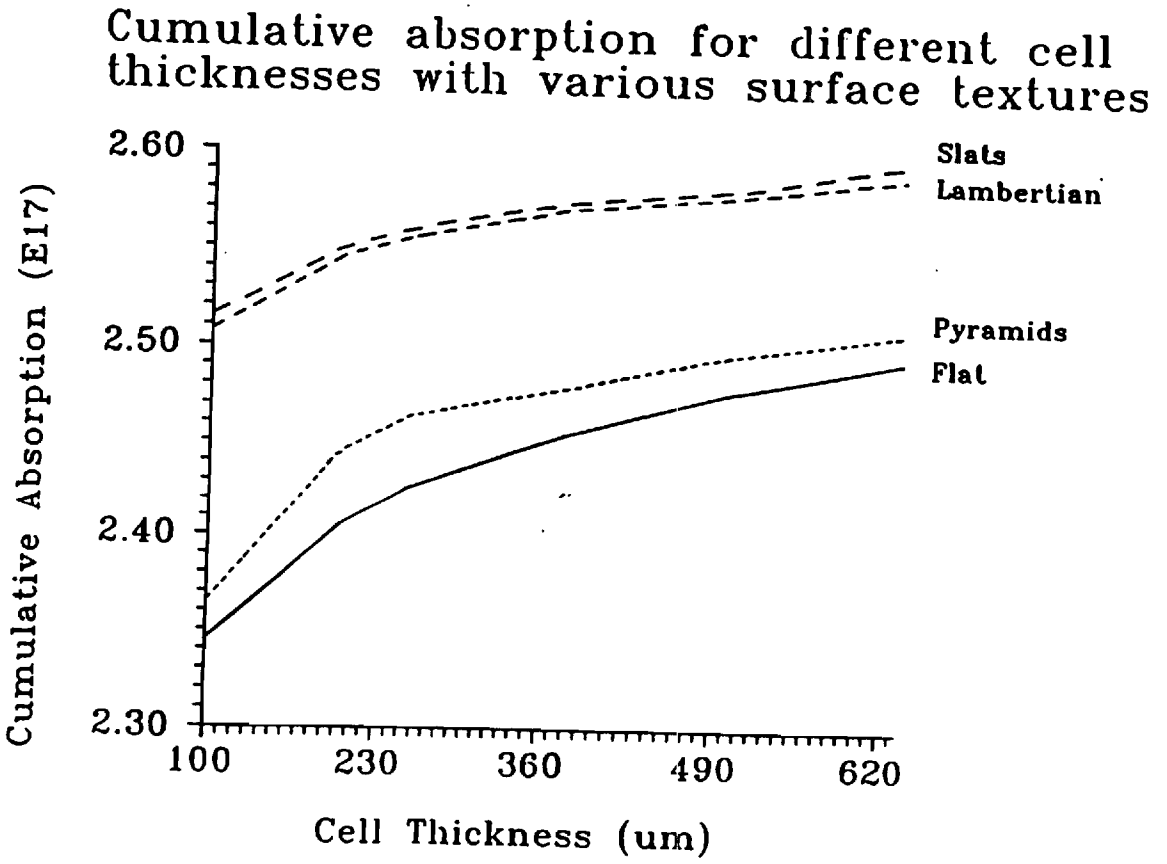

Figure 18. Increased Photon Absorption Due to Various Light Trapping Schemes.

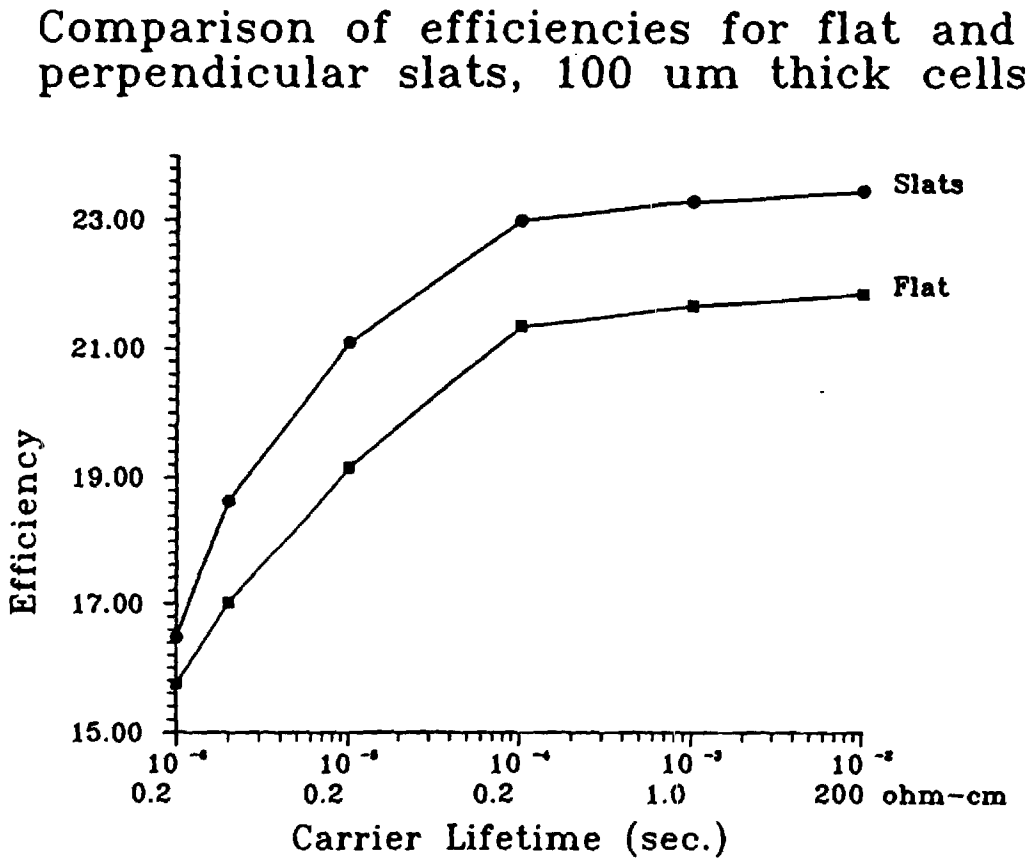

Figure 19. Effect of Light Trapping on the Efficiency of 100 Micron Thick Cells with Base Lifetime Ranging from 1 μsec to 10 msec.

2.3 MATERIAL QUALITY AND DESIGN OPTIMIZATION FOR HIGH EFFICIENCY GaAs SOLAR CELLS

2.3.1 Introduction

Minority carrier lifetime and interface recombination rates are major factors in limiting GaAs solar cell performance [1,2]. To optimize cell characteristics, it is crucial to determine these parameters in existing devices. However, at present, no satisfactory method exists which accurately accomplishes this for GaAs solar cells. The best one can do is to find a window of possible lifetime and recombination velocity values which will satisfy measured cell data [3]. In this paper, we present a methodology to find unique values for lifetime and surface recombination velocity in a GaAs p/n heteroface solar cell by simultaneously matching computer simulated and measured spectral response, leakage current, and I-V characteristics of the cell. The design optimization is done first by improving bulk and interface quality and then the cell structure to show that ~25% one sun efficiency is possible for a cell with a base lifetime of 15 ns. Furthermore, increasing the lifetime to unrealistically high values (~50 ns at 6 x $10^{17}cm^{-3}$ doping level) does not produce significantly higher efficiencies. Since the lifetime in GaAs is controlled by Shockley-Read-Hall (SRH) recombination at the doping levels used in the base of GaAs cells, it is shown that location of deep levels could become important in optimizing the cell design and doping. GaAs heteroface solar cells were fabricated, characterized, and modeled to demonstrate the above effects.

2.3.2 Experimental

GaAs heteroface solar cells were fabricated by the MOCVD technique. A typical cell structure is shown in Fig. 20. Cell performance and spectral response were determined under AM 1.5 conditions at 300 K. The diffusion component of reverse leakage current (J_{01}) was measured by transformed dark I-V measurements [4]. The PC-1D model [5] was used to calculate the spectral response and cell data using the appropriate material and structural parameters. All PC-1D calculations were performed assuming a 5% loss due to shadow and reflection. The reverse leakage current was calculated with the help of an effective recombination velocity (S_e) model which includes the effects of: bandgap narrowing [6]; radiative, Auger, and SRH recombination; front and back surface recombination velocities (FRSV and BSRV, respectively); and device structure. The details

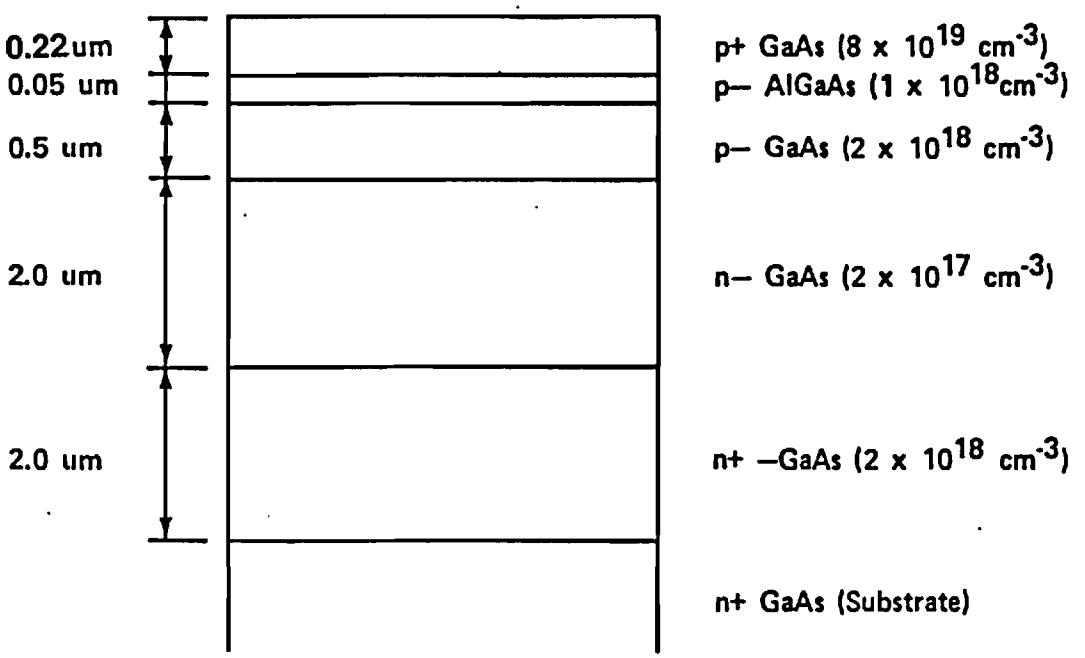

GaAs solar cell structure used in these experiments

V_{OC} = 1.013V J_{SC} = 24.5 mA/cm^2

F.F. = 0.855 Eff = 21.2%

Figure 20. GaAs p/n Heterface Cell Structure used in this Study. Measured Cell Data is Listed.

of this model have been published elsewhere [4,7]. The output of this model is an internal recombination velocity plot through the device structure. The value of S_e at either side of the depletion region yields the emitter and base components (J_{oe} and J_{ob}, respectively) of J_{01} according to

$$J_{01} = J_{oe} + J_{ob} = (q/n^2_i)(N_a S_{eje} + N_d S_{ejb}) \quad (17)$$

which are summed to match the measured J_{01}.

2.3.3 Results and Discussion

2.3.3a. Methodology for Determining Lifetime and Recombination Velocity

A threefold approach was established to accurately determine lifetime, FSRV, and BSRV for an MOCVD-grown GaAs p/n heteroface solar cell, Figure 20, with a cell efficiency of 21.2%. The first step was to match the spectral response.

Figure 21 shows a good match between the simulated and measured spectral response for a net base lifetime of 8 ns and FSRV equal to 1.25×10^5 cm/s. BSRV was found to have no effect on the spectral response of this particular device structure. Lifetimes in the emitter and buffer were determined to be 2 and 5.5 ns, respectively, by using the SRH lifetime calculated from the net base lifetime and by properly accounting for the doping dependence of the Auger (C) and radiative (B) recombination terms in the equation

$$1/T = 1/\tau_{SRH} + BN + CN^2 \quad (18)$$

as described previously [4]. The slight mismatch at wavelengths below 450 nm is due to absorption in the AlGaAs window layer which was not accounted for in the modeling. It should be recognized that it is possible to match the spectral response with a range of lifetime and FSRV values [3], therefore, further modeling steps were necessary to determine the exact values.

The second step in the methodology was to model J_{01}. This was calculated using the lifetime profile (T_e, T_b, T_{buffer}) and recombination velocities which gave a good spectral response match.

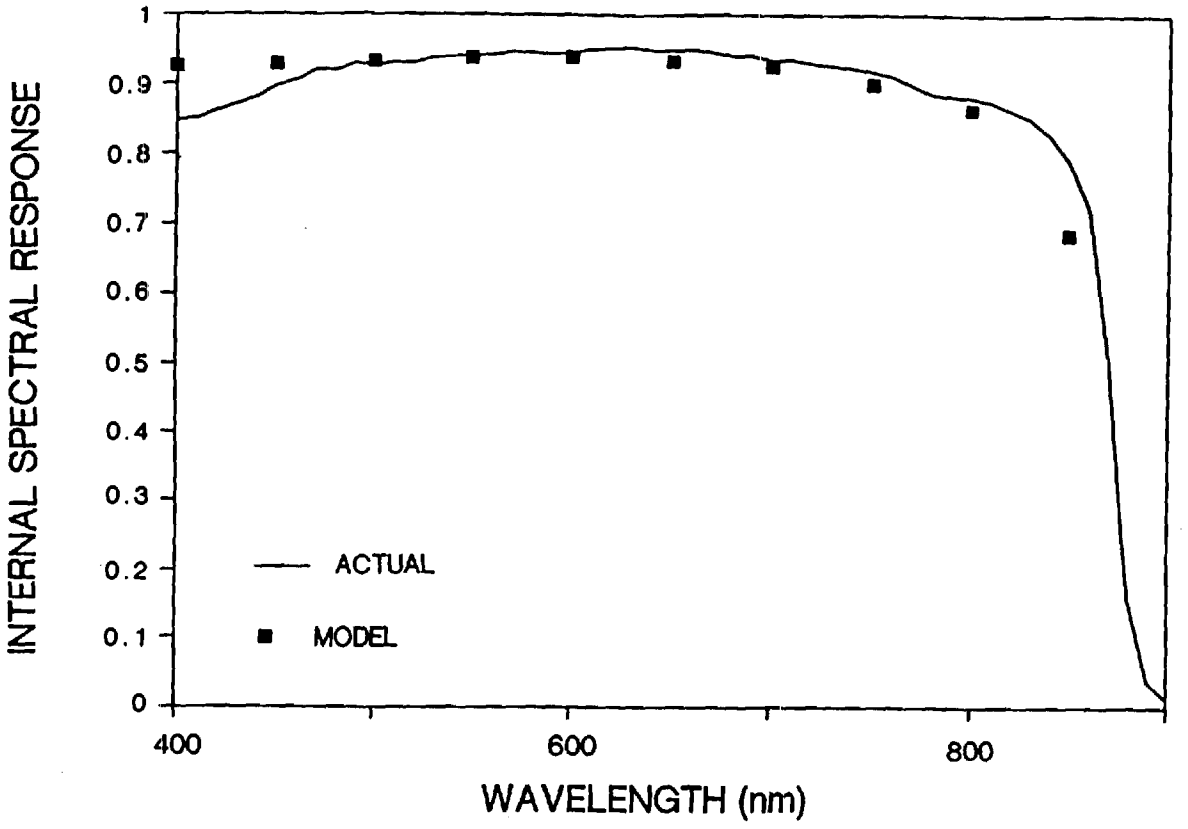

Figure 21. Comparison of Actual Spectral Response (solid line) with Modeled Spectral Response (blocks) as Calculated from PC-1D.

This simulation was done with the help of an effective recombination velocity model. Figure 22 shows a plot of S_e for various values of FSRV and BSRV. J_{ob} in this cell was found to be pinned at 0.85×10^{-19} A/cm^2 for all values of BSRV again supporting the fact that back surface passivation is not important for this design. In addition, it was found that $J_{oe} = 0.55 \times 10^{-19}$ A/cm^2 for FSRV = 1.25×10^5 cm/s, giving $J_{01} = (J_{oe} + J_{ob}) = 1.40 \times 10^{-19}$ A/cm^2, which is in good agreement with the measured J_{01} of 1.29×10^{-19} A/cm^2 and supports the choice of FSRV and base lifetime. Since J_{ob} ~ 70% of J_{01}, this cell is base/buffer dominated and not limited by the emitter side of the junction.

The third and final test of these values of FSRV and base lifetime is the match between the measured and calculated cell data. Table 3 shows excellent agreement between calculated and measured values of J_{sc}, V_{oc}, and efficiency for this cell.

2.3.3b. Design Optimization for High Efficiency Cells

2.3.3b1. Effect of Material Quality and Interface Recombination Velocity. Having established the threefold match using a single set of parameters in Section 2.3.3a, the cell design was optimized. Figure 22 shows that J_{oe} can be significantly lowered by improving the AlGaAs/GaAs heteroface quality so that FSRV = 1×10^4 cm/s which is attainable for the $Al_{0.9}Ga_{0.1}$ As/GaAs heteroface [8]. This will increase V_{oc} from 1.010 to 1.016 V by virtue of lower S_{eje} and J_{sc} from 26.56 to 26.59 mA/cm^2 due to reduced recombination in the emitter, raising cell efficiency to 23%. Figure 22 also shows that little would be gained for FSRV values below ~1×10^4 cm/s, even if better passivation was possible. Since for this device design, J_{ob} is independent of BSRV and is set by the base diffusion velocity, D/L, the obvious way to gain higher performance is to improve the base material quality. If the base lifetime in this cell is increased from 8 to 15 ns, the efficiency will increase to 24.1%, Table 3. The efficiency can be raised to ~24,4% by increasing the base doping to 5×10^{17}cm^{-3} and buffer doping to 2.5×10^{18}cm^{-3} which primarily increases V_{oc} without sacrificing J_{sc}, assuming the lifetime is independent of doping in the base, Table 3 [9,10]. If the base lifetime is increased further to 20 ns, the efficiency climbs to only ~24.76%, indicating it has apparently reached a plateau. Further increase in efficiency, without going to unreasonably high lifetime, can only come from optimizing the base and buffer regions since the emitter design is already near optimum.

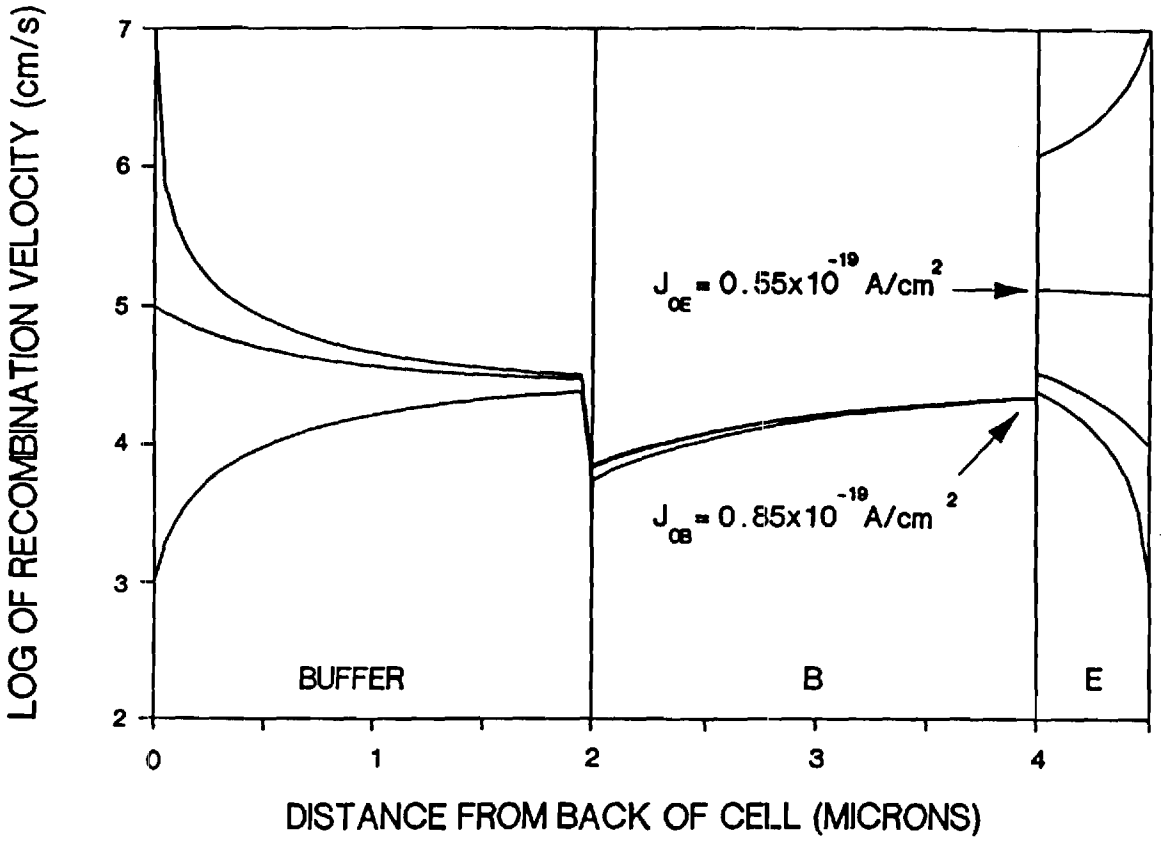

Figure 22. Plot of Effective Recombination Velocity, S_e, for Various Values of FSRV and BSRV. Emitter and Base Leakage Current Components are Noted for the Cell-Matching S_e Plot.

TABLE 3. Cell Data Calculated Using PC-1D for the Device Structures Listed. An 0.5 um Emitter with $N_A = 2x10^{18}cm^{-3}$ was Used in Each Calculation.

width (um) base	buffer	Doping (cm^{-3}) base	buffer	FSRV (cm/s)	BSRV (cm/s)	T_B (ns)	V_{oc} (volts)	J_{sc} (mA/cm^2)	Eff (%)
				Actual					
2.0	2.0	$2.0x10^{17}$	$2.0x10^{18}$				1.013	24.5	21.2
				Match					
2.0	2.0	$2.0x10^{17}$	$2.0x10^{18}$	$1.25x10^5$	$1.0x10^6$	8	1.01	24.56	21.39
				Material and Interface Optimization					
2.0	2.0	$2.0x10^{17}$	$2.0x10^{18}$	$1.0x10^4$	$1.0x10^6$	8	1.016	24.59	23.02
2.0	2.0	$2.0x10^{17}$	$2.0x10^{18}$	$1.0x10^4$	$1.0x10^4$	8	1.017	26.71	23.13
2.0	2.0	$2.0x10^{17}$	$2.0x10^{18}$	$1.0x10^4$	$1.0x10^4$	15	1.032	27.11	24.17
2.0	2.0	$5.0x10^{17}$	$2.5x10^{18}$	$1.0x10^4$	$1.0x10^4$	15	1.048	26.83	24.40
2.0	2.0	$5.0x10^{17}$	$2.5x10^{18}$	$1.0x10^4$	$1.0x10^4$	20	1.054	26.95	24.76
				Design Optimization					
1.2	1.2	$6.0x10^{17}$	$2.5x10^{18}$	$1.0x10^4$	$1.0x10^3$	15	1.055	27.04	24.75
1.3	1.1	$6.0x10^{17}$	$2.5x10^{18}$	$1.0x10^4$	$1.0x10^3$	20	1.059	27.10	25.05
1.5	1.1	$6.0x10^{17}$	$2.5x10^{18}$	$1.0x10^4$	$1.0x10^3$	30	1.063	27.19	25.31
1.9	1.1	$6.0x10^{17}$	$2.5x10^{18}$	$1.0x10^4$	$1.0x10^3$	55	1.068	27.31	25.62

2.3.3b2. Optimized Device Structures for High Efficiency. The next step toward increasing cell performance was to optimize the base and buffer region. Optimum thicknesses of the base and buffer are dictated by the lifetime. A tradeoff exists between high carrier collection efficiency in the base and the photon absorption in the lower lifetime, heavily doped buffer. To reduce the latter effect, the base width must be increased. However, the minority carrier diffusion length then limits the collection of carriers generated deep in the base which is compounded by the reduced effectiveness of the back surface field. In order to absorb ~97% of the incident photons in the base, a base width of ~3 um is necessary with an emitter thickness of 0.5 um. However, to collect nearly all the photogenerated carriers from the base it was found that a diffusion length of about three times the base thickness (~9 um) was necessary. This would require a base lifetime greater than the

fundamental limit at the doping levels used in GaAs solar cells. One way to circumvent this limitation is to employ a thin base to maximize collection by allowing the base to maximize collection by allowing the diffusion length to be much greater than the base thickness, while maintaining good material quality in the active buffer which would now require good back surface passivation. For a thin base cell, the buffer thickness should also be reduced because S_{ejb} depends upon S_e at the base/buffer interface which, in turn, depends on the buffer thickness and BSRV, Figure 23.

Based on the above considerations, optimized device structures and the corresponding cell efficiencies for base lifetimes of 15, 20, 30, and 55 ns are shown in Table 3. A p-type emitter with a thickness of 0.5 um, doping of 2 x $10^{18}cm^{-3}$, a lifetime of 2 ns, and an FSRV of 1 x 10^4 cm/s was used in all designs. Bandgap narrowing [6] in this emitter was found to lower V_{oc} by 14 mV without affecting the J_{sc}. Optimum values for base and buffer doping were found to be 6 x 10^{17} and 2.5 x $10^{18}cm^{-3}$, respectively, for each lifetime case, assuming base lifetime is independent of doping [9,10]. The base width for each lifetime was optimized for maximum efficiency. Figure 24 shows that the optimum base width increases from 1.1 um for a 15 ns base to 1.9 um for a 55 ns base. The optimized buffer thickness for each case is listed in Table 3. An FSRV of 1 x 10^4 cm/s and BSRV of 1 x 10^3 cm/s (achievable from an $Al_{0.3}Ga_{0.7}As$/GaAs heterojunction [11]) was found to be necessary to obtain maximum efficiency for each lifetime, Figures 25a and 25b. Model calculations indicate that a maximum efficiency of ~25.6% can be realized for a base lifetime of 55 ns (fundamental lifetime limit at 6 x $10^{17}cm^{-3}$ doping), Figure 24 and Table 3. This is less than one absolute percent higher than the maximum efficiency of ~24.75% obtained from the 15 ns base. Hence, there is apparently little point in improving base material quality beyond 15-20 ns if the proper device design is employed.

It is also noteworthy that the maximum efficiency (24.75%) for the 15 ns base design (base width of 1.1 um) is ~0.4% absolute higher than the "optimized" thicker device design (base + buffer thickness = 4 um). This increase occurs in spite of the fact that 5.5% of the incident light is not absorbed at all in this 2.9 um device, whereas all but ~1% of the incident light is absorbed in the 4.5 um device. Thus we run into a base lifetime dependent tradeoff between the increase in carrier collection for thinner structures and a decrease in total amount of photons absorbed within the device, Figure 24, which limits the practically achievable one sun efficiencies to less than 26%.

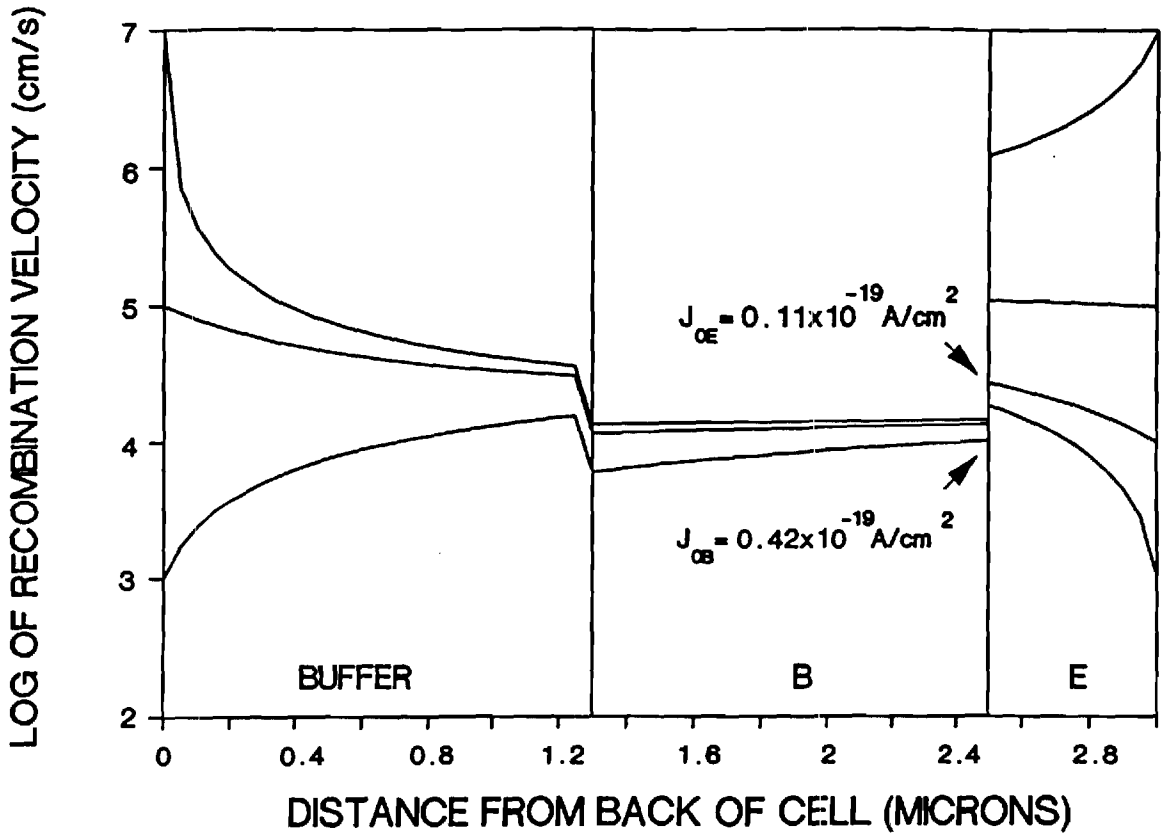

Figure 23. Plot of Effective Recombination Velocity, S_e, for Thinned Device Structure Indicating the Importance of BSRV and Buffer Thickness.

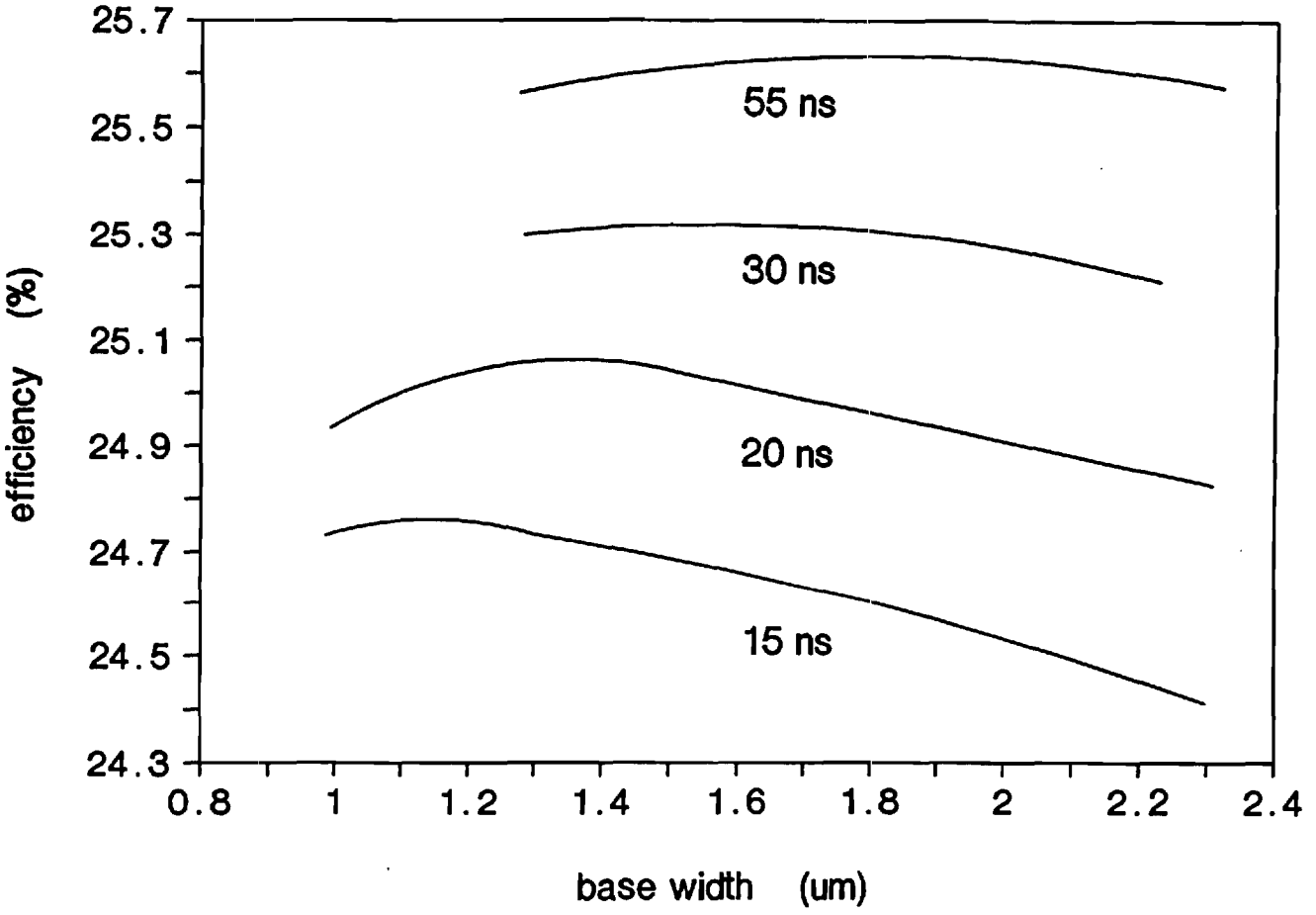

Figure 24. Variation of Cell Efficiency versus Base Thickness for Base Lifetime of 15, 20, 30, and 55 ns at the Optimized Designs Listed in Table 1.

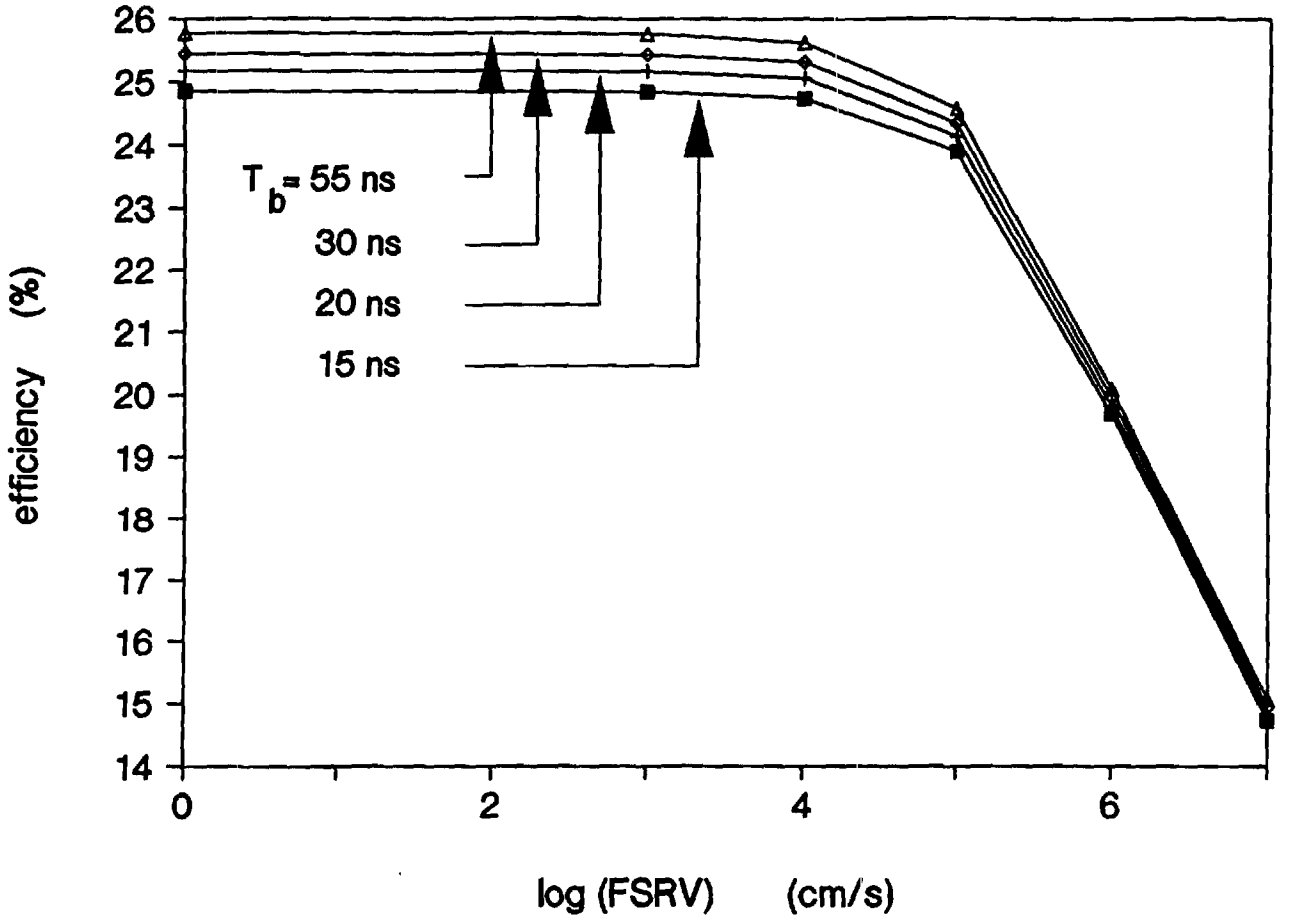

Figure 25.a. Variation of Cell Efficiency versus (a) FSRV and (b) BSRV for 15, 20, 30, and 55 ns Thin Base Designs.

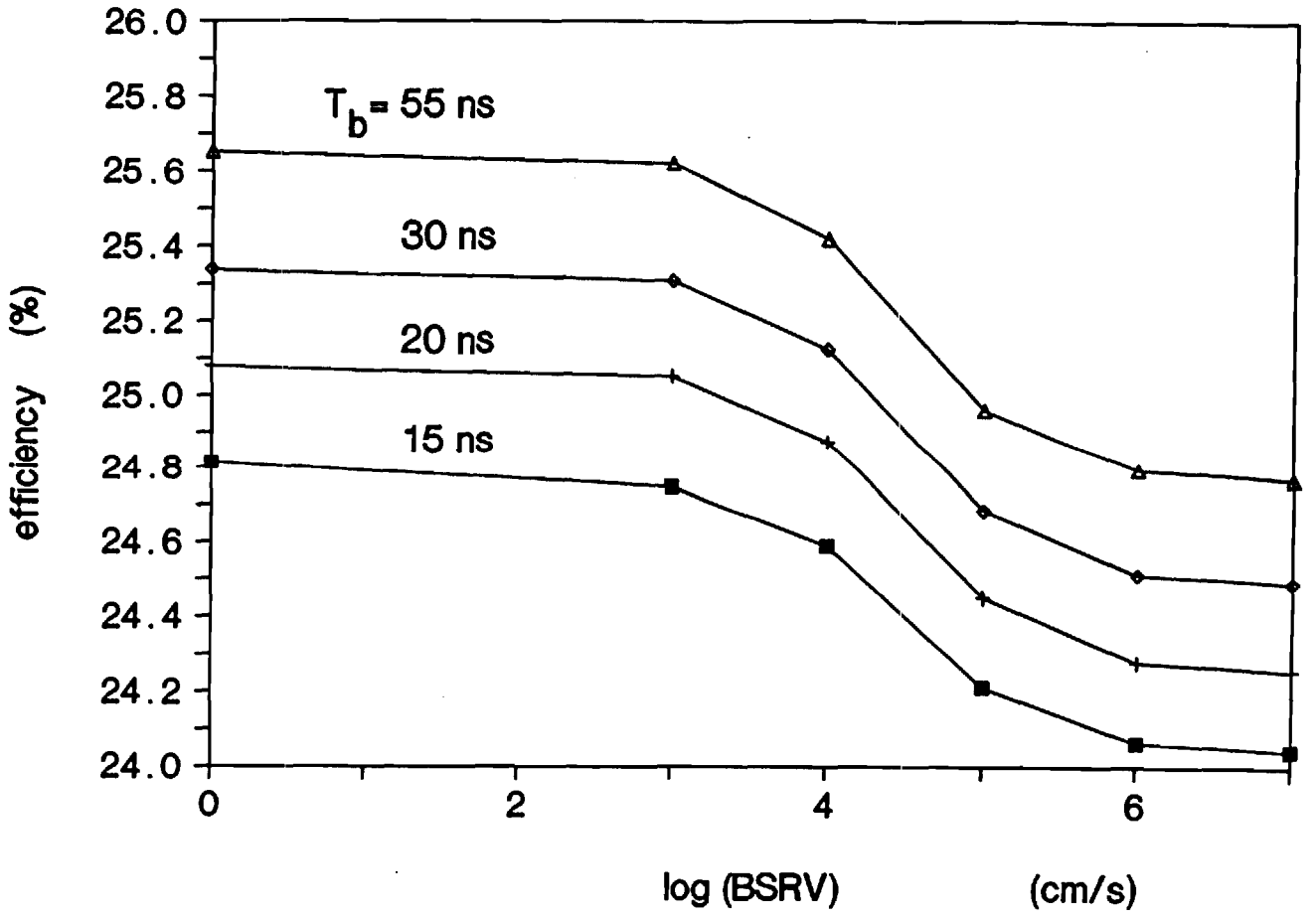

Figure 25.b. Variation of Cell Efficiency versus (a) FSRV and (b) BSRV for 15, 20, 30, and 55 ns Thin Base Designs.

Further increase in cell performance can only come from surface texturing or light trapping techniques to increase the photon absorption in the base without increasing the base width.

2.3.3c. Effect of Deep Level Position on Cell Optimization

All of the preceding model calculations assumed that the base lifetime, which is largely controlled by SRH recombination via deep levels, is independent of doping. This assumption is valid only if the lifetime limiting deep level is at or near the midgap region. While this has been found to be the case for melt-grown GaAs [10], this may not be necessarily true for all types of GaAs, especially expitaxially grown GaAs, where some deep levels have been found to reside as close as 0.17 eV below the conduction band edge [12] and 0.27 eV above the valence bandedge [13], respectively. To investigate what effects this has on the material lifetime as well as cell performance, the net lifetime was modeled according to

$$1/\tau = 1/\tau_{SRH} + BN + CN^2 \tag{19}$$

where

$$\tau_{SRH} = \tau_{no}(p_o + p_1) + \tau_{po}(n_o + n_1) \tag{20}$$

and n_1, p_1, τ_{no}, and τ_{po} are given their usual meanings as in [14], and B and C are the radiative and Auger recombination coefficients, respectively, as calculated from [9]. Assuming low level injection conditions and $\tau_{no} = \tau_{po}$, Eq. (19) has been plotted for n-type GaAs as a function of doping level for different deep levels, Figure 26. Indeed we see that the lifetime does not depend on doping in the range of interest here (1×10^{17} - $1 \times 10^{18}cm^{-3}$) and tails off above ~$1 \times 10^{18}cm^{-3}$ due to Auger recombination [9]. Deep levels apparently affect the lifetime only for doping levels below $1 \times 10^{16}cm^{-3}$ in both n-type and p-type GaAs.

In the above example, we assumed $\tau_{no} = \tau_{po}$ = a constant for each deep level which changed the initial value of the lifetimes. However, if the technology or the quality of the GaAs layer is defined by a fixed lifetime at some lower doping level ($1 \times 10^{16}cm^{-3}$), then the position of the deep level can influence the device design and cell performance. This case is plotted for n-type GaAs with a starting lifetime of 20 ns at $1 \times 10^{16}cm^{-3}$ doping (Figure 27a) and for p-type GaAs with a starting

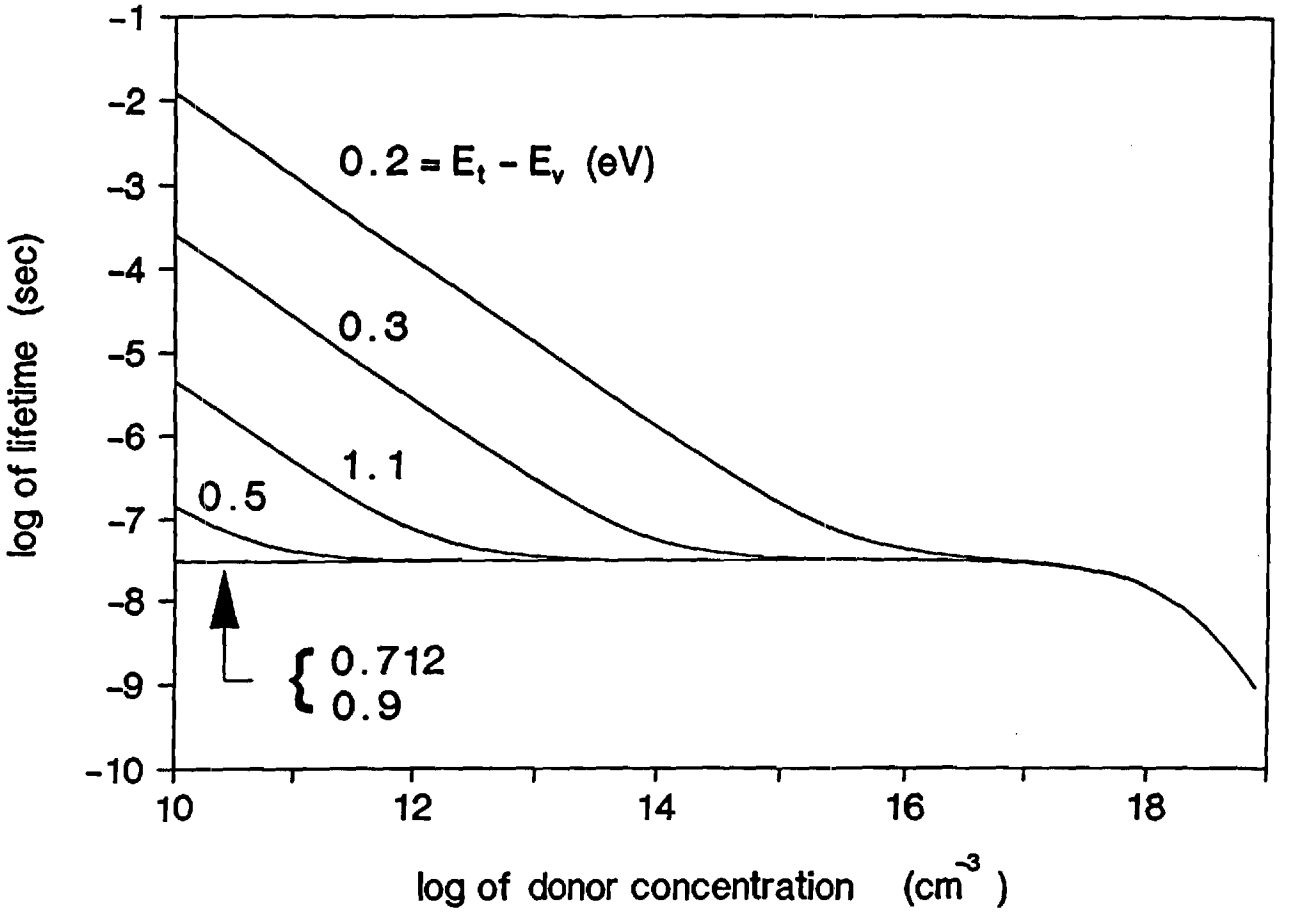

Figure 26. Total Minority Carrier Lifetime as a Function of Doping Density in n-type GaAs Including Doping Dependent SRH Lifetime and Radiative and Auger Lifetimes for Various Trap Levels as Measured with Respect to the VAlence Band Edge.

lifetime of 10 ns at 1 x $10^{16}cm^{-3}$ doping (Figure 27b). Here we see a strong doping dependence of lifetime dictated by deep level position in the doping concentration range of interest. N-type GaAs doped to 6 x $10^{17}cm^{-3}$ now shows a decrease in lifetime from 15 to 11 ns if the deep level is shifted from midgap to Ev + 0.2 eV. This results in a decrease of ~0.5 um in minority carrier diffusion length causing a reduction in cell efficiency from 24.75% to 24.50% for the thin base 15 ns optimized design in Table 3. A larger effect was observed for the original 4.5 um design, where efficiency dropped from 24.4% to 24.0% indicating that the thin base design, as would be expected, is more forgiving to lifetime variations. P-type GaAs shows similar behavior in Figure 27b. In both cases, we see that deep levels which are closest to the valence band severely limit the lifetime for both p and n-type GaAs, while those closer to the conduction band have little effect on the lifetime. This is a result of the large density of states in the valence band (N_v = 4.2 x $10^{17}cm^{-3}$ at 300 K) [15] which allows the p_1 term to dominate over the n_1 term in the SRH lifetime equation, even for traps which are very close to the conduction band. Hence, we see that this lifetime dependence on deep level position can influence optimized cell design by affecting the diffusion length. Future work will involve a more quantitative treatment of this observation and effect on GaAs devices.

2.3.4 . Conclusions

In conclusion, we have developed a threefold methodology which consists of simultaneously matching simulated and measured spectral response, leakage current, and cell data to determine minority carrier lifetime, FSRV, and BSRV. For a 21.2% p/n heteroface cell studied here, a net base lifetime of 8 ns and an FSRV of 1.25 x 10^5 cm/s was necessary to obtain the match. The cell performance was then optimized first by improving the material and interface quality without altering the cell structure which resulted in efficiencies of 24.4% for a 15 ns base. Further improvements were realized by thinning the base so that the buffer becomes an active part of the device, forming essentially a two-step base. This structure, however, requires back surface passivation and a thinner buffer to maximize cell efficiency. Optimized cell designs with efficiencies of 24.8% and 25.1% were established for 15 and 20 ns base lifetimes, respectively. Even if the lifetime is increased to the fundamental limit, efficiencies of only ~25.6% can be obtained for realistic values of recombination velocities, reflection losses, and AlGaAs absorption.

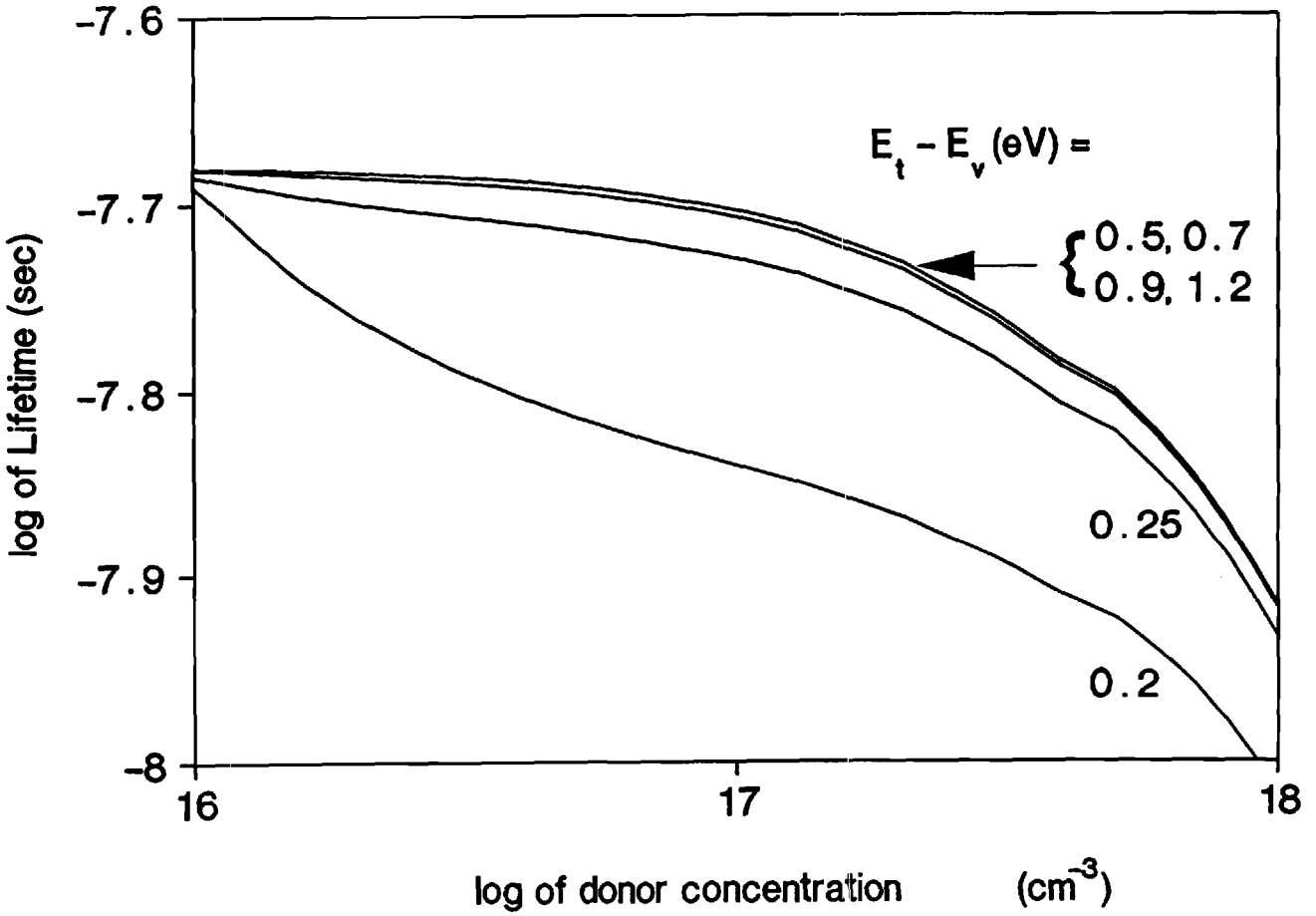

Figure 27.a. Total Minority Carrier Lifetime as a Function of Doping for Various Deep Levels Assuming a Constant Starting Lifetime of (a) 20 ns at 1 x 10^{16} cm^{-3} for n-GaAs and (b) 10 ns at 1 x 10^{16} cm^{-3} for p-GaAs.

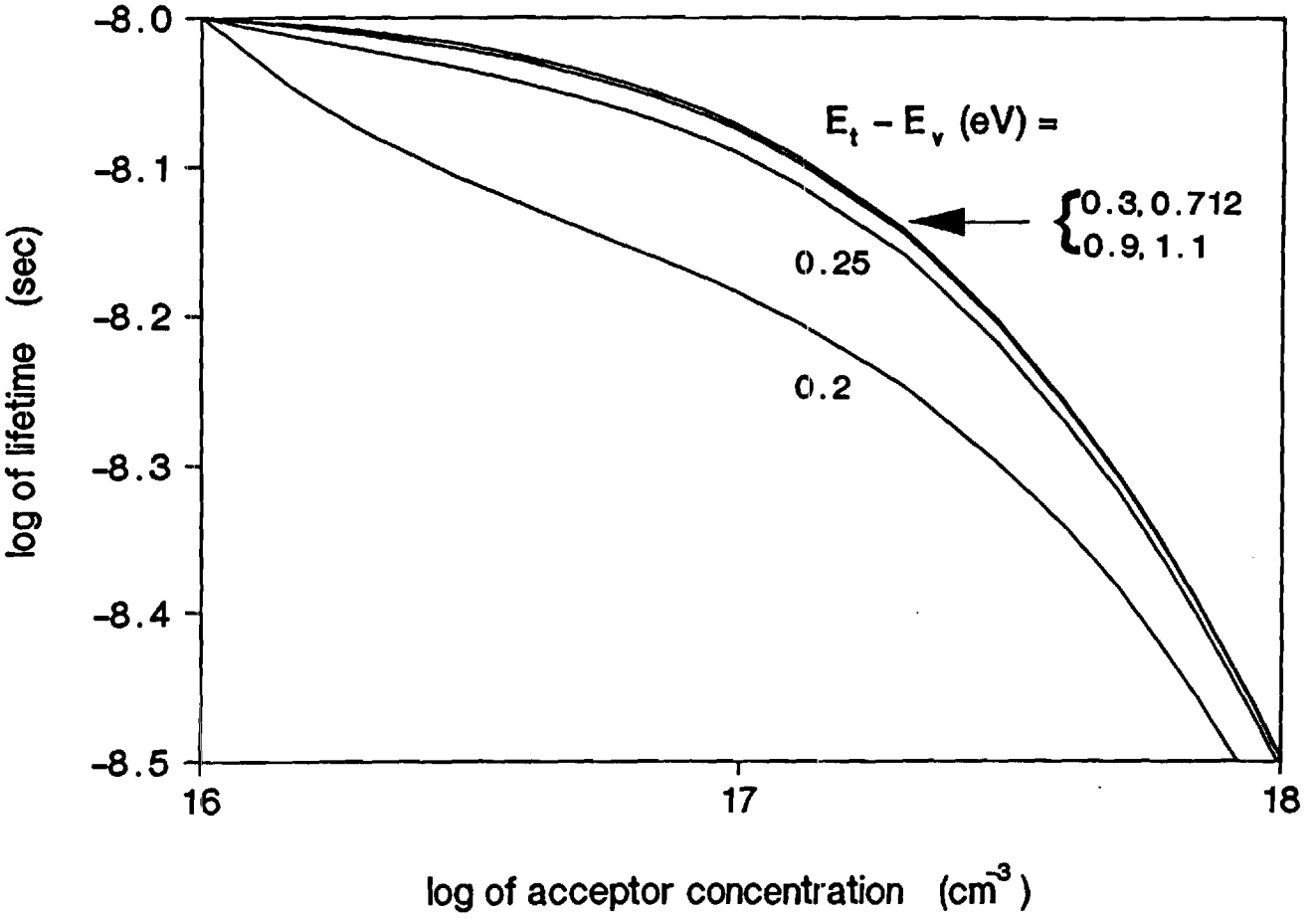

Figure 27. b. Total Minority Carrier Lifetime as a Function of Doping for Various Deep Levels Assuming a Constant Starting Lifetime of (a) 20 ns at 1 x 10^{16} cm^{-3} for n-GaAs and (b) 10 ns at 1 x 10^{16} cm^{-3} for p-GaAs.

The influence of a doping dependent SRH lifetime was investigated and it was found that deep levels near the valence band edge in GaAs can significantly lower the lifetime of doping levels commonly used in GaAs solar cells. This can have an impact on the cell performance and optimized cell design.

2.4 THE EFFECT OF DEEP LEVELS ON MINORITY CARRIER LIFETIME IN n-TYPE GaAs AND THEIR INFLUENCE ON SOLAR CELL DESIGN

2.4.1 Introduction

The bulk minority carrier lifetime in compound semiconductors such as GaAs is a crucial parameter for obtaining performance in optoelectronic devices such as solar cells, lasers, and LEDs. The optimum design of such devices requires a knowledge of the minority carrier lifetime dependence on both deep level characteristics (energy level, cross section, and density) and dopant concentration. While the effects of Auger [1,2] and radiative [3,4] recombination on the minority carrier lifetime have been well documented both experimentally and theoretically in the literature, relatively little has been done concerning the influence of the defect-specific Shockley-Read-Hall (SRH) lifetime on the overall minority carrier lifetime and device performance. This is in part due to earlier published experimental data which showed that the minority carrier lifetime in GaAs was constant below a doping concentration of ~1 x $10^{18}cm^{-3}$ for n-type material [5] and below ~ mid 10^{17}'s for p-type material [6]. However, other published experimental data shows a strong doping dependence of minority carrier lifetime down to a doping level of ~2 x $10^{15}cm^{-3}$ in LPE-grown GaAs where only defect induced (SRH) recombination is important [7]. This scatter in the reported lifetime values for different growth and preparation techniques can only be attributed to different defects and possible domination of SRH recombination because intrinsic recombination mechanisms such as Auger and radiative processes are independent of growth technique. This section shows that exact knowledge of lifetime variation with deep level characteristics and doping concentration is critical for optimum device design since much of the design criteria is centered about assumed lifetime behavior.

In this section, GaAs heteroface solar cells are used as an example to show the impact of the SRH lifetime on device performance and design optimization for various deep level positions and trap parameters (cross section and density). First, a theoretical calculation of the doping dependence of the SRH lifetime in n-type GaAs is performed for different quality GaAs as a function of the characteristics of deep levels within the bandgap. Then the effects of deep levels on the performance of p.n heteroface GaAs solar cells are revealed with the help of the PC-1D device modeling program [8]. It is shown how cell efficiency can be severely miscalculated, and device structures erroneously

designed if certain deep levels are present and not properly accounted for. Some of these effects were also experimentally validated by performing Deep Level Transient Spectroscopy (DLTS) measurements on GaAs heteroface solar cells whose poor efficiency was explained in terms of the observed deep level and calculated lifetime behavior(s). Finally, some novel heteroface cell designs are proposed, utilizing a thin base and thin passivated buffer, which not only make the cell performance relative insensitive to deep levels but also result in somewhat higher efficiencies than the conventional thick base (2-3 μm) designs [9,10]. It is shown that only when the lifetime reaches its intrinsic (fundamental) limit does the conventional thick base cell efficiency surpass the thin base cell efficiency.

2.4.2 Lifetime Calculations

The minority carrier lifetime in GaAs was calculated as a function of doping concentration according to

$$1/\tau = 1/\tau_{SRH} + BN + CN^2 \tag{21}$$

where C is the Auger recombination coefficient and B is the radiative recombination coefficient. Calculations were made for both n and p-type GaAs, however, only the n-type case is considered here since the heteroface solar cell structures to be discussed later utilizes an n-type base. For n-type GaAs, $C = 1.60 \times 10^{-29} cm^6/sec$ over the entire doping range [1]. However, B is not constant due to the Burstein shift [3,11] in n-type GaAs. This doping dependence of B [3,11] was accounted for in our model calculations. The SRH lifetime under low level injection can be expressed as [12]

$$\tau_{SRH} = \tau_{no}(p_o + p_1) + \tau_{po}(n_o + n_1) \tag{22}$$

where

$$\tau_{no} = (\sigma_n N_T v_{TH})^{-1} \tag{23}$$

$$\tau_{po} = (\sigma_n N_T v_{TH})^{-1} \tag{24}$$

$$n_1 = N_C \exp[(E_T - E_C)/kT] \quad (25)$$

$$p_1 = N_V \exp[(E_V - E_T)/kT] \quad (26)$$

The total minority carrier lifetime was calculated as a function of doping concentration from Eq. (19) for different deep levels specified by their characteristic values of τ_{no}, τ_{po}, and E_t. In all of our calculations τ_{SRH} was fixed at a particular starting lifetime value (at a given doping concentration), regardless of E_T so that τ_{no} and τ_{po} were not constant, in contrast to conventional practice where τ_{no} and τ_{po} are generally assumed to be the same for all traps. This approach is more realistic and important since GaAs supplied by different vendors, or grown by different technologies can have identical lifetimes at a given doping concentration due to traps with different combinations of E_T and τ_o. The values used for all trap parameters were chosen within the observed range of values reported in the literature [13,14] for both n and p-type GaAs. In all calculations, we have set $\tau_{no} = \tau_{po} = \tau_o = (\sigma N_T v_{TH})^{-1}$.

2.4.3 Device Modeling

In order to reveal the impact of deep levels on device performance, solar cell characteristics were calculated using the PC-1D device modeling program, described elsewhere, [9,10] with appropriate material and cell dimensional parameters. The effects of deep levels were taken into account by modifying the lifetime profile throughout the device structure according to the doping dependence of lifetime determined from Eq. (21) assuming that the particular deep level under consideration exists uniformly in the base and buffer regions. All simulations were performed under one sun AM 1.5 conditions.

2.4.4 Experimental

To support some of the theoretical findings by experimental results, p on n heteroface solar cells (Figure 28) were fabricated by the MOCVD technique and only those devices with poor performance (18-20% efficiency rather than ~23%) were selected for analysis. The minority carrier

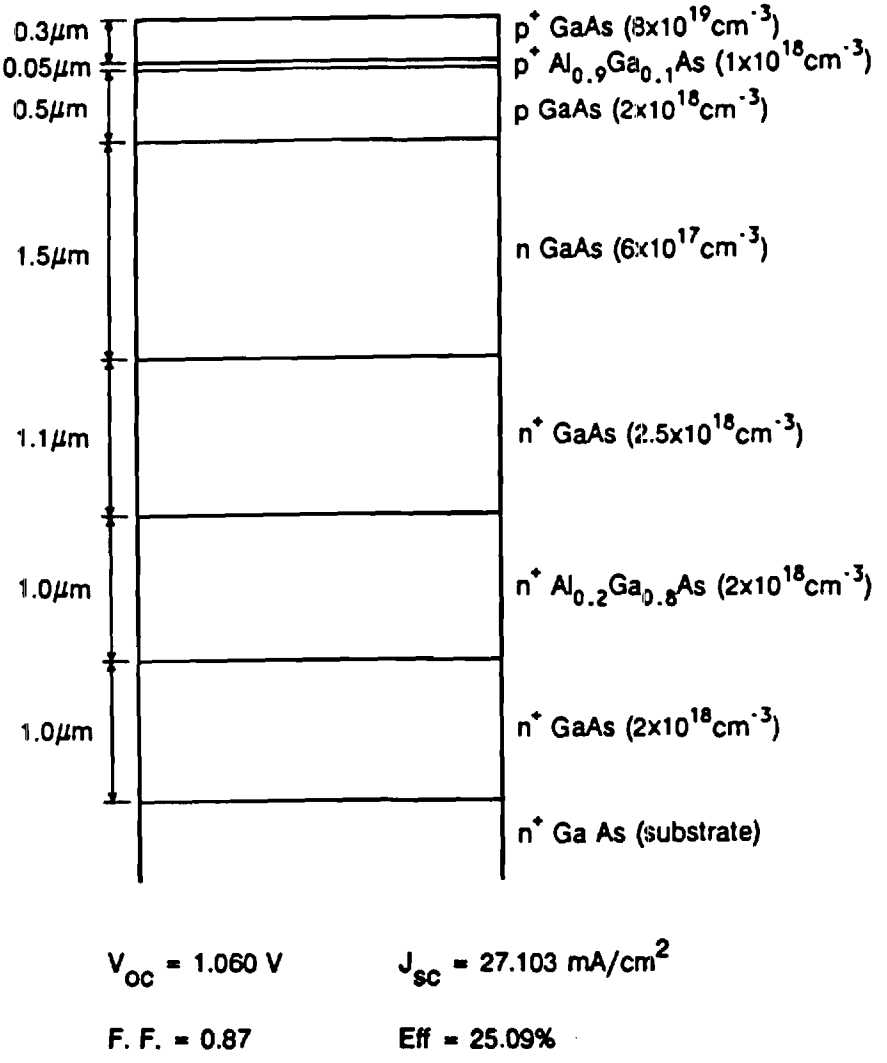

Figure 28. GaAs p/n Heteroface Solar Cell Structure used in this Study. The Cell Data Listed was Measured under One Sun AM 1.5 Conditions.

diffusion length and lifetime in the n-base of these low efficiency cells was estimated from the measured internal quantum efficiency [15].

In order to reveal the traps which limit the lifetime in the selected low efficiency devices, DLTS measurements were performed. Fifty mil diameter mesa dots were formed using Au/Zn for ohmic contacts on the p-type front surface, and Au/Ge ohmic contacts on the back. DLTS measurements were made using an automated wafer analyzer system which obtains data via a lock-in amplifier type set-up. The output signal was integrated and analyzed using five different weighting functions. The activation energy of the trap, ΔE, was found from the slope of the Arrhenius plot of $\log(T^2/e_m)$ vs 1000/T where the trap emission rate, e_m, is given by

$$e_m = N_v \sigma v_{TH} \exp[-\Delta E/kT] \tag{27}$$

and the terms in Eq. (25) have their usual meaning [16].

2.4.5 Results and Discussion

2.4.5a. Effects of Deep Levels on Lifetime vs. Doping Behavior in n-Type GaAs

In most n-type GaAs available today, the radiative and Auger lifetimes do not appreciably limit the net lifetime below a doping concentration of ~1 x $10^{18}cm^{-3}$ because the combined contribution of the Auger and band-to-band recombination processes to the lifetime is much greater than the total lifetime. Hence, SRH recombination generally dictates the lifetime behavior. An assessment of the effects of deep levels on the minority carrier lifetime was made by plotting Eq. (21) for various deep level characteristics (E_T and τ_o). Selected examples in Figure 29 shows lifetime vs doping plots for four possible scenarios depending upon starting material quality, position of the deep level, and the value of τ_o. The values of E_T and τ_o for each curve are indicated in the figure. Figure 29a represents the doping dependence for GaAs technologies that can produce starting lifetimes as low as 46 ns or as high as 1 μs at a doping concentration of 1 x $10^{14}cm^{-3}$, regardless of the deep level position. The former represents commonly observed lifetime values for n-type GaAs, [5,7] while the latter represents the highest lifetime for GaAs reported in the literature [17]. Model calculations in Figure 29b represent another scenario in which the lifetime is as low as 4 ns or as high

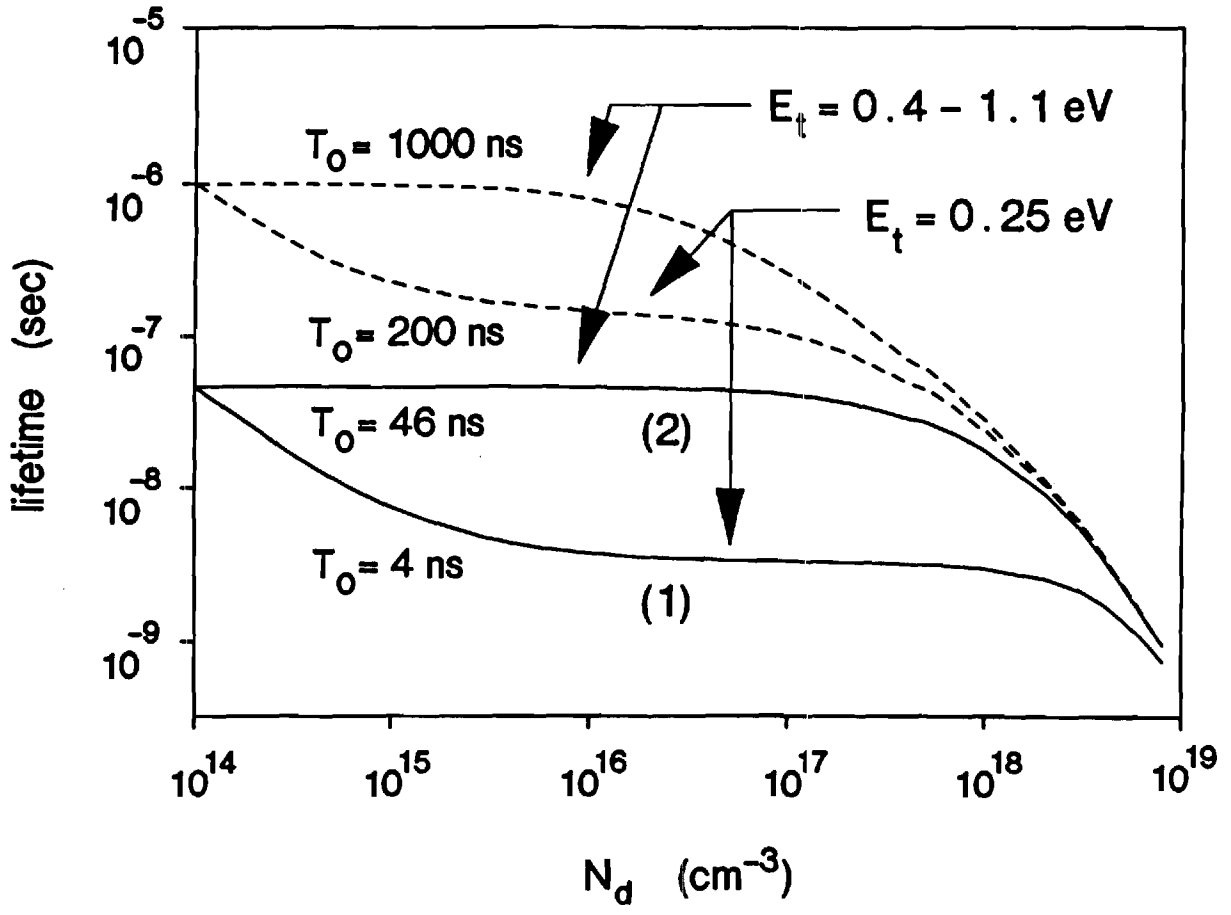

Figure 29.a. Minority Carrier Lifetime as a Function of Doping in n-Type GaAs for Materials with Starting Lifetimes of (a) 1000 and 46 ns at $N_d = 1 \times 10^{14}$ cm^{-3}, and (b) 230 and 4 ns at $N_d = 1 \times 10^{16}$ cm^{-3} for Different Trap Levels and τ_o Values as Indicated. Curves 1, 2, 3, and 4 are Referred in the Text.

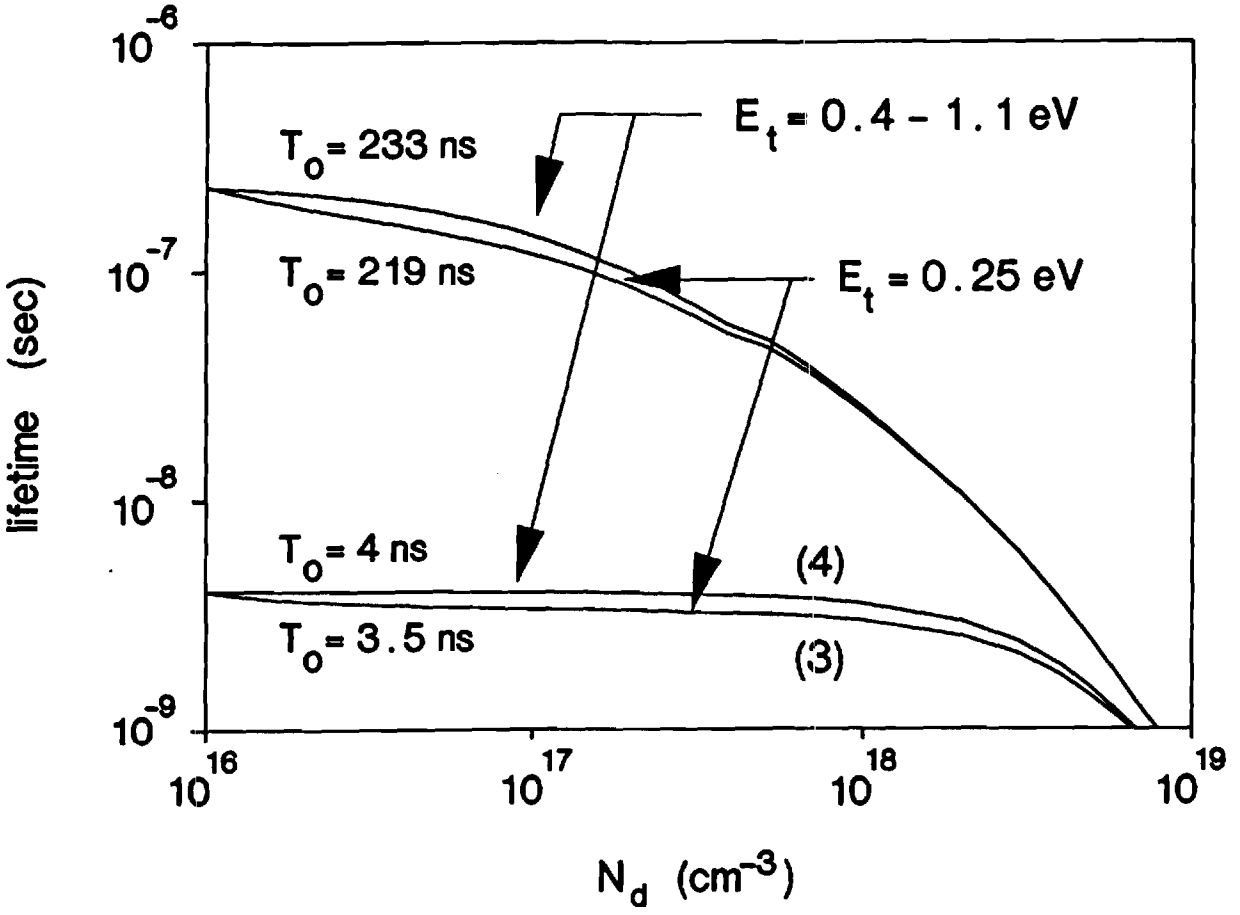

Figure 29.b. Minority Carrier Lifetime as a Function of Doping in n-Type GaAs for Materials with Starting Lifetimes of (a) 1000 and 46 ns at $N_d = 1 \times 10^{14}$ cm^{-3}, and (b) 230 and 4 ns at $N_d = 1 \times 10^{16}$ cm^{-3} for Different Trap Levels and r_o Values as Indicated. Curves 1, 2, 3, and 4 are Referred in the Text.

as 230 ns but at a starting donor concentration of 1 x $10^{16}cm^{-3}$ instead of 1 x $10^{14}cm^{-3}$. Each curve describes the net lifetime versus doping behavior for a material which has a given trap location within the bandgap and a calculated value of τ_0 based on both E_T and the starting value of τ_{SRH}. In the figure, only one example of a shallow trap (E_v + 0.25 eV) is shown to preserve clarity.

The most striking observation from these calculations is that the shallow traps (within ~0.4 eV from E_v and 0.3 eV from E_c) show a much more undesirable doping dependence than deeper traps. This is because in order to have the same starting lifetime, the values of τ_0 for the shallow traps are less than the values of τ_0 for the deeper traps (such behavior has been experimentally observed [13,14]). This is in contrast to the more commonly predicted higher lifetimes for shallow traps which resulted from fixing the value of τ_0 in Eq. (19), regardless of the value of E_T. As can be seen in Figure 29, for traps with E_T between E_v + 0.4 eV and E_c - 0.3 eV, the lifetime behaved as if the trap was located at midgap, i.e. independent of doping concentration until the onset of intrinsic (Auger and radiative) recombination processes. The observed kink in the lifetime curves near 5 x $10^{17}cm^{-3}$ for the highest lifetime curves is due to the effect of the Burstein shift on the radiative lifetime which partially limits the net lifetime in the high quality materials.

Thus the knowledge of trap location induced doping dependence could be very important for the design of lightly doped devices (< 1 x $10^{16}cm^{-3}$). Even more significant is the fact that the absolute value of lifetime at any doping concentration (Figure 29) can be orders of magnitude different depending upon the combination of the trap location and the nature of the trap dictated by $\tau_0 = (\sigma N_T v_{TH})$. This will influence the optimum design of both lightly and heavily doped devices. The effect of trap location on device performance is quantitatively demonstrated in the following section by fabricating and carefully analyzing selected GaAs solar cells.

2.4.5b. Effect of Deep Levels on the Performance of Conventional Thick Base Cell Designs

Figure 28 shows the device structure of a conventional GaAs p/n heteroface cell fabricated by the MOCVD technique. Based on our model calculations, this design was expected to yield high cell efficiencies (23-24%) assuming base lifetimes of 15-20 ns, but the selected experimental device showed a one sun efficiency of only 18.9%, J_{sc} = 22.11 mA/cm^2, and V_{oc} = 1.006 V. The minority carrier lifetime was estimated to be ~3 ns from D_p = 4.5 cm^2/s[18] and the diffusion length ($L = \sqrt{D\tau}$)

obtained from the measured internal quantum efficiency. Using this lifetime in conjunction with an FSRV (front surface recombination velocity at the $Al_{.9}Ga_{.1}As$/p-emitter interface) of ~1.0 x 10^5 cm/s and a BSRV (back surface recombination velocity at the n-base/$Al_{.2}Ga_{.8}As$ interface) of ~1 x 10^3 cm/s, we were able to match the measured and calculated cell data. The calculated efficiency from the PC-1D was 18.8% with a J_{sc} of 22.11 mA/cm^2 and a V_{oc} of 1.010. Even by lowering the observed high surface reflectance (~20%) to 5% in this cell, and further passivating the heteroface so that FSRV = 1 x 10^4 cm/s, the calculated efficiency for this cell could reach only 20.90%, which is well below the expected performance of 23-24%. This indicates that the low base lifetime is limiting this cell efficiency.

To determine the cause of the 3 ns lifetime, DLTS measurements were performed on this 18.9% cell and the DLTS spectrum is shown in Figure 30. A hole trap located at E_v + 0.25 eV with a trap density of 4 x $10^{13}cm^{-3}$ was detected within the n-type base. Model calculations in Figure 29a show that an E_v 0.25 eV trap can also result in a 3 ns lifetime at N_d = 8 x $10^{17}cm^{-3}$, curve 3 other possibilities exist as well). From curves 1 and 3, it can be seen that for this shallow trap little or no increase in lifetime can be gained by lowering the base doping concentration to as low as ~1 x $10^{15}cm^{-3}$. Hence, if the cell performance is limited by the E_v + 0.25 eV level, it can only be improved by changing the cell design. However, if the material had a midgap trap with a higher τ_o and belonged to the family of curves 1 and 2 (Figure 29a), then the lifetime would have been 21 ns instead of 3 ns at N_d = 8 x $10^{17}cm^{-3}$, resulting in the expected cell efficiency of 24.7%.

Thus, the dependence of cell efficiency on deep levels can be significant over a wide doping range for the conventional thick base design. Hence, to design an optimized thick base solar cell, it is necessary to know in advance the location and nature of the deep level in the material available. One way to circumvent this difficulty is to employ a design which is relatively insensitive to deep levels and lifetime. This is demonstrated in the following section.

2.4.5c. Relatively Defect Insensitive Thin Base GaAs Heteroface Cell Designs

The base thickness is a critical parameter for high efficiency cells. Typically, the base thickness is chosen so that most or all of the incident photons are absorbed within this region. For the 3 μm base design discussed earlier, ~97% of the photons are absorbed in the emitter and base

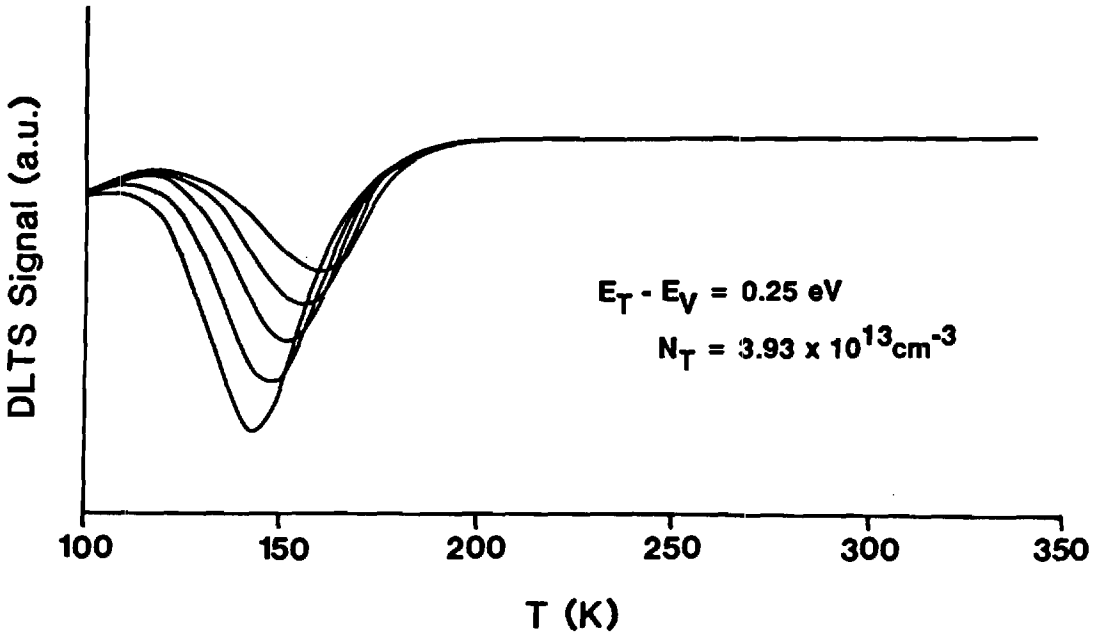

Figure 30. DLTS Scan for the GaAs Device Shown in Figure 1 Using Five Different Weighting Functions from 4 to 64 msec.

regions. However, it was found that a diffusion length of 2-3 times the base thickness is necessary to collect nearly all of the photogenerated carriers in the base which requires minority carrier lifetimes near the fundamental radiative and Auger limit. This is why the thick base cell efficiency is severely reduced when deep levels exist in the material which degrade the lifetime. Therefore, we propose and demonstrate by model calculations an alternative solution which employs a thinner base to relax the constraint on the diffusion length requirements without diminishing the cell performance. In fact, as shown below, it gives slightly higher efficiencies than the thicker base design unless the lifetime become very high.

We have previously shown [9,10] by device simulation that a GaAs p/n heteroface cell design utilizing a thin base and buffer can attain one sun efficiencies over 25% with a moderate base lifetime of 20 ns and a 5% shadow + reflection loss. An example of such a design is shown in Figure 31 which is optimized for a 20 ns base lifetime. The premise for this design is to maximize the collection efficiency of photogenerated carriers within the base by forcing the diffusion length to be greater than the base width and by bringing the buffer/base doping discontinuity step closer to the collecting junction. Detailed calculations show that high efficiency is achieved even though ~10% of the light is absorbed in the heavily doped buffer and an additional ~4.5% of the light is not absorbed anywhere within the active regions of the device. It should be noted that a thinner buffer, along with a BSF layer, is necessary to minimize the losses in the thin cell design, Figure 31.

To demonstrate the relative insensitivity of the thin base cell performance to the lifetime limiting deep levels, the performance of the thin base device in Figure 31 was calculated using the same lifetime (3 ns) found in the thick base experimental cell with an efficiency of 18.9% (20.9% with 5% surface reflection). Model calculations in Figure 32 show that even with such poor material, an efficiency of 22.92% is achievable with the thin base device (as compared to 20.9% for the thick base device), assuming a 5% shadow + reflection loss, an FSRV of 1×10^4 cm/s and a BSRV of 1×10^3 cm/s. Figure 32 exemplifies the superiority and relative insensitivity of the thin base structure to lifetime variation as compared to the thicker base structure for a starting material quality of 46 ns at $N_d = 1 \times 10^{14} cm^{-3}$. Figure 32 also shows that traps located close to the band edges (with low τ_o values) result in the largest degradation in cell efficiency for either design. However, for the

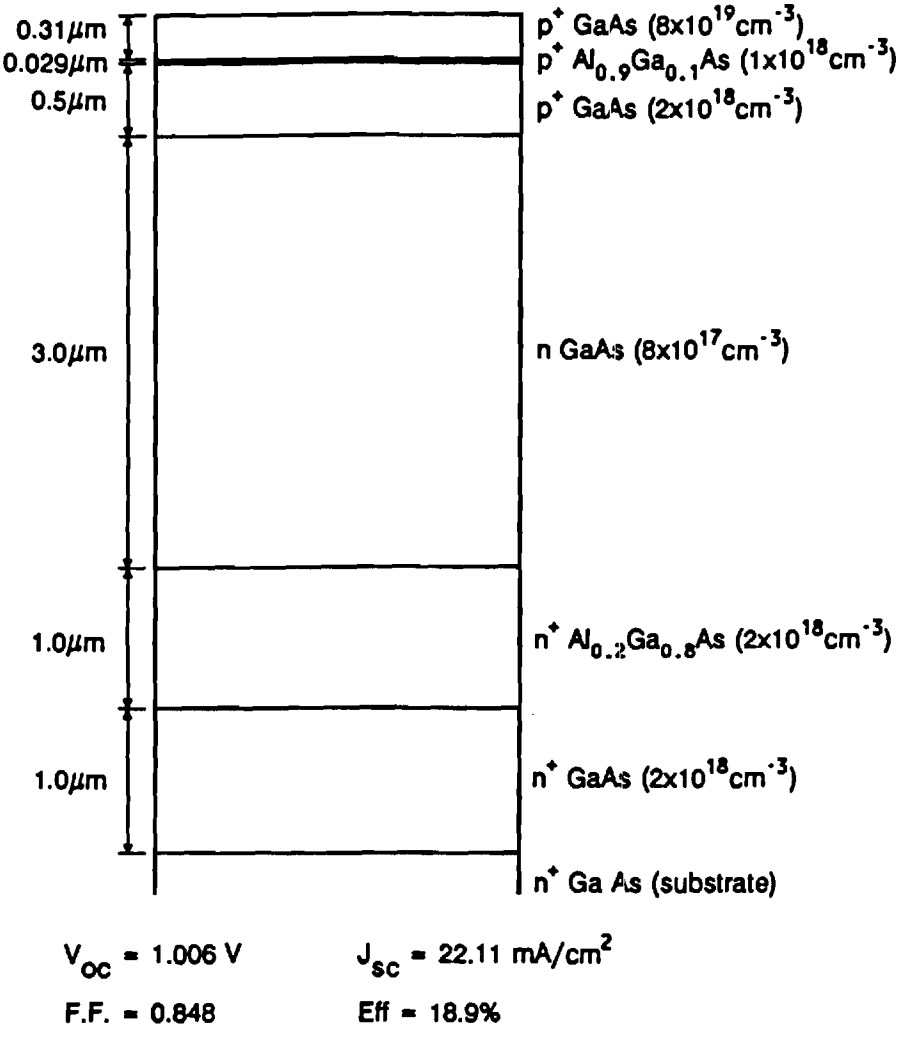

Figure 31. Example Device Structure for Thin Base Design. The Dimensions Shown are Optimized for a 20 ns Base Lifetime. The Simulated Cell Data for this Lifetime are Shown Assuming a 5% Loss to Shadow plus Reflection, an FSRV of 1 x 10^4 cm/s, a BSRV of 1 x 10^3 cm/s, and One Sun AM 1.5 Conditions.

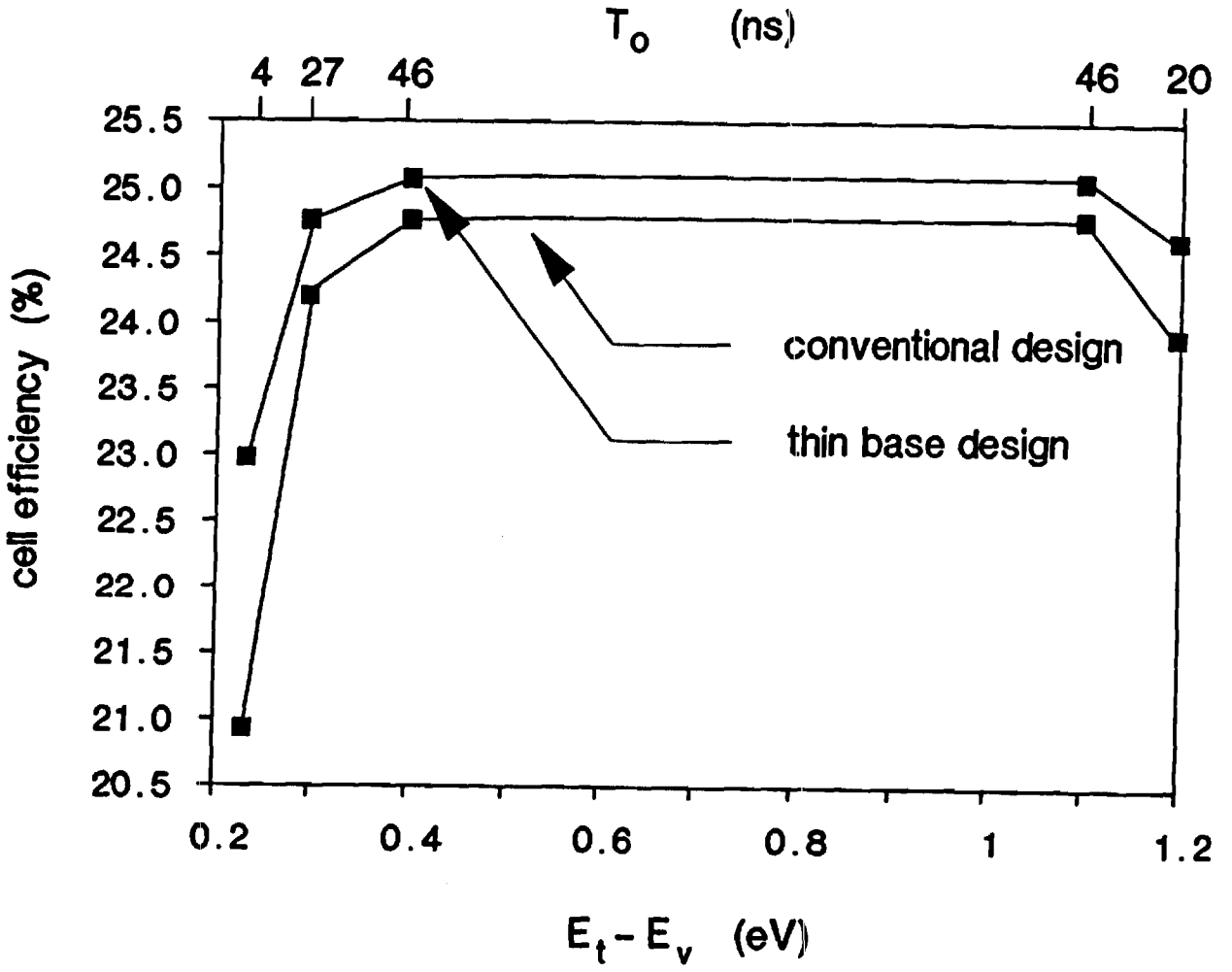

Figure 32. Cell Efficiencies Calculated by PC-1D are Shown for the Device Designs of Figure 1 (Conventional) and Figure 4 (Thin Base) as a Function of Trap Level (indicated with respect to the Valence Band Edge) with Associated τ_o Value. All Calculations assume a 5% Total Surface Loss, and FSRV of 1 x 10^4 cm/s, a BSRV of 1 x 10^3 cm/s, and one sun AM 1.5 Conditions.

thicker base, an absolute efficiency loss of ~4% results if a trap is moved from midgap (with τ_o = 46 ns) to 0.25 eV (with τ_o = 4 ns) while a dope of only 2% occurs for the thin base design.

The efficiency difference between the two designs is most striking for very low base lifetimes (shallow traps), where the diffusion length is 2-3 times less than the thicker base width, and becomes less significant for midgap traps where the lifetimes are significantly improved (recalling that τ_o changes with E_T). It was found that most of the efficiency difference results from improved J_{sc}, due to higher diffusion length to base width ratio. Further model calculations show that only if the lifetime reaches the intrinsic (fundamental) limit for GaAs at the designed base doping levels does the thicker base design attain a higher efficiency (25.50%) than the thin base cell (25.30%) because of the improved collection efficiency at long wavelengths. Thus the thin base design is predicted to result in higher cell efficiencies for practically achievable base lifetimes today and is much less sensitive to material quality variations than the standard thicker base (2-3 μm) GaAs p/n solar cells.

2.4.6 Conclusions

We have calculated the trap and doping dependence of lifetime in n-type GaAs and have shown that various realistic combinations of trap location and τ_o values can result in orders of magnitude variation in lifetime at all doping levels below 1 x $10^{18}cm^{-3}$. In addition, traps that are located within 0.4 eV of the valence band edge and 0.3 eV of the conduction band edge show the strongest doping dependence of lifetime below a doping level of ~1 x $10^{16}cm^{-3}$. It is also shown by device modeling that this has a large effect on the optimum design and performance of GaAs devices such as solar cells. It is experimentally demonstrated that a cell design which should have an efficiency over 24% using a 3 μm thick base resulted in a 20.9% eV trap. To minimize the influence of traps (and lifetime), which can only be found by difficult and time consuming DLTS-type measurements, an alternative design is proposed which employs thin base and buffer layers in addition to a heterojunction BSF to lower BSRV. This design minimizes the high lifetime requirement for high performance cells. It has been shown that this design is much less sensitive to deep level characteristics than the conventional thicker base design. It is also shown that the thin cell design is slightly superior to the thick base design for most GaAs p/n heteroface cells in which the base lifetime is limited by defects. Only when the lifetime is limited by intrinsic (fundamental)

recombination mechanisms (i.e. independent of defects) does the thick base cell efficiency slightly surpass that of the thin base cell design because of more absorption and carrier collection.

2.5 THE EFFECT OF SURFACE TEXTURING ON ABSORBED FLUX FOR HIGH EFFICIENCY SOLAR CELLS

2.5.1 Introduction

The achievable short circuit current of a solar cell is dependent upon the amount of flux absorbed in the cell structure. Conventional cells with flat surfaces allowed for only one pass of the incoming radiation. For material with a low absorption coefficient this meant that thick cells had to be fabricated. Having a thick cell required a large diffusion length to collect the generated carriers. Therefore, cells were designed using a tradeoff between absorption length and diffusion length. The implementation of a back surface reflector helped to increase the amount absorbed flux, but was only a first step. Today, high efficiency solar cells are being produced with various surface geometries in an attempt to increase the amount of absorbed flux by trapping the light in the cell structure by internal reflection. These light trapping schemes can increase the short circuit current anywhere from 2 to 5 mA for a 100 μm Si cell depending upon the effectiveness of the geometry.

In this section, texturing a ray tracing program is introduced. The program is capable of simulating many different surface structures. Most of these have been investigated by other researchers, we have included then so that comparisons of new structures can be easily accomplished. In order for the program to be applicable for a wide user base the criteria in Table 4 was followed in the development

2.5.2 Geometrical Texturing

Figure 33 shows the texturing proposed for the program. Included in the figure is the year and researcher who proposed the structure. In addition an estimated value of the short circuit current is given, if available this is compared to published estimates. In all cases our results compared favorably despite the inability to match conditions exactly. Currently the program is not complete, the status is given in Table 5, but several simulations are still possible. An estimated 3 months is required for completion and debugging of the program. At that time we suggest the program be distributed either as shareware or public domain. A sample users manual is included in the appendix.

GEOMETRICAL TEXTURING

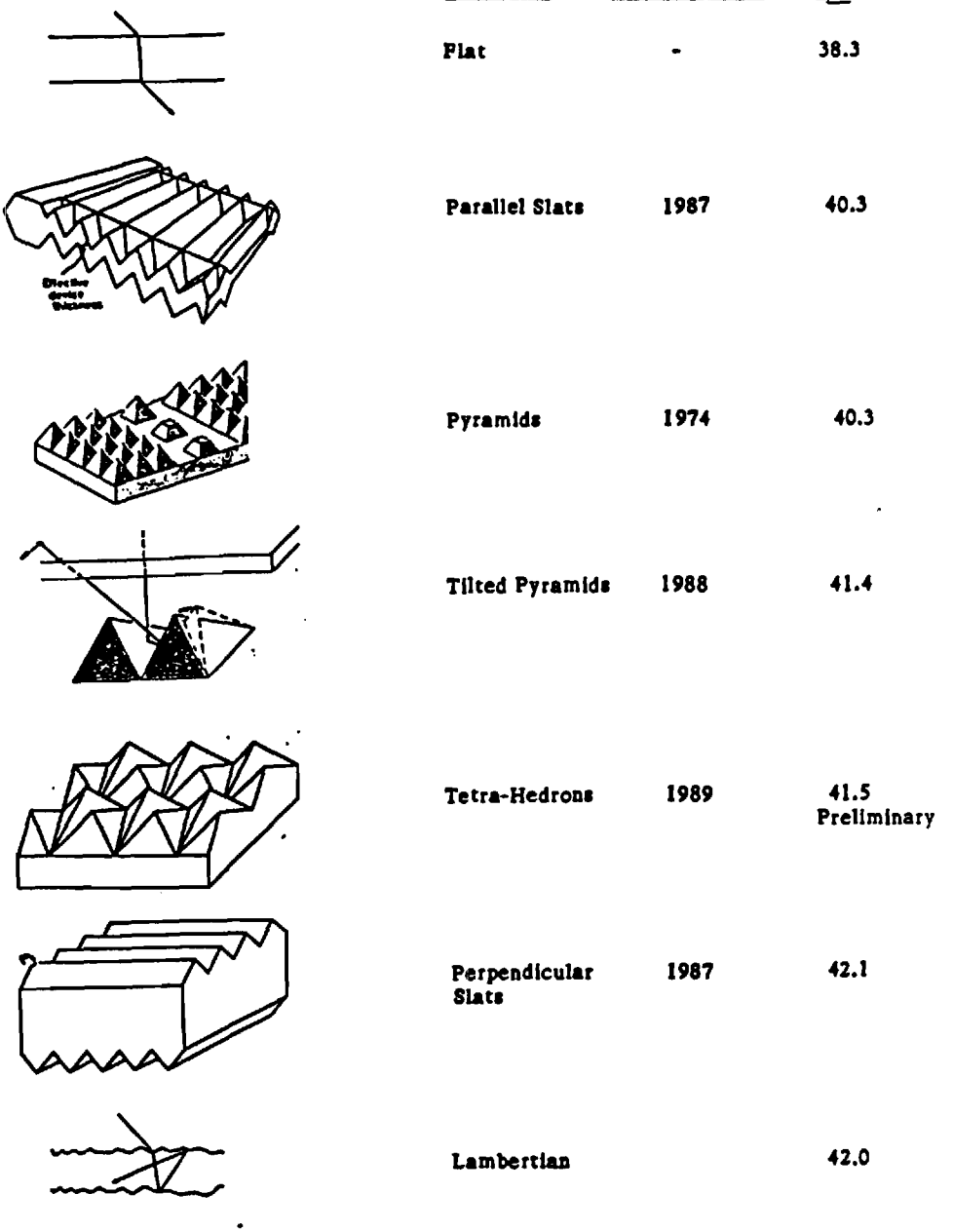

Geometry	Year Proposed	J_{sc}
Flat	-	38.3
Parallel Slats	1987	40.3
Pyramids	1974	40.3
Tilted Pyramids	1988	41.4
Tetra-Hedrons	1989	41.5 Preliminary
Perpendicular Slats	1987	42.1
Lambertian		42.0

*100 μm Si

Figure 33. Different Surface Texturing Purposed for Light Trapping.

2.5.3 Conclusions

A computer program is being written which will calculate the absorbed flux due to different surface texturing applicable to solar cells. In addition to the absorbed flux the program provides the increase in surface area, loss due to sides, loss due to grid, and losses due to imperfect back surface reflectance. A new geometry is introduced, tetrahedrons, which preliminary results show to be superior to tilted pyramids.

TABLE 4. Attributes of Ray Tracing Program

1. Applicable to any computer system with Fortran 77 and ANSI
2. Compatibility with current and future modeling programs
3. New structures easily incorporated due to modular nature of program
4. No simplification of structures, a 3 dimensional analysis in all modes of operation
5. Different modes of operation to provide different information as a compromise to speed
6. 1, 2, and 3 dimensional profiles should be available
7. Variable angle of incidence
8. Surface structures should be independent of each other
9. Different material systems should be easily modeled
10. Cover glass treated as fully as the semiconductor
11. Grid lines modeled as fully as possible
12. Loss in flux due to sides, back, grids, cover glass, and reflection should be provided
13. Average increase in surface area to be output
14. Various spectra and intensities accounted for

TABLE 5. Current Texture Program Status

General routines have been written and debugged for

1. angle of reflection
2. angle of refraction
3. material and spectra input routines to accommodate PC-1D version 2 files
4. variable angle of incidence and intensity
5. grid lines parallel to axes with variable reflectivity depending upon which side the ray strikes
6. four front structures
7. seven back structures
8. five cover structures
9. three out of five modes of operation
   a. average distance and percentage of ray remaining
   b. absorbed flux, losses, but no profile
   c. 1 dimensional profile with associated losses

Work to be completed

1. include Lambertain structures on cover, front, and back
2. complete 2 and 3 dimensional profile modes
3. assess applicability to heterostructures

2.6 SLOW POSITRON ANNIHILATION SPECTROSCOPY OF HETEROJUNCTIONS AND HOMOJUNCTIONS OF GaAs-BASED SEMICONDUCTOR THIN FILMS

2.6.1 Introduction

Positron annihilation spectroscopy (PAS) has been applied to the characterization of semiconductor materials over the past two decades. Until recently, the continuous energy distribution of positrons emitted from conventional sources limited the capabilities of the PAS probe to the determination of a spatial average of defect and charge states. However, within the last few years, the development of slow PAS (SPAS), a technique for controlling the positron implantation depth, has provided the means of profiling the local defect and charge distributions in semiconductors 10 A to several microns below the surface [1-3]. Since SPAS is a non-contact non-destructive evaluation technique with the ability to profile defect distributions and material interfaces selectively, it is potentially a powerful analytical tool.

Previous PAS studies using continuous energy positron sources have investigated such diverse phenomena as laser damage and annealing [4], radiation damage [5], and plastic deformation [8] of silicon, GaAs, HgCdTe and other semiconductors. The majority of these studies have been limited to single crystals, although some results have been reported on polycrystalline [9] as well as thin film semiconductors [10,14]. Very recent SPAS studies have investigated solar cell heterojunctions [1] and prior substrate conditioning on the growth of silicon on a (100) silicon wafer [3].

The purpose of this paper is to continue the development of SPAS for profiling multilayered heterojunctions by investigating an AlGaAs/GaAs solar cell for which a number of preliminary results have been presented previously [2]. The variable-energy PAS spectra obtained, in the previous work, were quite complex and could not be resolved using a simple Gaussian fitting function. Specifically, local minima in the PAS spectra were observed at the AlGaAs-GaAs (window-emitter) and the p-n junction (emitter-base) interfaces. These minima were attributed to space charge depletion effects, interfacial defects, and local quality of the semiconductor material. A series of experiments have been performed on one of the previous semiconductor structures, as a function of applied bias, in order to delineate the positron-space charge interactions.

2.6.2 Experiment

The $Al_xGa_{1-x}As$-GaAs (x = 0.9 for brevity, we will refer to the structure as AlGaAs) solar cell's structure is summarized in Table 6. This device was grown via metal-organic chemical vapor deposition in a Spire MO-450 reactor using trimethyl gallium, trimethyl aluminum and arsine reactants. Acceptor dopants are zinc, while donors are silicon. A rectangular gold contact was deposited around the perimeter of the 872B sample. A grid contact was rejected because of potential interference with the positron measurements. The back contact covered the entire surface. Copper wires were attached to the contacts using silver epoxy. A Hewlett-Packard 6281A d.c. power source was used to apply a variable bias to the solar cell. Slow PAS response were investigated for -2.0 0. and +0.25 V. The applied voltage was observed to have approximately ±0.5 V drift through the duration of each experiment possibly as a result of charge build-up.

TABLE 6. Solar Cell Heterojunction Structure

Layer	Material	Thickness (μm)	Type	Doping
Cap	GaAs	0.143	p^-	8.0×10^{19}
Window	AlGaAs	0.05	p^-	1.0×10^{18}
Emitter	GaAs	0.5	p	1.5×10^{18}
Base	GaAs	2.0	n	2.0×10^{17}
Buffer	GaAs	2.0	n	2.0×10^{18}
Substrate	Gaas			

This structure was previously identified as 872B.

The variable-energy positron beam has been described elsewhere [15]. In brief, the system consists of a ^{22}Na positron source moderated by a single-crystal tungsten foil of efficiency -5 x 10^{-4} and magnetically focused onto the sample. The source end of the chamber is floated at various potentials providing a beam energy from essentially 0 to 75 keV. Since the primary focus of the experiments was directed towards subsurface features within the solar cell, less stringent vacuum conditions of about 2 x 10^{-7} Torr were used for all PAS measurements. At each positron implantation energy, 2 x 10^6 counts (annihilation events) were recorded, with a count rate of 1.7 kHz. The change in the

where d_i is the depth of layer i below the surface and L^+ is the positron diffusion length in p-GaAs (cap and emitter) layers. The fractions of positrons annihilating in the cap, window and emitter layers (i = 1,2,3) are defined as follows:

$$\epsilon_1 = \int_0^{d_1} P(z,E)\{1 - P_{d1}(z)\}dz \tag{30}$$

$$\epsilon_2 = \int_{d_1}^{d_2} P(z,E)dz + \int_0^{d_1} P(z,E)P_{d1}(z)dz + \int_{d_2}^{d_3} P(z,E)P_{d2}(z)dz \tag{31}$$

$$\epsilon_3 = \int_{d_2}^{d_3} P(z,E)\{(1 - P_{d2}(z)\}dz \tag{32}$$

For a multilayer system the implantation profile must be modified to account for differences in material densities:

$$P(z,E) = \exp\{-(z-\delta_i)^2/z_o^2\} \tag{33}$$

where δ_i is defined by the requirement of continuous positron transmission [17]:

$$\delta_i = d_i - (z_{oi}/z_{oi-1})(d_i - \delta_{i-1}) \tag{34}$$

The energy-dependent Doppler response S(E) is then defined as

$$S(E) = \sum S_i\epsilon_i \tag{35}$$

The general trends of S(E) are better described by the above model than in the earlier analysis [1]: however, a much more sophisticated treatment will be necessary to account properly for localized defect, matrix, and compositional discontinuities within the layers and at layer interfaces.

annihilation energy distribution (which is related to the electron momentum distribution) has been calculated using the Doppler S parameter, which is defined as the number of detected events in a narrow window around 511 keV divided by the total number of detected annihilation events [16].

2.6.3 Slow Positron Annihilation Spectroscopy

The data have been modeled using a variation of an analysis used successfully in the investigation of an SiO_2-Si interface [2]. The implantation profile P(z,E) of positrons may be described by a makhovian profile [17]:

$$\begin{aligned} P(z,E) &= d/dz\{\exp(-z/z_o)^m\} \\ z_o &= \Gamma(1 + 1/m)\bar{z} \\ \bar{z} &= (\alpha/\rho)E^n \end{aligned} \tag{28}$$

where ρ is the material density, and the constants $x = 4 \pm 0.4\ \mu g\ cm^{-2}$, $n \approx 1.6$, and $m = 2$ (ref. 12). The Doppler response S(E) is found by summing the integral of P(z,E) over each layer and weighting by the characteristic S value for that layer. Such an approach assumes the homogeneity of each layer and a negligible positron diffusion coefficient, in addition to the absence of extended interfacial traps and/or electric field effects. However, if positron diffusion across an interface is important, then a model for S(E) incorporating the effects of layer interdiffusion and interfacial effects is required [2].

In the AlGaAs/GaAs sample of this study, the resolved S characteristic of the AlGaAs is significantly greater than in the GaAs layers and is suggestive of a higher defect concentration relative to the GaAs layers [1]. Thus, the positron diffusion length in the AlGaAs layer is assumed to be negligible relative to the GaAs layers. Therefore, both AlGaAs boundaries have the appearance of an extended trap to positrons diffusing towards them from the adjacent GaAs layers (cap and emitter). The probability that a positron will diffuse out of a p-GaAs layer into the AlGaAs layer is given by

$$P_{di}(z) = \exp(-|z - d_i|/L^+) \tag{29}$$

2.6.4 Results

The measured S(E) responses as a function of applied bias have been plotted for 0 and -2 V (Figure 33) and 0 and +0.25 V (Figure 34). The error bars result from a statistical analysis alone. Doppler S parameter data may be statistically described by a binomial distribution [18] representing photons that either fall inside or outside of the fixed energy window about 511 keV. Therefore, the mathematical uncertainty is defined as (S(1-S)'N) [1,2], where N is the total number of observations which is about 2 x 10^6 (counts). The uncertainty is approximately ±0.00035 for all observed S(E) values.

The fine structure of the zero-bias S(E) profile of this study is in good agreement with zero-bias measurements from the previous study [1], even though it is highly unlikely that the same spot on the solar cell surface has been sampled. Thus it appears that the sharper spectral details are reproducible and are not random statistical artifacts.

The continuous curves in Figures 34 and 35 are the best fit obtained according to the theoretical model described in the text. For the case of applied external bias, a second sink layer has been added at the surface, in a manner analogous to that for the AlGaAs layer. The thickness of the layer as determined by the bets fit was 50 Å. The positron diffusion length in the non-sink layers in all cases was 0.1 μm, which is the value obtained from estimates of the diffusion coefficient [19] and the positron lifetime in GaAs.

Figures 36 and 37 show the deconvoluted S parameter vs. implantation energy. For -2 V, the surface value of S_i is much higher, and the values in the cap and emitter regions are raised by an amount $\delta S = 0.002$ compared with the no-bias case. The changes in the window and base regions are only 0.0005 and 0.0007 respectively. In contrast, the deconvoluted values for the +0.25 V case are virtually identically to those of the no-bias case except at the surface, where it is much lower, and in the AlGaAs layer, where it is raised by an amount $\delta S = 0.001$.

2.6.5 Discussion

Comparison of the S(E) response as a function of the applied bias indicates that the changes are non-uniform with respect to zero bias. This indicates that a number of different effects may be responsible for the applied bias S_i characteristic values. Forward and reverse bias differ greatly from

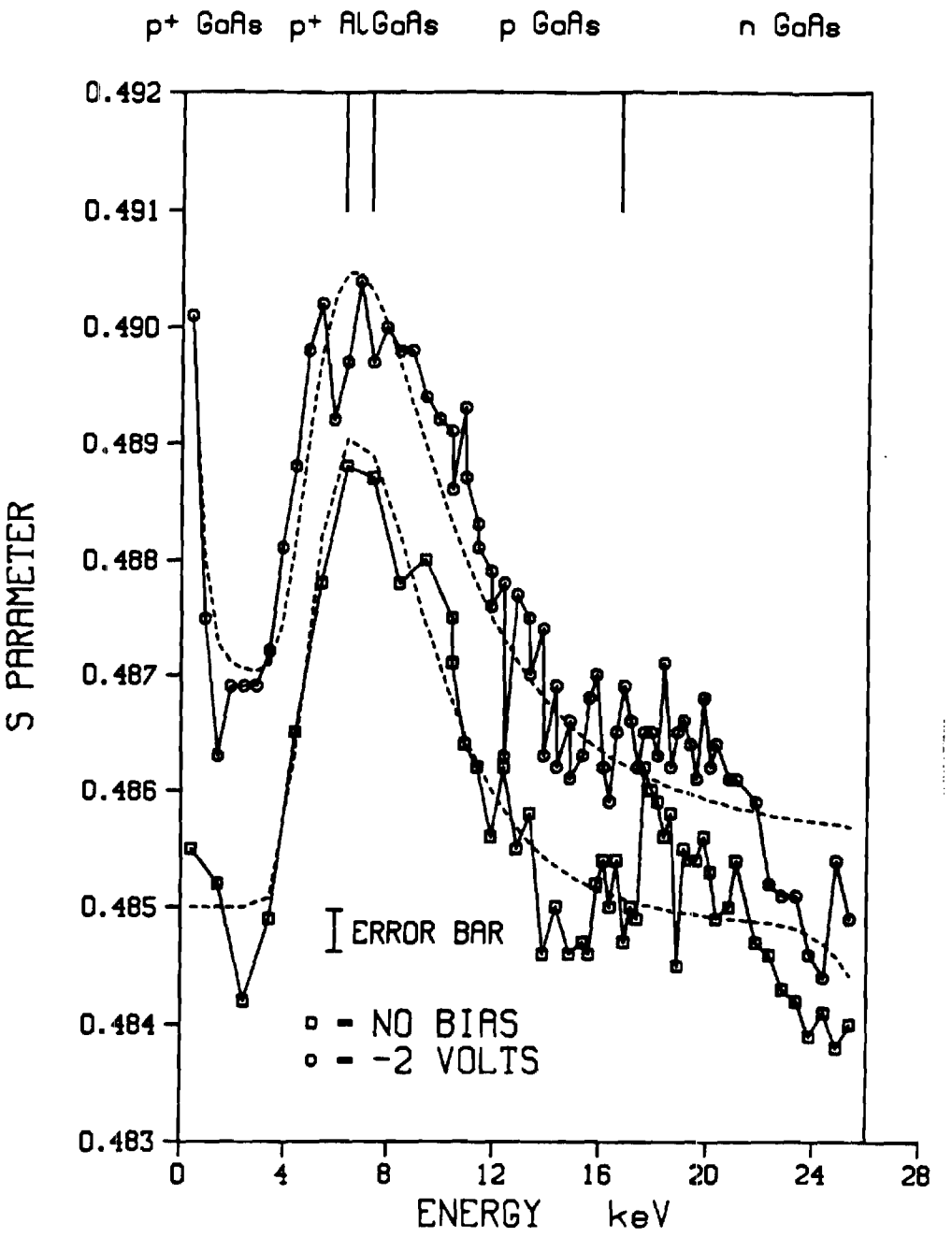

Figure 34. Results of SPAS Profiling of the AlGaAs/GaAs Structure with no Bias and 2 Volts Reverse Bias applied. The Dashed Curve Represents the Best Fit to the S(E) Response.

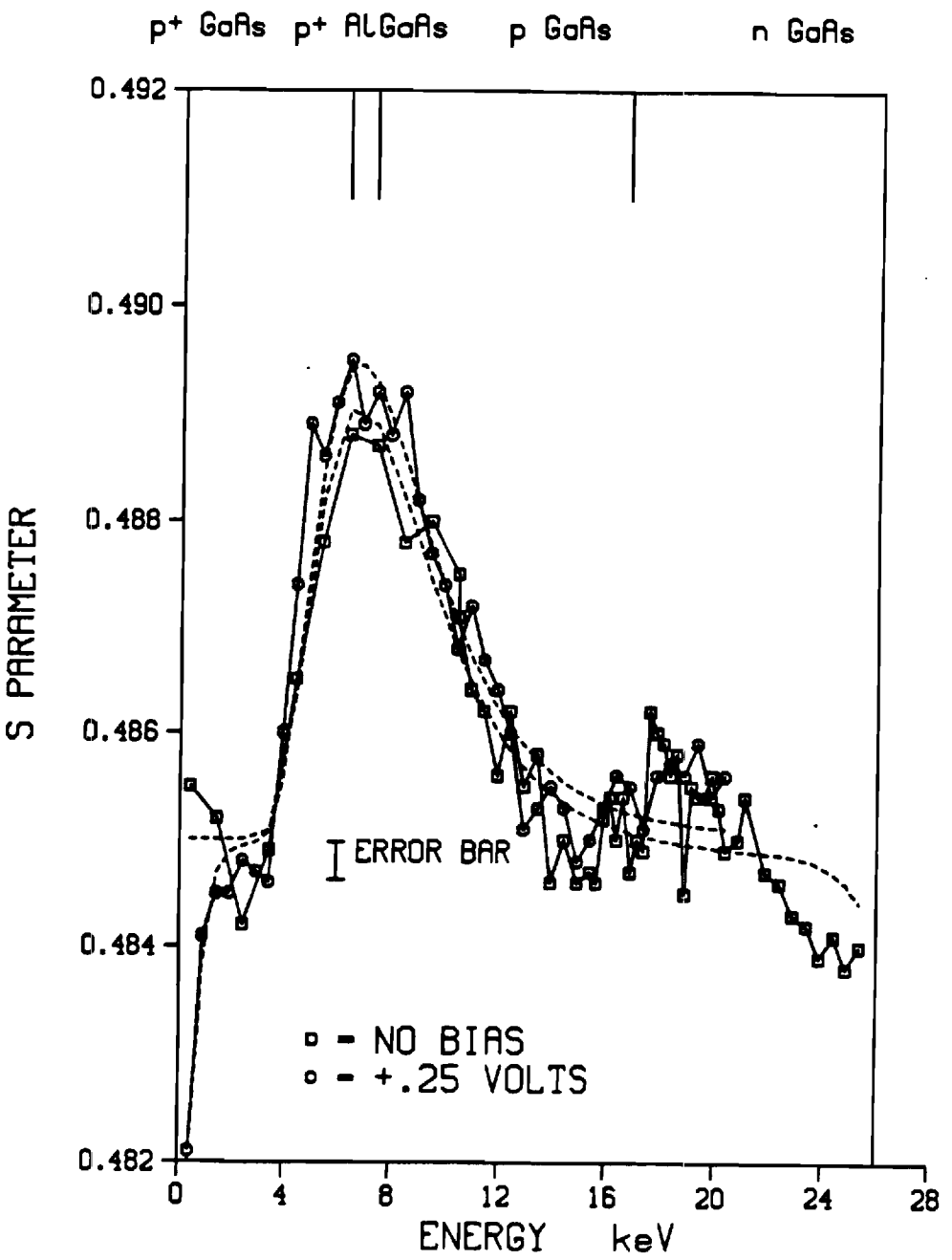

Figure 35. Forward Bias (+0.25 volt) SPAS Response Profile compared to the Zero Bias Case. The Dashed Curve Represent the Best Fit to the S(E) Response.

one another and both differ from the no-bias cae in the immediate surface region. Beyond the surface, the difference in S_i between the reverse and zero bias is large in the cap and emitter layers, while the only differences observed between forward and zero bias occur about the AlGaAs layer.

A systematic rise in the characteristic S_i values could result from an increase in free carrier electron concentration. Excess free carriers are generated by the application of an external bias and by raising the temperature of the sample. In a p-type region, electrons are the minority carrier; their concentration varies as the exponential of the applied bias V_A, increasing by 5 orders of magnitude with a forward bias of +0.25 volts. However, because of the high doping levels in the 872 B sample, the minority carrier electron concentration at equilibrium is only $10^{-4}cm^{-3}$. Thus an increase of 5 orders of magnitude results in a concentration of only 10 cm^{-3}, which is negligible compared with a total electron concentration of $10^{23}cm^{-3}$. Additionally, application of a reverse bias would actually decrease this concentration, decreasing the S_i values, which is in contradiction to the observed trends. Free carrier differences caused by varying doping levels and dopant types have been previously observed to have a negligible effect on the positron lifetime in GaAs [20].

The intrinsic carrier concentration n_i is a strong function of temperature. The voltage-current relationship for the sample was measured and indicates a maximum heat dissipation rate of about 0.17 W. Assuming only radiative heat transfer, a steady state temperature of about 77°C is found. This is actually a very conservative value, since the method by which the sample was mounted permitted significant conductive transfer as well. At 77°C, Sze [21] lists an intrinsic carrier concentration $n_i \approx 5 \times 10^8 cm^{-3}$, resulting in a minority carrier electron concentration of the order of 1 cm^{-3}, which is negligible compared with the total electron concentration. Thus an increase in minority carrier electron concentration caused by heating or bias effects is expected to be insignificant for the experimental conditions employed.

The complex behavior of S(E) near the AlGaAs/GaAs heterojunction and the p-n homojunction indicates that the junction regions play a key role in the S_i response. The electric field generated in the depletion region associated with the p-n junction may be the reason for the S_i behavior in the emitter layer for reverse bias. Assuming the depletion approximation is valid, the width of the depletion region and the p-side electric field for a step junction are given by [21]:

$$W = \{2\epsilon(V_{bi} - V_A)(N_A + N_D)\}/\epsilon N_A N_D \quad (36)$$

$$E(x) = \{-qN_A(x_p + x)\}/\epsilon \quad (37)$$

where V_A and V_{bi} are respectively the applied potential and built-in potential, N_A and N_D are the acceptor and donor doping levels, ϵ is the dielectric constant for GaAs, and q is the charge of an electron. E(x) on the n side is given by a similar expression. Application of a reverse bias ($V_A < 0$) increases the width of the depletion region and increases the strength of the electric field, while a forward bias will have the opposite effect. With a reverse bias of 2 V the depletion width is about 0.16 μm, and the electric field strength is on the order of $10^5 cm^{-1}$. Since $E(x) < 0$ for the entire region, electron-volt positrons implanted in or near the depletion region will be swept back toward the AlGaAs layer. This anisotropic drift coupled with a positron sink in the AlGaAs layer could generate an unbalanced positron current directed toward the presumably more defective window, resulting in an artificially enhanced S_i value in the emitter. Figure 36 shows an increased S_i value in the emitter layer for the reverse bias case, including a smoothing effect in the depletion region itself. Figure 37 shows no rise in the S_i in the emitter region for forward bias, consistent with a decreasing depletion region and electric field.

The value of S(E) at the surface for zero bias is raised above the rest of the cap layer, probably because of the presence of extended defect trap states, which are known to exist at a semiconductor surface. Figure 36 shows an increased S_i at the surface for the reverse bias case, while Figure 37 shows a decreased surface S_i. This effect is probably caused by band bending at the semiconductor-metal contact interface. A change in the charge state of defects has been previously observed by Dannefaer et al. [22], when the Fermi level is moved by heating the sample. Application of a reverse bias causes a local change as the valence band bends up toward the Fermi level, converting some trapping levels to neutral states. The free electrons created in this process have a lower energy than the trapped electrons and thus result in a higher S value when they annihilate. In contrast, a forward bias bends the conduction band away from the Fermi level, creating new negative trap states and, by analogy, decreasing S. The minimum in S(E) in the cap layer in both curves in Figure 34

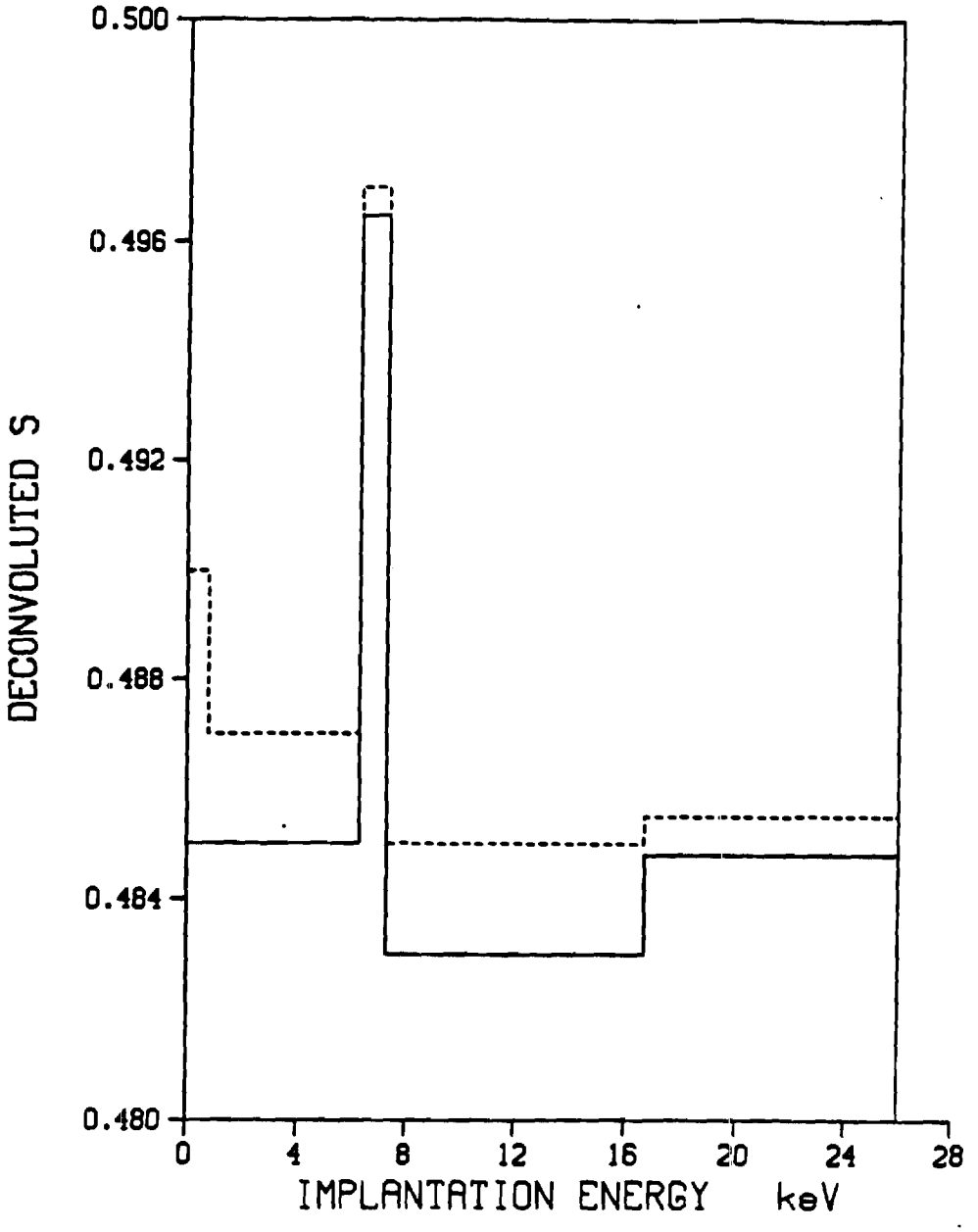

Figure 36. Deconvoluted S_1 Verse Implantation Energy for Reverse (Dashed Line) and No Bias (Solid Line).

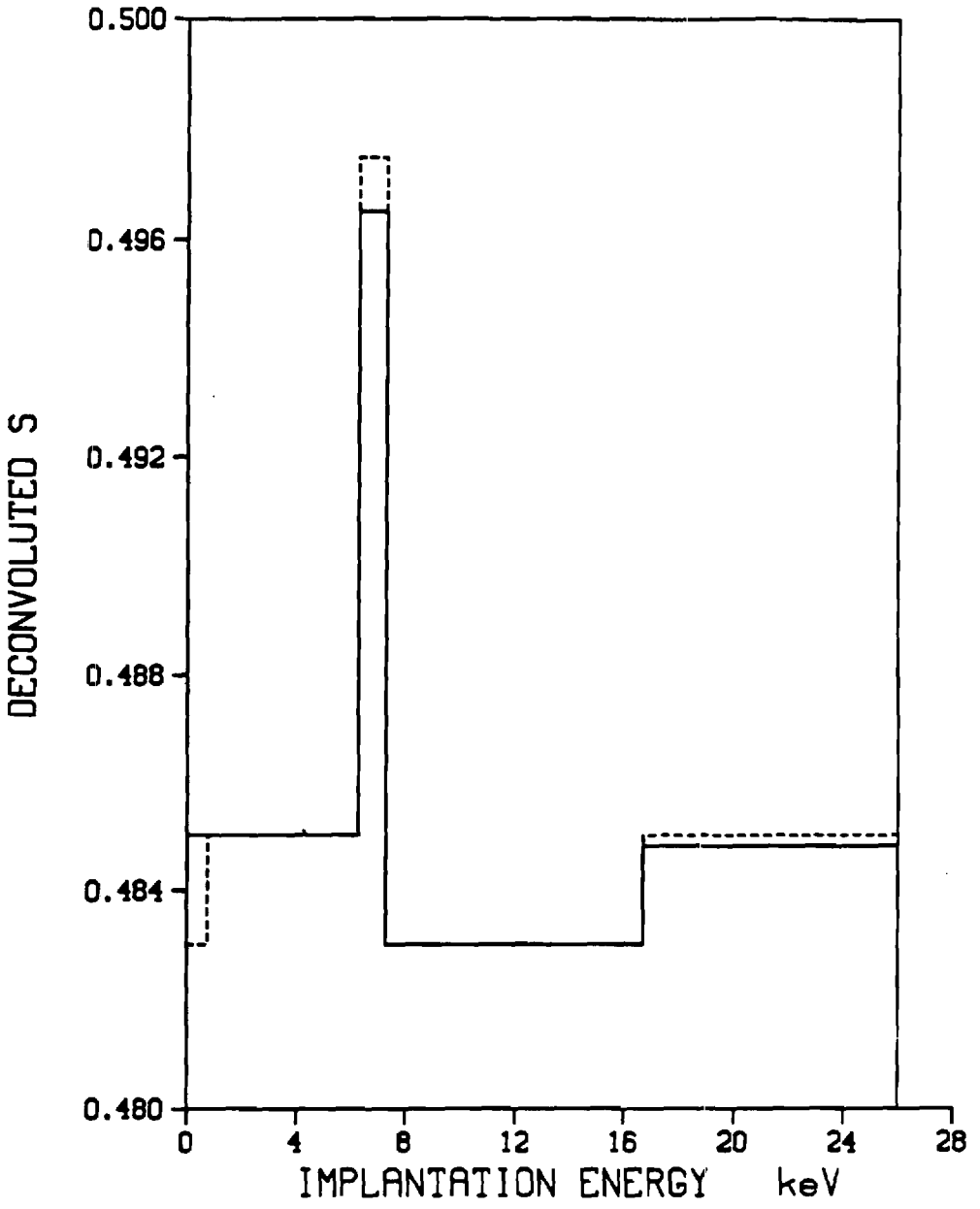

Figure 37. Deconvoluted S(E) Verse Implantation Energy for Forward (Dashed Line) and No Bias (Solid Line).

corresponds to the characteristic value S_i for this layer. It appears as a minimum simply because it is sandwiched between defective surface and interfacial regions.

For all values of applied bias, the maximum S_i is in the AlGaAs layer. The lattice constant of $Al_xGa_{1-x}As$ is a function of the fraction x of the aluminum present in the matrix. The lattice parameter mismatch at the AlGaAs-GaAs interface may result in the production of a significant interfacial dislocation density. Dlubek et al [23], have estimated that positron trapping at dislocations in GaAs becomes significant at a density of about $10^6 cm^{-2}$. Thus, the characteristic S_i value of the AlGaAs layer may result from a high interfacial defect trapping rate.

2.6.6 Summary

The Doppler response function S(E) in the AlGaaS structures studied has been modeled by modifying the implantation profile to account for diffusion of positrons to the presumably more defective AlGaAs layer. An analogous surface region is needed to describe the S(E) results with applied external bias. This model reproduces the general trends in S(E) but fails to account for the fine structure of S(E). A systematic rise in S(E) with applied external bias cannot be attributed to a change in minority carrier electron concentration, because of the small magnitudes of the concentrations involved. The enhancement of S_i in the emitter region for reverse bias may be caused by an anisotropic drift of positrons towards the AlGaAs layer as a result of the depletion region electric field. An abundance of defect levels at the surface of the cap layer causes an enhanced S_i value at equilibrium. Band bending with application of an external bias results in an increase in the surface S_i for reverse bias and a decrease for forward bias. The increase in S_i in the cap layer with reverse bias is not understood at this time and will be the subject of a future study.

A full realization of SPAS'S potential for characterizing multilayered semiconductors will require delineation of the effects at the heterojunction interface and at the p-n junction, a more accurate estimate of the positron diffusion length in AlGaAs and GaAs, and improved statistics of the finer details of the S(E) response function. Since SPAS is a relatively new technique, correlation with established techniques should be made wherever possible. Transmission electron microscopy and X-ray studies of the AlGaAs-GaAs interface would provide insight into the dislocation density and the extent of the defective regions, while deep level transient spectroscopy could identify

trapping levels. Finally, a model which can properly treat interfaces, bulk positron diffusion, and positron drift in an electric field will be required to deconvolute the data properly. Ongoing studies of the AlGaAs/GaAs and other semiconductor structures are expected to address these issues in the near future.

2.7 PROCESS DEVELOPMENT AND FABRICATION OF Si SOLAR CELLS

2.7.1 Introduction

We made the N+/P basic solar cells by using the metal etch method. The cell has yielded efficiencies of 9% under standard terrestrial conditions. Device fabrication and characterization are described below.

2.7.2 The Wafer used had the following Characteristics:

p-type, 3", FZ

(100) direction

0.2 [ohm-cm]

15 mils

2.7.3 The Process Flow Applied was as follows:

1. Substrate identification and initial cleaning
2. Silox deposition (back)
3. Wafer clean
4. Phosphorus diffusion (front)
5. Oxide etch
6. Premetal clean
7. Metallize front side
8. PR with contact grid mask
9. Etch metal
10. Strip PR
11. Metallize back side
12. Electroplating
13. Annealing
14. PR with mesa mask
15. Etch silicon
16. Strip PR both sides

2.7.4 Detailed Process Flow using Metal Etch Method

1. Substrate identification and initial cleaning
    0. Check out the resistivity and thickness of wafers
    1. Boil out tweezers and boat in DI water for 15 minutes
    2. Boil quartz beakers in 5:2:1 H_2O_2:H_2O:HCl for 2 hours
    3. Boil the wafers in TCE for 10 minutes
    4. Boil the wafers in acetone for 10 minutes
    5. Boil the wafers in methanol for 10 minutes
    6. DI rinse for 5 minutes
    7. Etch the wafer in a 50:1 HNO_3:HF solution for 1 minutes
    8. DI rinse for 5 minutes
    9. Dip wafers in a 1:10 HF:H_2O:H_2O_2:HCl for 10 minutes
    10. DI rinse for 5 minutes
    11. Boil the wafers in 5:2:1 H_2O:H_2O_2:HCl for 10 minutes
    12. DI rinse for 5 minutes
2. Silox deposition: Plasma assisted CVD of Si_2O_2: ~5000 Å
3. Wafer clean: same as in step 1, but skip 7-10
4. Phosphorous diffusion: 830°C, 20 min = 60-100 [ohm/], X_j = 0.3 μm
5. Oxide etch: dip 1:10 HF:H_2O until oxide removed
6. Premetal clean
    1. H_2SO_4:H_2O_2, 87°C, 5 minutes
    2. 1:10 HF:H_2O, 10 seconds
7. Metallize front side: T_i/A_g = 1500-2000 Å
8. PR with contact grid mask
    1. Clean with TCE, acetone, methanol & DI rinse
    2. Prebake: 120°C, 10 min
    3. Prime: HMDS coat - 4000 rpm, 25 sec & dry 30 sec
    4. Spin resist: +PR (1350J, full strength), 4000 rpm, 25 sec

5. Softbake: 95°C, 25 min
6. Expose: 5 sec
7. Develop: 1:3.5 developer:water for 45 sec
8. Postbake: 110°C, 20 min

9. Metal etch:
   1. Ti etch: 150 ccH_20 + 60 cc HCl + 30 ccNH_4F
   2. Ag etch: 20 H_20_2 + 60 NH_40H
10. Strip PR: Microposit 140, 60°C, 5 min & DI rinse
11. Metallize back side: T_i/A_g = 1500-2000 Å
12. Electroplating: current density = 2.5 [mA/Cm^2], 30 min, t = 8 μm
13. Annealing: 400°C, N_2 ambient, 15 min
14. PR with mesa mask: front first
    1. Prime: HMDS coat = 4000 rpm, 25 sec & dry 30 sec
    2. Spin on resist: -PR (waycoat IC, full strength), 3000 rpm, 25 sec
    3. Softbake: 80°C, 20 min
    4. Expose: 5 sec
    5. Develop: IC developer 1 min, N butyl acetate 1 min, methanol 1 min DI rinse 1 min
    6. Check the pattern under the μ-scope
    7. Hardbake: 110°C 20 min
15. Etch Si: 44 cc HF: 26 cc $HN0_3$: 29 cc acetic acid for 5-10 sec
16. Remove PR both sides: remove it with microstrip @ 60°C for 5 min and rinse with methanol and DI

TABLE 7. Cell Data Without AR Coating

Cell ID	J_{sc}[mA/cm^2]	V_{oc} [volts]	FF	Eff. [%]
7-1	22.72	0.537	0.7656	9.35
7-2	23.02	0.545	0.7172	8.99
7-3	17.95	0.545	0.7987	7.82
7-4	22.34	0.544	0.6500	7.90
7-5	22.67	0.544	0.6770	8.34
7-6	23.09	0.544	0.6895	8.66
7-7	22.67	0.546	0.7200	8.92
7-8	22.76	0.545	0.6959	8.64
7-9	22.04	0.544	0.7083	8.49

2.7.5 Summary

We have put together the necessary equipments for the Si solar cell fabrication. We are in the process of developing the basic fabrication processes and baseline solar cells. In the near future we will fabricate advanced solar cells with BSF thin passivation layer, textured surface, and μ-grooved cell structures. We also plan to investigate different silicon materials such as CZ, FZ, MCZ with different dopants.

3. ACKNOWLEDGEMENTS

The authors would like to thank P. Basore of Sandia Labs, T. Elfe, and S. Neel of the Georgia Tech Research Institute for helpful discussions concerning traps and ray tracing for the Si work. The authors would also like to recognize the assistance of S. P. Tobin of Spire Corp. for supplying the GaAs solar cells, J. Gee of Sandia Labs for valuable discussions, EPRI for the support for developing the lifetime modeling programs, Prof. DeWald and Robert Frost for PAS measurements, Mike Harris and Earl Meeks for silicon facility development, and graduate students Jalal and Lee for fabricating solar cells.

4. REFERENCES

Section 2.1

1. D. T. Rover, P. A. Basore, and G. M. Thorson, "Solar Cell Modeling on Personal Computers," *Proc. 18th IEEE Photovoltaic Specialists Conf.*, pp. 703-709, 1985.

2. W. Schockley and W. T. Read, "Statistics of the Recombinations of Holes and Electrons," *Phys. Rev.*, vol. 87, pp. 835-842, 1952.

3. R. N. Hall, "Electron-Hole Recombination in Germanium," *Phys. Rev.*, vol. 87, pp. 387-388, 1952.

4. D. L. Kendall, *Conf. on the Physics and Applications of Li Diffused Silicon*, 1969.

5. M. A. Green, *Solar Cells*, Prentice-Hall, p. 81, 1982.

Section 2.2

1. D. T. Rover, P. A. Basore, and G. M. Thorson, "Solar Cell Modeling on Personal Computers," *Proc. 18th IEEE Photovoltaic Specialists Conf.*, pp. 703-709, 1985.

2. A. W. Smith and A. Rohatgi, "Modeling the Effect of Trap Levels on the Optimum Resistivity of Silicon Solar Cells," to be published in *21st Photovoltaic Specialists Conf.*, Las Vegas, October 1988.

3. M. A. Green and P. Campbell, "Light Trapping Properties of Pyramidally Textured and Grooved Surfaces," *Proc. 19th IEEE Photovoltaic Specialists Conf.*, pp. 912-917, 1987.

Section 2.3

1. H. J. Hovel, "Solar Cells," in *Semiconductors and Semimetals*, R. K. Willardson and A. C. Beer (Eds.), vol. 11, Academic Press, New York, 1975.

2. R. C. Knechtli, R. Y. Loo, and G. S. Kamath, "High Efficiency GaAs Solar Cells," *IEEE Trans. Electron. Dev.*, vol. ED-31, no. 5, pp. 577-588, 1984.

3. S. P. Tobin, S. M. Vernon, C. Bajgar, L. M. Geoffrey, C. J. Keavney, M. M. Sanfacon, and V. E. Haven, "Device Processing and Analysis of High Efficiency GaAs Cells," *Solar Cells*, vol. 24, p. 103-115, 1988.

4. S. A. Ringel, A. Rohatgi, and S. P. Tobin, "An Approach Toward 25% Efficient GaAs Heteroface Solar Cells," *IEEE Trans. Electron. Dev.*, vol. 36, no. 7, pp. 1230-1237, 1989.

5. P. A. Basore, "Numerical Analysis of Semiconductor Devices on Personal Computers," *Proc. of the Sixth Biennial University/Government/Industry Microelectronics Symp.*, p. 73-76, 1985.

6. H. Van Cong, "Impurity Band Structure in Degenerate Semiconductors for Both Dense Donors and Acceptors," *Phys. Stat. Sol.*, vol. 56A, pp. 395-405, 1979.

7. A. Rohatgi and P. Rai-Choudhury, "Design, Fabrication, and Analysis of 17-18 Percent Efficient Surface-Passivated Silicon Solar Cells," *IEEE Trans. Electron. Dev.*, vol. Ed-31, no. 5, pp. 596-601, 1984.

8. L. D. Partain, M. S. Kuryla, L. M. Fraas, P. S. McLeod, and J. A. Cape, "A New Sequentially Etched Quantum-Yield Technique for Measuring Surface Recombination Velocity and Diffusion Lengths of Solar Cells," *J. Appl. Phys.*, vol. 61, pp. 5150-..., 1987.

9. P. D. DeMoulin and M. S. Lundstrom, "Theoretical Comparison of Conventional and Unconventional GaAs Cell Design," *19th Photovoltaic Specialists Conf.*, pp. 925-930, 1987.

10. C. J. Hwang, "Doping Dependence of Hole Lifetime in n-type GaAs," *J. Appl. Phys.*, vol. 42, no. 11, 1971.

11. R. J. Nelson, "Interfacial Recombination in GaAlAs-GaAs Heterostructures," *J. Vac. Sci. Technol.*, vol. 15, no. 4, 1978.

12. G. M. Martin, A. Mitonneau, and A. Mircea, "Electron Traps in Bulk and Epitaxial GaAs Crystals," *Electron. Lett.*, vol. 13, no. 22, pp. 191-192, 1977.

13. A Mitonneau, G. M. Martin, and A. Mircea, "Hole Traps in Bulk and Epitaxial GaAs Crystals," *Electron. Lett.*, vol. 13, no. 22, 1977.

14. W. Shockley and W. T. Read, "Statistics of the Recombination of Holes and Electrons," *Phys. Rev.*, vol. 87, no. 5, 1952.

15. J. S. Blakemore, "Semiconducting and Other Major Properties of Gallium Arsenide," *J. Appl. Phys.*, vol. 53, no. 10, pp. R123-R181, 1982.

Section 2.4

1. A. Haug, *J. Phys. C.*, vol. 16, p. 4159, 1983.

2. M. Takeshima, *J. Appl. Phys.*, vol. 58, p. 3846, 1985.

3. C. J. Hwang, *Phys. Rev. B*, vol. 6, p. 1355, 1972.

4. H. Van Cong, *J. Phys. Chem. Solids*, vol. 42, p. 95, 1981.

5. C. J. Hwang, *J. Appl. Phys.*, vol. 42, p. 4408, 1971.

6. H. C. Casey and M. B. Panish, in *Heterostructure Lasers*, Academic Press, New York, 1978.

7. R. J. Nelson and R. G. Sobers, *J. Appl. Phys.*, vol. 49, p. 6103, 1978.

8. P. A. Basore, *Proc. of Sixth Biennial University/Government Industry Microelectronics Symp.*, p. 73, 1985.

9. S. A. Ringel and A. Rohatgi, *IEEE Trans. Elec. Dev.*, vol. 36, no. 7, pp. 1230-1237, 1989.

10. S. A. Ringel and A. Rohatgi, *Proc. of 20th IEEE Photovoltaic Spec. Conf.*, in print, 1988.

11. P. D. Demoulin and M. S. Lundstrom, *Proc. of the 19th IEEE Photovoltaic Spec. Conf.*, p. 925, 1987.

12. W. Shockley and W. T. Read, Jr., *Phys. Rev.*, vol. 87, p. 835, 1952.

13. G. M. Martin, A. Mitonneau, and A. Mircea, *Electron. Lett.*, vol. 13, p. 191, 1977.

14. A. Mitonneau, G. M. Martin, and A. Mircea, *Electron. Lett.*, vol. 13, p. 666, 1977.

15. N. D. Arora, S. G. Chamberlain, and D. J. Roulston, *Appl. Phys. Lett.*, vol. 37, p. 325, 1980.

16. A. Rohatgi, J. R. Davis, R. H. Hopkins, and P. G. McMullin, *Solid State Electron.*, vol. 23, p. 1039, 1983.

17. E. Yablonovitch, R. Bhat, J. P. Harbison, and R. A. Logan, *Appl. Phys. Lett.*, vol. 50, p. 1197, 1987.

18. S. M. Sze, in *Physics of Semiconductor Devices*, John Wiley and Sons, New York, p. 29, 1981.

Section 2.5

None

Section 2.6

1. A. B. DeWald, R. L. Frost, S. A. Ringel, J. P. Schaffer, A. Rohatgi, B. Nielsen and K. G. Lynn, *J. Vac. Sci. Technol. A.*, to be published.

2. B. Nielsen, K. G. Lynn, Y.-C. Chen and D. O. Welch, *Appl. Phys. Lett.*, vol. 51, p. 1022, 1987.

3. P. J. Schultz, K. G. Lynn, E. Tandberg, N. Nielsen, T. E. Jackman, L. C. Feldman, J. Bean and M. W. Denhoff, submitted to *Phys. Rev. Lett.*

4. A. P. Druzhkov, L. B. Khaibullin, R. M. Bayazitov, E. I. Shtyrkov and L. A. Suslov, *Soc. Phys. Semicond.*, vol. 13, p. 574, 1979.

5. J. C. Bourgoin, H. J. von Bardeleben and D. Stievenard, *Phys. Status Solidi A.*, vol 102, p. 499, 1987.

6. K. P. Aref'ev, V. N. Brudnyi, D. L. Budnitskii, S. A. Vorobev and A. A. Tsoi, *Sov. Phys. Semicond.*, vol. 13, p. 669, 1979.

7. S. E. Bochkarev, L. A. Ivanyutin, V. P. Komlev, E. P. Prokpolev, V. M. Samollow, V. G. Firsov and Yu, V. Funitlov, *Sov. Phys. Solid State*, vol 23, p. 118, 1981.

8. S. Dannafaer, N. Fruensgaard, S. Kupea, B. Hogg, and D. Kerr, *Cam. J. Phys.*, vol. 61, p. 451, 1983.

9. P. Hautojarvi, P. Moser, M. Stucky, C. Corbel and F. Plazaloa, *Appl. Phys. Lett*, vol. 48, p. 809, 1986.

10. K. P. Arefev, S. A. Vorobev and V. G. Stardubov, *Soc. Phys. Semicond.*, vol. 8, p. 794, 1974.

11. A. P. Druzhkov, E. P. Prokoplev, Y. N. Kuznetsov, A. I. Sidorov and V. A. Fedorov, *Soc. Phys. Semicond.*, vol. 14, p. 119, 1980.

12. Y. J. He, M. Hasegawa, R. Lee, S. Berko, D. Adler and A. Lung, *Phys. Rev. B.*, vol. 33, p. 5924, 1985.

13. H. E. Schaefer, R. Wurschum, R. Schwartz, D. Slobodin and S. Wagner, *Appl. Phys. A.*, vol. 40, p. 145, 1986.

14. V. G. Bhide, R. O. Dusane, S. V. Rajarshi, A. D. Shangram and S. K. David, *J. Appl. Phys.*, vol. 62, p. 108, 1987.

15. K. G. Lynn, B. Nielsen and T. H. Quateman, *Appl. Phys. Lett.*, vol. 47, p. 239, 1985.

16. I. K. MacKenzie, J. A. Eady and R. R. Gingerich, *Phys. Lett. A.*, vol. 35, p. 4606, 1987.

17. A. Vehanen, K. Saarinen, P. Hautojarvi and H. Huomo, *Phys. Rev. B.*, vol. 35, p. 4606, 1987.

18. J. L. Campbell, *Appl. Phys.*, vol. 13, p. 365, 1977.

19. G. Dlubek, R. Krause, O. Brummer and J. Tittes, *Appl. Phys. A.*, vol. 42, p. 125, 1987.

20. O. Takai, Y. Hisamatsu, N. Owada, H. Ishimura, K. Hinode, S. Tanigawa and M. Doyama, *Phys. Lett. A.*, p. 76, p. 157, 1980.

21. S. M. Sze, *Physics of Semiconductors*, Wiley-Interscience, New York, 1981.

22. S. Dannefaer, B. G. Hogg and D. P. Kerr, *Phys. Rev. B.*, vol. 30, p. 3355, 1984.

23. G. Drubeck, O. Brummer, F. Plazaola, and P. Hautojarvi, *J. Phys. C.*, vol. 19, p. 331, 1986.

APPENDIX

RAY TRACING PROGRAM - TEXTURE

Texture is a 3 dimensional ray tracing program designed to provide the solar cell community with a method to quantitatively describe the enhancement in absorbed flux for various surface texturing. The program is designed to run on an IBM-pc compatible computer with a co-processor or any computer with FORTRAN 77. The program is intended to be a companion to PC-1D version 2. A one dimensional generation profile can be output in the proper format to be easily incorporated into PC-1D, this will only be valid if the surface texturing is small. In addition, texture uses the same absorption or material files as PC-1D version 2. Options within the program allow for five modes of operation. The first is a full 3 dimensional response to the incoming light. The second and third modes are again a 3 dimensional response to the light but a reduction to a one or two dimensional generation profile. The last two options are qualitative modes which provide characterizing information. Output from texture includes a generation profile, all of the material information entered (for cataloging), and the amount of photons lost due to all surfaces and structures. In the qualitative mode the output includes the average path length, the number of rays remaining after each pass, the number of rays that re-enter, and other information.

At the start of each run you will be asked a number of questions concerning the mode of operation, typical options are as follows; material parameters, cell structure, grid lines, angle of incidence of the light, files for index of refraction and reflection as a function of wavelength, and the number of photon packets to be followed. Each of the options will be explained in detail in the following paragraphs. First an explanation of how the program works is in order.

The incoming light is broken up into different wavelengths and energy, these are determined from the spectrum and incident energy that you have chosen. The number of photons is determined from this information. The number is then divided by the number of rays that you would like to trace. The more rays traced the longer the execution time, but the more statistically accurate the answer. When these rays are incident upon a surface some photons are reflected while other penetrate. Those that enter the structure are broken down further into an exponentially decreasing

profile which is followed until all of the photons are absorbed, lost out the front or sides or back of the structure. Those photons which are reflected are followed until they strike a surface or it is determined that they will never enter the cell. Those photons which are reflected from within the cell in an outward direction are followed in the same manner as a reflected ray.

The angle of incidence is an important variable which the user is allowed to specify. Two random numbers are generated to determine where on a plane located just above the cell structure the ray strikes. If a cover glass option is chosen the top of the glass is the plane of incidence. If no cover glass is present then the plane of incidence is located at the thickness of the cell plus the height of the front structure, Figure A1. If the front surface is a flat plane then no further modification is required. If the surface is textured then a routine is called which will determine exactly where the ray strikes the surface. When more rays are traced in this manner then more of the cell surface is sampled to determine its effects on the incoming light.

The incoming ray which contains x#-photons, is now broken up into two distinct rays. The first carries FSR*x#-photons, where FSR is the front surface reflection factor for the wavelength in question. This ray will be reflected from the surface and followed until a surface is encountered or it escapes completely from the cell structure. The second ray carries (1 - FSR)*x#-photons and is intended to enter the cell. The angle of refraction will depend upon the incident angle, the wavelength of the radiation, the index of refraction of the first material, and the index of refraction of the second material. The absorption coefficient of the material at the wavelength in question will be outlined from a separate routine.

Once the ray has entered the cell and the direction is determine, the point where the ray hits the structure again is found. This is done by first checking to see if the ray rehits the front surface. If it does not rehit the front, it must be going towards the back. But before it hits the back there is the possibility that it could hit the side of the cell, and this is also checked. If it does not hit the side then the point where it hits the back is found. Now two points are available, the point of incidence and the new point of interaction. The distance between the two points is found and checked to see if any of the photons could have been absorbed in this distance. If any are absorbed, then the position along the axes where absorption takes place is recorded along with the number of photons

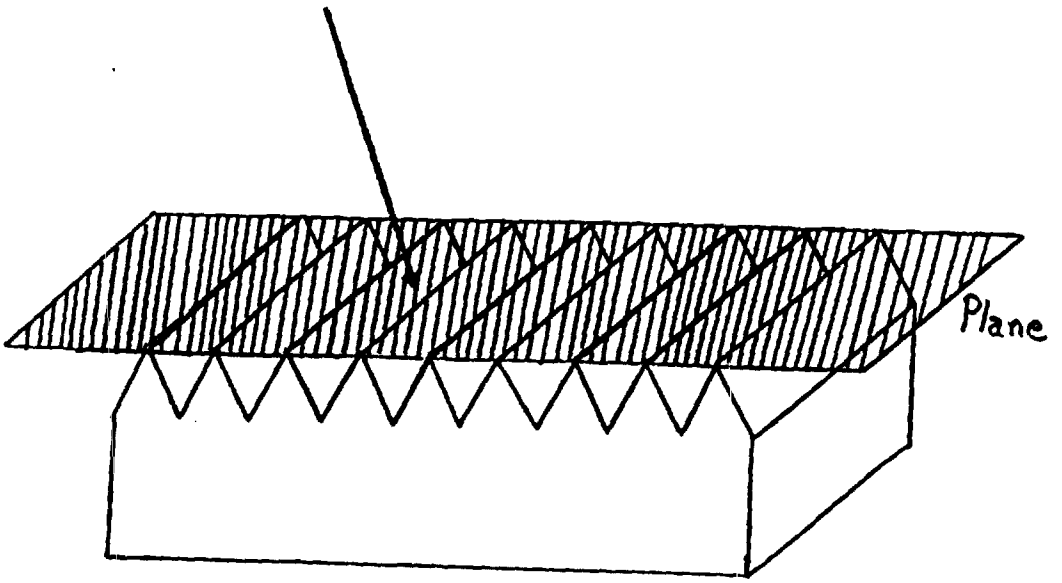

Figure A1. Plane of Incidence for a Textured Cell Surface.

absorbed. This is how the generation profiles are obtained. The ray is then reflected and its next intersection with a surface is found.

The process will continue until all of the photons are absorbed or leave the structure and can not re-enter. At this time a new ray is started and the whole process is repeated until all packets are traced. Then the next wavelength is treated in the same manner.

INPUT VALUES

This section will describe the input values and options for the user. The questions in the program are fairly self-explanatory.

The first input encountered will be for the option of a cover glass. Since most cells today incorporate some sort of encapsulant material this is a necessary option for real cell simulation. If a cover glass is chosen then the program will prompt for the file containing the index of refraction to be used. The next prompt will be for cover glass texturing. This option is mainly for thin cells deposited on glass substrates where the front surface has been mechanically textured, it may also be useful for other applications. The back surface of the glass will be assumed to be flat, but an encapsulating material will be assumed to fill the spaces between the plate and the cell. The final input for the cover glass will be its thickness.

The second input is the front structure of the cell. Currently there are 4 available choices:

1. flat
2. slats in the x direction
3. pyramids (four sided figures, fifth side down)
4. tetrahedrons (three sides, fourth side down)

The basic structures and distances which can be specified are shown in Figure A2. Notice that none of the characteristics imply any dimensions. These will be determined at a later time. A structure is determined by inputing the integer preceding the description. A note must be placed here concerning certain structures. In most cases a choice of front structure will have no bearing on the choices or dimensions of the back structure. Only in the case when the back structure is chosen to be positive slats in the x direction and the thickness of the cell is less than the height of the slat, will

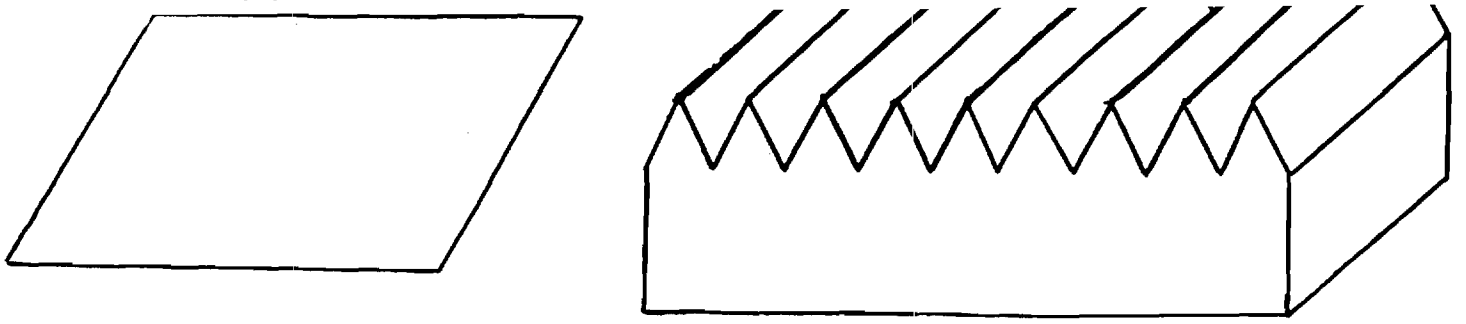

(a)

(b)

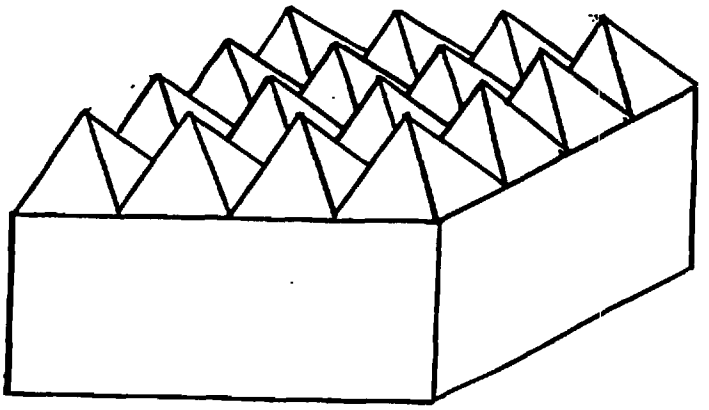

(c)

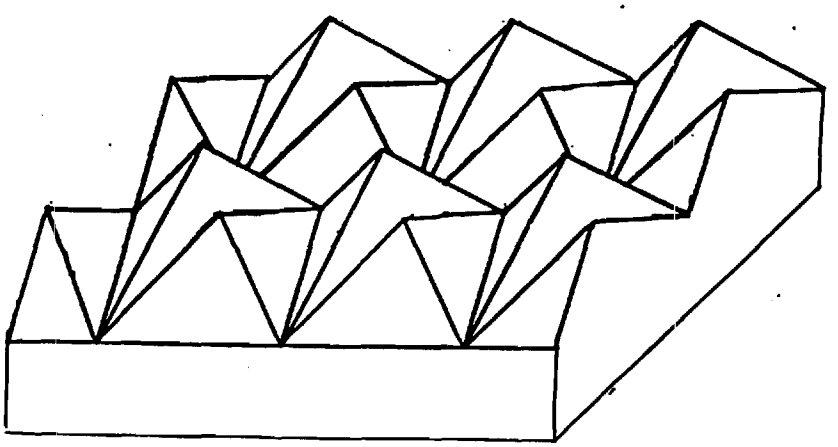

(d)

Figure A2. Various Front Surface Texturing Geometries: (a) Flat, (b) Slats, (c) Pyramids, and (d) Tetrahedrons.

there be a problem. This situation will not be allowed, and the user will be prompted for new values of the dimension of the structure.

Once the structure is chosen, questions will be asked concerning the dimensions of the structure. Enter all values in microns and as positive values!! Figure A3 contains diagrams concerning all the data which can be entered for each structure. Different values can be entered at any point allowing for an infinite number of structures to be modeled.

The next input will control the structure of the back surface. As in the structure of the front surface the choice is made by selecting the appropriate integer. Currently these are the back structures supported:

1. flat
2. slats in the x direction
3. slats in the y direction
4. pyramids
5. positive slats in the x direction
6. tetrahedrons
7. square wells

Figure A4 shows the possible configurations. Again note that no dimensions are given, these will occur in the next question. Remember the choice of the back structure is independent of the choice of the front structure.

Once the back structure has been determined the program will ask for the important dimensions of the structure. Input the dimensions in microns and as positive values, the program will do any interpretation of the values!!

The next input is for the thickness of the cell. Do not include the thicknesses of the front or back structure, these have already been taken into account. The values of various thicknesses is shown in Figure A5. At this point the structure dependence will take effect. If the back structure is positive slats in the x direction and the height is greater than the thickness then an error will occur for any front structure other than slats in the x direction. Even so, if the lengths of the front and back structure are not the same an error will occur and you will be returned to the front structure input menu. A very thin cell will produce a longer execution time because of the amount of time to

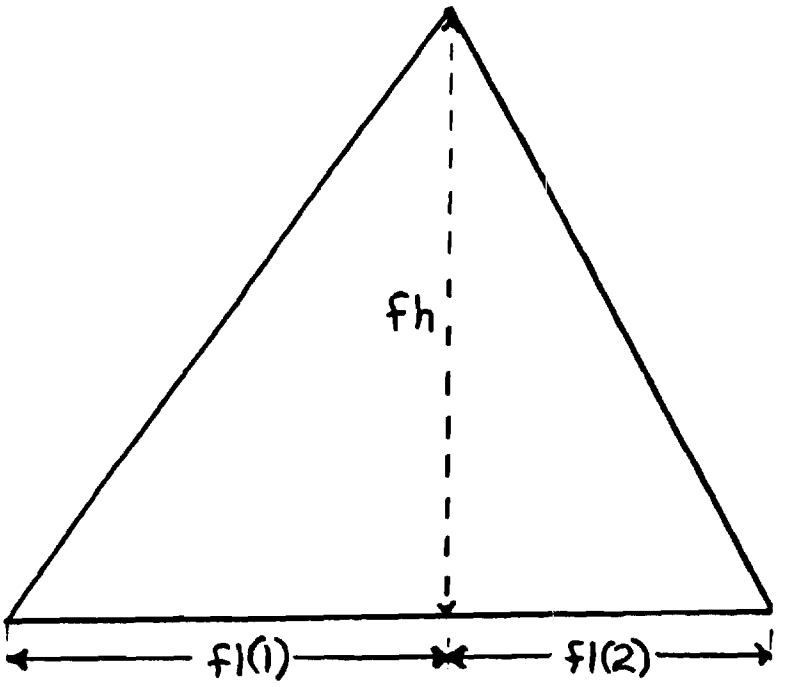

Figure A3. Example of Input Data for Slats on the Front Surface.

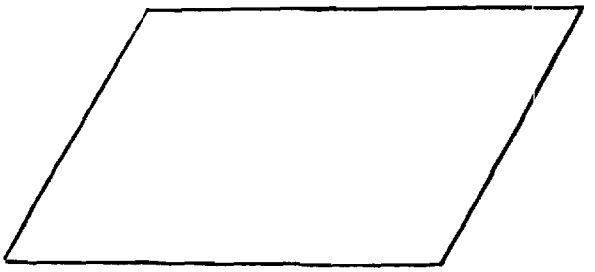

(a)

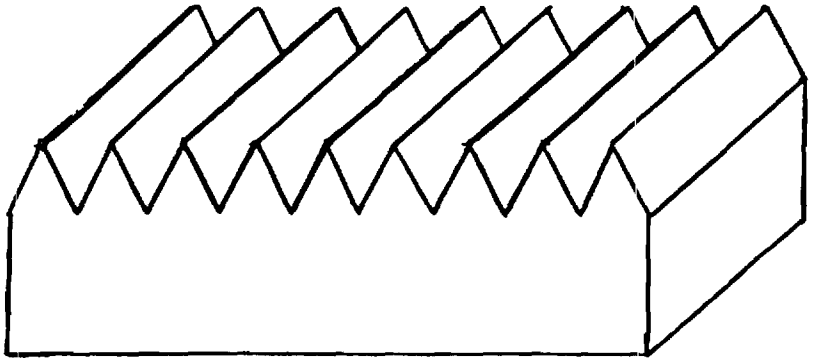

(b)

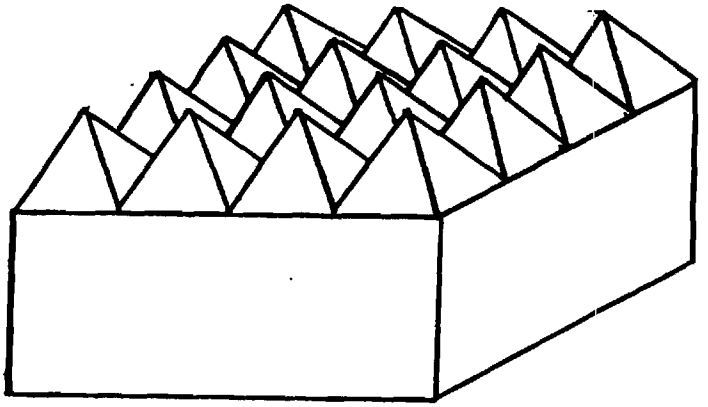

(c)

Figure A4. Various Back Surface Texturing Geometries: (a) Flat, (b) Slats in x or y, (c) Pyramids, (d) Tetrahedrons, and (e) Square Wells.

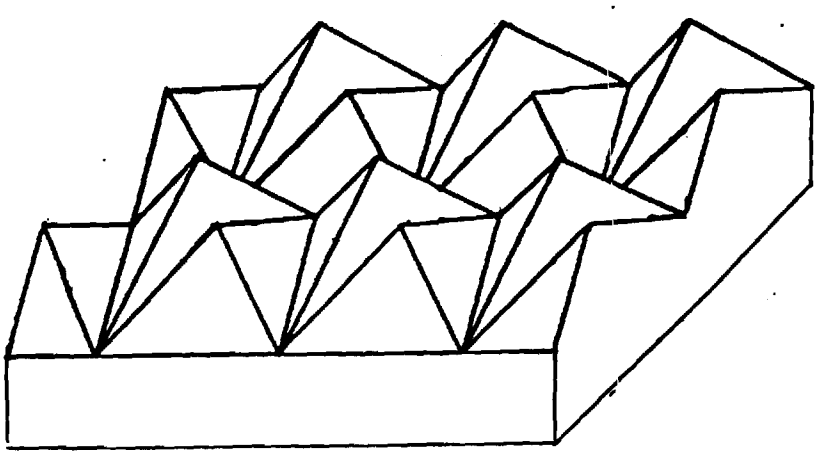

(d)

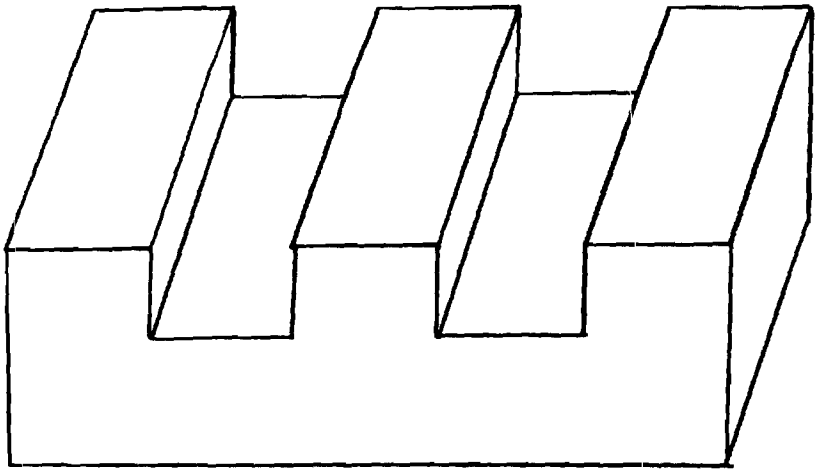

(e)

Figure A4. Various Back Surface Texturing Geometries: (a) Flat, (b) Slats in x or y, (c) Pyramids, (d) Tetrahedrons, and (e) Square Wells.

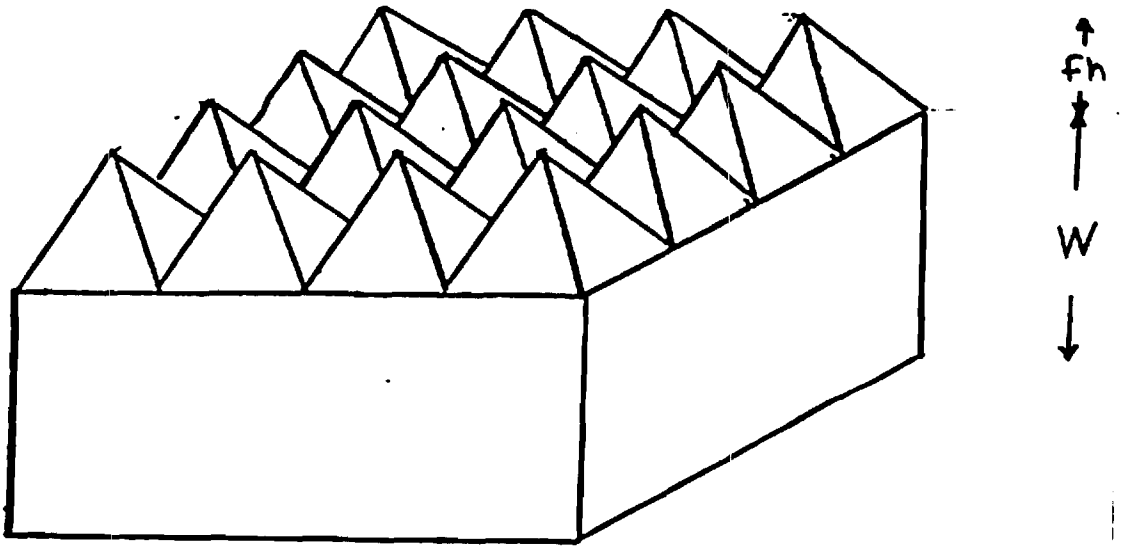

Figure A5. Examples of Relationship of Various Thickness of the Cell.

produce refraction routines and check all of the possible combinations of where the ray could go. The ray will tend to leave the cell more often and therefore produce more reflected rays which must be traced.

The next input is for the number of rays to be traced at each wavelength. A large number here will produce a long execution time due to the amount of work in tracing each ray. The number of photons traced in each ray will be given by the formula

$$X\#\text{-photons} = (\text{energy}*\text{lambda})/(q*1.2399*\text{number of rays})$$

It can be clearly seen that the more rays traced, the closer the solution is to the exact solution, therefore; there is a compromise between the speed of solution and the accuracy. Only for cells with both flat front and back structures will it be appropriate to follow only one ray at each wavelength.

The next input is to chose whether to use a file which contains the reflection and index of refraction data. If a file is used then the program will read the file and use the data. The file should contain values for the whole range of wavelengths in the spectrum to be used. The wavelengths do not have to match exactly with the spectrum file. Interpolation using cubic splines will be used to determine values at the wavelengths required. If no file is given then the program will prompt the user for the front surface reflection factor, the static index of refraction of the semiconductor, and the static index of refraction of the outer medium, a value of 1.0 implies no bonding material.

The grid line option is the next input. If no grid lines are required then input "no". If grid lines are needed then the number of lines required is asked first. Then the program will prompt for the (X,Y) coordinate of the lower left corner of the grid line. This will produce a grid line similar to Figure A6. At this time only grid lines parallel to the axes are supported. If a ray strikes a grid line from the inside of the cell then it will be internally reflected, with some loss in intensity regardless of the angle of incidence. If a grid line is struck on the outside of the cell then the ray is treated as if it were a reflected ray, again with some loss in intensity. The absorption which takes place at a grid line depends upon the metal forming the grid. The next two inputs are for the effectiveness of reflection from the grid lines. The first is for the ray that is external, this value will usually be close to one since silver is used as the top of the grid line. The second input is for rays

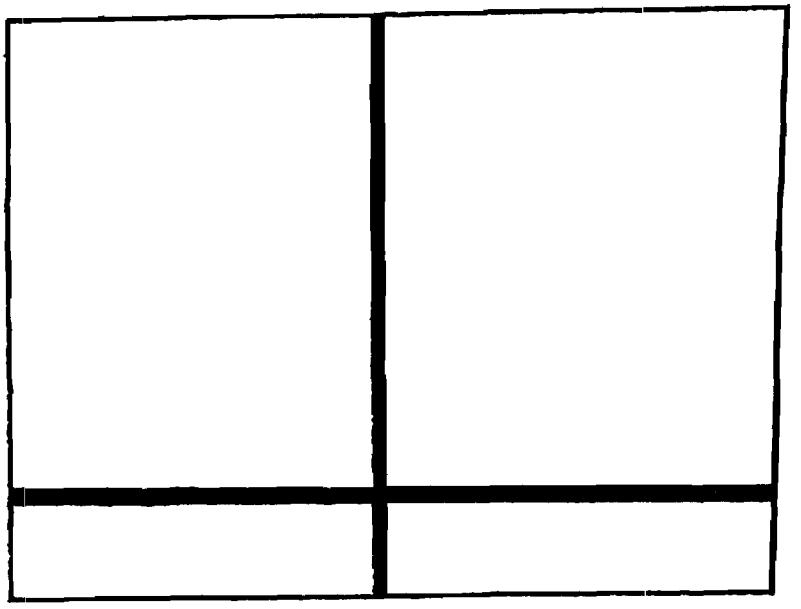

Figure A6. Example of Grid Lines Parallel to Coordinate Axes.

internal to the cell. This value will be closer to 0.8, because the reflectivity of titanium is lower than for some other metals.

The angle of incidence of the incoming light is specified with the next input. Changing from normal incidence will produce a longer execution time because the initial contact point of the ray and the structure must be calculated. This option allows the user to determine the degradation/enhancement the cell in question due to tracking errors or stationary configurations. The angle of incidence must be given in direction cosines of the angle. That is normalized to one as will be explained later.

The next input is for the spectrum to be used. Since these cells may be used in any application most common spectrums are supported. The spectrum files from PC-1D version 2 are the best examples. Or the user can create original spectrum to match specific applications.

The energy density of the incoming ray is the next consideration. The user is allowed to specify the exact energy distribution for the spectrum. This will allow for concentrator systems to be modeled or attenuation of energy due to atmospheric conditions to be modelled.

The final input is the material file which will contain either the absorption as a function of wavelength or the values for the internal model absorption for the material in question. Again a PC-1D version 2 material file is supported or the user can make a custom file.

THEORY OF OPERATION

The formulas used in the derivation are as follows.

The equation of a line is given by

$$(X1 - X0)/CALF = (Y1 - Y0)/CBET = (Z1 - Z0)/CGAM$$

where X1, Y1, and Z1 are the coordinates of the new point and X0, Y0, and Z0 are the coordinates of the initial point. Calf, Cbet, and Cgam are the direction cosines of the line.

The equation of a plane is given by

$$X/a + Y/b + Z/C = 1$$

where a, b, and c are the intercepts of the x, y, and z axes respectively. The direction cosines of the normal of the plane would be given by

$$Calfn = a/(a^2 + b^2 + c^2)$$

$$Cbetn = b/(a^2 + b^2 + c^2)$$

$$Cgamn = c/(a^2 + b^2 + c^2)$$

The main idea of the program is to find the intersection of the line (ray) and the plane of the cell structure.

The first step is to constrain the ray into a fixed area. In this fixed area the only planes the ray may hit are determined by the structure of the cell. This is called normalization. The point of intersection is found and translated into normalized coordinates and then translated back to the structure. The following example and Figure A7 should help the explanation. If the ray is traveling from the front of the cell towards the back then the point of intersection of the line and the x-y plane located at z = 0 is found. Then using the coordinates of the point and the characterizing distances of the back structure the point is translated to a new coordinate system. This new coordinate system will have its origin located at the peak of the structure, and all other points will be referenced to this point. The following formulas are for slats running in the x direction.

$$XOFFSET = (b1(1) + b1(2))*INT(X1/(b1(1) + b1(2)) + b1(1)$$

$$XN = X1 - XOFFSET$$

The value of XN is between -b1(1) and b1(2), with XOFFSET given by an integer multiple of (b1(1) + b1(2)). For slats running in the y direction the results would be similar with just a replacement of y for x. The normalization of the pyramid structure on the back surface would be given by

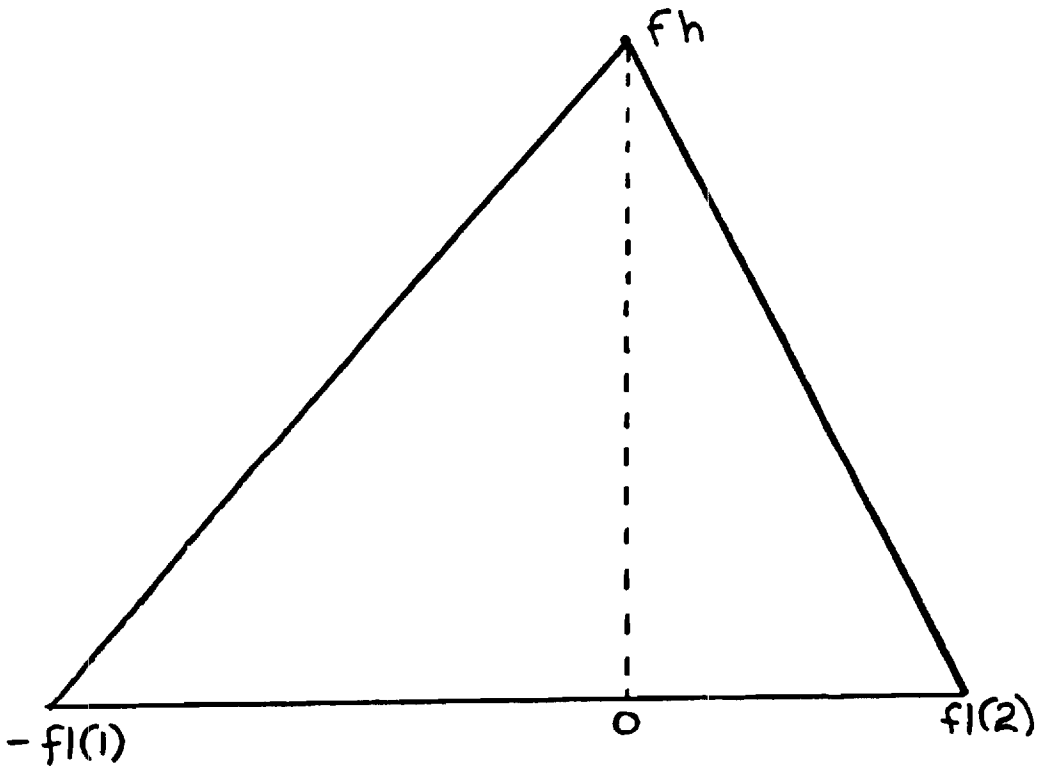

Figure A7. Normalized Slat Structure.

$$XOFFSET = (b1(1) + b1(3))*INT(X1/(b1(1) + b1(3)) + b1(1)$$

$$XN = X1 - XOFFSET$$

$$YOFFSET = (b1(2) + b1(2))*INT(X1/(b1(2) + b1(4)) + b1(2)$$

$$YN = Y1 - YOFFSET$$

The normalized structures are diagrammed in Figure A7. These structures will be used to find the point where the ray strikes. This is done by checking all of the distinct planes in the structure. To ensure that the program does not repeat calling the same plane over and over, and to save time, the routine does not consider the plane of origin. This can be done because a ray cannot rehit the same plane without hitting another plane first. If the ray does not strike any of the planes in the region given by the normalized constraints then it must be heading towards the opposite surface.

If the ray is heading towards the opposite surface then there is the possibility that it will strike a side before arriving. This alternative is accounted for. If the ray does strike the side and the angle of incidence is such that the ray is coupled out of the cell then this energy is lost. If the ray is reflected the new direction is found and tracing continues.

Once the new point is found the angle of reflection or refraction must be calculated for the ray to continue. The normal of the surface is found from the side of the structure that the ray strikes. Then the direction numbers of a line perpendicular to both the surface normal and incident ray is found. This is done by tracking the cross product of the direction cosines, between the surface normal and incident ray.

incident ray⊗surface normal = abc-line

aa = Cbet*Cgamn - Cbetn*Cgam

bb = Calfn*Cgam - Cgamn*Calf

cc = Calf*Cbetn - Calfn*Cbet

The reflected/refracted ray will also be perpendicular to this line. This will produce the first condition on the reflected/refracted ray. This condition is given by the dot product of the

reflected/refracted ray and the line given by aa, bb, and cc. Because the lines are perpendicular, their dot product is zero.

$$0.0 = aa*Calfr + bb*Cbetr + cc*Cgamr$$

It is also known that since the surface normal and the incident ray are unit vectors then the dot product of the two vectors is the cosine of the angle between them (angle of incidence)

$$Cos(\theta_1) = Calf*Calfn + Cbet*Cbetn + Cgam*Cgamn$$

For the case of a reflected ray and the surface normal this expression is also valid since the angle of reflection is equal to the angle of incidence.

$$Cos(\theta_r) = Cos(\theta_i) ,$$

$$Cos(\theta_i) = Calfr*Calfn + Cbetr*Cbetn + Cgamr*Cgamn$$

This is the second condition on the reflected ray. The third and final condition is also given by the knowledge that the angle of incidence is equal to the angle of reflection. Then the angle between the incident and reflected ray is twice this angle.

$$Cos(\theta_{i+r}) = Cos(2\theta_i)$$

$$Cos(2\theta_i) = Calfr*Calf + Cbetr*Cbet + Cgamr*Cgam$$

This leads to a system of the three equations with 3 unknowns, (Calfr, Cbetr, and Cgamr), which must be solved simultaneously.

$$0.0 = aa*Calfr + bb*Cbetr + cc*Cgamr$$

$$Cos(\theta_i) = Calfr*Calfn + Cbetr*Cbetn + Cgamr*Cgamn$$

$$Cos(2\theta_i) = Calfr*Calf + Cbetr*Cbet + Cgamr*Cgam$$

In this case the refracted ray the first condition is the same. For the second condition the knowledge of Snell's refraction law must be employed, Figure A8.

$$Sin(\theta_i)/Sin(\theta_r) = \eta_r/\eta_i$$

$$Cos(\theta_r) = Cos(arcSin(Sin(\theta_i)*\eta_r/\eta_i)$$

Then the second condition would be given by

$$Cos(\theta_r) = Calfr*Calfn + Cbetr*Cbetn + Cgamr*Cgamn$$

Which is the dot product between the surface normal and the refracted ray. The third condition is the angle between the incident ray and the refracted ray. This would be given by

$$Cos(\theta_{ri}) = Cos(ArcCos(\theta_r) - arcCos(\theta_i))$$

where

$$Cos(\theta_i) = Calf*Calfn + Cbet*Cbetn + Cgam*Cgamn$$

These three conditions lead to the following 3 equations in Calfr, Cbetr, and Cgamr. (In this case these are refracted angles)

$$0.0 = aa*Calfr + bb*Cbetr + cc*Cgamr$$

$$Cos(\theta_r) = Calr*Calfn + Cbetr*Cbetn + Cgamr*Cgamn$$

$$Cos(\theta_{ri}) = Calfr*Calf + Cbetr*Cbet + Cgamr*Cgam$$

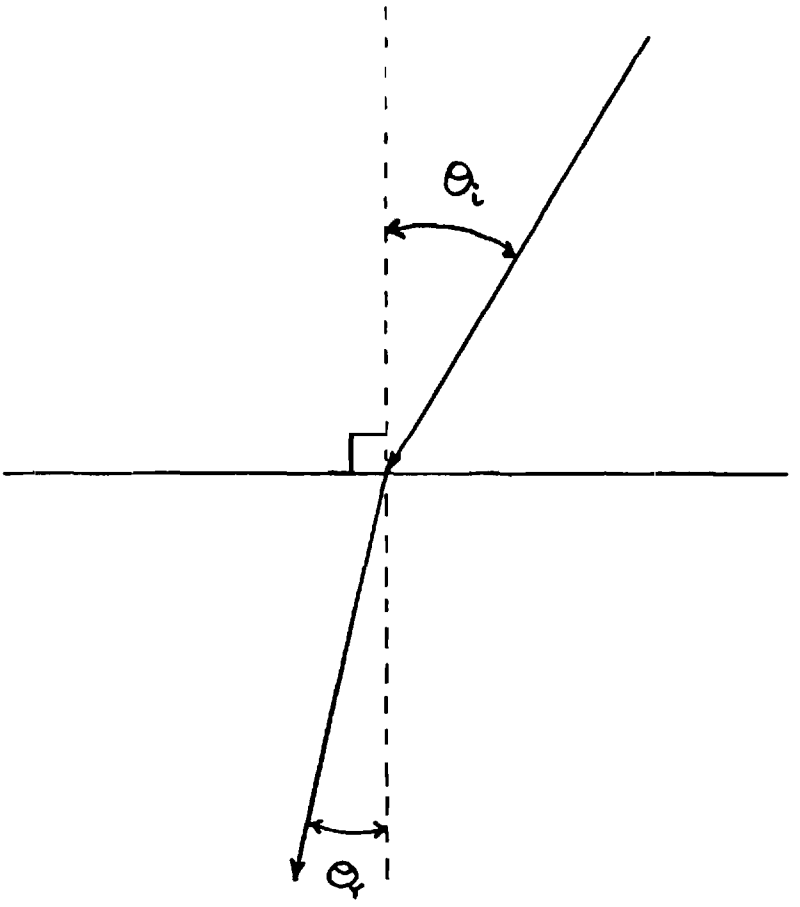

Figure A8. Example of Snell's Law.

Solving the appropriate system for the ray in question gives the new direction for the ray to follow.

The absorption coefficient is found in the same manner as in PC-1D. As either a function of the wavelength or an interpolation between two input values. The number of photons absorbed is found at each node by calculating the number of photons that could be absorbed in a volume surrounding that node. The intensity is then lowered by the amount absorbed and the absorption at the next node is calculated using this lower intensity as the incident flux. This is continued from the incident point to the new point of intersection. Then by knowing the distance the ray has traveled, given by the distance formula

$$\text{distance} = (X0 - X1)^2 + (Y0 - Y1)^2 + (Z0 - Z1)^2$$

and the incremental distances, if the distance is greater than the incremental distance then a portion of the ray is absorbed. The coordinate of absorption is noted and the absorbed intensity in the incremental volume is increased by the amount absorbed.

If a ray strikes a grid line or a non-perfect rear surface reflector then the intensity of the light remaining in the ray is decreased by the loss due to the metal absorption. This is similar to the treatment the ray receives when it is coupled out of the side of the cell. In that case though, all of the remaining intensity is lost. In all the cases, counters are incremented to tell the user exactly how much energy is lost due to each phenomena. This is done to aid in the design of even better cells by pointing out areas where the most improvement may be obtained.

PROGRAM OUTPUT

The output of the program will depend upon which mode of operation was selected by the user. The basic output will contain the cell structure used, with the dimensions, the files or static numbers for material parameters, the spectrum chosen, and the mode dependent data.

The cell structure will be listed from the top to the bottom of the cell. If the cover glass was present then the structure thickness and the other dimensions will be output first. Then if a file was chosen for the index of refraction and reflection its name will be output, otherwise the static number will be output. The structure and its parameters for the front surface will come next in the output.

To be followed by the back surface numbers. Then the file or static numbers for the semiconductor will be presented.

If the grid option was chosen the beginning and ending points of the grid will be output in the following form

$$X_{11} \quad Y_{11} \quad X_{ur} \quad Y_{ur}$$

Then the outer reflectivity will be given along with the number of photons which were absorbed due to this grid. The inner reflectivity values will be given in a similar manner.

The name of the spectrum file will be given next in the output file with the energy density that the user requested. If the program was run in the distance mode then the energy density will not be given. If the program was not run in the distance mode then the next values output will be the cumulative number of photons absorbed and the maximum number that could be absorbed. This maximum number is calculated by finding the number of photons available at each wavelength where the absorption coefficient is non-zero.

If the program has been run in the distance mode then the next output is the percentage of rays remaining as a function of the number of passes through the cell. The last value will be the total average distance the ray traced before exciting the cell. This value divided by the thickness of the cell gives the relative improvement of the cell structure over a flat cell of the same dimensions. The last output value for this case is the average reflectivity of the surface. This value is found by R^n where n is the number of bounces, the number of times a reflected ray can strike the surface before it is lost out of the cell.

If a one dimensional profile mode was the option chosen then the output will consist of the cumulative and actual absorption which takes place at each node. In addition the output will contain the number of photons lost due to refraction out the sides of the cell, the front of the cell, and the number lost out the back of the cell.

In a two or three dimensional mode the output will consist of cumulative absorption on a small normalized X-Y plane at a constant Z value. Since these are really a three or four dimensional plots there will be values at each value of Z where a node was placed.